

MARINE GEOPHYSICAL APPLICATIONS OF SEASAT ALTIMETRY AND  
THE LITHOSPHERIC STRUCTURE OF THE SOUTH ATLANTIC OCEAN

by

ADAM PAUL FREEDMAN

B.S. Physics, Yale University  
(1980)

Submitted to the Department of  
Earth, Atmospheric, and Planetary Sciences  
in Partial Fulfillment of the Requirements  
For the Degree of

DOCTOR OF PHILOSOPHY

at the

MASSACHUSETTS INSTITUTE OF TECHNOLOGY

February 1987

© Massachusetts Institute of Technology 1987

Signature of Author: . . . *Adam Paul Freedman* . . . . .  
Department of Earth, Atmospheric, and Planetary Sciences  
February, 1987

Certified by: . . . . .  
Thesis Supervisor

Accepted by: . . . . .  
Chairman, Departmental Committee on Graduate Students

**WITHDRAWN**  
**FROM**  
**MIT LIBRARIES**

Lindgren

Dedicated to my grandfather

Dr. Louis Freedman

who knew I could.

## Table of Contents

List of Figures . . . . .	6
List of Tables . . . . .	9
Acknowledgements . . . . .	10
Biographical Sketch . . . . .	11
Abstract . . . . .	12
Chapter 1. Introduction . . . . .	13
1.1 Satellite Altimetry . . . . .	14
1.2 The Geoid . . . . .	19
1.3 Geophysical Applications of Altimetry . . . . .	24
1.4 Marine Geophysical Problems Considered in This Thesis . . . . .	27
1.5 Additional Comments . . . . .	31
1.6 References . . . . .	34
Chapter 2. Seasat-Derived Gravity Over the Musicians Seamounts . . . . .	37
2.1 Abstract . . . . .	38
2.2 Introduction . . . . .	39
2.3 Geophysical Setting . . . . .	43
2.4 Data Adjustment and Interpolation . . . . .	48
2.5 Determination of Gravity From the Geoid and Bathymetry . . . . .	55
2.6 Resolution and Accuracy . . . . .	60
2.7 Results . . . . .	62
2.8 Discussion . . . . .	67
2.9 Acknowledgements . . . . .	74
2.10 References . . . . .	75
2.11 Plate Captions . . . . .	78
Color Plates (with black and white copies) . . . . .	80

Chapter 3. Geoid Anomalies Over Two South Atlantic Fracture Zones . . .	87
3.1 Abstract . . . . .	88
3.2 Introduction . . . . .	90
3.3 Geophysical Setting . . . . .	94
3.4 The Data . . . . .	98
3.4.1 Seafloor Ages . . . . .	98
3.4.2 Seasat Data . . . . .	101
3.4.3 Altimetry Profiles . . . . .	102
3.5 The Geoid Steps . . . . .	111
3.5.1 Step Estimation Procedure . . . . .	111
3.5.2 Sample Profile Fits . . . . .	113
3.5.3 Step Height Versus Age . . . . .	115
3.6 Discussion . . . . .	121
3.7 Geoid and Gravity Maps . . . . .	125
3.8 Conclusions . . . . .	132
3.9 Acknowledgements . . . . .	134
3.10 References . . . . .	135
Chapter 4. Intermediate-Wavelength Depth and Geoid Anomalies of the South Atlantic Ocean . . . . .	139
4.1 Abstract . . . . .	140
4.2 Introduction . . . . .	141
4.2.1 Geoid and Depth Anomalies . . . . .	143
4.2.2 Geographic Area . . . . .	145
4.3 Depth Anomalies . . . . .	148
4.3.1 Bathymetry . . . . .	148
4.3.2 Sediment Corrections . . . . .	150
4.3.3 Lithospheric Ageing . . . . .	157

4.3.4	Theoretical Depths . . . . .	162
4.3.5	Residual Depth Anomalies . . . . .	165
4.4	Geoid Anomalies . . . . .	171
4.4.1	Seasat Data . . . . .	171
4.4.2	Long-Wavelength Geoid . . . . .	172
4.4.3	Corrected Geoid . . . . .	174
4.4.4	Theoretical Geoid . . . . .	180
4.4.5	Residual Geoid Anomalies . . . . .	184
4.5	Discussion . . . . .	188
4.5.1	Visual Correlation . . . . .	188
4.5.2	Quantitative Correlation . . . . .	192
4.6	Acknowledgements . . . . .	201
4.7	References . . . . .	202
Chapter 5.	Summary and Conclusions . . . . .	207
5.1	Seamounts and Compensation Studies . . . . .	208
5.2	South Atlantic Fracture Zones and the Surrounding Lithosphere . . . . .	209
5.3	Mantle Convection Beneath the South Atlantic . . . . .	211
5.4	Implications for the Lithosphere . . . . .	213
5.5	Implications for Future Altimetry Studies . . . . .	218
5.6	References . . . . .	220

## List of Figures

## Chapter 1.

- Figure 1. Schematic of Seasat data collection system. . . . . 17
- Figure 2. Schematic cross-section of the crust and mantle. . . . . 22

## Chapter 2.

- Figure 1. Geoid and gravity anomalies versus width for a circular Gaussian seamount. . . . . 42
- Figure 2. Map of northern Pacific Ocean showing location of the Musicians seamounts. . . . . 44
- Figure 3. Bathymetric map of the Musicians seamount province. . . . . 45
- Figure 4. Seasat track coverage over the Musicians province. . . . . 49
- Figure 5 (a,b). Synthetic gravity anomalies over a Gaussian seamount. . . . . 63
- Figure 6. Bathymetry, geoid, and gravity of profiles interpolated from the maps. . . . . 68
- Figure 7 (part 1). Comparison of Seasat-derived gravity and predicted gravity along profiles. . . . . 69
- Figure 7 (part 2). . . . . 70
- Plate 1 (a,b,c). Comparison of gridding and filtering techniques on gravity anomaly maps. . . . . 80
- Plate 2. Geoid map of the Musicians region. . . . . 81
- Plate 1 (black-and-white versions). . . . . 82
- Plate 2 (black-and-white version). . . . . 82
- Plate 3. Seasat-derived gravity field over the Musicians region. . . . . 83
- Plate 4 (a,b,c). Gravity fields predicted from the bathymetry. . . . . 83
- Plate 3 (black-and-white version). . . . . 85
- Plate 4 (black-and-white versions). . . . . 85

## Chapter 3.

Figure 1.	Reference map of area surrounding the Falkland-Agulhas fracture zone. . . . .	95
Figure 2.	Reference map of area surrounding the Ascension fracture zone. . . . .	97
Figure 3 (a,b).	Ocean floor ages around each fracture zone. . . . .	100
Figure 4 (a).	Altimetry profiles across the west branch of the Falkland-Agulhas fracture zone. . . . .	103
Figure 4 (b).	Altimetry profiles across the east branch of the Falkland-Agulhas fracture zone. . . . .	104
Figure 5 (a).	Altimetry profiles across the west branch of the Ascension fracture zone. . . . .	109
Figure 5 (b).	Altimetry profiles across the east branch of the Ascension fracture zone. . . . .	110
Figure 6.	Four representative altimetry profiles with their geoid step fits. . . . .	114
Figure 7 (a,b).	Step height versus mean age along the Falkland-Agulhas fracture zone. . . . .	117
Figure 8 (a,b).	Step height versus mean age along the Ascension fracture zone. . . . .	118
Figure 9 (a,b).	Comparison of observed and theoretical geoid step heights as a function of age. . . . .	119
Figure 10 (a,b).	Geoid and gravity surrounding the Falkland-Agulhas fracture zone. . . . .	127
Figure 11 (a,b).	Geoid and gravity surrounding the Ascension fracture zone. . . . .	130

## Chapter 4.

Figure 1.	Map of the South Atlantic Ocean. . . . .	146
Figure 2.	Bathymetric map derived from DBDB5 data. . . . .	149
Figure 3.	Sediment thickness map. . . . .	151
Figure 4.	Bathymetry corrected for sediment loading. . . . .	155
Figure 5.	Age map of the South Atlantic . . . . .	163

Figure 6.	Comparison of observed and theoretical depth profiles. . . . .	164
Figure 7.	Residual depth anomaly map. . . . .	166
Figure 8 (a,b).	Low-pass filtered versions of the residual depth. . . . .	170
Figure 9.	Seasat-derived geoid map. . . . .	173
Figure 10.	GEM 9 long-wavelength geoid. . . . .	175
Figure 11.	Corrected geoid map. . . . .	177
Figure 12 (a,b).	Alternate corrected geoid maps. . . . .	179
Figure 13.	Comparison of observed and theoretical geoid profiles. . . . .	181
Figure 14.	Residual geoid anomaly map. . . . .	185
Figure 15 (a,b).	Alternate residual geoid maps. . . . .	187
Figure 16.	Residual geoid made from a high-pass filtered theoretical geoid. . . . .	189
Figure 17.	Scatter plot and profile location map. . . . .	194
Figure 18.	Scatter plots of geoid anomaly versus corrected depth. . . . .	196
Figure 19.	Schematic diagram of Airy compensation both shallow and deep. . . . .	198
Figure 20.	Comparison of observed geoid with the geoid predicted from depth. . . . .	200

## List of Tables

## Chapter 2.

Table 1. Crossover Minimization Technique . . . . . 51

Table 2. Values of Parameters . . . . . 59

## Chapter 3.

Table 1. Parameter Definitions and Values . . . . . 93

Table 2. Summary of Profile Information . . . . . 106

## Chapter 4.

Table 1. Parameters and Their Values . . . . . 154

## Acknowledgements

ב"ה

Many people, from the technical realm through the academic and social realms, have helped to make this thesis a reality. For all their help, I am grateful.

Barry Parsons, my advisor, was instrumental in suggesting research problems, helping me to formulate methods for attacking them, critically reviewing my manuscripts, and providing extensive editorial advice.

To all who contributed to the development of the SSCONT computer program for processing the massive amounts of Seasat data, I am very thankful--especially to Linda Meinke and Steve Daly. Though they may not realize how helpful they have been, my officemates Mavis Driscoll, Bernard Celerier, and Paul Filmer have helped me through many a difficult time. I wish to thank Dorothy Frank and Tina Freudenberger, who typed large parts of this manuscript, as well as the other administrative and headquarters staff members who pushed many of the bureaucratic boulders out of my way (or told me how to detour around them).

I wish to sincerely thank the extended family of Theo Bayit, who helped make my sojourn as a graduate student in Boston a time of incomparable friendship and support. My parents, David and Rhoda Freedman, I cannot thank enough; their trust and patience have been phenomenal. Lastly, my wife Joy. With her I have shared the exultation and the suffering; our efforts together comprise this thesis. I sincerely thank her.

## Biographical Sketch

Adam Paul Freedman was born in Camden, New Jersey in 1958. He spent most of his youth in Cinnaminson, N.J., where he graduated as valedictorian with top honors at Cinnaminson High School in 1976. A National Merit Scholar, Adam entered Yale University that autumn. Active as president and treasurer of the Young Israel House at Yale, and dabbling in artistic pursuits with the Yale Gilbert & Sullivan Society and the Kochavim Israeli Dance Troupe, he still found time to earn the Bachelor of Science degree in Physics, cum laude, with distinction in the major in 1980.

Entering the Massachusetts Institute of Technology, he planned to specialize in planetary sciences. After two years, Adam reversed his gaze and began thesis research in marine geophysics. Along the way he was nominated for the Goodwin Medal for graduate teaching and was elected to Sigma Xi.

After completing his doctorate, Adam plans to begin research work at the Jet Propulsion Lab in Pasadena, California.

His publications include:

"Weak dynamical effects in the Uranian ring system," by Adam P. Freedman, Scott Tremaine, and J.L. Elliot, The Astronomical Journal, Vol. 88:7, pp. 1053-1059, July 1983.

"Seasat-derived gravity over the Musicians seamounts," by Adam P. Freedman and Barry Parsons, Journal of Geophysical Research, Vol. 91:B8, pp. 8325-8340, July 1986.

MARINE GEOPHYSICAL APPLICATIONS OF SEASAT ALTIMETRY AND  
THE LITHOSPHERIC STRUCTURE OF THE SOUTH ATLANTIC OCEAN

by  
ADAM PAUL FREEDMAN

Submitted to the Department of Earth, Atmospheric, and Planetary Sciences  
on February 18, 1987 in partial fulfillment of the requirements  
for the Degree of Doctor of Philosophy in Geophysics

ABSTRACT

Seasat altimetry data, because of their uniform and worldwide coverage, have been used in conjunction with other less comprehensive data sets to investigate three distinct problems in marine geophysics. In the first study, we examined the two-dimensional gravity field over the Musicians seamount province in the Pacific Ocean with the objective of estimating the form of crustal compensation, either local or regional, of the seamounts. The algorithms that produce maps from along-track altimetry data were tested, and frequency domain filters were developed that yield the gravity field from the geoid and predict the gravity from the bathymetry. Estimates of the form of compensation were made by comparing maps of the Seasat-derived gravity to gravity predicted for compensated bathymetry. The seamounts appear to be regionally compensated by flexure of the lithosphere with an effective elastic thickness of  $\sim 5$  km, though local variations suggesting a weaker elastic plate are also seen. The seamounts appear to have formed on young lithosphere near a mid-ocean ridge, probably over an extended period of time.

In the second study, altimetry profiles across two fracture zones in the South Atlantic were examined. By estimating the height of step-like variations in the geoid over the fracture zones, we hoped to constrain the lithospheric thermal plate thickness in the South Atlantic. The geoid profiles are very noisy, making geoid steps hard to obtain, but the variations in step height with age of the lithosphere suggest that standard thermal plate models do not control the geoid variations in this ocean. Rather, small-scale convection or tectonic surface deformation can better explain the geoid observations. This study underscores the need for better bathymetric information in the South Atlantic, especially in the younger, central portions of the ocean where fracture zones can best be observed.

The third study focused on the intermediate-wavelength depth and geoid of the South Atlantic Ocean. By removing as many lithospheric sources of depth and geoid variation as possible (such as sediment loading and lithospheric cooling), the residual depth and geoid anomalies should be diagnostic of convection within the mantle. The geographic correlation of depth and geoid anomalies appears good. Large geoid lows are associated with basins, while more modest geoid highs appear over aseismic ridges and other positive depth anomalies. Quantitative estimates of this correlation strongly favor compensation depths in or below the lower lithosphere, consistent with mantle convection on intermediate length scales.

Thesis Supervisor: Dr. Barry Parsons  
Title: Assistant Professor of Marine Geophysics

## Chapter 1. Introduction

### 1.1 Satellite Altimetry

The remote sensing of the earth from orbiting satellites is a powerful method of collecting geophysical data that possesses many advantages over ground-based in-situ observations and over remote sensing from aircraft. Foremost among them is the ability to survey the entire globe in a period of time and at a relative cost considerably less than would be necessary at the earth's surface. Remote sensing from space in the visual, infrared, and radio wavelengths has advanced our knowledge of the earth tremendously, especially in regions particularly distant or inaccessible from centers of human population.

Most of these remote sensing systems have been passive, collecting electromagnetic radiation emanating naturally from the earth. A radar altimeter mounted on board a satellite is an example of an active remote sensing device. It transmits a signal down towards the earth and monitors the energy that bounces back. Radar altimeters enable the precise determination of the distance between a satellite and the point of the earth's surface directly beneath. If the position of the spacecraft is accurately known, this distance gives the height of the subsatellite point, yielding a measure of the topographic relief over land and the height of the surface of the sea over the oceans. Over a period of a few months, a single satellite radar altimeter can determine the height of the ocean's surface over an area that would take decades from traditional ocean-going ships.

The height or shape of the ocean surface is influenced by many geophysical factors. At the smallest scales, air-water interactions produce waves and sea swells. Currents and tides perturb the ocean's surface over much longer distances. The largest sea surface height variations are caused by the earth's gravitational field, however. Since water is free to

flow in the direction of the strongest gravitational tug, it will tend to pile up where there is excess mass (positive density anomalies) on or beneath the ocean floor, and to flow away from mass deficits (negative density anomalies). These sea surface height variations can exceed many tens of meters and appear on many different length scales, or wavelengths.

Since the mid-1970's, a number of increasingly precise and accurate altimeters have been placed into orbit. The earliest measurements from Skylab [Leitao and McGoogan, 1975] taken over short segments of single orbits revealed the potential of satellite altimetry for viewing the gravitational effects of significant bathymetric features such as deep-sea trenches, seamounts, plateaus, and aseismic ridges. The first dedicated satellite altimetry mission was GEOS 3 [Stanley, 1979]. Launched in 1975, GEOS 3 obtained extensive sea surface height measurements with a vertical resolution of 50 cm or better and enabled satellite altimetry to be used extensively for geophysical analysis. Since the satellite could not store altimetry data while it was out of range of a tracking station, large expanses of ocean were not comprehensively covered, however.

In 1978, the Seasat mission, carrying a more precise altimeter, was launched [Lame and Born, 1982]. Although it only returned data for three months, its demise caused by a massive short-circuit, it provided global coverage of the sea surface with unprecedented resolution. Seasat measured sea surface heights with a vertical precision of  $\sim 10$  cm and a horizontal resolution of 2 to 12 km, depending on the sea state. Geographic coverage extended to  $\pm 72^\circ$  of latitude, with a data spacing along each arc of  $\sim 6.7$  km. Its short life limited the density of its coverage, however, and data gaps as large as 120 km can appear between arcs, especially near the equator. Present and future orbiting altimeters, such as those on Geosat

and Topex/Poseidon, promise to fill in these gaps and yield even more precise knowledge of the sea surface. Altimeters on planetary spacecraft are expected to provide even better topography of the surfaces of Venus and Mars in the not-too-distant future, also.

The radar aboard Seasat emitted a short (3 ns), narrow, 13.5 GHz pulse from an orbital altitude of 800 km (Figure 1). After bouncing off the ocean surface, the signals were received by the satellite a few milliseconds later. The one-way travel time yields the approximate distance between the satellite and the ocean surface below, but in order to determine the sea surface height, the position of the satellite needs to be precisely known and many other adjustments to the travel time need to be made.

The sea surface height  $h_{ss}$  measured relative to some reference level (see below, section 1.2) is determined from

$$h_{orb} = h_{alt} + h_{ss} + h_i + h_a + h_{os} + \epsilon \quad (1)$$

[Tapley et al., 1982] where  $h_{orb}$  is the height of the satellite above the reference level based on knowledge of its orbit,  $h_{alt}$  is the satellite height measured by the altimeter,  $h_i$  is the effect on the height measurement of instrument errors,  $h_a$  is the effect on the height measurement of atmospheric delays,  $h_{os}$  is the effect of ocean surface-radar pulse interactions on the height measurements, and  $\epsilon$  is random measurement noise (Figure 1). The atmospheric delays include corrections for the ionosphere, the atmospheric air mass, and atmospheric water vapor. The ocean surface corrections are due to the effects of sea state, wave height and wave shape. All these errors can be reliably modeled and removed, leaving residual errors whose total is less than 10 cm over a wide range of wavelengths. Liquid water in clouds and rain and the effects of storms

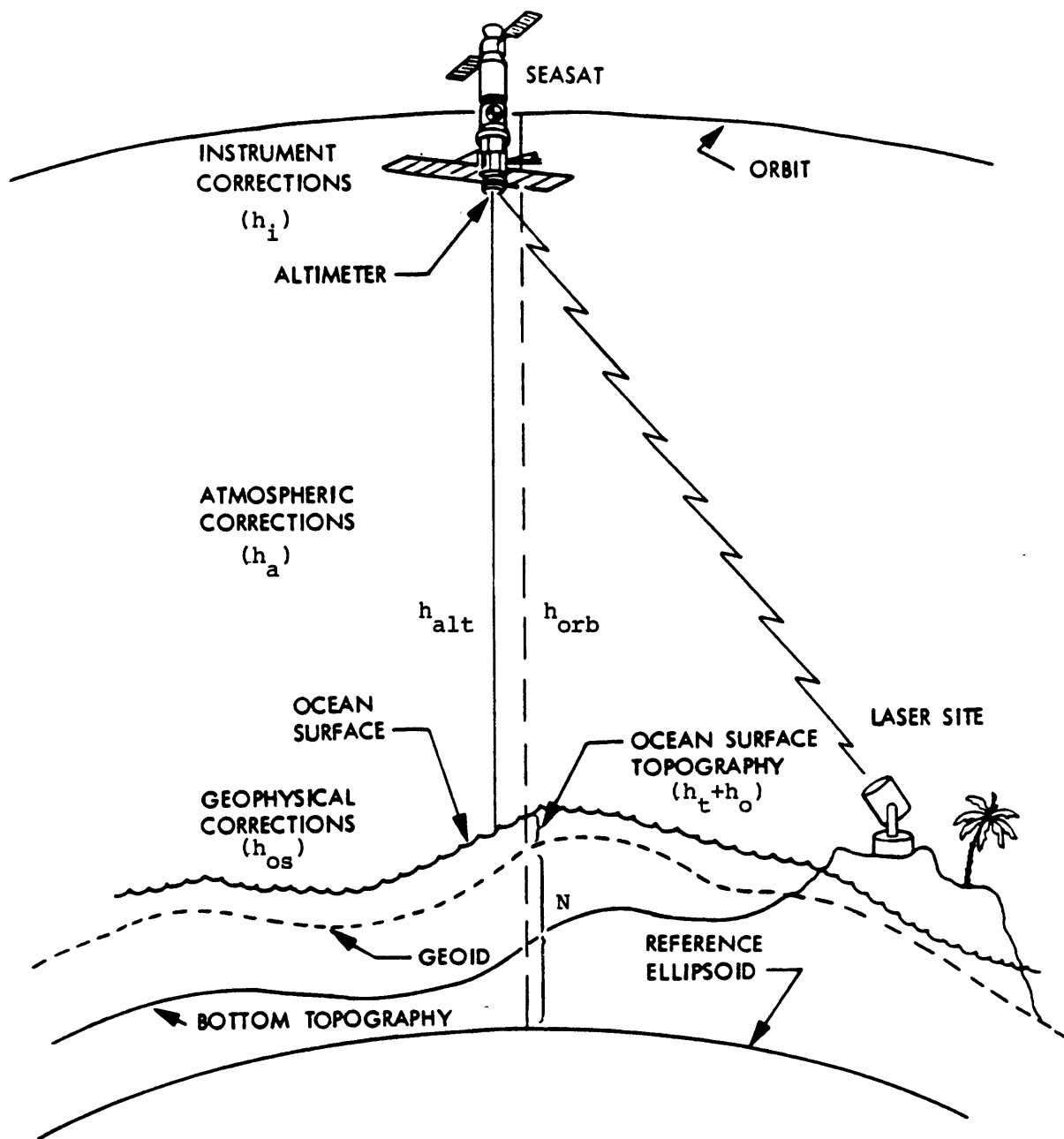


Figure 1. Schematic of Seasat data collection system [after Tapley *et al.*, 1982]. Some of the many height adjustments involved in the computation of sea surface and geoid heights are shown. See text for further description.

usually result in noticeably bad data which can be eliminated on a point-by-point basis. Anomalous data points are also produced by radar reflections off sea ice; these too can be eliminated fairly easily.

The largest errors remaining in the determination of sea surface height are those due to uncertainties in the orbit position of the satellite (ephemeris errors). These errors result from uncertainties in the earth's gravity field, atmospheric drag and solar radiation forces acting on the satellite, and uncertainties in the positions of the tracking stations. These errors can lead to over 2 m uncertainty in the height of the satellite, but they are principally of long wavelength, i.e., they only change noticeably over distances of many thousands of kilometers. Thus they can be treated as simple bias and trend errors of the Seasat altimetry arcs and can be substantially removed by adjusting the arcs to minimize the differences in sea surface heights at the intersection points of ascending and descending arcs. These crossover corrections are described more fully in Chapter 2.

The sea surface height is a sum of gravitational, oceanographic, and meteorological effects. This is represented by

$$h_{SS} = N + h_t + h_o \quad (2)$$

where  $N$  is the height of the ocean surface above the reference level due solely to terrestrial density anomalies and their gravitational perturbations, otherwise called the geoid height (see below, section 1.2),  $h_t$  are the corrections due to solid earth and ocean tides, and  $h_o$  includes the effects of oceanographic currents and eddies, large-scale wind effects, and the effects of atmospheric pressure variations on sea surface height. These are described more fully by Wunsch and Gaposchkin [1980]. Tidal effects can be modeled well and removed in most geographic areas, and the

other oceanographic effects tend to have magnitudes less than 1 m and wavelengths of thousands of kilometers. In most cases, the oceanographic terms are so much smaller than the geoid heights that they can safely be ignored by those intent on studying the geoid. But near large boundary currents, such as the Gulf Stream, the oceanographic terms may be substantial.

## 1.2 The Geoid

On a non-rotating, perfectly spherical, homogeneous planet floating alone in space, surfaces of equal gravitational potential would be spheres about the planet. If the planet were covered by water, this global ocean would be uniformly deep and its surface would coincide with a particular equipotential surface where the force of gravity would be constant and perpendicular to the ocean's surface at all points. If the planet were rotating, centrifugal force would cause the water to flee the poles and pile up at the equator, but the water would flow only until the combined gravitational and centrifugal forces were again perpendicular to the ocean surface everywhere on this global sea. If this planet were not quite spherical and homogeneous, but had an oblate shape and small density anomalies scattered over its surface and through its interior, the water would again flow until the total sum of forces were perpendicular to the ocean's surface. On the earth, this equipotential surface that corresponds to sea level, determined solely by the terrestrial mass distribution and the effects of the earth's rotation, is known as the geoid [see e.g. Heiskanen and Moritz, 1967; Turcotte and Schubert, 1982].

To determine changes in geoid height (undulation of the geoid) as well as variations in height of the more general sea surface, a reference surface must be defined. The traditional reference surface used for most

measurements of geoid height and satellite altitude is the mean ellipsoid, a spheroidal surface that includes the flattening due to earth's rotation and equatorial bulge and roughly corresponds to mean geoid height. For geodynamic purposes, perhaps a better reference ellipsoid would be that constructed under the assumption that the earth is in perfect hydrostatic equilibrium. Departures from this ellipsoid would then be indicative of either dynamically maintained density anomalies within the earth, or of density variations maintained by the finite strength of earth materials. Differences between these two reference surfaces appear only at the longest wavelengths. At smaller length scales, geoid and sea surface heights show essentially a shift in zero level depending on the reference ellipsoid used; removing a mean value or looking at peak-to-peak variations obviates the decision of which reference ellipsoid to use.

Density variations anywhere within the earth will contribute to variations in the geoid height. Since the gravitational potential anomaly of a perturbing mass is inversely proportional to the distance to the mass, these disturbing potentials will tend to be attenuated with depth. Thus deeper masses will lead to smaller geoid height variations than identical masses closer to the surface. In addition, deeper density anomalies will tend to cause smoother geoid variations, as shorter-wavelength geoid components are more strongly attenuated with depth.

Any surface geoid anomaly can theoretically be produced by one of an infinite number of density distributions within the earth. For example, a slowly varying, shallow density anomaly can have the identical effect on the geoid as a deeper, more compact mass concentration with a much greater density contrast. One cannot, therefore, determine the earth's interior mass distribution by simply inverting the gravity or geoid observed at the

earth's surface.

If we know the depth and lateral extent of a mass anomaly, we can predict what its effect on the geoid will be. We can divide the total geoid anomaly into individual components produced by various source terms with different spatial distributions at different depths as follows:

$$N_T = N_D + N_L + N_S \quad (3)$$

where the total geoid  $N_T$  is produced by mass anomalies at depth in the earth,  $N_D$ , within the lithosphere,  $N_L$ , and at the surface,  $N_S$  (Figure 2). These are somewhat loose divisions, and many perturbing masses may span more than one depth region.

Surface anomalies are those caused by topography on continents or on the ocean floor, density variations within the crust, either thermal or chemical, and variations in depth of the Moho, which defines the thickness of the crust. These geoid anomalies are often of short wavelength (less than a few hundred kilometers) and closely reflect the topography that generates them. Some surface anomalies, however, such as thickened crust, can extend over much larger spatial scales.

Lithospheric anomalies are produced below the crust, but are often integrally related to topographic or crustal features. Variations in the thermal structure of the lithosphere produced, for example, by the conductive cooling of the earth's surface layers or by excess heat input from below will result in substantial geoid height variations. Lithospheric anomalies may also be the result of tectonic stress and strain or geochemical variations within the outermost 50 to 100 kilometers of the earth. These geoid anomalies tend to appear over short and intermediate wavelengths, i.e., they have less than a few thousand kilometers lateral extent. The shorter-wavelength anomalies tend to be maintained by the

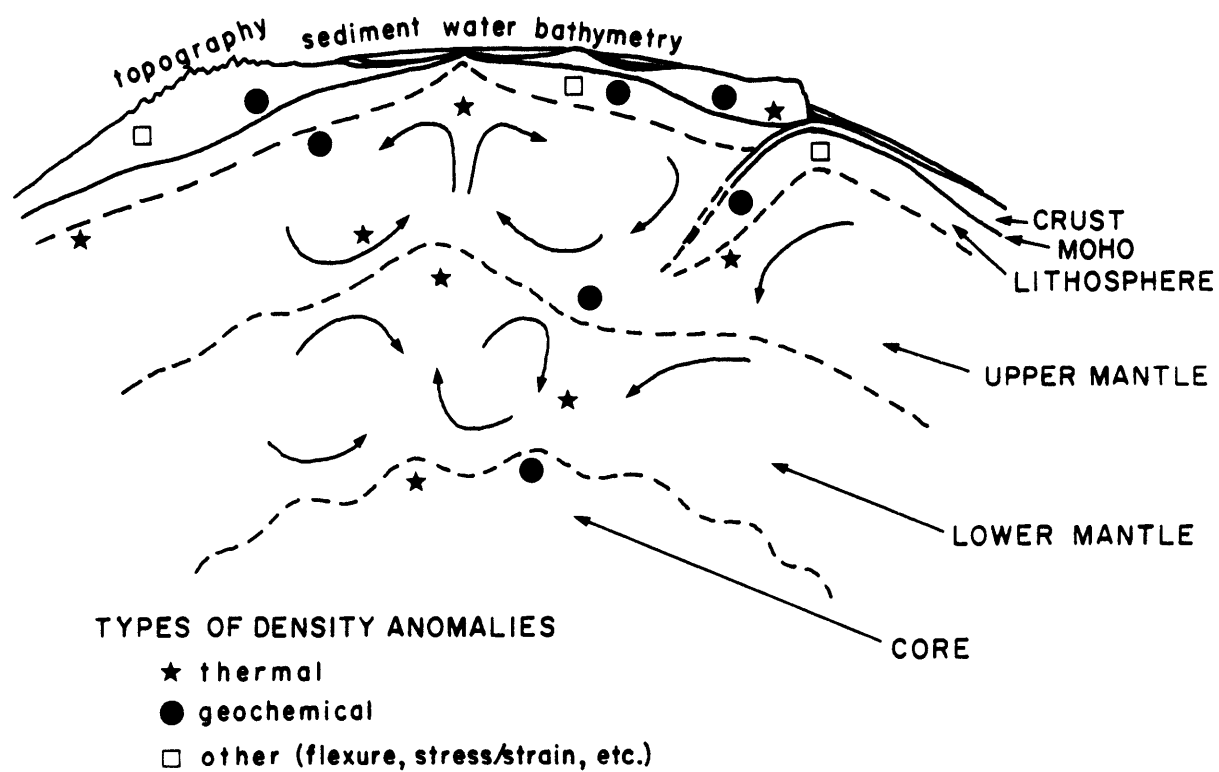


Figure 2. Schematic cross-section of the crust and mantle of the earth showing the types and relative depths of density anomalies which may contribute to surface geoid height variations.

finite strength of the lithosphere, while the longer wavelengths are usually supported by buoyancy forces within or at the base of the lithosphere.

Deep geoid anomalies may derive from the upper or lower mantle or from the core-mantle boundary. These anomalies may be produced by density variations of a thermal and/or chemical nature, but are thought to be dynamically maintained by flow within the mantle. They are generally of intermediate and long wavelengths. The largest observed geoid anomalies are probably produced at depth, but many deep density variations will exhibit only subtle or negligible geoid signals.

As we mentioned above, there is no unique solution to the inverse problem of determining the source region of a given geoid anomaly. With the addition of independent constraints on the size and location of density anomalies, however, the geoid can be used to study earth structure. Many of these constraints are primarily theoretical. Models of the lithosphere and mantle, for example, place limits on the temperature structure, viscosity, and rheology of these regions; hence, they limit the size, magnitude, and depth of possible density anomalies.

More solid constraints on density variations are provided by geophysical observations of many types. Simple knowledge of topography and bathymetry, density of surface rocks, and surface heat flow are of primary importance in studying crustal density variations. Seismic observations yield the thickness of the crust and of sedimentary layers, and can indicate the presence of density anomalies, melted rock, or low velocity zones within or beneath the lithosphere. Seismic tomography is currently providing independent density information throughout the entire mantle.

These observations are all invaluable in characterizing the nature of the density variations that produce geoid anomalies. Part of the puzzle of deciphering geoid anomalies thus lies in determining which additional observable data are useful and practicable for the specific problem being considered. As we discuss the wide variety of geophysical research that has utilized geoid height data, it is important to keep in mind the quality of this auxiliary information and whether it is theoretical or observational in nature.

### 1.3 Geophysical Applications of Altimetry

Satellite altimetry has been applied towards a multitude of problems in marine geophysics. We briefly review some of these problems below. This is not an all-inclusive list, by any means; rather, we highlight a few of the geophysical uses of altimetry with an emphasis on those that are more relevant to the research work presented in this thesis.

The comprehensive global coverage of Seasat combined with the tendency of the short- and intermediate-wavelength geoid to correlate closely with bathymetric features make altimetry data useful for charting unknown features in the oceans. Seasat altimetry has been particularly important in the sparsely surveyed southern oceans, where even first-order bathymetry is not well known. Dixon and Parke [1983] and Sandwell [1984] used Seasat altimetry for close-up looks at the Pacific and Indian oceans, noting seamounts, plateaus, and other features for the first time. Sailor and Okal [1983] used the mapping ability of the altimetry to augment a seismic study of the tectonic structure of a poorly surveyed area of the Pacific. Other studies have focused on the capability to detect seamounts with the altimetry data [Lambeck and Coleman, 1982; Lazarewicz and Schwank, 1982] or

to use the data to predict bathymetry [Dixon et al., 1983].

The question of the isostatic compensation mechanism of submarine features is one that comprehensive knowledge of the gravity or geoid together with comprehensive bathymetry can readily address. Compensation of seamounts and other features at shallow depths by flexure of the lithosphere has long been modeled using surface ship gravity data. Studies such as Watts [1979] and Cazenave et al. [1980] extended this analysis with satellite altimetry. Watts and Ribe [1984] present a summary of much recent work on seamount compensation. McAdoo and Martin [1984] and others have used the geoid to study the flexure of the lithosphere seaward of deep-sea trenches. The compensation of seamount chains and aseismic ridges has also been examined using altimetry [Angevine and Turcotte, 1983; Cazenave and Dominh, 1984].

Compensation beneath the Moho is more difficult to investigate. Bathymetry and theoretical ideas about the physical behavior of the lithosphere are often augmented by heat flow, petrologic and seismic data. Mid-ocean swells and hotspots, such as Hawaii [Crough, 1978; McNutt and Shure, 1986] and Cape Verde [Crough, 1982], thought to be thermally compensated within or below the lithosphere, are tempting targets for study with satellite altimetry, as are larger oceanic regions [Sandwell and Poehls, 1980; Kogan et al., 1985] whose compensation mechanisms are uncertain.

The sensitivity of the geoid to density variations within the lithosphere has made satellite altimetry a powerful tool for probing the thermal structure and evolution with time of the lithosphere. In these studies, the bathymetry is either of limited usefulness or not well known, so geoid data are supplemented by theoretical models of the thermal and rheological structure and evolution of the lithosphere. The thickening

with age of the lithosphere and its effect on the geoid have been studied by Haxby and Turcotte [1978], Turcotte and McAdoo [1979], and Sandwell and Schubert [1980]. A number of studies have used geoid height variations across fracture zones to constrain the thickness and thermal structure of the lithosphere [Crough, 1979; Detrick, 1981; Sandwell and Schubert, 1982; Cazenave et al., 1983]. Parmentier and Haxby [1986] have recently used the geoid at fracture zones to study the thermal contraction of the lithosphere as it cools.

Features such as mid-ocean swells may yield apparent compensation depths within the lower lithosphere. Parsons and Daly [1983] have shown, however, that if features are supported dynamically, compensation actually occurs over a large depth region extending from the lithosphere through the upper mantle. To get a feel for the pattern of density variations within the upper mantle believed to be produced by convective flow of mantle rock over geologic time, a number of studies have examined the pattern of depth and geoid anomalies at intermediate wavelengths in the oceans. Theoretical models of convection predict certain correlations of the geoid with bathymetry, but lack of knowledge of mantle rheological and physical properties limit their reliability. McKenzie et al. [1980] and Watts et al. [1985] have studied the Pacific, while Jung and Rabinowitz [1986] and Cazenave et al. [1986] have examined the North Atlantic and global oceans, respectively, looking for correlations of depth and geoid anomalies that might be indicative of convection. Recent analysis of Seasat altimetry by Haxby and Weissel [1986] yields strong evidence for small-scale convection occurring just beneath the lithosphere in the Pacific.

Other studies have tried to explore convective patterns in the lower mantle by looking for correlations between deep subduction and the geoid

[Chase, 1979; Hager, 1984] or hotspot positions and the geoid [Crough and Jurdy, 1980]. The powerful technique of seismic tomography, which provides an independent estimate of lateral density variations with depth, is being supplemented with geoid data to explore in more detail the deep structure of the earth [Hager et al., 1985]. This latter work holds great promise for future studies of mantle convection.<sup>†</sup>

#### 1.4 Marine Geophysical Problems Considered in This Thesis

In the present work, we examine three distinct problems in marine geophysics, utilizing Seasat altimetry as a primary observational tool. Each problem emphasizes different wavelength bands and employs different auxiliary data sets in somewhat different geographic locations, but all are united by the power of satellite altimetry to provide geographically comprehensive, high-resolution information on the gravity field at sea.

In Chapter 2, we investigate the isostatic compensation of the Musicians seamounts, a small group of submarine mountains located in the Pacific Ocean north of Hawaii. They are noteworthy in that their bathymetry is particularly well known from detailed ship surveys. The quality of the bathymetry and altimetry allow a detailed two-dimensional estimate of the nature and extent of compensation of these seamounts. Prior to the present study, compensation estimates for these seamounts utilized only the altimetry along individual Seasat arcs and were based on one-dimensional flexural models. Chapter 2 contains one of the first true two-dimensional compensation studies using altimetry data; as such, it contributes

---

<sup>†</sup>These last studies looked at long-wavelength features and did not in fact use satellite altimetry. They used instead spherical harmonic expansions of the gravity field determined from satellite tracking. They are included here for completeness.

substantially to our knowledge of the ocean floor in the Pacific.

Since the Musicians seamounts are of short wavelength (on the order of a few hundred kilometers at most), compensation is expected to be fairly shallow, i.e., at the Moho, and to be somewhat regionally distributed around the seamounts by the flexure of the lithosphere. Additional information about the seamounts and the crust on which they stand is provided by limited magnetic, paleomagnetic, and petrologic age data. Using all this information, we estimate the effective elastic thickness or rigidity of the lithosphere supporting the seamounts and discuss its tectonic implications. Our results confirm previous work indicating that the seamounts formed on fairly young crust; in addition, we are able to detect local and regional variations in the ages of the seamounts relative to the age of the lithosphere.

The relatively small sizes of these seamounts, their small geoid anomalies, and their well known positions provide a stringent test of the short-wavelength resolving ability of our Seasat data. The two-dimensional interpolation and gridding algorithms that we use to map the geoid are also described and tested in this chapter. Since the compensation of these seamounts is more easily studied with gravity rather than geoid anomalies, we also discuss the filters that we use to predict the gravity field from either the geoid or the bathymetry. Even in an area like the Musicians seamounts where bathymetry is unusually well known, significant features may still be missed. We therefore examine our geoid and gravity maps for indications of uncharted or poorly charted seamounts.

In Chapter 3, we examine the variations in geoid height with age of the ocean floor across two major fracture zones in the South Atlantic ocean. Across a fracture zone, lithosphere of two different ages and

thermal structures is juxtaposed. The resulting geoid anomaly is expected to take the form of a step, descending in height as one crosses from the younger to the older side of the fracture zone. Studies of geoid anomalies across Pacific fracture zones have successfully been able to constrain the local thermal structure of the lithosphere, but more recent work suggests that certain areas may exhibit anomalous thermal structure [Cazenave, 1984]. Chapter 3 describes the first attempt to characterize South Atlantic fracture zones and the South Atlantic lithosphere in the manner used in the Pacific.

We examine the Ascension fracture zone and the Falkland-Agulhas fracture zone in the South Atlantic using the along-track Seasat altimetry as our primary data set. Since the age of the ocean floor is reasonably well known in the South Atlantic, the set of altimetry arcs traversing these fracture zones provides an evolutionary sequence of geoid anomalies as we proceed away from the mid-ocean ridge. Using theoretical models for the temporal evolution of the lithosphere together with the known lithospheric ages and a limited knowledge of South Atlantic bathymetry, we attempt to set limits on the thermal structure of the lithosphere in this poorly studied area. In particular, we attempt to arrive at an effective lithospheric thermal plate thickness for the South Atlantic.<sup>†</sup>

The data, it turns out, are not so cooperative. Atlantic fracture zones tend to exhibit geoid variations more irregular, hence more difficult to study with simple models, than those in the Pacific. But we are able to

---

<sup>†</sup>Note that the thermal plate thickness is not the same as the elastic plate thickness discussed in Chapter 2. The thermal plate is a conductively cooling boundary layer whose thickness is determined by the depth to a specified temperature isotherm. The elastic plate, generally much thinner, is defined by the mechanical behavior of the lithosphere under surface loads.

isolate steps in the geoid across the fracture zones and to study their variations with age of the lithosphere. We conclude that simple thermal plate models do not describe the geoid behavior seen across fracture zones in the South Atlantic, and we suggest that either small-scale convection or tectonically produced bathymetric structure may better explain the observed geoid variations.

In a study of this sort, both the short and intermediate wavelengths of the along-track altimetry are important for evaluating the quality of the geoid data and for estimating the geoid step height. Unfortunately, no other information, bathymetric or otherwise, is available with sufficient coverage to aid in constraining the depths of the source density variations that produce the geoid anomalies. This problem is, by its nature, somewhat underconstrained; the challenge lies in extracting as much information as possible from the altimetry data. To this end, we supplement the along-track altimetry with gridded geoid and gravity maps of the regions surrounding the fracture zones. These maps show features in the South Atlantic geoid not previously described in the literature, adding to our basic knowledge of this sparsely surveyed ocean and allowing us to understand some of the difficulties encountered in our analysis of the along-track data.

Chapter 4 presents a somewhat more well constrained problem. Here, we examine the intermediate-wavelength bathymetry and geoid in the South Atlantic for evidence of convection within the upper mantle. Surface ship studies have provided knowledge of the bathymetry, sediment load, crustal ages, and gravity field with sufficient coverage to be useful for studies of intermediate wavelength, i.e., with length scales greater than  $\sim 500$  km and smaller than  $\sim 4000$  km. Both the bathymetry and geoid must be corrected

for the effects of sediment loading and lithospheric evolution. By comparing the resultant residual depths and geoid, we can look for correlations--either spatial or quantitative--that are diagnostic of the mantle convection regimes predicted by numerical convection experiments.

Although similar studies have been performed in other oceans, ours is one of the first in the South Atlantic. We have taken pains to clarify and quantify some of the data processing ambiguities and uncertainties suggested, but rarely elaborated upon, by previous researchers. Our results favor the presence of mantle convection at intermediate-wavelength scales beneath the South Atlantic; in the process, however, we demonstrate the difficulties of obtaining reliable quantitative estimates of residual depth and geoid height.

In this problem, as in many problems dealing with geoid interpretation, a key difficulty lies in the separation of lithospheric and sublithospheric density anomalies. A major portion of our analysis lies in utilizing all available geophysical data to exclude as many crustal and lithospheric effects unrelated to mantle convection as possible from the residual depth and geoid. As a result, we are aware of what data are lacking and what are more urgently needed, and can point out which future observations will be most valuable for constraining density variations within the lithosphere.

#### 1.5 Additional Comments

In the marine geophysical literature, there is relatively little discussion of the formal errors present in geophysical mapping. We have, unfortunately, continued this tradition of benign neglect in producing our gridded maps of geoid and gravity by not calculating maps of formal

estimated error. Instead, we have relied on knowledge of the qualitative behavior of our interpolator, given a known pattern of satellite arcs and altimetry data with a known accuracy. The accuracy of our maps is usually attested to by comparison with similar maps and models arrived at independently. We feel that our geoid and gravity maps are generally accurate to the order of their contour interval or better. Cases where this is not so are indicated, and these maps are usually employed qualitatively rather than quantitatively. But artifacts may exist in almost any map, particularly in those locations where actual data are lacking.

The above statements are true for most wavelengths bands. At the shortest wavelengths, however, errors increase due to noise in the data [e.g. Sailor, 1982]. We usually filter our data to remove these problematic wavelengths. Recently there has been increased discussion as to the accuracy of the longest wavelengths, also. Lambeck and Coleman [1983], for example, question the reliability of the long-wavelength GEM 9 geoid used extensively in this thesis and other altimetry work. They maintain that errors of a few meters or more may exist in the long-wavelength geoid. In addition, there may be periodic long-wavelength errors in the altimetry data itself (C. Wunsch, personal communication, 1987).

Of the three studies included in this thesis, only the last, dealing with intermediate-wavelength geoid anomalies, would be substantially affected by longer-wavelength geoid errors. Some of these errors would be similar in magnitude to the geoid changes, described in Chapter 4, produced by varying the GEM 9 coefficients of the long-wavelength field. Our basic results do not change when the GEM 9 coefficients vary, so presumably they would not be affected by these long-wavelength geoid errors, either. Other errors are probably mitigated by the Seasat altimetry arc crossover

corrections, but the magnitude of the errors that remain is unknown.

We stress that the maps presented in Chapter 4 should be used cautiously; they may contain long-wavelength errors of a few meters magnitude from a variety of sources. The reader should be aware that future improvements in the longer-wavelength geoid field and altimetry data may require corrections to the maps in this thesis, particularly those of Chapter 4.

The contents of Chapter 2 were published in their present form as "Seasat-Derived Gravity Over the Musicians Seamounts" by Adam P. Freedman and Barry Parsons (Journal of Geophysical Research, Vol. 91, pp. 8325-8340, July, 1986). Although Barry Parsons is included as coauthor, his contributions to this chapter are those consonant with his duties as a graduate research advisor and thesis supervisor. He suggested the research topic and the general method of attacking the problem. We discussed together ideas for overcoming a number of the difficulties encountered along the way. He critically reviewed this manuscript more than once and helped me to whittle it down to its present concise yet thorough form. In the end, however, all of the actual research and writing in this chapter is my own.

## 1.6 References

- Angevine, C.L., and D.L. Turcotte, Correlation of geoid and depth anomalies over the Agulhas Plateau, Tectonophysics, 100, 43-52, 1983.
- Cazenave, A., Thermal cooling of the oceanic lithosphere: New constraints from geoid height data, Earth Planet. Sci. Lett., 70, 395-406, 1984.
- Cazenave, A., and K. Dominh, Geoid heights over the Louisville Ridge (South Pacific), J. Geophys. Res., 89, 11,171-11,179, 1984.
- Cazenave, A., K. Dominh, C.J. Allegre, and J.G. Marsh, Global relationship between oceanic geoid and topography, J. Geophys. Res., 91, 11,439-11,450, 1986.
- Cazenave, A., B. Lago, and K. Dominh, Thermal parameters of the oceanic lithosphere estimated from geoid height data, J. Geophys. Res., 88, 1105-1118, 1983.
- Cazenave, A., B. Lago, K. Dominh, and K. Lambeck, On the response of the ocean lithosphere to sea-mount loads from Geos 3 satellite radar altimetry observations, Geophys. J. R. Astron. Soc., 63, 233-252, 1980.
- Chase, C.G., Subduction, the geoid, and lower mantle convection, Nature, 282, 464-468, 1979.
- Crough, S.T., Thermal origin of mid-plate hot-spot swells, Geophys. J. R. Astron. Soc., 55, 451-469, 1978.
- Crough, S.T., Geoid anomalies across fracture zones and the thickness of the lithosphere, Earth Planet. Sci. Lett., 44, 224-230, 1979.
- Crough, S.T., Geoid anomalies over the Cape Verde Rise, Mar. Geophys. Res., 5, 263-271, 1982.
- Crough, S.T., and D.M. Jurdy, Subducted lithosphere, hotspots, and the geoid, Earth Planet. Sci. Lett., 48, 15-22, 1980.
- Detrick, R.S., Jr., An analysis of geoid anomalies across the Mendocino fracture zone: Implications for thermal models of the lithosphere, J. Geophys. Res., 86, 11,751-11,762, 1981.
- Dixon, T.H., M. Naraghi, M.K. McNutt, and S.M. Smith, Bathymetric prediction from Seasat altimeter data, J. Geophys. Res., 88, 1563-1571, 1983.
- Dixon, T.H., and M.E. Parke, Bathymetry estimates in the southern oceans from Seasat altimetry, Nature, 304, 406-411, 1983.
- Hager, B.H., Subducted slabs and the geoid: Constraints on mantle rheology and flow, J. Geophys. Res., 89, 6003-6015, 1984.

- Hager, B.H., R.W. Clayton, M.A. Richards, R.P. Comer, and A.M. Dziewonski, Lower mantle heterogeneity, dynamic topography and the geoid, Nature, 313, 541-545, 1985.
- Haxby, W.F., and D.L. Turcotte, On isostatic geoid anomalies, J. Geophys. Res., 83, 5473-5478, 1978.
- Haxby, W.F., and J.K. Weissel, Evidence for small-scale mantle convection from Seasat altimeter data, J. Geophys. Res., 91, 3507-3520, 1986.
- Heiskanen, W.A., and H. Moritz, Physical Geodesy, 364 pp., W.H. Freeman and Co., San Francisco, 1967.
- Jung, W.-Y., and P.D. Rabinowitz, Residual geoid anomalies of the North Atlantic Ocean and their tectonic implications, J. Geophys. Res., 91, 10,383-10,396, 1986.
- Kogan, M.G., M. Diament, A. Bulot, and G. Balmino, Thermal isostasy in the South Atlantic Ocean from geoid anomalies, Earth Planet. Sci. Lett., 74, 280-290, 1985.
- Lambeck, K., and R. Coleman, A search for seamounts in the southern Cook and Austral region, Geophys. Res. Lett., 9, 389-392, 1982.
- Lambeck, K., and R. Coleman, The Earth's shape and gravity field: A report of progress from 1958 to 1982, Geophys. J. R. Astron. Soc., 74, 25-54, 1983.
- Lame, D.B., and G.H. Born, Seasat measurement system evaluation: Achievements and limitations, J. Geophys. Res., 87, 3175-3178, 1982.
- Lazarewicz, A.P., and D.C. Schwank, Detection of uncharted seamounts using satellite altimetry, Geophys. Res. Lett., 9, 385-388, 1982.
- Leitao, C.D., and J.T. McGoogan, Skylab radar altimeter: Short-wavelength perturbations detected in ocean surface profiles, Science, 186, 1208-1209, 1975.
- McAdoo, D.C., and C.F. Martin, Seasat observations of lithospheric flexure seaward of trenches, J. Geophys. Res., 89, 3201-3210, 1984.
- McKenzie, D., A. Watts, B. Parsons, and M. Roufousse, Planform of mantle convection beneath the Pacific Ocean, Nature, 288, 442-446, 1980.
- McNutt, M.K., and L. Shure, Estimating the compensation depth of the Hawaiian swell with linear filters, J. Geophys. Res., 91, 13,915-13,923, 1986.
- Parmentier, E.M., and W.F. Haxby, Thermal stresses in the oceanic lithosphere: Evidence from geoid anomalies at fracture zones, J. Geophys. Res., 91, 7193-7204, 1986.

- Parsons, B., and S. Daly, The relationship between surface topography, gravity anomalies, and temperature structure of convection, J. Geophys. Res., 88, 1129-1144, 1983.
- Sailor, R.V., Determination of the resolution capability of the Seasat radar altimeter, observations of the geoid spectrum, and detection of seamounts, Final contract report TR-3751, (The Analytic Sciences Corporation, One Jacob Way, Reading, MA 01867), May 1982.
- Sailor, R.V., and E.A. Okal, Applications of Seasat altimeter data in seismotectonic studies of the South-Central Pacific, J. Geophys. Res., 88, 1572-1580, 1983.
- Sandwell, D.T., A detailed view of the South Pacific geoid from satellite altimetry, J. Geophys. Res., 89, 1089-1104, 1984.
- Sandwell, D.T., and K.A. Poehls, A compensation mechanism for the central Pacific, J. Geophys. Res., 85, 3751-3758, 1980.
- Sandwell, D.T., and G. Schubert, Geoid height versus age for symmetric spreading ridges, J. Geophys. Res., 85, 7235-7241, 1980.
- Sandwell, D.T., and G. Schubert, Geoid height-age relation from Seasat altimeter profiles across the Mendocino fracture zone, J. Geophys. Res., 87, 3949-3958, 1982.
- Stanley, H.R., The Geos-3 project, J. Geophys. Res., 84, 3779-3783, 1979.
- Tapley, B.D., G.H. Born, and M.E. Parke, The Seasat altimeter data and its accuracy assessment, J. Geophys. Res., 87, 3179-3188, 1982.
- Turcotte, D.L. and D.C. McAdoo, Geoid anomalies and the thickness of the lithosphere, J. Geophys. Res., 84, 2381-2387, 1979.
- Turcotte, D.L., and G. Schubert, Geodynamics, Applications of Continuum Physics to Geological Problems, 450 pp., John Wiley and Sons, New York, 1982.
- Watts, A.B., On geoid heights derived from Geos 3 altimeter data along the Hawaiian-Emperor seamount chain, J. Geophys. Res., 84, 3817-3826, 1979.
- Watts, A.B., D.P. McKenzie, B. Parsons and M. Roufousse, The relationship between gravity and bathymetry in the Pacific Ocean, Geophys. J. R. Astron. Soc., 83, 263-298, 1985.
- Watts, A.B., and N.M. Ribe, On geoid heights and flexure of the lithosphere at seamounts, J. Geophys. Res., 89, 11,152-11,170, 1984.
- Wunsch, C., and E.M. Gaposchkin, On using satellite altimetry to determine the general circulation of the oceans with application to geoid improvement, Rev. Geophys. Space Phys., 18, 725-745, 1980.

## Chapter 2.

### Seasat-Derived Gravity Over the Musicians Seamounts

## 2.1 Abstract

The two-dimensional gravity field over the Musicians seamount province in the Pacific Ocean has been derived from Seasat altimetry. Geoid maps were produced by fitting a minimum curvature surface to the sea surface height data. As a check on the quality of this interpolation method, we also gridded the data using weighted grid point averages. Fourier transforms of the geoid and, alternatively, the geoid gradient were used to determine the gravity field. We have compared gravity maps produced these different ways in order to identify the problems involved in pushing Seasat data to the limits of its spatial resolution and accuracy. Our minimum-curvature interpolation scheme was determined to be the more accurate and cost-effective mapping method, while gravity obtained by transforming the geoid produced more reliable gravity maps.

The bathymetry of this area was used to predict the gravity field through the use of a bathymetric filter that assumed regional compensation by a thin elastic plate. Gravity fields predicted for a variety of effective elastic thicknesses were compared to the Seasat-derived gravity, particularly in areas with good track coverage. The derived gravity tends to favor a thin plate with an effective elastic thickness of  $\sim 5$  km, though the east-west ridges in the south display a smaller signal more consistent with Airy compensation. This variation may be indicative of early fracturing of the lithosphere in the south, or it may be a manifestation of the age difference and early thermal structure across the Murray fracture zone, which separates the seamount province into northern and southern sections. Neighboring seamounts with differing flexural signatures, particularly in the south, may indicate that volcanism occurred in the same location over an extended period of time.

## 2.2 Introduction

Many studies have shown that gravity and bathymetry in the oceans are highly correlated for short- and medium-wavelength features [e.g. McNutt, 1979; Watts and Daly, 1981]. The details of this correlation can yield information about how topographic features are compensated, hence about the thermal structure and tectonic history of the region being studied. The gravity-bathymetry relationship can be characterized through the use of a response function, or admittance. The admittance  $Z$  is a function of wave number  $k$ , and is defined by

$$Z(k) = \overline{G}(k)/\overline{B}(k) \quad (1)$$

where  $k = 2\pi/\lambda$ ,  $\lambda$  is the wavelength of the bathymetric and gravimetric features, and  $\overline{G}(k)$  and  $\overline{B}(k)$  are the Fourier transforms of the gravity and bathymetry, respectively. In many studies,  $\overline{G}$  and  $\overline{B}$  determined from observation are used to compute  $Z$ , which is then compared to theoretical admittance models [Lewis and Dorman, 1970; McKenzie and Bowin, 1976; Banks *et al.*, 1977; Watts, 1978; McNutt, 1979; Ribe and Watts, 1982; Ribe, 1982]. Alternatively, as in this study, a theoretical admittance is used as a filter in conjunction with a known value of  $\overline{B}$  or  $\overline{G}$  to predict the other quantity and to compare it to the observations [Watts, 1978, 1979; McNutt, 1979; Watts *et al.*, 1980; Dixon *et al.*, 1983; Watts and Ribe, 1984].

The radar altimeter on board the Seasat satellite obtained uniform-coverage, high-resolution sea surface height information over most of the ocean surface during a 70 day period from July through October 1978 [Lame and Born, 1982]. The shape of the sea surface closely approximates the marine geoid. Other factors that affect sea surface height, such as tides, currents, and atmospheric and meteorological effects, can be removed from the data or have small magnitudes (less than 50 cm) compared to many

features of interest in the geoid (with magnitudes  $> 1$  m) [Wunsch and Gaposchkin, 1980]. Global geoid maps are easily made using Seasat data [e.g. Parke and Dixon, 1982]. The use of these geoid maps with comprehensive bathymetric maps, such as the digital global bathymetric data set SYNAPS, facilitates admittance studies of features whose gravity could never before be studied in detail.

Most previous admittance studies have concentrated on linear features such as mid-ocean ridges, aseismic ridges, fracture zones, and hotspot-related island chains, where one-dimensional modeling is adequate. In the case of individual seamounts or seamount provinces with randomly located seamounts, however, two-dimensional analysis is required [Ribe, 1982; Watts and Ribe, 1984]. Only a few truly two-dimensional comparisons of the short and intermediate wavelength ( $\lambda < 500$  km) marine gravity or geoid field with the bathymetry have been made [Watts et al., 1975; McNutt, 1979; Cazenave et al., 1980; Watts and Ribe, 1984].

These previous studies have focused on the methods of compensation of bathymetric features. The oceanic lithosphere tends to act as an elastic plate overlying a fluid asthenosphere. Crustal loads formed on old, thick lithosphere are supported by elastic stresses produced by the bending of the plate. The plate distributes the compensating masses over a large area. Directly over the load, therefore, the gravity anomaly is large. For crustal loads formed on young sea-floor, the effective elastic plate thickness is small and the lithosphere is weak. Elastic stresses play a small part in the support of the load. Support is instead provided by buoyancy forces due to the compensating masses located beneath the load. Hence directly over the load the gravity anomaly is small. The actual behavior of the plate depends on the horizontal dimensions of the crustal

load as well as the plate thickness, so the ratio of gravity to bathymetry as a function of wavelength, i.e. the admittance, can indicate the effective elastic thickness of the lithosphere. By relating the elastic thickness to the age of the lithosphere at the time of loading, Watts et al. [1980] and others have shown how the elastic thickness is a function of time and increases with age.

In the present study, we compare two-dimensional maps of gravity derived from Seasat data for the Musicians seamount province north of Hawaii with gravity predicted from the bathymetry of that area using a theoretical admittance. The Musicians have provided an excellent test region for previous gravity studies [Schwank and Lazarewicz, 1982; Dixon et al., 1983]. The high-resolution bathymetric data available for them and their relatively weak geoid signals ( $<1$  m) make them a good test of satellite altimetry as a bathymetric prediction tool. In addition, since the largest intertrack spacings ( $\sim 120$  km) are larger than most of the seamounts, this area provides a test of the spatial accuracy and resolution of the data and the two-dimensional mapping techniques. Previous studies have looked at the one-dimensional geoid along the Seasat tracks, which, for a region as irregular as the Musicians, is not as useful as examining the two-dimensional geoid.

Maps of the geoid have the disadvantage of tending to emphasize longer wavelength features than the seamounts. The gravity field, however, is more sensitive to short wavelengths. Figure 1 compares the maximum geoid and gravity signals of model circular Gaussian seamounts on lithosphere with four elastic thicknesses. The geoid response is largest for seamounts whose widths are larger than the 40 to 80 km sizes of the Musicians seamounts, particularly if the effective elastic thickness is high. In con-

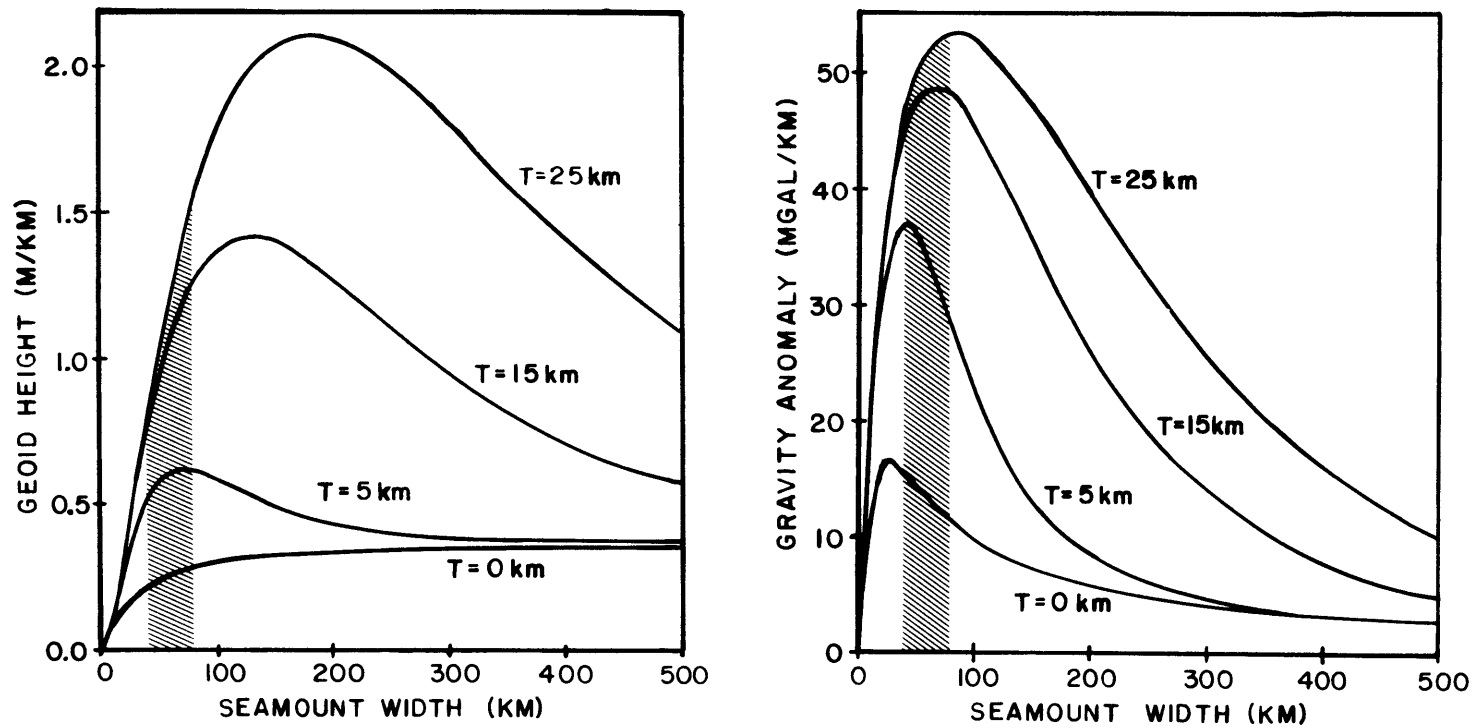


Figure 1. Geoid (left) and gravity (right) anomalies over the peak of a circular Gaussian seamount (with topography  $h$  defined by  $h(r) = h_0 \exp(-r^2/\sigma^2)$ , where  $h_0$  is the maximum height set to 1 km, and  $\sigma$  is the half-width), versus the width ( $2\sigma$ ) of the seamount computed for four effective elastic thicknesses  $T$  of the lithosphere supporting the seamount. The shaded region indicates the size range (40-80 km) of most Musicians seamounts. Note that gravity anomalies, unlike geoid heights, are largest for seamounts the size of the Musicians. (Adapted from Watts and Ribe [1984]).

trast, the peak sensitivity of the gravity response is located close to or within the size range of the Musicians seamounts for all reasonable elastic thicknesses. Thus seamounts the size of the Musicians appear more prominent with respect to larger bathymetric features in gravity maps than in geoid maps. Figure 1 also shows that the gravity field can help to distinguish between the thin-plate and thick-plate regimes somewhat more easily than the geoid. Since it is not difficult to convert the two-dimensional geoid into gravity, we chose to use the gravity field to study the Musicians seamounts.

Another advantage that two-dimensional gravity maps have over one-dimensional profiles is that regional variations in the gravity signals or in the apparent effective elastic thickness can be observed. For example, nearby seamounts with comparable bathymetric relief and similar Seasat track coverage may have very different gravity signals. Gravity maps allow one to see this difference more easily than individual track profiles do, although track profiles are helpful in quantifying this difference.

### 2.3 Geophysical Setting

The Musicians seamount province is located in the central Pacific Ocean north of the Hawaiian Islands (Fig. 2). It is bounded on the north by the Pioneer fracture zone and extends southward beyond the Murray fracture zone, with one large group of seamounts north and one large group south of the Murray. In this study, the area of interest extends from  $24^{\circ}\text{N}$  to  $34^{\circ}\text{N}$  and from  $156^{\circ}\text{W}$  to  $166^{\circ}\text{W}$ .

Rea and Naugler [1971] describe three seamount populations within the province (Fig. 3). In the north is an elongated steep-sided block of large seamounts (including Verdi, Wagner, and Schubert) known as the Musicians

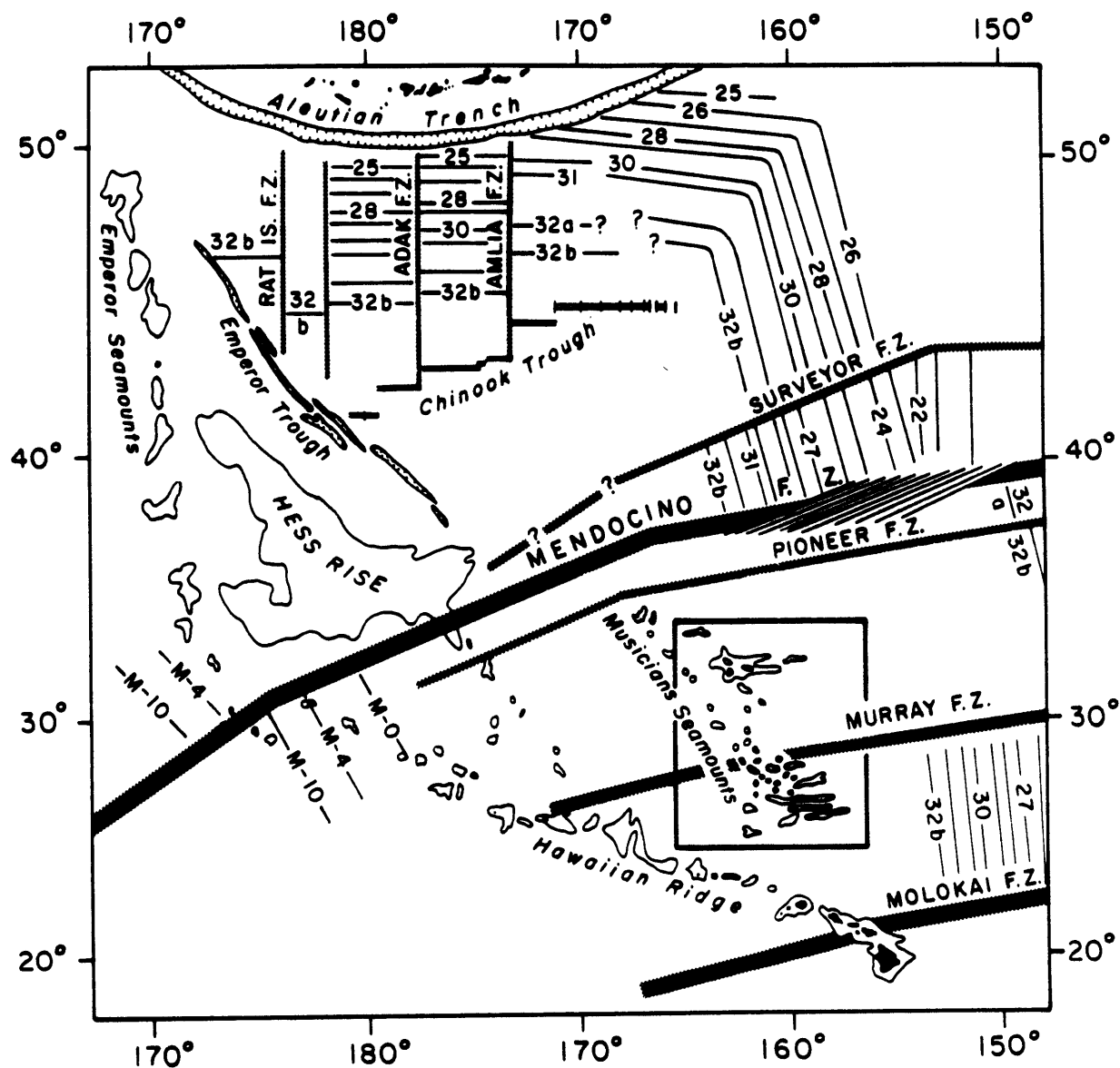


Figure 2. Tectonic map of the northern Pacific Ocean showing the location of the Musicians seamounts [after Rea and Dixon, 1983]. Major fracture zones and magnetic anomalies are also shown. The Musicians region lies within the Cretaceous magnetic quiet zone and is cut by the Murray fracture zone.

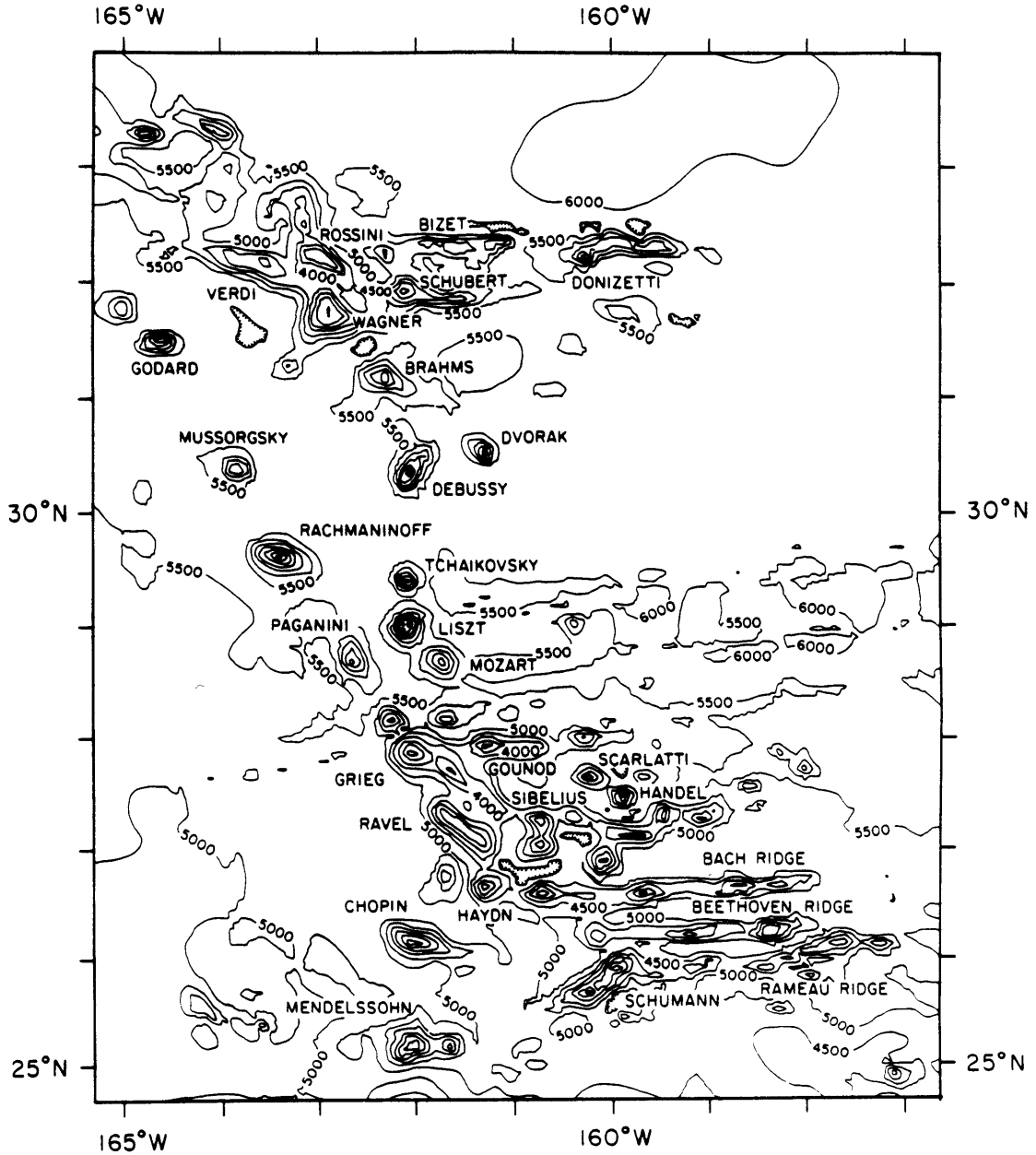


Figure 3. Bathymetric map of the Musicians seamount province with major features named [after Naugler, 1968; and Rea, 1969]. The contour interval is 500 m. Areas to the northeast and southwest have not been digitized, as relief there is generally less than 500 m.

horst. In the south are a number of east-west trending ridges (such as Bach and Beethoven ridges) with larger seamounts (such as Schumann and Sibelius) strung out along them. The third population consists of scattered seamounts found primarily on the western edge of the province and in the area between the horst to the north and the ridges to the south (including Brahms, Debussy, Rachmaninoff, and Chopin). The seamounts tend to be elliptical in shape with dimensions no greater than 60 x 100 km, but the majority have sizes of about 25 x 50 km. Their heights range from 1000 to 4000 m with most having about 2500 m of relief.

The Murray fracture zone runs through the middle of the province but it seems to have no effect on the seamount distribution; the seamounts neither prefer nor avoid the fracture zone more than adjacent areas. Rea and Naugler [1971] believed this implied that the Murray was of sufficient age to act as a welded and inactive fracture zone when the Musicians were emplaced. They also noted that the westernmost seamounts fall along a path that closely coincides with a line along which the major North Pacific fracture zones change their trends and their bathymetric and magnetic characteristics. This line is referred to as the "bending line", and the seamounts falling along it, such as Mussorgsky, Rachmaninoff, Grieg and Ravel, will be referred to as bending line seamounts. There also may be a line of seamounts which trend north-south, including Debussy, Liszt, Chopin, and Mendellsohn.

Because the seafloor surrounding the Musicians lies in the Cretaceous magnetic quiet zone and reliable age dating of the seamounts themselves is only now becoming available, the tectonic history of this area has been difficult to determine. The age offset across the Murray fracture zone to the east is 15-20 m.y., with the north side being older [Atwater and

Menard, 1970], whereas there is no observed age offset to the west [Pitman et al., 1974]. If the age of the seafloor under the Musicians is determined by interpolation, the floor south of the Murray is 80-90 Ma, while to the north it is 90-100 Ma. Thus the age offset across the Murray in the vicinity of the Musicians is probably less than 20 m.y., but large enough (>5 m.y.) to leave a substantial bathymetric fracture zone signal. Straight age interpolation is unrealistic, however, as ridge jumps due to changes in plate motion almost certainly occurred in this area [Rea and Dixon, 1983] and would have resulted in younger crust being emplaced next to older crust from another plate. The Musicians themselves may be the site of a ridge jump, as Rea and Dixon [1983] suggest, or they may represent a dying spreading center similar to the Mathematician-Clipperton seamounts. What can be stated with reasonable certainty despite the complexities of this area is that the crust is at least 85 Ma, with enough age offset across the Murray to result in a major bathymetric fracture zone feature.

The ages of two Musicians seamounts were first presented by Clague and Dalrymple [1975]. M. Pringle (personal communication, 1985) has examined many more seamounts and corrected the earlier K-Ar age estimates. He finds a range in ages of 75-95 Ma, with the seamounts sampled north of the fracture zone having ages of 85-95 Ma and those to the south having ages of 75-85 Ma. He also finds evidence that the western bending-line seamounts show an age progression from northwest (older) to southeast (younger). Sager [1984] has estimated seamount ages based on their paleomagnetic pole positions and their fit to a polar wander path. He has found ages of 80-90 Ma for the bending-line seamounts and similar ages for the east-west ridges in the south. For some other seamounts in the northeastern and southern

parts of the Musicians, he estimates ages of 65-75 Ma. Schwank and Lazarewicz [1982] also suspect an age progression of the southernmost bending-line seamounts from compensation studies using along-track Seasat altimetry. And from flexural studies using the along-track data, Dixon et al. [1983] conclude that the Musicians were formed on young lithosphere, 5-30 m.y. after the crust was produced at the ridge crest.

The published age data favor formation of the Musicians seamounts beginning shortly after the crust was formed and extending over a period of 20-25 m.y. It is not clear, however, if all the seamounts in a specific subpopulation, such as the northern horst or southern ridges, were formed in one short episode of volcanism or in repeated volcanic episodes over an extended period of time.

#### 2.4 Data Adjustment and Interpolation

The extent of Seasat coverage in the vicinity of the Musicians seamount province can be seen in Figure 4. The Seasat arcs have an along-track data spacing of 6.7 km, but the intertrack spacing can be as large as 120 km. This leaves some geographic points as much as 60 km from the nearest geoid measurement.

The Seasat data were provided by R. Rapp at Ohio State University (OSU) [Rapp, 1982, 1983], who removed spurious data points and corrected the remaining data for atmospheric effects, ephemeris errors (by minimizing crossover errors, those discrepancies in geoid height at the intersections of ascending and descending arcs), sea state bias, and tides. The altimeter precision is estimated to be about 10 cm [Tapley et al., 1982], but the OSU data had an rms crossover error of 33 cm in the North Pacific. The track errors that remained contributed to anomalies in the final gravity

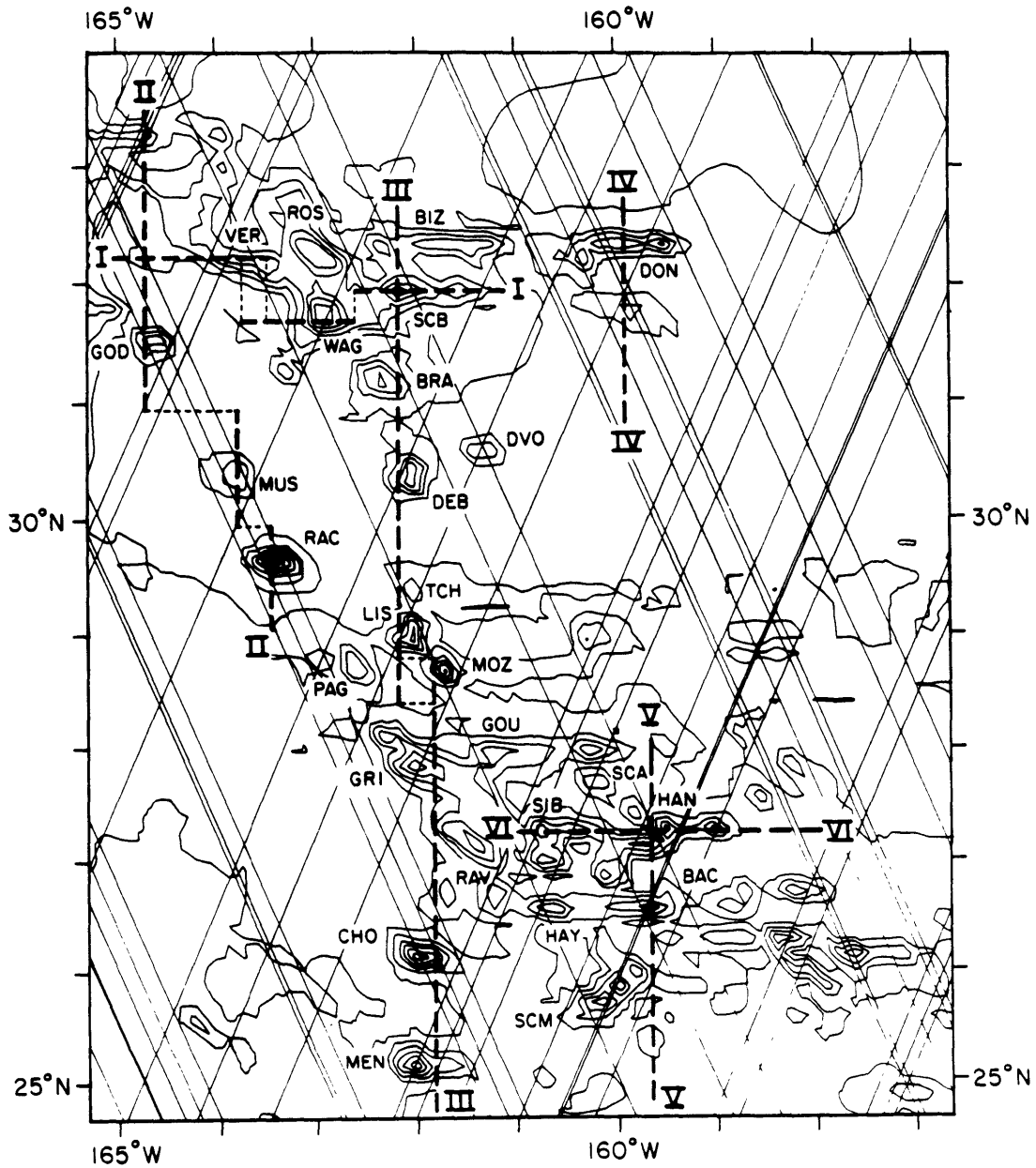


Figure 4. Seasat track coverage superimposed over the bathymetry interpolated onto a 15-km grid. The positions of the six profiles of Figures 6 and 7 are shown. Features are identified by three-letter abbreviations. Note that some seamounts are well sampled by Seasat tracks but others are missed entirely.

maps, so the data were independently readjusted to minimize crossover errors in the Musicians region. Following the techniques of Brace [1977] and Liang [1983], a bias and trend were removed from each track containing more than two crossover points. This procedure is outlined in Table 1. Before our adjustment the rms error for the region was 15 cm and the largest magnitude error was 99 cm. After adjustment the rms and maximum magnitude errors were reduced to 8 cm and 40 cm, respectively.

Since only the short- to intermediate-wavelength geoid was desired, long-wavelength geoid signals and short-wavelength noise were removed from the data. A reference geoid based on the GEM 9 potential coefficients [Lerch et al., 1979] complete to degree and order 10 was subtracted from the data, effectively removing wavelengths  $>4000$  km. The data were then smoothed along track using a Gaussian weighting, defined by  $w(x) = \exp(-x^2/\sigma^2)$ , with a half-width  $\sigma$  of 5 km. This removed wavelengths less than  $\sim 15$  km due primarily to random noise. The along-track geoid data could then be interpolated onto a grid for further processing. Alternatively, the geoid gradient could be obtained by differencing the geoid along track and interpolated to produce maps of the geoid gradient along ascending or descending arcs.

The bathymetric data for the Musicians seamount province were digitized from the Seamap project maps of Naugler [1968] and Rea [1969]. These maps were made from a network of parallel north-south ship tracks spaced  $\sim 18$  km apart, with east-west tie lines at frequent intervals. The bathymetry in the northeastern and southwestern corners of the study area was not digitized, as the abyssal hills there, with relief  $<500$  m, produce minor anomalies ( $<10$  mgal) in the predicted gravity maps that can safely be ignored. We originally used the 5 arc min x 5 arc min digital SYNBAPS

Table 1.

## Crossover Minimization Technique

---

a) The positions of all the points where ascending and descending arcs cross are determined by successively approximating shorter and shorter arc segments as straight lines and computing the intersection points of these lines.

b) The crossover error (descending geoid height minus ascending geoid height) is calculated at each of these points and is inserted into an array at a position corresponding to the subscripts of the ascending and descending arcs which cross. The array has dimensions of (number of ascending arcs) x (number of descending arcs) and is usually about half full.

c) The distance along the arc and the value of the crossover error at each crossover location are used to determine a least squares, best fitting line to the crossover errors for that arc.

d) The crossover data are then adjusted by removing the best fitting line. Arcs that have just one crossover have only a constant bias removed. All the ascending arcs are adjusted first, then the descending arcs. The biases and trends obtained for each arc are stored and accumulated over successive iterations.

e) This process (steps c and d) is repeated until the total rms error and maximum error stabilize. This occurs very quickly, within 2 or 3 iterations.

f) The accumulated biases and trends for each arc are then applied to the original track data to produce adjusted track data with the crossover errors minimized.

---

[1979] bathymetric data set, but it contained linear artifacts which were amplified in the conversion to gravity, producing east-west lineations throughout the map. Seamount dimensions and orientations also differed substantially from the original maps.

We have used a number of methods to interpolate and grid the Seasat altimetry and digitized bathymetry data sets which differ from those of other investigators such as Dixon and Parke [1983], Haxby et al. [1983], and Sandwell [1984]. An earlier version of the mapping program that we use is discussed by McKenzie et al. [1980], where interpolated grid point values are calculated using a weighted average of the surrounding data points. In the present study, we have defined the grid point values by fitting a minimum curvature surface to the observed data [Briggs, 1974; Swain, 1976]. This surface has the property that the total squared curvature  $C$  is a minimum. The squared curvature is defined as:

$$C = \sum_{ij} C_{ij}^2 \quad \text{and} \quad C_{ij} = \left( \frac{\partial^2 u}{\partial x^2} + \frac{\partial^2 u}{\partial y^2} \right) \Big|_{x=x_i, y=y_j} \quad (2)$$

where  $u = u(x_i, y_j)$  is the displacement or height of the surface at position  $(x_i, y_j)$ . This minimum curvature condition leads to a differential equation -- the biharmonic -- which is then expressed in finite difference form including both grid point values and off-grid data values. This set of finite difference equations is then solved iteratively. The resulting smooth surface can take on an extreme value of the data if it coincides with a grid point. No attempt is made to enhance linear trends; any trend present is a result of the data alone. Thus our interpolation strategy differs significantly from that of Haxby et al. [1983], who search for trends in the along-track data to use as guides for directional interpolation.

Since the Musicians seamounts have small dimensions relative to the intertrack spacing and since interpolating data onto a grid can lead to artifacts in the resulting maps, we have compared the maps derived assuming a minimum-curvature surface to maps obtained with three other interpolation schemes. These other techniques are all weighting methods, which search for data within a specified distance of each grid point and assign a weighted average of the data to the value at that point. That is, the value  $u_i'$  at grid point  $i$  is computed by  $u_i' = (\sum w_{ij} u_j) / (\sum w_{ij})$  from the data values  $u_j$  at positions  $j$  within some radius  $\ell$  of the grid position. The weights  $w_{ij}$  are only a function of the distance  $r_{ij}$  ( $0 < r_{ij} < \ell$ ) between points  $i$  and  $j$ .

The weighting methods used were: a) a Gaussian weighting, with  $w(r) = \exp(-r^2/\sigma^2)$  for a specified half-width  $\sigma$ , b) a  $1/r^3$  method falling off more slowly than a Gaussian, with  $w(r) = [1 + (2r^2/\sigma^2)^{3/2}]^{-1}$  [Sandwell, 1984], and c) a weighting from Swain [1976] with  $w(r) = (\ell-r)^2/r^2$  for  $\epsilon < r < \ell$ , where  $\epsilon$  denotes a small radius around the grid point  $i$ , or if any data points lie closer to the grid point than  $\epsilon$ ,  $w(r) = 1$  for the closest data point and is zero for all others. All three weighting techniques were computationally much more expensive than the minimum-curvature method. The Gaussian weighting (a) had severe difficulty interpolating between tracks when a half-width narrow enough for useful resolution was used. Methods (b) and (c) yielded maps very similar to each other but different in minor ways from the minimum-curvature map. For example, Plate 1a shows the gravity field derived from a geoid map produced by fitting a minimum-curvature surface, while Plate 1b shows the gravity derived from a geoid map gridded using method (c). Seamount positions and sizes, as well as the overall map "textures," are all very similar. Only the seamount shapes are

noticeably different, but these differences are minor.

We have used a grid spacing of 15 km for all the maps discussed in this paper. We did, however, construct geoid, gravity, and bathymetry maps using grid spacings of 10 km and 20 km, and grids offset slightly in position from one another. Spatial resolution varied with the grid spacing, as expected. Seamount amplitudes, shapes, and positions changed slightly as the grids were offset and the grid points sampled different areas around the seamount peaks, but the overall effects were similar to those produced by the different interpolation methods discussed above. The chosen grid spacing of 15 km was satisfactory for studying most seamounts and allowed us to produce maps at reasonable computation costs.

Since the region being studied is small (~1000 km across), a plane was subtracted from the grid. This removes wavelengths larger than the size of the region and allows intermediate-wavelength features to be seen. Plate 2 shows the geoid after a plane was removed. A number of prominent east-west trending "rolls" can be seen. These are primarily a result of the Hawaiian arch north of the Hawaiian Islands. Individual seamounts are also apparent in the center of the map, but these signals are small compared to longer-wavelength features. To prevent the large geoid anomaly of the Hawaiian ridge in the southwest corner from overwhelming the smaller seamount signals and to avoid unwanted edge effects when the data are Fourier transformed, a cosine taper was applied to the border of the map extending 10% of the distance into the interior along each side. Thus features seen near the edges of the gravity maps are reduced in amplitude.

## 2.5 Determination of Gravity from the Geoid and Bathymetry

The geoid height, the gravity field, and the deflection of the vertical due to a mass anomaly are related to each other through the disturbing potential  $U$  of the anomalous mass. To first order,  $U|_{z=0} = g_0 N$  where  $N$  is the geoid height above a reference surface at  $z = 0$  and  $g_0$  is the magnitude of the unperturbed vertical gravity acceleration. Then

$$\Delta g = - \frac{\partial U}{\partial z} \quad (3)$$

$$\xi \approx - \frac{g_x}{g_0} = - \frac{1}{g_0} \frac{\partial U}{\partial x} \approx - \frac{\partial N}{\partial x} \quad (4)$$

$$\eta \approx - \frac{g_y}{g_0} = - \frac{1}{g_0} \frac{\partial U}{\partial y} \approx - \frac{\partial N}{\partial y} \quad (5)$$

where  $\Delta g$  is the vertical gravity anomaly,  $\xi$  the east component of deflection of the vertical,  $\eta$  the north component of deflection of the vertical, and  $g_x$  and  $g_y$  are the horizontal components of the anomalous gravity in the east or  $x$  direction and north or  $y$  direction respectively.

By Fourier transforming the above equations the derivatives can be computed:

$$\bar{G} = g_0 |k| \bar{N} \quad (6)$$

$$\bar{\xi} = -ik_x \bar{N} \quad (7)$$

$$\bar{\eta} = -ik_y \bar{N} \quad (8)$$

where  $\bar{G}$ ,  $\bar{N}$ ,  $\bar{\xi}$ ,  $\bar{\eta}$  are the transforms of gravity, geoid height, east deflection, and north deflection respectively, and all are functions of the wave number  $\underline{k} = (k_x, k_y)$ , with  $|k| = (k_x^2 + k_y^2)^{1/2}$  the magnitude of the wave number vector. Maps of the geoid that have been fast Fourier transformed can be multiplied by the filters in equations (6), (7), and (8) and inverse transformed to derive maps of the gravity field and deflection of

the vertical. For this procedure, we assume that our map projection method minimally distorts distances and that the earth can be approximated by a plane (the flat earth approximation). Since the Musicians region covers an area approximately  $10^\circ \times 10^\circ$  centered on  $30^\circ\text{N}$  latitude and we use a standard Mercator projection, both assumptions should be valid.

Plates 1a and 3 illustrate the gravity field derived using equation (6) from the geoid of Plate 2. The large east-west rolls in the geoid are barely visible in the gravity map, while individual seamounts and seamount groups are more prominent. Since the conversion from geoid to gravity amplifies short-wavelength features, many Seasat track errors and track-related anomalies are also amplified. A few prominent tracks can be seen in the gravity map. They are visible because the interpolator puts "bubbles" around small-scale features that do not extend to nearby tracks and because some closely spaced tracks have small but nonnegligible offsets even after crossover errors have been minimized.

The gravity field can also be determined from the original along-track geoid gradients in a manner similar to that of Haxby et al. [1983]. The geoid gradients along the ascending and descending arcs are interpolated and gridded independently. Since the angle that a satellite track makes with respect to north is a function of latitude, the two grids are easily combined [Sandwell, 1984] to yield north and east components of deflection at each grid point. From Laplace's equation and equations (3), (4), and (5),

$$\nabla^2 U|_{z=0} = \left[ \frac{\partial}{\partial x}(-g_0\xi) + \frac{\partial}{\partial y}(-g_0\eta) + \frac{\partial}{\partial z}(-\Delta g) \right] = 0 \quad (9)$$

and

$$\frac{\partial \Delta g}{\partial z} = -g_0 \left( \frac{\partial \xi}{\partial x} + \frac{\partial \eta}{\partial y} \right) \quad (10)$$

After Fourier transforming (10), we obtain

$$\bar{G} = ig_0 \left[ \frac{k_x}{|k|} \bar{\xi} + \frac{k_y}{|k|} \bar{\eta} \right] \quad (11)$$

The two gridded deflections of the vertical are transformed, combined according to equation (11), and inverse transformed. The resulting gravity field of the Musicians province is shown in Plate 1c.

All of the major seamounts that appear in the gravity map produced directly from the geoid (Plate 1a) appear in the map produced from deflections of the vertical. Spatial resolution is lower in the latter map, however, and most seamount amplitudes are reduced. Some seamount shapes differ substantially, and a few large negative anomalies appear. The differences between the two maps are due primarily to the separate processing of ascending and descending tracks for the second map. The combination of two separately gridded maps, each produced using only one half the data, introduces small anomalies which are amplified when the north and east deflections are computed. When the gravity field is produced, these artifacts appear as significant anomalies. Agreement between the two maps is reasonable, however, and the textures of the maps are similar.

Just as the geoid may easily be converted to gravity in the wave number domain, so too may gravity be calculated from bathymetry using an admittance filter function, i.e.

$$\bar{G}(k_x, k_y) = Z(|k|) \bar{B}(k_x, k_y) \quad (12)$$

The admittance function used is that derived for a thin elastic plate supported by a fluid region [e.g. Watts and Daly, 1981].

$$Z(|k|) = 2\pi G(\rho_2 - \rho_w) e^{-|k|d} \left\{ 1 - \Phi^{-1} \left[ \frac{(\rho_3 - \rho_2) e^{-|k|t_2} + (\rho_m - \rho_3) e^{-|k|(t_2 + t_3)}}{(\rho_m - \rho_2)} \right] \right\} \quad (13)$$

where  $\Phi = 1 + [D|k|^4/(\rho_m - \rho_2)g_0]$  and  $G$  is the gravitational constant;  $\rho_w$ ,  $\rho_2$ ,  $\rho_3$ ,  $\rho_m$  are the densities of seawater, crustal layers 2 and 3, and the mantle, respectively; and  $d$ ,  $t_2$ ,  $t_3$  are the average thicknesses of the water (depth), layer 2 and layer 3. The flexural rigidity  $D$  is defined by

$$D = ET^3/12(1-\nu^2) \quad (14)$$

where  $E$  is Young's Modulus,  $\nu$  is Poisson's ratio, and  $T$  is the effective elastic thickness of the lithosphere. The admittance computed with the more complete theory of McKenzie and Bowin [1976] gave nearly the same results as the thin plate admittance. These filters are linear, stationary, and isotropic. Large bathymetric features are not modeled accurately because the linear theory breaks down for them. Compensation parameters that vary on short spatial scales or that are directional in nature cannot be modeled, either.

The values of the parameters in equations (13) and (14) that we used are listed in Table 2. We varied  $\rho_2$  and  $\rho_3$  by up to  $1 \text{ gm/cm}^3$  and found very little change in the resulting predicted gravity; to avoid making our model needlessly complicated, we therefore set  $\rho_2 = \rho_3$ . We also varied  $t_2$  and  $t_3$  by a few kilometers and  $E$  by more than 50%, but found the resulting changes to be minor compared to the effects (described below) produced by varying  $T$ , as other studies have also found [e.g. Dixon et al., 1983].

All the gridded gravity maps went through one additional filtering. A Gaussian smoothing with a half-width of 10 km was applied in the wave number domain (i.e. the transformed signal was multiplied by a filter of form  $\exp(-\sigma^2 k^2/4)$ , where  $\sigma = 10 \text{ km}$ ). Done primarily to reduce the track anomalies in the Seasat-derived gravity map, we then filtered all the gravity maps to permit fair comparisons among them.

Table 2.  
Values of Parameters

parameter	definition	value, units
$\rho_w$	density of water	1.0 g/cm <sup>3</sup>
$\rho_2$	density of crustal layer 2	2.8 g/cm <sup>3</sup>
$\rho_3$	density of crustal layer 3	2.8 g/cm <sup>3</sup>
$\rho_m$	density of mantle	3.4 g/cm <sup>3</sup>
d	average depth of bathymetry	5.8 km
$t_2$	thickness of layer 2	2.0 km
$t_3$	thickness of layer 3	3.0 km
$g_0$	acceleration of gravity	9.80 m/sec <sup>2</sup>
E	Young's modulus	$7 \times 10^{10}$ N/m <sup>2</sup>
$\nu$	Poisson's ratio	0.25
T	effective elastic thickness	0, 5, 15 km

## 2.6 Resolution and Accuracy

Previous authors have remarked that two-dimensional maps made from Seasat data might be inadequate due to the large intertrack spacing. In the Musicians, the intertrack spacing of up to 120 km provides a test for the usefulness of two-dimensional mapping. We need to determine whether a sufficient number of seamounts can be resolved in the data and whether the interpolated sizes, shapes, and positions of these seamounts are sufficiently accurate for this technique to be useful.

Seamounts that are seen as substantial features in the gravity field are found within 25 kilometers of their mapped bathymetric positions. This is excellent agreement, considering that the grid spacing is 15 km and that the bathymetry itself was determined from ship tracks ~18 km apart. Most larger features with wavelengths greater than 100 km are well constrained in size and position by the track coverage. Shapes and sizes of smaller seamounts, however, tend to be less accurate, as few seamounts are sampled by more than two satellite crossings. Yet single track crossings can yield surprisingly accurate shapes if the area surrounding the seamount is also sampled by satellite data. Wagner in the north and Grieg in the south, for example, have limited track coverage, yet the shapes of their gravity anomalies reflect their bathymetric shapes quite well.

Unfortunately, many significant seamounts are either missed entirely by Seasat tracks, or are encountered so far off center as to be barely detectable. As shown in Figure 4, for example, Rossini and Bizet in the north and Paganini and Ravel in the south are missed completely. Although this is an unavoidable problem due to the limited Seasat coverage and it reduces the usefulness of the Seasat data for seamount detection, it is not an insurmountable obstacle to estimating flexural thicknesses from the

gravity field. Care must be taken to determine which seamounts and other features are constrained adequately by the track coverage.

The difficulties resulting from the limited coverage of the Seasat data can be overcome if additional satellite altimetry is available. GEOS 3 data would be able to fill in some of the gaps in the Seasat data set, but their lower precision of 20–50 cm [Stanley, 1979], larger crossover errors of  $\pm 50$  cm [Rapp, 1979], and limited coverage in the central Pacific would lead to only marginal improvement over the Seasat data alone. Future orbiting altimeters may generate much denser, higher-resolution data. For an area as small as the one in this study, local crossover corrections and minimum-curvature interpolation should still be feasible and cost-effective. At some data density, however, the altimetric coverage will exceed the bathymetric coverage; an increase in data beyond this point without more detailed bathymetry will not significantly improve on earlier results.

In order to check the reliability of our data analysis, we generated synthetic seamount data and processed them in the same manner as real data. For bathymetry, we used elliptical Gaussian seamounts with dimensions and orientations similar to those of actual Musicians seamounts. The bathymetry was defined using

$$h(x,y) = h_0 \exp[-(x' \cos \theta - y' \sin \theta)^2 / 2\sigma_x^2 - (x' \sin \theta + y' \cos \theta)^2 / 2\sigma_y^2]$$

$$x' = x - x_0; \quad y' = y - y_0 \quad (15)$$

where  $h_0$  is the maximum height of the seamount at point  $(x_0, y_0)$ ,  $\sigma_x$  and  $\sigma_y$  are Gaussian half-widths, and  $\theta$  indicates the orientation of the seamount. After predicting the geoid and gravity anomalies over the seamounts, assuming they are supported by an elastic lithosphere, we interpolated the

geoid data along tracks similar to those of actual Seasat arcs. These were our synthetic data.

Figure 5a shows the gravity anomaly predicted for a model seamount similar to Rachmaninoff on an elastic plate with  $T = 5$  km. The track coverage for the synthetic data is also shown. Figure 5b shows the gravity anomaly map derived from the synthetic along-track geoid data.

The amplitudes of the derived gravity anomalies seem accurate to within  $\pm 10$  mgal of the actual gravity anomalies along the tracks. Positions of high and low anomalies are reasonably consistent and the overall dimensions of the anomalous regions agree. The seamount shapes do suffer in the derived gravity maps, but shape is not a characteristic that we often use in the analysis of our results.

## 2.7 Results

We now compare the Seasat-derived gravity of Plate 3 with the gravity fields predicted for three different effective elastic thicknesses shown in Plate 4. Our visual comparisons pay close attention to the magnitudes and peak-to-peak values of the highs and lows associated with seamounts and to the areal extent of their surrounding lows. The roughness and texture of the maps are also useful characteristics. Seamount shapes, as mentioned above, may not be reliable, so they are not used in our comparisons. In all cases, the actual Seasat track coverage is examined to see how well constrained by actual data the above characteristics may be.

In the derived gravity map (Plate 3), major seamounts in the northern horst, along the western bending line, and along the central north-south line have gravity maxima of 40-60 mgal and rise from a base level of zero mgal. Many are partially surrounded by gravity lows of -10 to -20 mgal.

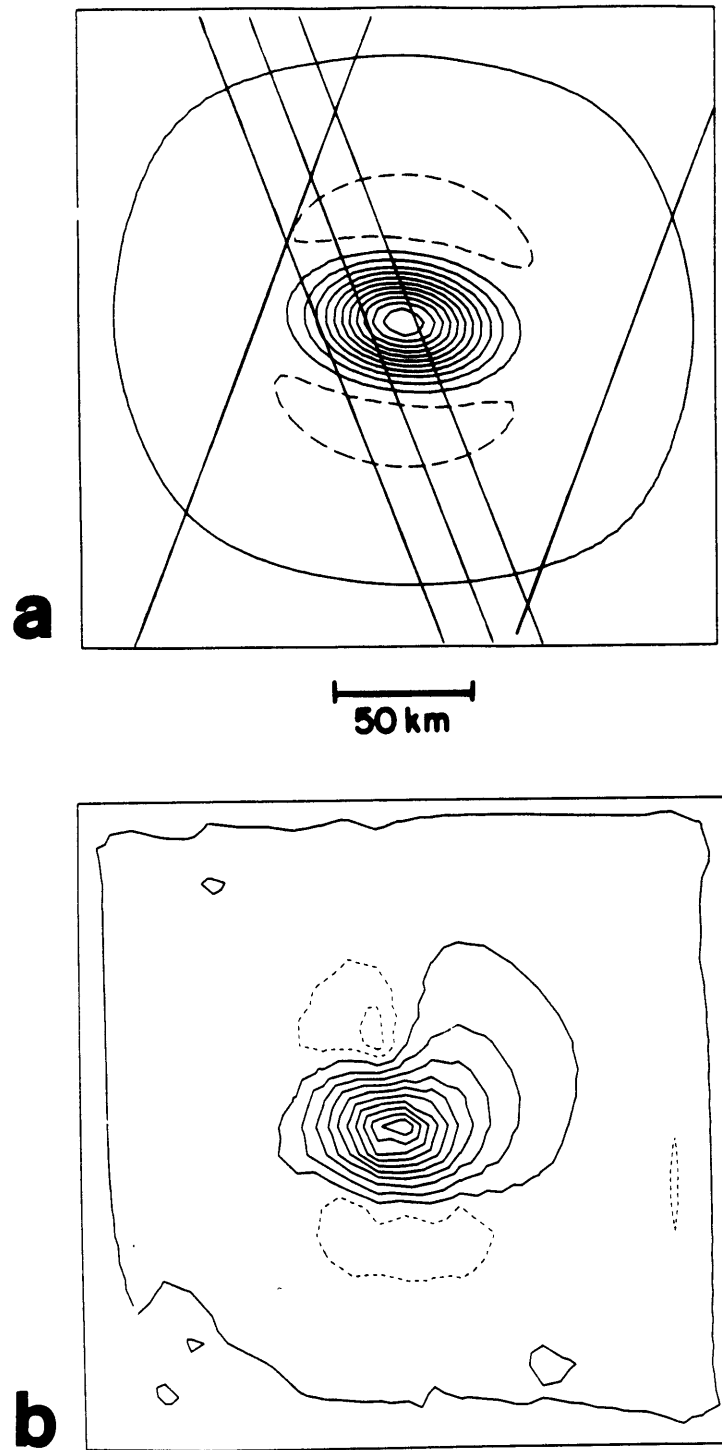


Figure 5. Processing of synthetic data produced from an elliptical Gaussian seamount with size and orientation similar to those of Rachmaninoff.

(a) Gravity over the seamount predicted from the bathymetry (for  $T = 5$  km) together with the track coverage. (b) Gravity field derived from geoid data taken along the track lines in (a) and interpolated onto a minimum-curvature surface. The contour interval is 10 mgal, and negative values are dashed.

The Murray fracture zone can be seen as a linear belt of lows traversing the region from 30°N in the east to 28°N in the central and western portions of the map. It is prominent even though the interpolation scheme chosen does not favor linear features. The east-west ridges in the south tend to have low gravity relief, with peak-to-peak amplitudes of ~20 mgal and few significant negative anomalies. There is a broad region of negative anomalies that extends from 29°N to 31°N and from 160°W to 165°W and contains lows in excess of -20 mgal. This area is located within a belt of lows running west-northwest to east-southeast, which, together with a parallel band of highs to the south, are the gravity effects of the long-wavelength rolls seen vividly in the geoid of Plate 2.

Although bathymetric coverage in this area is good, there is evidence in the derived gravity for at least one uncharted seamount. It is located southwest of Grieg at position 27.5°N, 162.5°W and has a peak anomaly of ~30 mgal. The bathymetric map of Rea [1969] and SYNBAAPS [1979] show nothing at this location. The area has moderately good Seasat track coverage, and the gravity anomaly appears in all the maps of Plate 1, so it is probably not an artifact of our interpolation methods. Although it is of fairly large geographic extent, it is narrowest in the east-west direction; thus the seamount could have escaped detection by the north-south ship tracks in the area.

Plate 4a shows the gravity field predicted using our thinnest plate model with  $T = 0$  km, corresponding to local Airy isostatic compensation. This might be the effective compensation mechanism for seamounts formed on a mid-ocean ridge or on lithosphere that had been highly fractured. Most seamounts have gravity peaks less than 30 mgal and there are few negative anomalies less than -10 mgal. A number of seamounts in the Seasat-derived

gravity map may actually have amplitudes as low as these. In the north, Godard, Donizetti, and Dvorak all have good track coverage but show conspicuously small gravity signals. In the south, many of the east-west ridges, such as Bach, Beethoven, Rameau, and the ridge north of Bach, have gravity signatures as small as those predicted by Airy compensation.

For the thickest elastic plate model, we set  $T = 15$  km (Plate 4b). This corresponds to a lithospheric age of 15-40 Ma (based on depths to the 600°C and 300°C isotherms respectively for a 125-km-thick thermal plate [Parsons and Sclater, 1977; McNutt, 1984; Watts and Ribe, 1984]). Increasing the value of  $T$  further did not significantly change the predicted gravity field, as lithosphere with  $T \approx 15$  km is already strong enough to rigidly support most seamounts in the Musicians' size range (Fig. 1). The gravity predicted over major seamounts is in excess of 80 mgal, while large areas of the northern horst and southern ridges are predicted to have  $>30$  mgal gravity anomalies. Large magnitude gravity lows,  $\leq -20$  mgal, are predicted south and west of Wagner and in between the southern ridges. None of these features are seen; the data, therefore, do not favor this model.

The spatial coverage of the Seasat and bathymetric data does not allow a thick elastic plate to be completely ruled out, however. The areas predicted to have signals of the largest amplitude are for the most part small in size. If the Seasat tracks miss these areas or if the bathymetry is incorrect in position by a few kilometers, the Seasat-derived gravity maps will exhibit maxima and minima smaller in magnitude than those in the actual gravity field. The predicted gravity low south of Wagner, for example, could be diagnostic of the plate strength there, but it is sampled by tracks only at the edges of its extent.

The intermediate strength plate model shown in Plate 4c has an effective elastic thickness of  $T = 5$  km. This corresponds to an on-ridge or near-ridge environment with a crustal age  $\leq 5$  Ma. The larger seamounts have predicted gravity signals of 50-70 mgal. The northern horst and southern ridges are predicted to have broad anomalies of 10-20 mgal. The lows adjacent to seamounts and ridges are less geographically extensive and not as strongly negative as those predicted by the  $T = 15$  km model.

The seamounts most obvious on the derived gravity map have gravity anomalies comparable to those of the  $T = 5$  km model. These include Verdi, Wagner, and Schubert in the northern horst, Debussy, Mussorgsky, Rachmaninoff, and Mozart in the central portion of the Musicians, and Grieg, Chopin, Mendelssohn, and Schumann in the southern section. Some seamounts, as mentioned above, have smaller anomalies more suggestive of the  $T = 0$  km model. These include Dvorak, Donizetti, Godard, and Scarlatti. The small sizes of the gravity anomalies over the southern ridges favor the  $T = 0$  km model for these features also. Some seamounts that seem physically related to the ridges, however, such as Sibelius, Haydn, and Schumann, appear to have more substantial gravity anomalies.

With the exception of the lows along the Murray fracture zone, Seasat-derived negative anomalies do not correspond well in either position or amplitude to those predicted. The derived lows are small in size in the north, almost nonexistent in the south, yet very extensive in the center. This may be a result of the long-wavelength geoid rolls noted above. These extended anomalies do not appear in the bathymetry or predicted gravity maps; thus they effectively add a bias of +10 mgal to the southern gravity anomalies and -5 to -10 mgal to the central features in the Seasat-derived map relative to the predicted gravity. When this effect is considered, the

sizes of the negative anomalies become more reasonable. Although their positions still differ from those predicted, in general appearance and extent the Seasat-derived lows correspond more closely to the  $T = 5$  km model than to either of the two other models.

To illustrate these conclusions in another manner, we have examined interpolated profiles over a number of seamounts. The locations of these profiles are shown in Figure 4. The bathymetry, geoid, and Seasat-derived gravity along them are shown in Figure 6. Most of the seamounts visible in the bathymetry also appear in the geoid, though their relative sizes differ. The amplification of shorter-wavelength features in the gravity profiles is also apparent.

The predicted and Seasat-derived gravity profiles are compared in Figure 7. Agreement between the profiles is rarely close; however, the derived anomalies tend to lie in between those predicted for  $T = 0$  km and  $T = 5$  km. Profile I indicates that gravity over the horst is consistent with a  $T = 5$  km model, while profiles II and III imply the same for most of the bending line and north-south line of seamounts. Profiles IV, V, and VI show that, indeed, the east-west ridges and Donizetti are often fit better by  $T = 0$  km. However, one cannot draw rigorous conclusions from these profiles alone, since the amount of actual data that goes into these profiles varies from section to section along each profile. They should only be used as an aid to two-dimensional mapping.

## 2.8 Discussion

In the Musicians seamount province, we find that Seasat-derived gravity is best fit by a thin elastic plate model with an effective elastic thickness of  $T \approx 5$  km. The principal exceptions are the southern ridges,

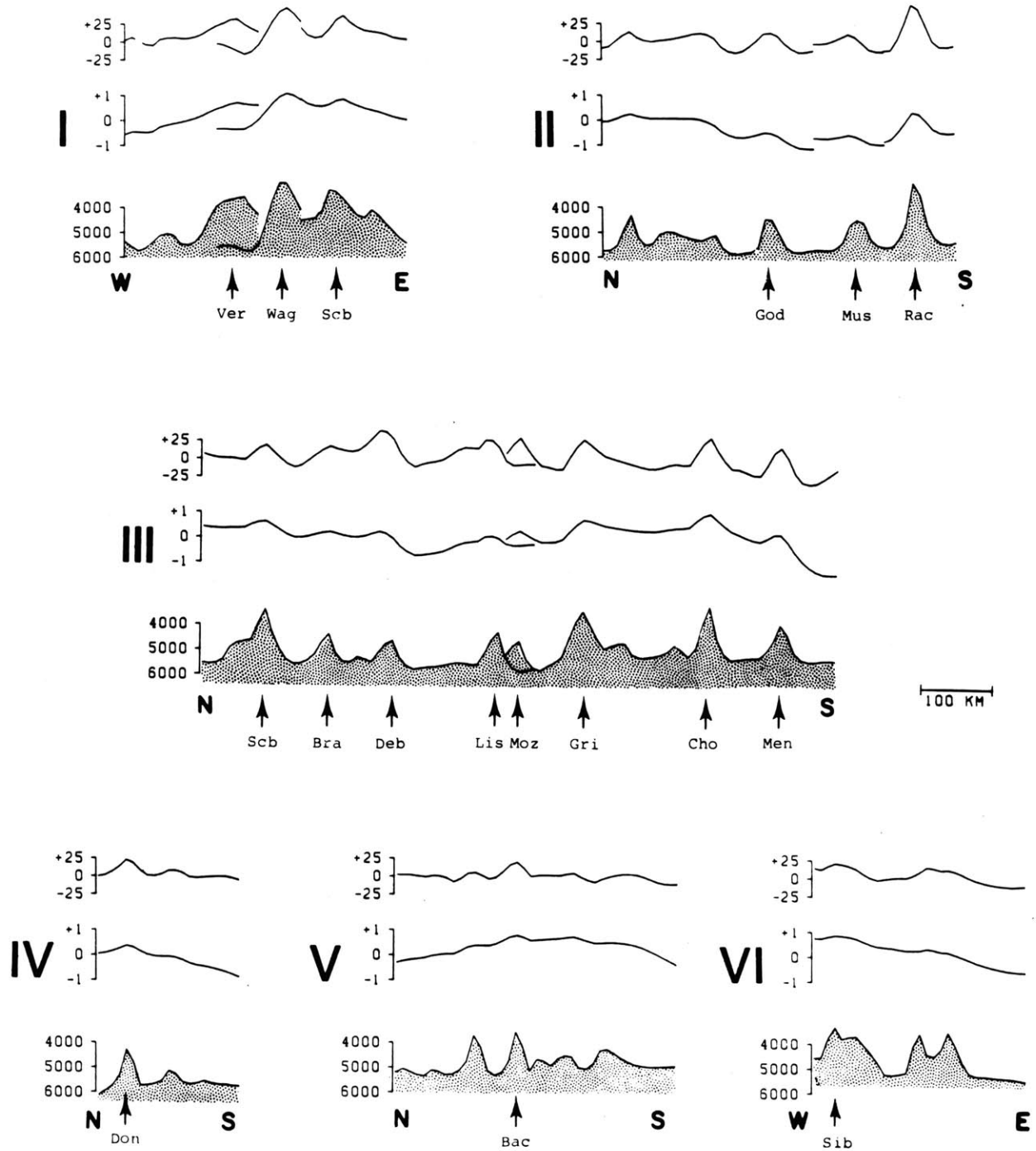


Figure 6. Bathymetry (bottom), geoid (middle), and Seasat-derived gravity (top) of profiles interpolated from the maps. The vertical axes are in meters, meters, and milligals respectively. Profile locations are shown in Figure 4, as are the three-letter abbreviations used to identify prominent features.

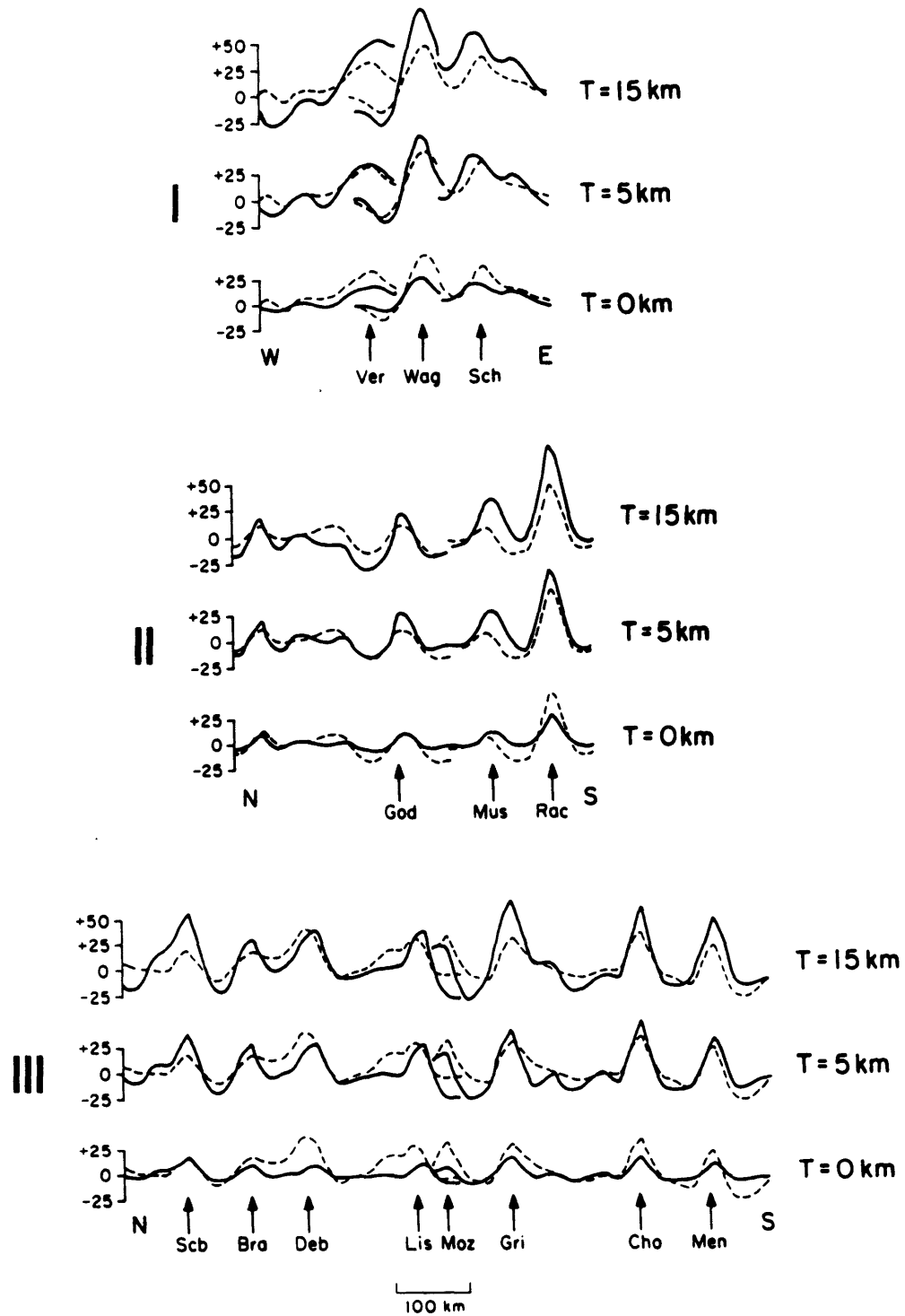


Figure 7 (part 1). Comparison of Seasat-derived gravity with predicted gravity along the profiles of Figures 4 and 6. The predicted profiles for the T = 0 km, T = 5 km, and T = 15 km cases are shown as solid lines, with the derived gravity shown as a dashed line. Gravity is measured in mgal and features are identified by the three-letter codes of Figure 4. Note that the derived gravity profiles usually fall between the T = 0 km and T = 5 km profiles.

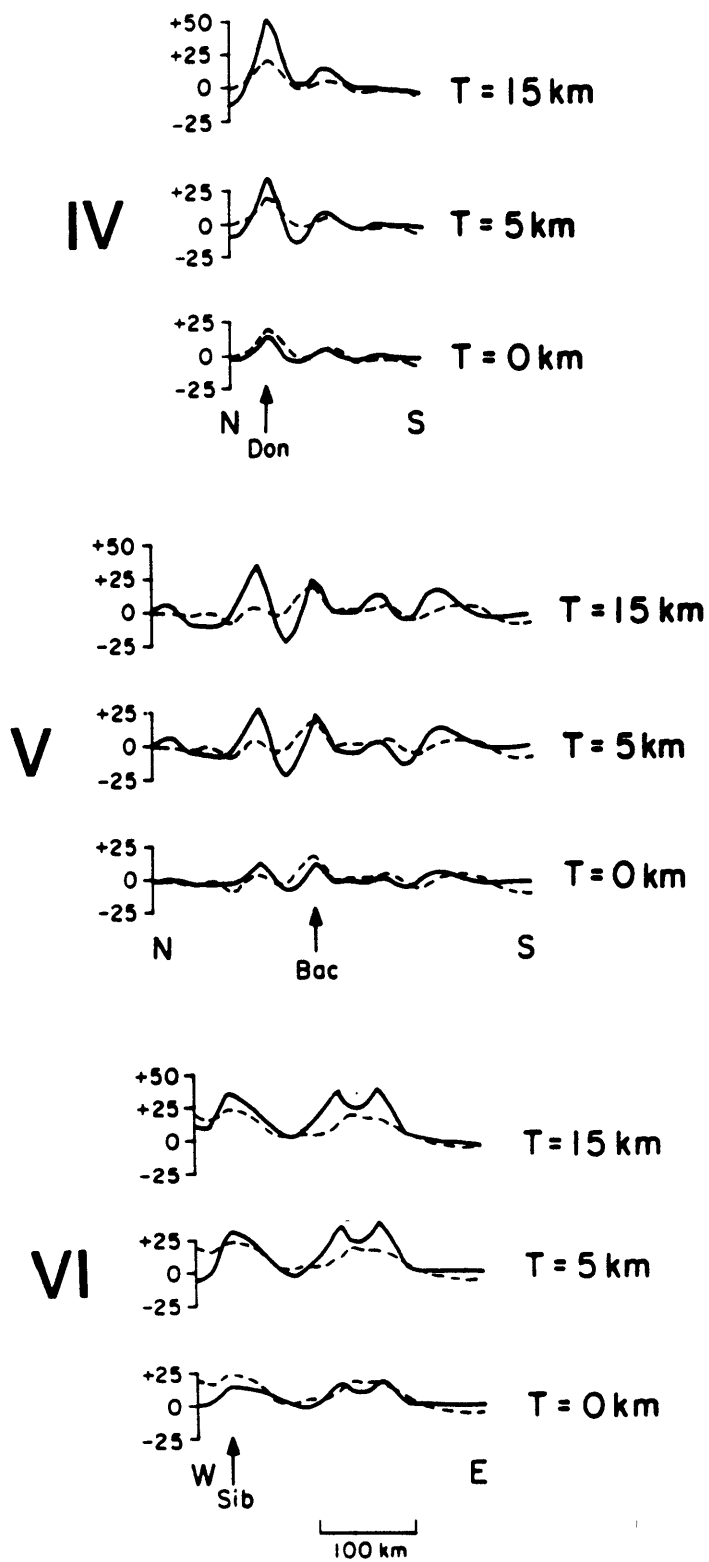


Figure 7 (part 2).

which are better modeled by a  $T \approx 0$  km plate. Low effective elastic thicknesses with  $T < 5$  km imply that the Musicians were either formed on young lithosphere on or near a mid-ocean ridge or on older lithosphere later reheated to reset its effective elastic thickness [e.g. McNutt, 1984]. If reheating has recently occurred in this area, it should be associated with a residual depth anomaly. The primary depth anomaly in the Musicians region today is that due to the recent ( $< 20$  Ma) Hawaiian swell. Any reheating and thinning of the lithosphere related to the swell would most likely yield an effective elastic thickness on the flanks greater than that for Hawaii at the top of the swell, where Watts [1979] found that  $T > 25$  km. If the low rigidity is due to a reheating event, this event must substantially predate the formation of the Hawaiian swell. Therefore, the Musicians seamounts would still have to have formed relatively early. We conclude, in agreement with previous researchers, that all or most of the Musicians features were formed on young lithosphere less than 20 Ma. And if the measured elastic thicknesses are indeed reliable and there has been no thermal rejuvenation, most of the seamounts were formed on lithosphere less than  $\sim 5$  Ma.

If the Musicians seamounts all formed simultaneously, the 5-15 m.y. offset across the Murray fracture zone might result in a detectable elastic plate thickness difference across the fracture zone, with the older, thicker plate being to the north. Indeed, the east-west ridges, suggesting  $T = 0$  km in the south, and the horst, implying  $T = 5$  km in the north, may be present day "frozen-in" evidence of this early flexural difference. If the east-west ridges actually formed first and the northern seamounts later, as Sager's [1984] paleomagnetic results suggest, a significant flexural difference across the fracture zone would still be evident. Only if

the age offset across the Murray were particularly small, or if the southern ridges were formed after the northern features, would we expect no flexural difference from north to south.

There is an alternative explanation for the low rigidity in the south, however. Rea and Naugler [1971] believed that the east-west ridges formed at preexisting parallel zones of weakness in the young crust. Stresses that created these weak zones might have been sufficient to crack the early lithosphere. Hence seamounts built in this area at that time would have been supported by the extremely weak, fractured lithosphere through a local, Airy mechanism.

There are a number of seamounts in the south with larger flexural signals. Some of these are located along the western bending line, while others lie along the north-south trend. If the bending-line seamounts show an age progression, volcanism could have begun along the northern segment of the bending line and propagated southwards as the horst and ridges were extruded; by the time the "hot-spot" reached the southern ridges, the southern lithosphere would have been 5-10 m.y. older and would have behaved as a thicker, more rigid plate. Alternatively, either the bending-line seamounts or the north-south seamount line might represent delayed volcanic episodes, perhaps along dying spreading centers. In any case, the gravity data suggest that seamounts in close physical proximity have formed on lithosphere with significantly different flexural thicknesses. This implies that neighboring seamounts have formed at least 5 m.y. apart, and that, particularly in the southern ridges, separate episodes of volcanism probably occurred in the same geographic area.

Our results generally agree with those of Schwank and Lazarewicz [1982] who found that many seamounts in the southern half of the Musicians

province are fully compensated using an Airy model. They noted a line of partially compensated seamounts trending southeast across the southern ridges which can be seen clearly in our Plate 3 as seamounts with anomalies greater than +20 mgal. But a few seamounts which they found to be well compensated, such as Grieg and Schumann, are fit poorly by an Airy model in our study. They used an idealized seamount model, however, which could yield erroneous compensation estimates for unusually shaped seamounts.

There remains a possibility that a series of ridge jumps in the area could have complicated the sequence described above considerably by juxtaposing thicker lithosphere next to thinner lithosphere. Unfortunately there are no age data that could constrain the sequence of events. But one suggestive detail is the trend noted by Rea and Naugler [1971] in the southernmost of the Musicians ridges. Although the ridge extends east-west, there are subunits trending east-northeast that are parallel to Necker Ridge, a feature 600 km to the southwest. Necker Ridge lies on seafloor dating from before the change of plate motion which resulted in the change in fracture zone trends delineated by the bending line. If this east-northeast trend dates from before the change in spreading direction, and volcanism along the southernmost Musicians ridge is partially determined by this trend, then a ridge jump may have isolated a piece of older seafloor on which this last Musicians ridge formed.

We have found that maps of satellite-derived gravity and gravity predicted from the bathymetry are helpful in characterizing the compensation processes of an area. This technique is only useful, however, when the bathymetry is known at least as well as the gravity field. Two-dimensional maps can also illustrate spatially varying compensation mechanisms more readily than can one-dimensional along-track data. Many previous studies

have used one-dimensional data and have assumed that features were sufficiently linear perpendicular to the data track to use a one-dimensional admittance model. With two-dimensional maps these assumptions can be checked, both for ridges and fracture zones where the linearity assumption is reasonable, and for seamount chains and irregular bathymetric features where linearity is not necessarily a valid assumption. Dixon et al. [1983], for example, concluded on the basis of two parallel Seasat profiles which cross the Musicians area that the regional elastic thickness must be less than  $T \approx 15$  km. We have been able to constrain this value significantly and to propose a regional variation in elastic thickness from north to south.

## 2.9 Acknowledgements

We thank Dan McKenzie, Steve Daly, and Linda Meinke for their contributions to the mapping program used in this study, and Marcia McNutt and Mavis Driscoll for valuable discussions. We also thank Woods Hole Oceanographic Institution and Kelly Luetkemeyer for the use of the R.S.V.P. image processing system. This research was supported by the Office of Naval Research under contract N00014-80-C-0273.

## 2.10 References

- Atwater, T., and H.W. Menard, Magnetic lineations in the northeast Pacific, Earth Planet. Sci. Lett., 7, 445-450, 1970.
- Banks, R.J., R.L. Parker, and S.P. Huestis, Isostatic compensation on a continental scale: Local versus regional mechanisms, Geophys. J. R. Astr. Soc., 51, 431-452, 1977.
- Brace, K.L., Preliminary ocean-area geoid from GEOS-III satellite radar altimetry, Defense Mapping Agency Aerospace Center, St. Louis Air Force Station, Missouri, 1977.
- Briggs, I.C., Machine contouring using minimum curvature, Geophysics, 39, 39-48, 1974.
- Cazenave, A., B. Lago, K. Dominh, and K. Lambeck, On the response of the ocean lithosphere to seamount loads from GEOS-3 satellite radar altimetry observations, Geophys. J. R. Astr. Soc., 63, 233-252, 1980.
- Clague, D.A., and G.B. Dalrymple, Cretaceous K-Ar ages of volcanic rocks from the Musicians Seamounts and the Hawaiian Ridge, Geophys. Res. Lett., 2, 305-308, 1975.
- Dixon, T.H., M. Naraghi, M.K. McNutt, and S.M. Smith, Bathymetric prediction from Seasat altimeter data, J. Geophys. Res., 88, 1563-1571, 1983.
- Dixon, T.H., and M.E. Parke, Bathymetry estimates in the southern oceans from Seasat altimetry, Nature, 304, 406-411, 1983.
- Haxby, W.F., G.D. Karner, J.L. LaBrecque, and J.K. Weissel, Digital images of combined oceanic and continental data sets and their use in tectonic studies, EOS Trans. AGU, 64, 995-1004, 1983.
- Lame, D.B., and G.H. Born, Seasat measurement system evaluation: Achievements and limitations, J. Geophys. Res., 87, 3175-3178, 1982.
- Lerch, F.J., S.M. Klosko, R.E. Laubscher, and C.A. Wagner, Gravity model improvement using Geos 3 (GEM 9 and 10), J. Geophys. Res., 84, 3897-3916, 1979.
- Lewis, B.T.R., and L.M. Dorman, Experimental isostasy 2. An isostatic model for the U.S.A. derived from gravity and topographic data, J. Geophys. Res., 75, 3367-3386, 1970.
- Liang, C.-k., The adjustment and combination of GEOS-3 and Seasat altimeter data, Report #346 of Dept. Geodetic Science & Surveying, Ohio State University, 1983.
- McKenzie, D., and C. Bowin, The relationship between bathymetry and gravity in the Atlantic Ocean, J. Geophys. Res., 81, 1903-1915, 1976.

- McKenzie, D., A. Watts, B. Parsons, and M. Roufousse, Planform of mantle convection beneath the Pacific Ocean, Nature, 288, 442-446, 1980.
- McNutt, M., Compensation of oceanic topography: An application of the response function technique to the Surveyor area, J. Geophys. Res., 84, 7589-7598, 1979.
- McNutt, M.K., Lithospheric flexure and thermal anomalies, J. Geophys. Res., 89, 11,180-11,194, 1984.
- Naugler, F.P., Bathymetry of a region (PORK-421-2) north of the Hawaiian Ridge - ESSA Tech. Rept. ERL 82-POL1, U.S. Govt. Printing Office, Washington, D.C., 1968.
- Parke, M.E., and T.H. Dixon, Nature, 300, 317, 1982.
- Parsons, B., and J.G. Sclater, An analysis of the variation of ocean floor bathymetry and heat flow with age, J. Geophys. Res., 82, 803-827, 1977.
- Pitman, W.C., III, R.L. Larson, and E.M. Herron, Magnetic lineations of the oceans, Geol. Soc. Am. Map Ser., 1974.
- Rapp, R.H., Geos 3 data processing for the recovery of geoid undulations and gravity anomalies, J. Geophys. Res., 84, 3784-3792, 1979.
- Rapp, R.H., A summary of the results from the OSU analysis of Seasat altimeter data, Report #335 of Dept. of Geodetic Science & Surveying, Ohio State University, 1982.
- Rapp, R.H., The determination of geoid undulations and gravity anomalies from Seasat altimeter data, J. Geophys. Res., 88, 1552-1562, 1983.
- Rea, D.K., Bathymetry and magnetics of a region (POL-421-3) 29° to 35°N, 155° to 165°W - ESSA Tech. Rept. ERL 146-POL4, U.S. Govt. Printing Office, Washington, D.C., 1969.
- Rea, D.K., and J.M. Dixon, Late Cretaceous and Paleogene tectonic evolution of the North Pacific Ocean, Earth Planet. Sci. Lett., 65, 145-166, 1983.
- Rea, D.K., and F.P. Naugler, Musicians Seamount Province and related crustal structures north of the Hawaiian Ridge, Mar. Geol., 10, 89-111, 1971.
- Ribe, N.M., On the interpretation of frequency response functions for oceanic gravity and bathymetry, Geophys. J. R. Astr. Soc., 70, 273-294, 1982.
- Ribe, N.M., and A.B. Watts, The distribution of intraplate volcanism in the Pacific Ocean basin: A spectral approach, Geophys. J. R. Astr. Soc., 71, 333-362, 1982.

- Sager, W.W., Implications of paleomagnetism for the volcanic history of the Musicians Seamounts, EOS Trans. AGU, 65, 1076, 1984.
- Sandwell, D.T., A detailed view of the South Pacific geoid from satellite altimetry, J. Geophys. Res., 89, 1089-1104, 1984.
- Schwank, D.C., and A.R. Lazarewicz, Estimation of seamount compensation using satellite altimetry, Geophys. Res. Lett., 9, 907-910, 1982.
- Stanley, H.R., The Geos 3 project, J. Geophys. Res., 84, 3779-3783, 1979.
- Swain, C.J., A FORTRAN IV program for interpolating irregularly spaced data using the difference equations for minimum curvature, Comp. Geoscience, 1, 231-240, 1976.
- Synthetic Bathymetric Profiling System (SYNBAPS, U.S. Navy, NORDA), Nat. Geograph. Solar-Terr. Data Center, NOAA, Boulder, CO 80302, 1979.
- Tapley, B.D., G.H. Born, and M.E. Parke, The Seasat altimeter data and its accuracy assessment, J. Geophys. Res., 87, 3179-3188, 1982.
- Watts, A.B., An analysis of isostasy in the world's oceans 1. Hawaiian-Emperor seamount chain, J. Geophys. Res., 83, 5989-6004, 1978.
- Watts, A.B., On geoid heights derived from GEOS-3 altimeter data along the Hawaiian-Emperor seamount chain, J. Geophys. Res., 84, 3817-3826, 1979.
- Watts, A.B., J.H. Bodine, and N.M. Ribe, Observations of flexure and the geological evolution of the Pacific Ocean basin, Nature, 283, 532-537, 1980.
- Watts, A.B., J.R. Cochran, and G. Selzer, Gravity anomalies and flexure of the lithosphere: A three-dimensional study of the Great Meteor Seamount, northeast Atlantic, J. Geophys. Res., 80, 1391-1398, 1975.
- Watts, A.B., and S.F. Daly, Long wavelength gravity and topography anomalies, Ann. Rev. Earth Planet. Sci., 9, 415-448, 1981.
- Watts, A.B., and N.M. Ribe, On geoid heights and flexure of the lithosphere at seamounts, J. Geophys. Res., 89, 11,152-11,170, 1984.
- Wunsch, C., and E.M. Gaposchkin, On using satellite altimetry to determine the general circulation of the oceans with application to geoid improvement, Rev. Geophys. Space Phys., 18, 725-745, 1980.

## 2.11 Plate Captions

Plate 1a. Comparison of gravity anomaly maps made with different gridding and wave number domain filtering techniques (anomalies measured in milligals): Gravity produced from the geoid gridded using minimum-curvature interpolation.

Plate 1b. Gravity produced from the geoid gridded using Swain's [1976] weighted average interpolation method. Note the similarity to Plate 1a.

Plate 1c. Gravity produced from deflection of the vertical maps made from along-track geoid gradients gridded using minimum-curvature interpolation. Note the lower resolution and more extensive lows than in Plate 1a.

Plate 2. Geoid map of the Musicians region. The Seasat altimetry was interpolated onto a 15-km grid by fitting a minimum curvature surface to the data. The geoid has a GEM 9 field complete to degree and order 10 (for wavelengths larger than 4000 km) and a best fitting plane removed. Geoid height is measured in meters. Note the large, long-wavelength east-west geoid undulations compared to the smaller seamount anomalies.

Plate 3. Seasat-derived gravity field over the Musicians produced by transforming and filtering the geoid map of Plate 2. Gravity anomalies are measured in mgal. Prominent anomalies are identified with the three-letter abbreviations of Figure 4.

Plate 4a. Gravity field predicted from the bathymetry, assuming  $T = 0$  km. The bathymetry filter is an admittance function constructed under the assumption that the seamounts are regionally compensated by a thin elastic plate overlying a fluid asthenosphere. Gravity anomalies are measured in milligals.

Plate 4b. Gravity field predicted for  $T = 15$  km.

Plate 4c. Gravity field predicted for  $T = 5$  km. Note that this map resembles Plate 3 more closely than either Plate 4a or 4b.

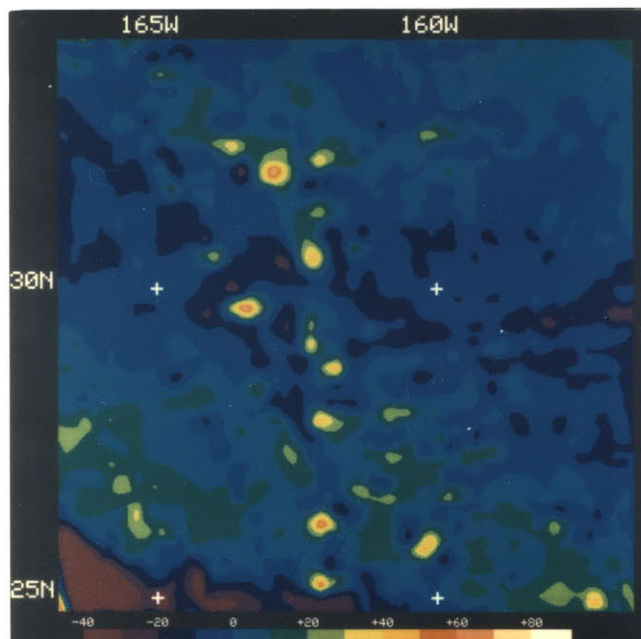


PLATE I (a)

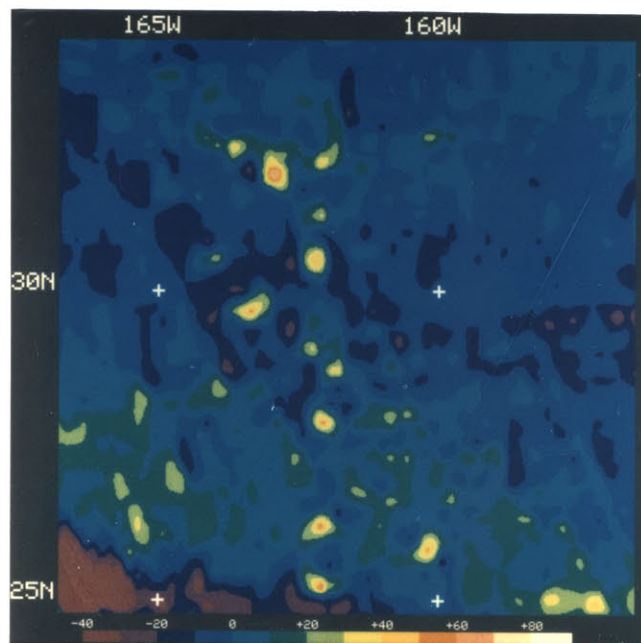


PLATE I (b)

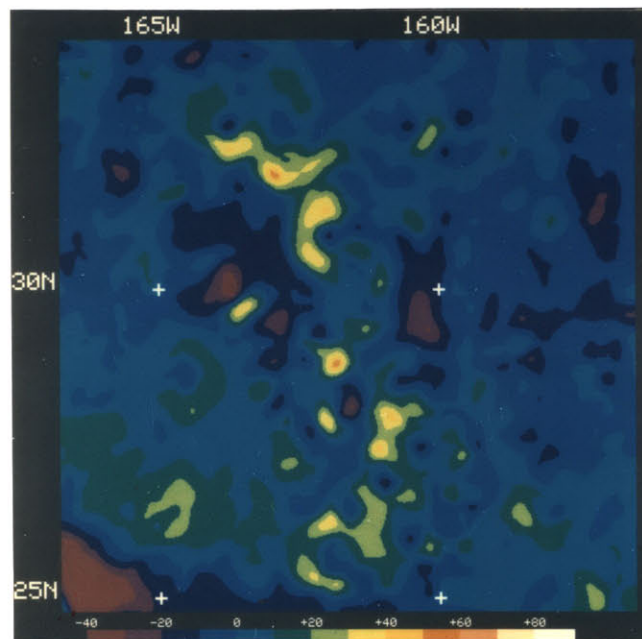


PLATE 1(c)

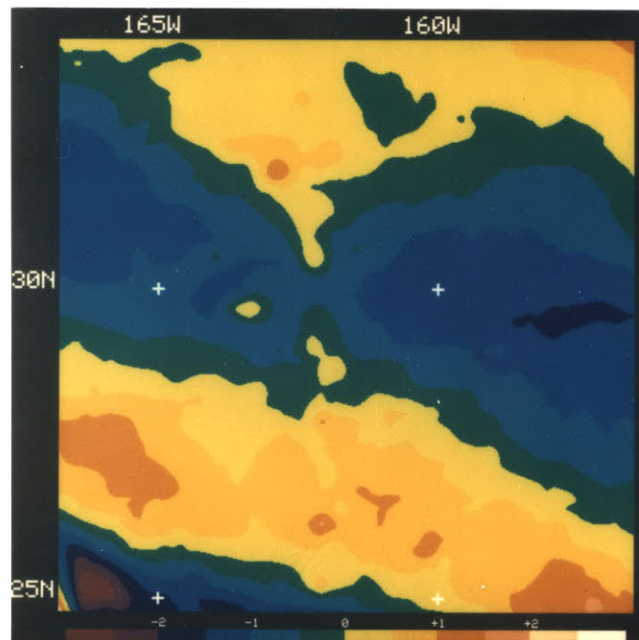


PLATE 2

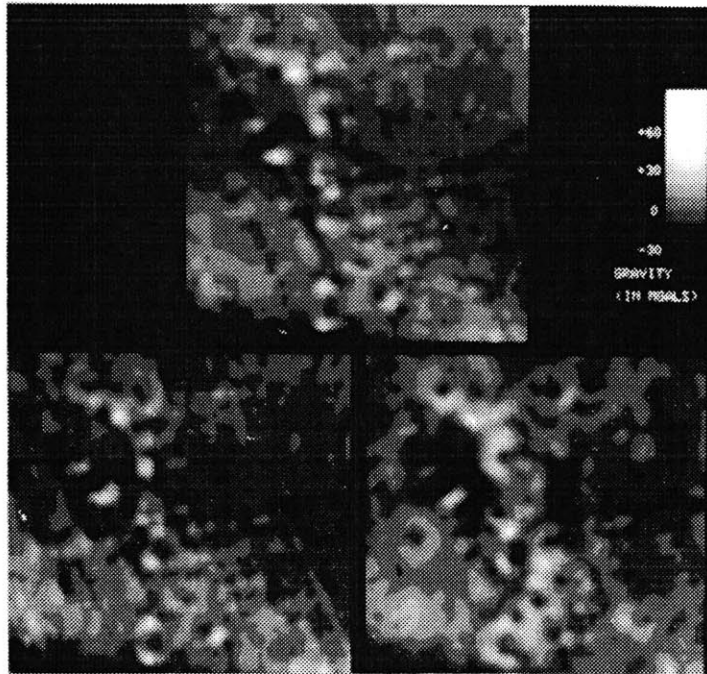


PLATE 1 (a-top, b-left, c-right)

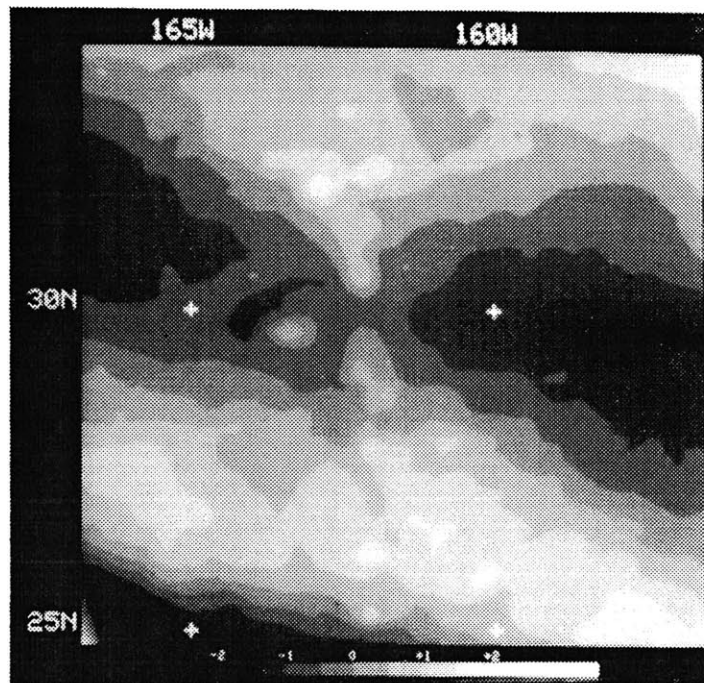


PLATE 2

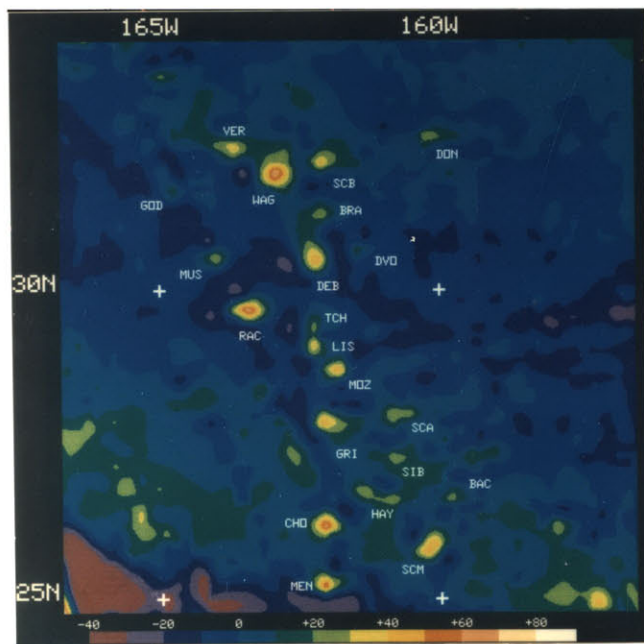


PLATE 3

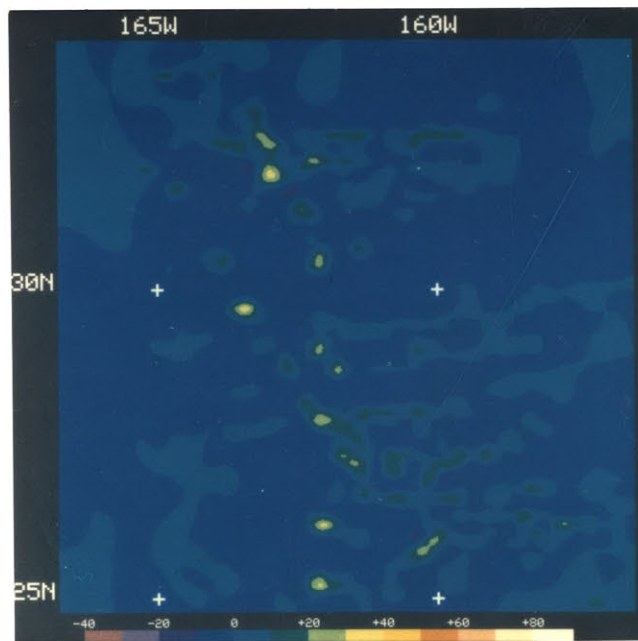


PLATE 4(a)

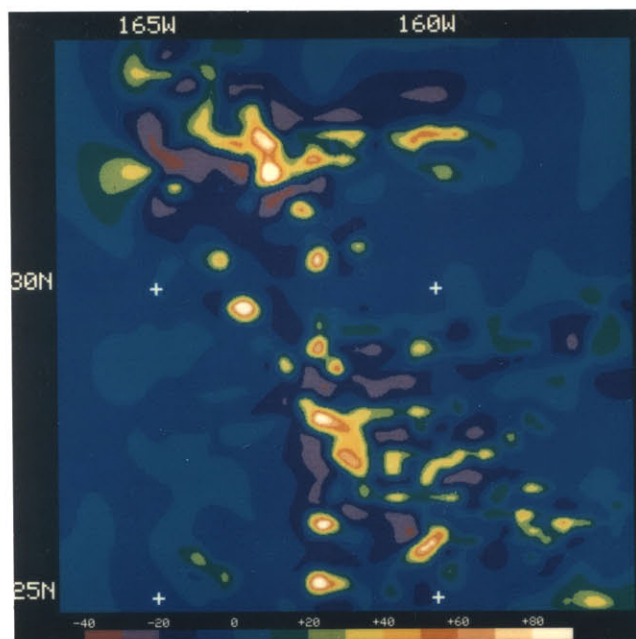


PLATE 4(b)

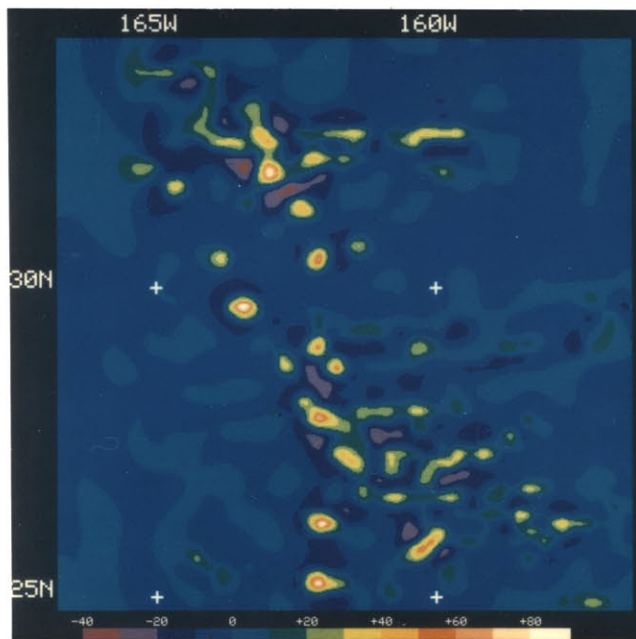


PLATE 4(c)

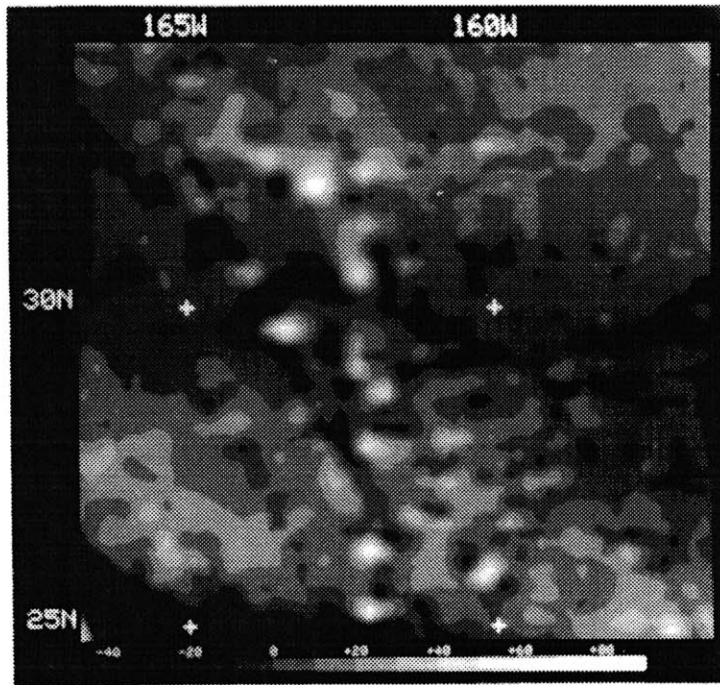


PLATE 3

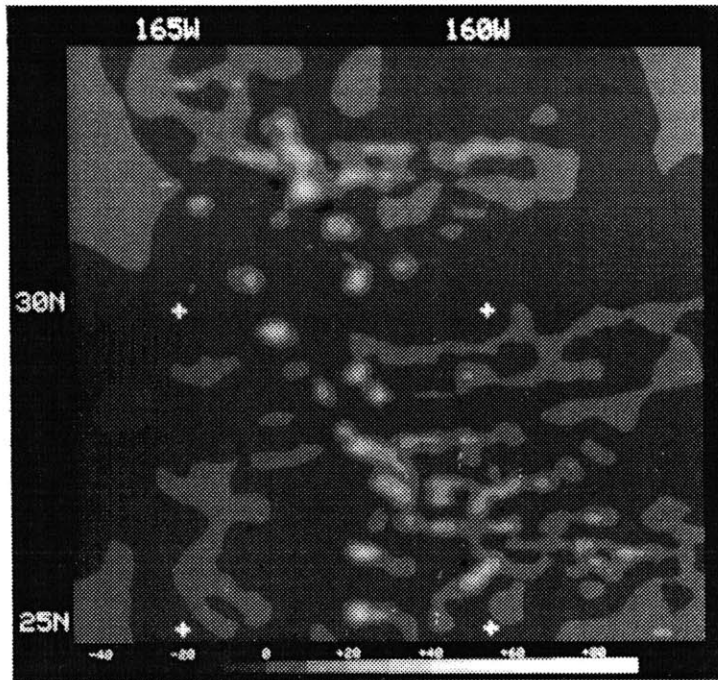


PLATE 4(a)

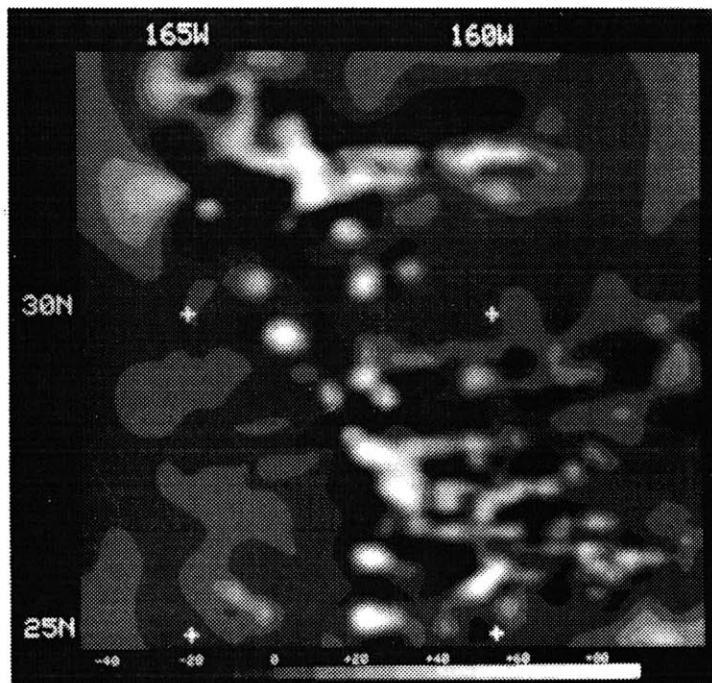


PLATE 4 (b)

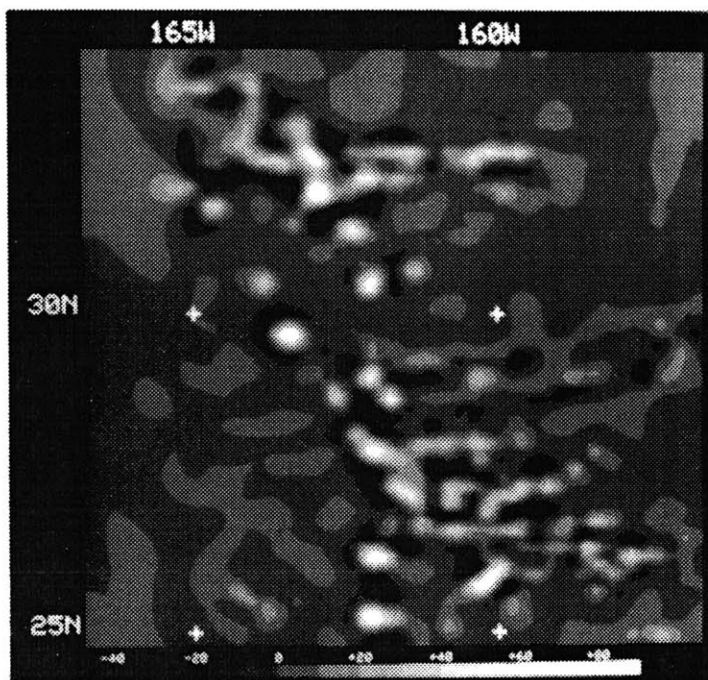


PLATE 4 (c)

### Chapter 3.

#### Geoid Anomalies Over Two South Atlantic Fracture Zones

### 3.1 Abstract

Seasat altimetry profiles across the Falkland-Agulhas fracture zone (FZ) and the Ascension FZ were examined in order to compare the geoid anomalies over these fracture zones to step-like geoid offsets predicted based on thermal models of the lithosphere. The heights of the geoid steps were estimated by the least squares fitting of quadratic curves incorporating a step function to the altimetry profiles. Geoid profiles tended to be noisy and the steps were often quite small, so reliable step estimates were difficult to obtain. A best estimate geoid step was determined for each profile by taking the average of step heights computed with various distances around the fracture zone excluded from the fit. Crustal ages surrounding the fracture zones were determined from surface ship magnetic anomaly data and from existing ocean floor age maps.

The variations in step height with age of the lithosphere determined from our data are not compatible with those predicted for standard thermal plate models. For ages less than ~30 Ma, the geoid step variations across the Falkland-Agulhas FZ decrease in a manner appropriate for an unusually thin plate with a thickness of 50-75 km. At greater ages, the steps are reversed, an effect probably caused by bathymetric highs adjacent to the fracture zone. Geoid steps at the Ascension FZ, for ages less than ~30 Ma, are again consistent with a thin plate. At older ages, the steps appear to quickly jump in size, then gradually decrease in magnitude. Preliminary depth-age data do not support the presence of a plate as thin as 50 or 75 km at either fracture zone, however.

Behavior of the geoid step at both fracture zones can be explained by invoking small-scale convection beneath the lithosphere induced by the temperature gradient across the fracture zone. Alternatively, tectonically

produced surface deformations may account for a large part of the geoid signal. Better knowledge of the bathymetry around these fracture zones is needed before a definite source for these unusual geoid patterns can be determined.

### 3.2 Introduction

Fracture zones on the ocean floor have until recently been very difficult to study over their entire lengths. As linear bathymetric features that extend for thousands of kilometers, fracture zones can be surveyed by ocean-going vessels either at widely spaced locations or in geographically small local areas. Satellite altimetry, from spacecraft such as Seasat and GEOS 3, has provided a dense and uniformly spaced set of global sea surface height measurements which closely approximate the marine geoid. These data finally permit study of fracture zones with sufficient coverage and resolution to accurately determine their geographic positions and trends and to study their variations with age and location.

In the Pacific Ocean, where many fracture zones are longer, more topographically distinct, and have larger age offsets than in other oceans, Seasat altimetry was first used to examine fracture zones. In southern oceans, where ship coverage is often extremely poor, fracture zones observed in the geoid have been of prime interest. Both along-track altimetry profiles and gridded maps of the geoid derived from Seasat data have been used to map positions and trends of South Pacific and Indian Ocean fracture zones [Dixon and Parke, 1983; Sandwell, 1984a; Driscoll et al., 1987].

The geoid across fracture zones, it was hoped, would be useful in constraining thermal models of the structure and evolution of the oceanic lithosphere. Crough [1979], Detrick [1981], Cazenave et al. [1982], and Sandwell and Schubert [1982] have all examined variations in the geoid with age across the Mendocino fracture zone (FZ) in the North Pacific and have compared them to model geoid "steps" produced by the juxtaposition of lithosphere of different ages that occurs along fracture zones. This

comparison has been extended to a number of South Pacific fracture zones [Cazenave et al., 1983; Cazenave, 1984; Driscoll and Parsons, 1987].

An early model of the geoid step [Crough, 1979] employed the observed bathymetry to compute an effective depth of compensation for the fracture zone. Subsequent studies have used the geoid step to discriminate between two complementary models of the lithosphere: the infinite half-space cooling model [Davis and Lister, 1974; Haxby and Turcotte, 1978] which predicts that seafloor depth will vary with the square-root of seafloor age and geoid height linearly with age, and the plate model [McKenzie, 1967; Parsons and Sclater, 1977; Parsons and Richter, 1980] which predicts behavior similar to the half-space model for young ages, but at older ages predicts that the depth and geoid will asymptotically approach constant values as the bottom boundary of the plate (maintained at a constant temperature) is felt.

At a fracture zone, lithosphere of two different ages and thermal structures abut one another. Offsets in the depth and geoid across the fracture zone result from these thermal variations. For a fracture zone whose older side is of age  $t_a$ , younger side of age  $t_b$ , with age offset  $\Delta t = t_a - t_b$ , the geoid step  $\Delta N(t)$ , at mean age  $t = (t_a + t_b)/2$ , predicted to first order by the plate model with a plate thickness of  $a$  is

$$\begin{aligned} \Delta N(t) &= N(t_a) - N(t_b) \\ &= \frac{4G\rho_0\alpha(T_m - T_0)a^2}{g_0\pi} \sum_{n=1}^{\infty} \frac{(-1)^n}{n^2} \left[ 2 \cdot \sinh\left(\frac{n^2\pi^2\kappa\Delta t}{2a^2}\right) \right] \exp\left(\frac{-n^2\pi^2\kappa t}{a^2}\right) \end{aligned} \quad (1)$$

Other parameters are defined in Table 1. When  $t$  is small with respect to  $\Delta t$ , the plate model yields a step identical to that of the half-space model:

$$\Delta N = N(t_a) - N(t_b) = \frac{-2\pi G}{g_0} \rho_0 \alpha (T_m - T_0) \kappa \Delta t = \text{constant} \quad (2)$$

In either case, the geoid is expected to be higher on the younger side and lower on the older side.

These models assume a step-function thermal offset, local isostasy, and bathymetry and geoid variations with wavelengths large compared to the plate thickness. Near the fracture zone, many factors act both to smooth out the geoid step and to add short-wavelength geoid anomalies, such as geoid edge effects and lateral heat conduction [Detrick, 1981; Loudon and Forsyth, 1976], lithospheric flexure [Sandwell, 1984b], thermal stresses within the lithosphere [Parmentier and Haxby, 1986], and crustal structure within and adjacent to the fracture zone [Loudon and Forsyth, 1982]. Most previous studies have avoided regions within ~100 km of a fracture zone when determining the geoid step in order to minimize these complications.

Results from Pacific fracture zone studies tend to support the plate model of the lithosphere, but much of the geoid signal remains poorly understood. Unusual variations of the geoid step with age have been observed across the Udintsev and other fracture zones in the South Pacific [Cazenave, 1984; Driscoll and Parsons, 1987]. Fits to observed geoid anomalies with the models of Sandwell [1984b] and Parmentier and Haxby [1986] leave a significant amount of power in the geoid signal unaccounted for. Small-scale convection induced by temperature differences across the fracture zone may be responsible for an additional portion of the geoid signal [Buck and Parmentier, 1986; Craig and McKenzie, 1986; Robinson et al., 1987].

In this study, we use the geoid obtained from Seasat to investigate two major fracture zones in the South Atlantic and the seafloor adjacent to

Table 1.  
Parameter Definitions and Values

Parameter	Definition	Value
$G$	Universal gravitation constant	$6.67 \times 10^{-11} \text{ m}^3 \text{ kg}^{-1} \text{ s}^{-2}$
$g_0$	Gravitational acceleration	$9.80 \text{ m s}^{-2}$
$\alpha$	Thermal expansion coefficient	$3.1 \times 10^{-5} \text{ }^\circ\text{C}^{-1}$
$T_m$	Mantle Temperature	$1365 \text{ }^\circ\text{C}$
$T_0$	Surface Temperature	$0 \text{ }^\circ\text{C}$
$\rho_0$	Density of lithosphere	$3330 \text{ kg m}^{-3}$
$\kappa$	Thermal diffusivity	$8.0 \times 10^{-7} \text{ m}^2 \text{ s}^{-1}$
$a$	Thickness of plate	50, 75, 100 km

them: the Falkland-Agulhas FZ and the Ascension FZ. These fracture zones represent significant age offsets of the oceanic crust and lithosphere of 10-15 million years, and they appear prominently on global geoid and gravity maps [Haxby, 1985]. They have geoid anomalies and age offsets comparable to those of Pacific fracture zones such as the Udintsev FZ; they are, therefore, likely candidates for study in a manner similar to that used in the Pacific. We determine whether there are measurable steps in the geoid and study the variations in step height as a function of age of the lithosphere across the fracture zones, in hope that the geoid will yield information on the regional structure and evolution of the lithosphere.

### 3.3 Geophysical Setting

The Falkland-Agulhas fracture zone (Fig. 1) extends from the Falkland Plateau off the southeastern coast of Argentina to the southern tip of Africa. West of 30°W, the position of the fracture zone is marked by the Falkland ridge, a large aseismic ridge with over 2 km of relief. From 49°S 29°W the fracture zone trends east-northeast to 43°S 5°E, where its position is again marked by a linear pattern of bathymetric highs referred to here as the Agulhas ridge. The Mid-Atlantic ridge intersects the fracture zone with a left-lateral transform offset of ~200 km between 13°W and 11°W. The present day age offset at the ridge is ~12 m.y.

On the eastern branch of the fracture zone, just west of the Agulhas ridge, two large seamount groupings have been mapped. The Discovery seamounts at 42°S 0°W, thought to mark the location of a mantle hotspot [Morgan, 1981], lie about 300 km north of the fracture zone, while the Herdman and Schwabenland seamounts, at 46°S 0°W, lie about 100 km to the

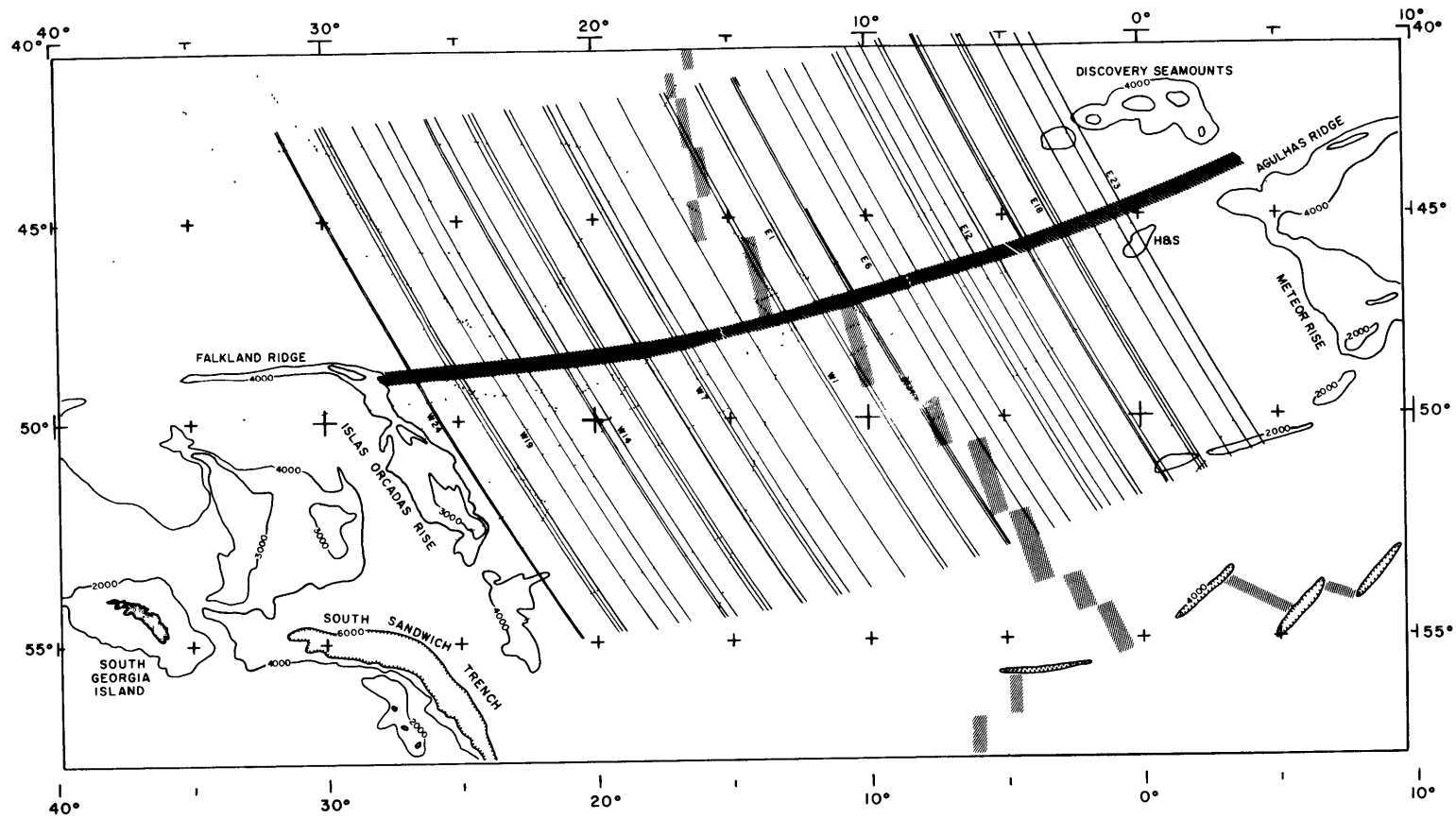


Figure 1. Reference map of the area around the Falkland-Agulhas fracture zone. Major bathymetric features and selected bathymetric contours are shown. Dark shading shows the position of the Falkland-Agulhas FZ, light shading indicates the approximate position of the Mid-Atlantic ridge. "H&S" marks the location of the Herdman and Schwabenland seamounts. Solid curves show the locations of the Seasat arcs used in this study. Selected arcs are labelled with W (west side) or E (east side) and the arc numbers as listed in Table 2. Dotted lines indicate the tracks of ships whose magnetic anomaly data were used to produce the age map of Fig. 3b.

south of the fracture zone [GEBCO, 1978]. Since this entire region is poorly mapped, other seamounts of substantial size probably remain undiscovered.

South of the fracture zone at the points where it meets the Falkland and Agulhas ridges lie two conjugate aseismic ridges: the Islas Orcadas rise and Meteor rise respectively. These are thought to mark the initial position of the Mid-Atlantic ridge after its most recent jump from a more easterly location [Barker, 1979; LaBrecque and Hayes, 1979]. Since the time of this last ridge jump, some 50-60 Ma, seafloor spreading both north and south of the Falkland-Agulhas FZ has consisted of straightforward opening about the rotation poles determined for the entire South Atlantic [Barker, 1979; LaBrecque and Hayes, 1979; Ladd, 1974]. Prior to 60 Ma, however, when the conjugate ridges and rises mentioned above were being formed, spreading south of the fracture zone was quite complex [LaBrecque and Hayes, 1979; Rabinowitz and LaBrecque, 1979]. We therefore confine our study to the younger portion of the Falkland-Agulhas FZ lying between the aseismic ridges on seafloor less than ~50 Ma.

The Ascension fracture zone (Fig. 2) extends from the coast of South America at 9°S 35°W eastward to the Mid-Atlantic ridge at 14°W and 11°W, then trends east-northeasterly to the Gulf of Guinea and the African coast at 3°S 5°E. The Mid-Atlantic ridge is offset right-laterally at the fracture zone by ~230 km, yielding a present day age offset of 11-14 m.y.

Ascension Island, rising from a depth of 3 km, lies 50 km south of the fracture zone and 100 km west of the Mid-Atlantic ridge. The region from the Ascension FZ to the south about the Mid-Atlantic ridge has been studied in detail by Van Andel et al. [1970; 1973] and Brozena [1986]. To the east of 0° longitude, numerous small seamounts and seamount chains have been

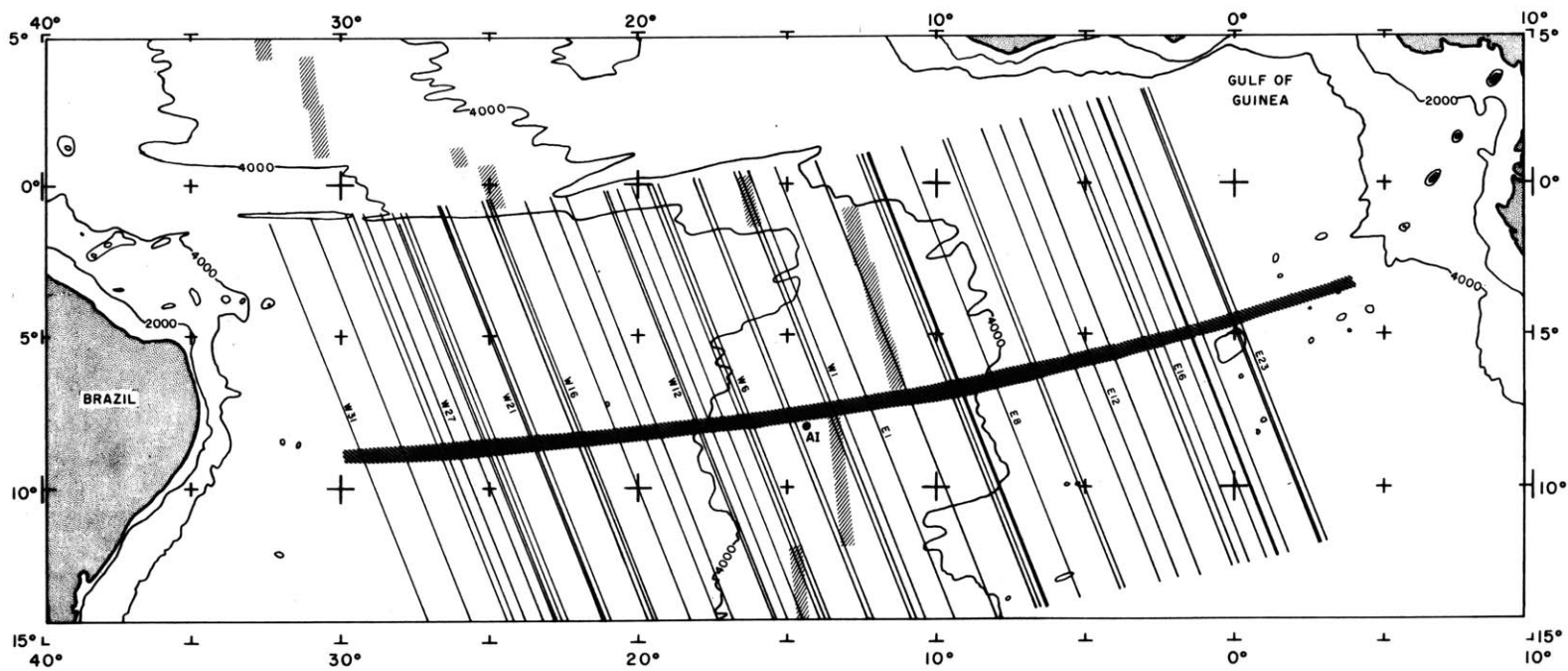


Figure 2. Reference map of the area around the Ascension fracture zone. "AI" marks the position of Ascension Island. Figure conventions are the same as in Fig. 1.

mapped near the fracture zone trace [GEBCO, 1978; Emery and Uchupi, 1984]. Since the Ascension FZ extends all the way to the continental margins, its oldest sections are covered by sediment layers over a kilometer thick [Ewing et al., 1973; Sibuet and Mascle, 1978].

The location, size, and age of Ascension Island suggest that it may be related to a hotspot. Various locations for the hotspot have been suggested, from the island itself [Morgan, 1981] to the ridge 200 km south of the island [Brozena, 1986] to the Circe bathymetric high 450 km east of the ridge [Van Andel and Heath, 1970; Schilling et al., 1985]. The numerous seamounts around the easternmost section of the fracture zone are thought to be associated with the St. Helena hotspot [Morgan, 1981].

### 3.4 The Data

#### 3.4.1 Seafloor Ages

Of critical importance to understanding the geoid step is accurate knowledge of the age offset across the fracture zone and the absolute ages of the crust on either side. In the South Atlantic, seafloor spreading has consisted, for the most part, of steady, slightly asymmetric opening between South America and Africa [Ladd, 1974; Rabinowitz and LaBrecque, 1979; Sibuet and Mascle, 1978]. Although the spreading history of these two fracture zones has been relatively simple, there is quite a bit of age uncertainty around them.

In the region of the Falkland-Agulhas FZ, most of the ship-based magnetic surveys have been confined to areas adjacent to the continental margins and to areas with more complex tectonic histories south of the fracture zone. In the simpler areas north of the fracture zone and near the Mid-Atlantic ridge, there are only a handful of magnetic anomaly

profiles.

To estimate the ages across the Falkland-Agulhas FZ, we obtained magnetic anomaly data from all cruises in this area for which the National Geophysical Data Center (NGDC, Boulder, Colorado) had data. Additional cruise data [Barker, 1979] provided age constraints just south of the fracture zone. The track coverage of the magnetic data is shown with dotted lines in Figure 1. We selected and identified our own anomaly picks with the aid of synthetic magnetic anomalies based on the time scale of LaBrecque et al. [1977]. Using fracture zone locations and trends seen in the sparse along-track ship bathymetry, the GEBCO [1978] bathymetric maps, and gridded geoid and gravity field maps, we interpolated the ages between the known magnetic anomalies. The crustal ages and anomaly picks surrounding the Falkland-Agulhas FZ are shown in Figure 3b. They agree well with other age determinations [Ladd, 1974]. Age errors are estimated at  $\pm 1-2$  m.y. based on uncertainties in our interpolation procedure.

At the Ascension FZ, near equatorial east-west spreading results in very weak magnetic anomalies and unreliable magnetic data. Only the region just south of the fracture zone out to age  $\sim 20$  Ma has been well studied [Van Andel and Heath, 1970; Van Andel et al., 1973]. Most published age of the ocean maps [Sclater et al., 1980; Larson et al., 1985] have extrapolated Ladd's [1974] data northward in the South Atlantic using fracture zone locations and offsets, mid-ocean ridge positions, and finite rotation poles determined for the entire South Atlantic.

We initially employed the digitized isochrons of Sclater et al. [1980] (Fig. 3a) and obtained the ages along the fracture zone by linearly interpolating between the isochrons. Comparison with Brozena's [1986] detailed map south of the Ascension FZ indicates that these interpolated

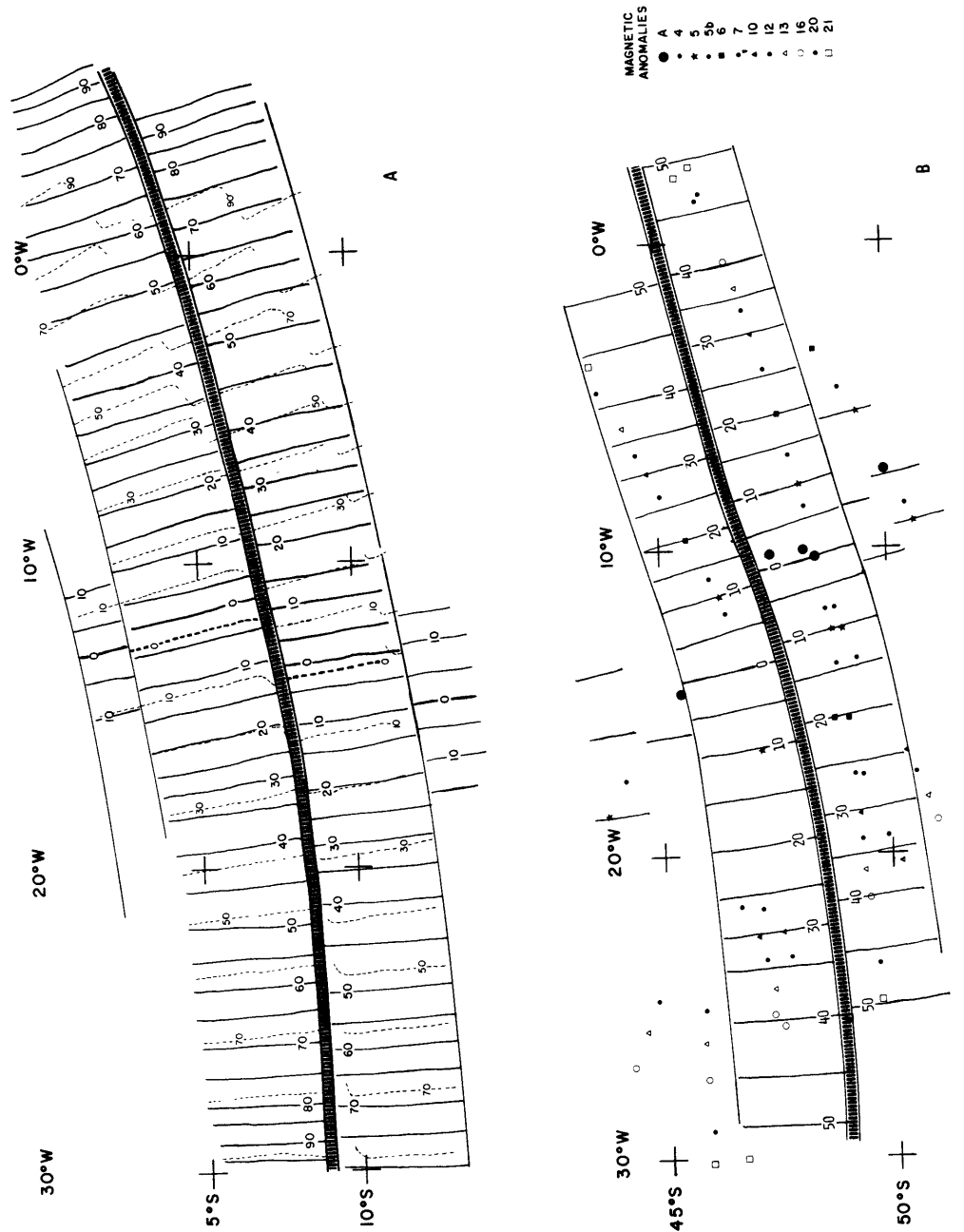


Figure 3. Age of the ocean floor around each fracture zone. (a) Ascension FZ. Solid isochrons (shown every 5 m.y.) are from Sclater *et al.* [1980] and are the ages used in our analysis. Dashed isochrons (shown every 10 m.y.) are from Cande *et al.* [1984]. Note the large differences between the two data sets along the east branch of the fracture zone. (b) Falkland-Agulhas FZ. Solid isochrons (shown every 5 m.y.) have been interpolated from the illustrated magnetic anomaly picks. The magnetic data were obtained along the ship tracks shown in Fig. 1.

ages are in error by less than 3 m.y., similar to the age uncertainties in the magnetic time scale itself [LaBrecque et al., 1977; Harland et al., 1982]. In another check on these ages, we compared them with the gridded seafloor age data base of Cande et al. [1984] (Fig. 3a). West of the Mid-Atlantic ridge, the two age maps are consistent to within ~5 m.y., with age offsets across the Ascension FZ disagreeing by less than 3 m.y. East of the ridge, ages differ by up to 20 m.y. at the 50 Ma and 70 Ma isochrons of the Sclater et al. [1980] and Cande et al. [1984] data bases, respectively. Age offsets are in better agreement, however, differing by less than 4 m.y. over most of the 0-90 Ma age range examined.

In the following analysis, we use the ages and age offsets of the Sclater et al. [1980] data. Note that the mean ages may be in error on the east side of the fracture zone by up to 20 m.y., but that most age offsets are reliable to within  $\pm 2-3$  m.y.

#### 3.4.2 Seasat Data

The radar altimeter aboard Seasat obtained high resolution (10 cm vertical precision, 6.7 km horizontal data point spacing) measurements of sea surface height [Tapley et al., 1982]. The major sources of error that remain in the data after correcting for tides, atmospheric propagation, meteorological conditions and sea state, are ephemeris errors and ocean currents. These tend to be of long wavelength except near western boundary currents. They should not affect our geoid step profiles, as long wavelengths are removed in our analysis.

Since our two fracture zones trend from east to east-northeast, we have worked primarily with ascending geoid arcs (shown in Figs. 1 and 2). They cross the fracture zones at steep angles, less than  $15^\circ$  from perpendicular. Descending arcs have been used to periodically check step

height results, but their smaller angles of intersection with the fracture zones combined with the large seafloor age gradients parallel to the fracture zones make these data much less reliable for purposes of estimating the geoid step.

The along-track ascending arc data have had long-wavelength geoid anomalies removed by subtracting a reference geoid based on the GEM 9 potential coefficients [Lerch et al., 1979] complete to degree and order 10. Short-wavelength anomalies were also removed by smoothing the geoid along track with a Gaussian filter  $w(x) = \exp(-x^2/\sigma^2)$  with a half-width  $\sigma$  of 5 km. Neither of these procedures should seriously affect estimates of the geoid step, and tests with unfiltered data bear this out.

### 3.4.3 Altimetry Profiles

In Figures 4 and 5, we present the Seasat arcs that we examined on each side of the two fracture zones. The profiles across youngest seafloor are at the top of each figure and the mean age increases downwards. Data describing each profile are listed in Table 2.

On the west side of the Falkland-Agulhas FZ (Fig. 4a), the ocean floor is younger to the north and older to the south; hence the theoretical step decreases from north to south. West of the profiles that cross the active transform fault region, a step of the correct orientation is seen. The step is visible on profiles 3-7 but becomes smaller and less distinct on profiles 8-13. On profiles 14-16 no step is obvious, but a characteristic geoid trough continues to mark the location of the fracture zone. Profiles 17-19 show the geoid higher to the south. A step such as this, of the opposite sign, could be produced with our models only if the lithosphere were younger on the south side of the fracture zone. Our age control here (Fig. 3b) is reasonably good, however, so it is highly





unlikely that this anomalous step is the result of an age reversal across the fracture zone. Whatever causes this apparent step reversal is limited in geographic extent, as the step again becomes small and vague on profiles 20-24.

The east side profiles across the Falkland-Agulhas FZ (Fig. 4b) show similar behavior, but short-wavelength features confuse the step interpretation. On this branch of the fracture zone the seafloor is younger to the south, and we do indeed (in profiles 3-5) see a step of the correct orientation. The step shrinks in size in profiles 6-8, but a large seamount- or ridge-like geoid anomaly just south of the fracture zone makes a true step estimate difficult.

A glance down this figure shows a number of small-scale seamount-like features near the fracture zone. Seamounts make step estimates difficult because they force you to look farther from the fracture zone to obtain the normal baseline geoid height, and their loads on the ocean floor bend the lithosphere down creating a moat around the seamounts [Watts and Ribe, 1984]. For large seamounts on older lithosphere, this flexure can extend for hundreds of kilometers radially around the seamount, biasing the estimated baseline geoid heights in the region towards lower values.

The seamount-like geoid signal appearing on profiles 6-8 fades away on subsequent profiles, but beginning with profile 9 we see an apparent step reversal developing. Unlike the west branch of the fracture zone, where the step reversal extended over seafloor with mean ages of 35-40 Ma, the anomalous step on this side begins at a mean age of ~20 Ma and extends to at least 35 Ma (profile 17). The higher north side geoid narrows and begins to appear block-like by profile 14, but it degenerates into twin seamount-like anomalies by profiles 17 and 18. Profiles 22, 23 and

Table 2. Summary of Profile Information

Profile Number	Revnum <sup>a</sup>	North Age <sup>b,c</sup> (m.y.)	South Age (m.y.)	Mean Age (m.y.)	Age Offset (m.y.)	Step Height (meters)	$\frac{-\Delta N}{\Delta t}$ (cm/m.y.)	Quality <sup>d</sup>
Falkland-Agulhas Fracture Zone: West Side								
1	RO175	(3)	9	6.0	-6	0.01±0.10	0.10±1.90	G
2	RO419	(2)	9	5.5	-7	-0.01±0.28	-0.09±4.36	A
3	RO620	3	15	9.0	-12	0.10±0.14	0.85±1.19	G
4	PO577	7	20	13.5	-13	0.71±0.30	5.46±2.63	G
5	RO778	10	22	16.0	-12	0.87±0.19	7.24±2.38	G
6	RO290	12	23	17.5	-11	0.73±0.28	6.67±3.15	G
7	PO534	12	24	18.0	-12	0.58±0.22	4.82±2.21	G
8	RO247	15	27	21.0	-12	0.48±0.34	3.96±3.09	A
9	PO735	16	28	22.0	-12	0.22±0.40	1.81±3.44	A
10	RO491	16	28	22.0	-12	0.56±0.41	4.67±3.68	A
11	RO204	20	32	26.0	-12	0.53±0.29	4.40±2.66	G
12	PO448	20	33	26.5	-13	0.30±0.30	2.30±2.42	A
13	RO692	21	33	27.0	-12	0.29±0.28	2.44±2.45	A
14	PO161	24	37	30.5	-13	0.06±0.29	0.43±2.27	A
15	PO649	25	38	31.5	-13	0.00±0.21	0.02±1.64	A
16	RO850	25	38	31.5	-13	-0.01±0.16	-0.11±1.24	A
17	RO606	30	42	36.0	-12	-1.06±0.34	-8.80±3.56	S
18	PO807	33	44	38.5	-11	-0.90±0.48	-8.14±4.95	S
19	PO563	36	46	41.0	-10	-0.26±0.26	-2.61±2.82	S
20	RO764	39	49	44.0	-10	0.43±0.31	4.29±3.47	A
21	RO276	39	50	44.5	-11	0.61±0.38	5.55±3.86	A
22	RO520	40	50	45.0	-10	0.44±0.31	4.39±3.49	G
23	RO477	43	53	48.0	-10	0.25±0.17	2.53±1.94	G
24	RO721	43	53	48.0	-10	0.65±0.15	6.46±2.43	G
Falkland-Agulhas Fracture Zone: East Side								
1	RO462	7	(5)	6.0	2	0.05±0.36	-2.50±31.44	G
2	RO218	8	(4)	6.0	4	-0.44±0.25	10.92±10.77	A
3	RO505	13	1	7.0	12	-1.41±0.37	11.72±4.21	G
4	RO749	13	1	7.0	12	-1.34±0.31	11.20±3.76	G
5	RO261	14	2	8.0	12	-0.92±0.28	7.65±3.02	A
6	PO548	19	6	12.5	13	-0.63±0.23	4.87±2.12	G
7	RO792	22	8	15.0	14	-0.68±0.44	4.87±3.33	P
8	RO591	24	12	18.0	12	-0.19±0.65	1.55±5.61	P
9	RO835	29	15	22.0	14	0.43±0.27	-3.06±2.04	S
10	RO634	30	16	23.0	14	0.70±0.26	-5.01±2.17	S
11	PO146	32	18	25.0	14	0.86±0.28	-6.17±2.40	S
12	RO878	34	20	27.0	14	0.93±0.35	-6.63±2.89	S
13	RO433	36	22	29.0	14	1.61±0.63	-11.51±5.12	S
14	RO189	37	23	30.0	14	1.28±0.71	-9.14±5.51	S
15	RO720	41	27	34.0	14	1.25±0.74	-8.96±5.72	S
16	PO476	41	27	34.0	14	1.13±0.57	-8.09±4.46	S
17	RO232	42	28	35.0	14	1.04±0.49	-7.44±3.85	S
18	PO519	45	33	39.0	12	0.59±0.16	-4.93±1.77	P
19	RO275	45	33	39.0	12	0.31±0.25	-2.57±2.19	P
20	RO763	46	34	40.0	12	0.17±0.32	-1.39±2.77	P
21	RO562	48	37	42.5	11	-0.42±0.12	3.78±1.49	G
22	RO806	51	41	46.0	10	0.07±0.62	-0.74±6.41	P
23	RO605	52	42	47.0	10	0.25±1.10	-2.45±11.47	P

<sup>a</sup> REVNUM is the J.P.L. revolution number as modified by Rapp [1982].

<sup>b</sup> Error estimates: north, south ages ±2 m.y., mean age ±1.4 m.y., age offset ±2.8 m.y.

<sup>c</sup> Ages in parentheses indicate areas within the transform fault region of the fracture zone.

<sup>d</sup> Quality: G-good, A-ambiguous, S-anomalous (strange), P-poor.

Table 2 (Continued).

Profile Number	Revnum	North Age (m.y.)	South Age (m.y.)	Mean Age (m.y.)	Age Offset (m.y.)	Step Height (meters)	$\frac{-\Delta N}{\Delta t}$ (cm/m.y.)	Quality
Ascension Fracture Zone: West Side								
1	R0777	10	(3)	6.5	7	-0.92±0.72	13.09±12.32	A
2	R0289	11	(1)	6.0	10	-1.04±0.79	10.43±8.71	A
3	R0533	12	(0)	6.0	12	-0.96±0.68	7.98±6.16	G
4	R0246	18	7	12.5	11	-0.72±0.33	6.53±3.52	G
5	P15000	19	8	13.5	11	-0.48±0.38	4.36±3.75	G
6	R0203	25	14	19.5	11	-0.15±0.32	1.36±3.00	P
7	R0447	26	15	20.5	11	-0.29±0.33	2.63±3.18	A
8	R0691	26	15	20.5	11	-0.58±0.44	5.29±4.33	A
9	P25000	30	17	23.5	13	-0.19±0.24	1.45±1.87	P
10	R0160	33	20	26.5	13	-0.25±0.31	1.89±2.48	G
11	P0648	35	21	28.0	14	-0.46±0.37	3.30±2.78	A
12	R0849	35	21	28.0	14	-0.38±0.43	2.70±3.15	A
13	R0605	41	30	35.5	11	-1.18±0.61	10.76±6.35	A
14	R0806	43	32	37.5	11	-1.10±0.57	10.00±5.96	G
15	R0562	46	38	42.0	8	-0.79±0.91	9.84±12.58	A
16	R0763	50	42	46.0	8	-0.62±0.43	7.76±6.32	G
17	R0275	51	42	46.5	9	-0.68±0.35	7.60±4.74	G
18	P0519	52	43	47.5	9	-0.45±0.26	5.04±3.40	G
19	R0232	58	47	52.5	11	-0.88±0.27	8.02±3.29	G
20	P0476	59	48	53.5	11	-0.99±0.16	9.02±2.75	G
21	R0720	60	48	54.0	12	-1.18±0.20	9.81±2.88	G
22	R0189	65	52	58.5	13	-0.30±0.29	2.34±2.36	G
23	R0433	66	53	59.5	13	-0.29±0.33	2.26±2.66	G
24	R0677	67	54	60.5	13	-0.29±0.33	2.21±2.61	A
25	P05002	67	54	60.5	13	-0.19±0.40	1.44±3.19	A
26	R0878	69	56	62.5	13	-0.28±0.33	2.14±2.63	G
27	P0146	73	60	66.5	13	-0.55±0.51	4.25±4.11	A
28	R0634	74	62	68.0	12	-0.49±0.33	4.12±3.02	G
29	R0835	75	63	69.0	12	-0.54±0.21	4.47±2.09	G
30	R0591	82	70	76.0	12	-0.65±0.23	5.39±2.36	G
31	P0548	93	77	85.0	16	-0.35±0.55	2.20±3.51	A
Ascension Fracture Zone: East Side								
1	R0576	(5)	7	6.0	-2	-0.09±0.33	-4.50±29.22	A
2	P0619	2	14	8.0	-12	0.09±0.70	0.78±6.03	A
3	R0662	9	20	14.5	-11	0.09±0.92	0.86±8.64	A
4	R0418	9	20	14.5	-11	0.38±0.64	3.47±6.02	A
5	R0174	10	21	15.5	-11	0.21±0.72	1.91±6.73	A
6	R01035	10	21	15.5	-11	0.46±0.56	4.16±5.34	A
7	R01379	10	21	15.5	-11	0.17±0.72	1.55±6.76	A
8	R0461	15	27	21.0	-12	0.72±0.71	5.98±6.22	G
9	R0504	22	36	29.0	-14	0.89±0.25	6.38±2.25	G
10	P0260	23	37	30.0	-14	0.80±0.30	5.71±2.49	G
11	R0547	30	42	36.0	-12	0.70±0.41	5.81±3.74	G
12	R0791	34	44	39.0	-10	0.83±0.47	8.31±5.42	A
13	P0590	38	46	42.0	-8	0.34±0.32	4.27±4.56	A
14	P0834	42	50	46.0	-8	-0.02±0.24	-0.23±3.15	S
15	R0633	43	51	47.0	-8	-0.44±0.45	-5.45±6.32	S
16	R0145	44	53	48.5	-9	-0.34±0.37	-3.73±4.46	S
17	R0877	46	56	51.0	-10	-0.21±0.23	-2.05±2.47	S
18	P05002	47	58	52.5	-11	-0.14±0.29	-1.29±2.78	S
19	R0676	47	58	52.5	-11	-0.20±0.30	-1.85±2.87	S
20	R0188	49	60	54.5	-11	-0.24±0.50	-2.21±4.73	S
21	R0719	53	66	59.5	-13	0.30±0.63	2.30±5.00	P
22	R0475	54	66	60.0	-12	0.51±1.16	4.28±9.95	P
23	R0231	55	67	61.0	-12	0.26±0.66	2.14±5.71	P

subsequent profiles (not shown) are overwhelmed by the large Discovery seamount chain north of the fracture zone.

Across the west side of the Ascension FZ (Figure 5a), the seafloor is younger and, as expected, the geoid step higher to the south. The step appears to decrease in amplitude and become somewhat ambiguous in profiles 6-12. A large step, or perhaps a double step, reappears in profiles 13-15. Although the fracture zone might be double in this area, the total age offset across the two parts, hence the total geoid step, should remain constant. By profile 16, the step has again diminished. It remains small but relatively constant as the north side geoid slopes more steeply upward. Beyond profile 30 (~75 Ma) the fracture zone geoid signal fades out entirely. Although baseline slopes change dramatically on this side of the fracture zone, no obvious step reversals occur. A step "rejuvenation" appears instead between the mean ages of 35 and 45 Ma.

The profiles on the east side of the Ascension FZ behave quite differently. Since younger seafloor lies north of the fracture zone, the step in profile 2 is of the expected sign. The step remains small and somewhat vague in profiles 3-7, but appears clearly in profiles 8-10. Starting from profile 11, however, an apparent step reversal occurs. It is caused by a baseline bulge south of the fracture zone which moves gradually northward. This bulge is centered just south of the fracture zone in profiles 17-20. The diagnostic fracture zone geoid trough is still present at this point and the fracture zone still appears to exhibit a small step, though of the opposite sign. Beyond profile 21 (~60 Ma) the fracture zone appears to fade away and its location becomes uncertain, as it did on the west branch, but the geoid bulge remains. This longer-wavelength high may be associated with one of the hotspots mentioned above.

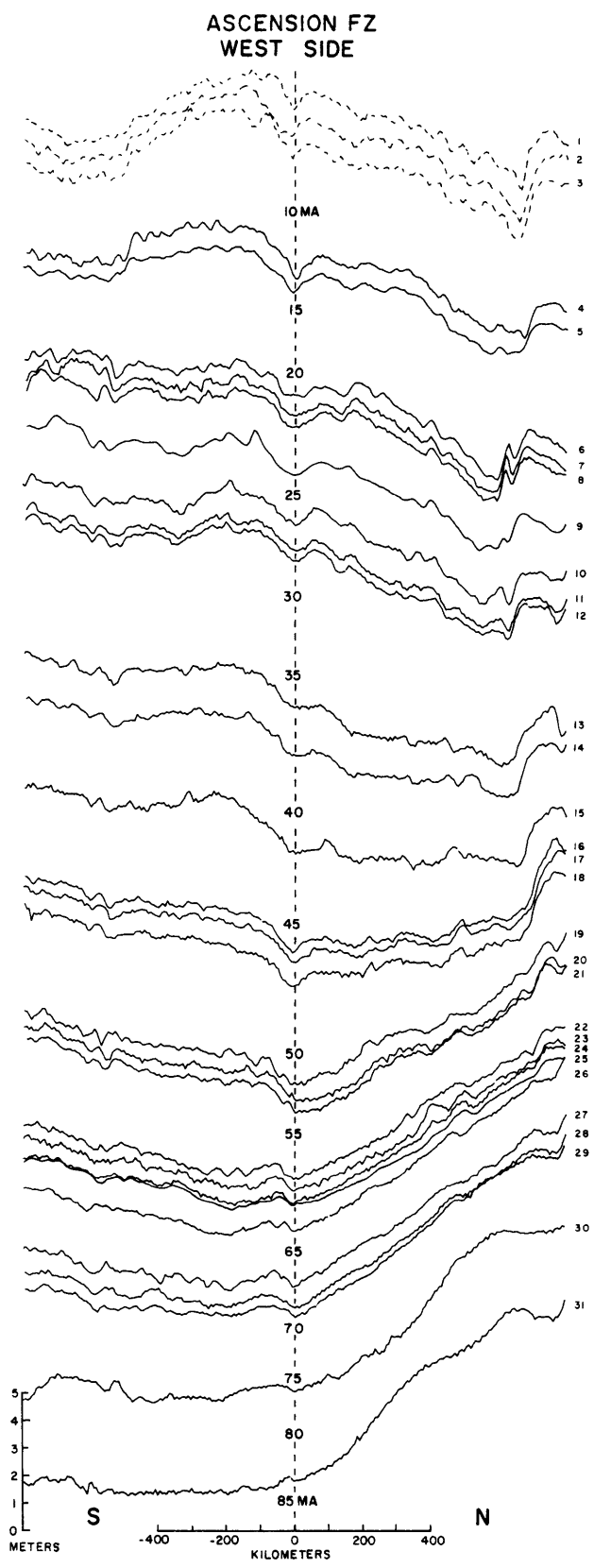


Figure 5 (a). Seasat altimetry profiles across the west branch of the Ascension fracture zone. See Fig. 4 caption for further explanation.

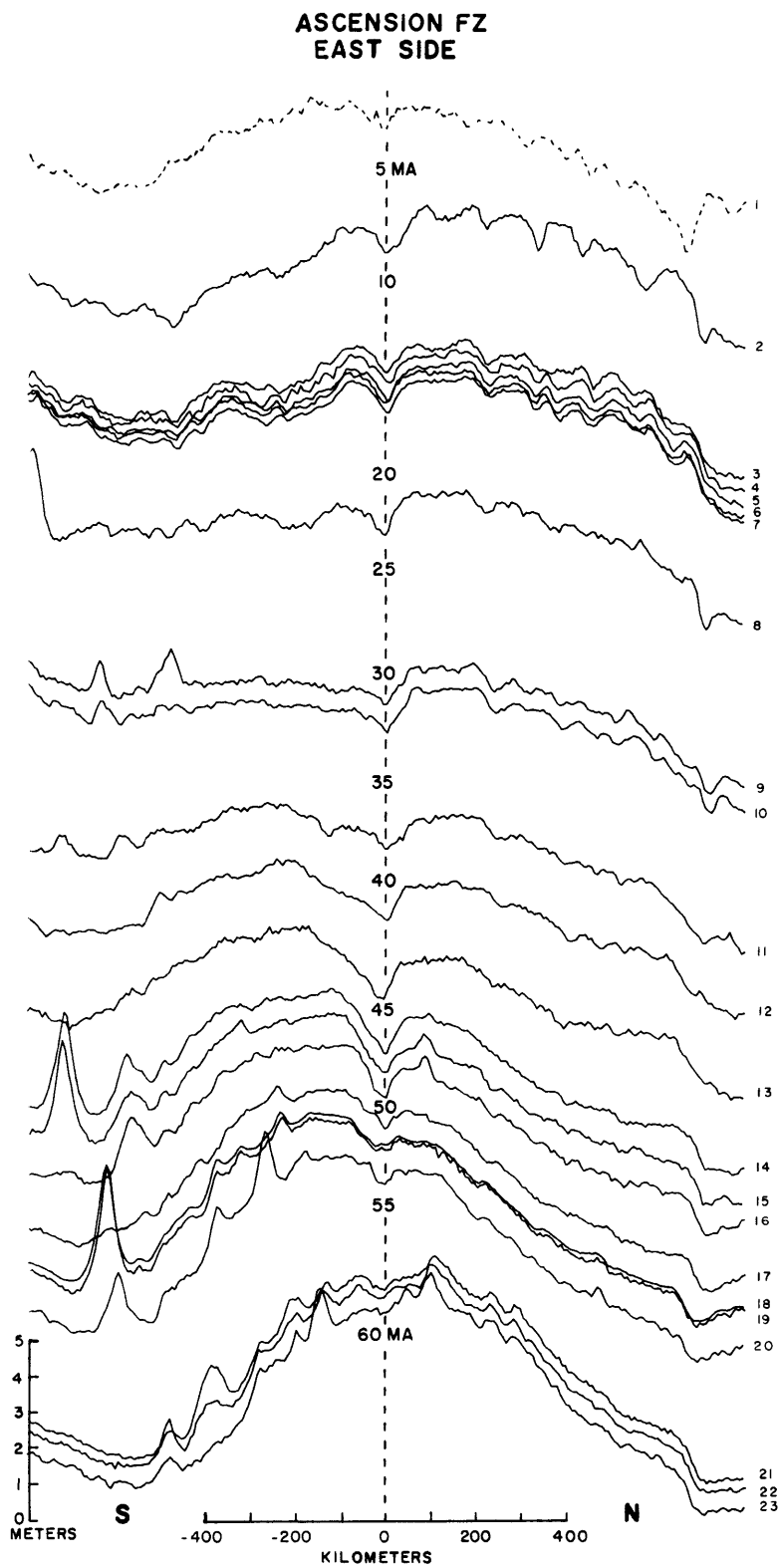


Figure 5 (b). Seasat altimetry profiles across the east branch of the Ascension fracture zone.

The disappearance of the characteristic fracture zone geoid trough, as well as the geoid step, at ages of 60-70 Ma on both sides of the Mid-Atlantic ridge suggests that this fracture zone may not have existed, or may have had a much smaller age offset, before this time. Alternatively, burial by sediments in these older areas may be reducing shorter-wavelength geoid anomalies below detectable levels.

### 3.5 The Geoid Steps

We cannot simply ignore the many geoid profiles that do not exhibit clear, unambiguous step signatures, as others have done in the Pacific where the short-wavelength geoid power tends to be much lower. To do so would leave us with only a handful of profiles across our two fracture zones. We therefore estimate geoid steps for almost all the profiles and only exclude those for which there is solid evidence that what we are seeing is not a simple fracture zone with normal lithosphere. For example, we exclude profiles in which we find large aseismic ridges or seamounts. Even if a step offset does not seem to be an appropriate description of the geoid on an individual profile, it still provides some manner of characterizing the behavior of the geoid over many profiles.

#### 3.5.1 Step Estimation Procedure

Our technique for estimating the geoid step across a fracture zone is similar to one commonly in use [Crough, 1979; Detrick, 1981; Cazenave et al., 1983; Driscoll and Parsons, 1987]. We fit a quadratic polynomial containing a step function to each geoid profile. This curve  $P(x)$  is described by

$$P(x) = Ax^2 + Bx + C + \Delta N \cdot H(x-x_0) \quad (3)$$

$$H(x-x_0) = \begin{cases} 0, & x < x_0 \\ 1, & x > x_0 \end{cases}$$

where  $x$  is the distance along the profile,  $x_0$  is the fracture zone position,  $\Delta N$  is the geoid step,  $A$ ,  $B$ ,  $C$  are constants of the polynomial, and  $H$  is the unit step function. Using a least squares fitting procedure, we determine the best values for  $A$ ,  $B$ ,  $C$ , and  $\Delta N$  for each profile.

A number of variables can substantially affect the estimated step, such as:  $x_0$ , the exact position of the fracture zone,  $x_s$  and  $x_e$ , the distances from the fracture zone where the fitting procedure begins and ends respectively, and  $w$ , the exclusion width, i.e., the distance on each side of  $x_0$  that is excluded from the fit. The fracture zone position  $x_0$  was assumed to be the deepest point of the characteristic fracture zone geoid trough since this was the easiest position to determine, but positions of  $x_0$  corresponding to the steepest slope in the geoid adjacent to the trough, believed to more accurately reflect the fracture zone position [Driscoll et al., 1987], were also tried on many profiles. Where the fracture zone position was still ambiguous, values of  $x_0$  were chosen visually based on the shapes and fracture zone positions of adjacent profiles. A variety of values for  $x_s$ ,  $x_e$ , and  $w$  were used to fit each profile. Some of these values we obtained by inspection, selecting the segments along the profiles least contaminated by anomalies. We also tried somewhat arbitrary parameter values that were similar for all profiles, to see how our step estimates changed when fewer subjective choices were made. We obtained a selection of step estimates for each profile based on typical values of:  $x_s$ ,  $x_e \approx \pm(200-400)$  km,  $w = 25, 50, 100$ , and in some cases 150 km, and variations of  $x_0$  of 10-30 km.

Most previous studies have tended to use exclusion widths greater than 100 km. Our noisy profiles with their rapid changes in geoid baseline slope make it very difficult to obtain reasonable geoid steps using exclusion widths greater than 100 km. Thus we have avoided these larger exclusion widths except for long baselines on relatively smooth and well behaved geoid profiles. Detrick [1981] has shown that for small exclusion widths, the amount of step underestimation is predictable and should not exceed 25% for a 10 m.y.-offset plate model fracture zone. If our step estimates increase regularly with increasing  $w$ , we can predict what the true step should be at large exclusion widths. If the step estimates do not behave simply, we can still use them to put bounds on what the real geoid step might be and to gauge the quality of the profile that we are fitting.

### 3.5.2 Sample Profile Fits

In Figure 6, we present a number of sample profiles and their best fit quadratic curves. We have divided our fits into four quality categories: good, anomalous, ambiguous, and poor. Profile 1 is an example of a "good" fit. A geoid step is clearly visible and is of the expected sign. The background geoid slope remains constant for at least 300 km on each side of the fracture zone. All the quadratic fits, each with a different exclusion width, yield similar geoid step estimates. Both short and long baselines give consistent step heights.

Profile 2 is an example of an "anomalous" step. The apparent quality of the step estimate is good, but the geoid step obtained is of the opposite sign from that expected based on the age offset across the fracture zone. This anomalous step is evident with both short and long baselines and various exclusion widths.

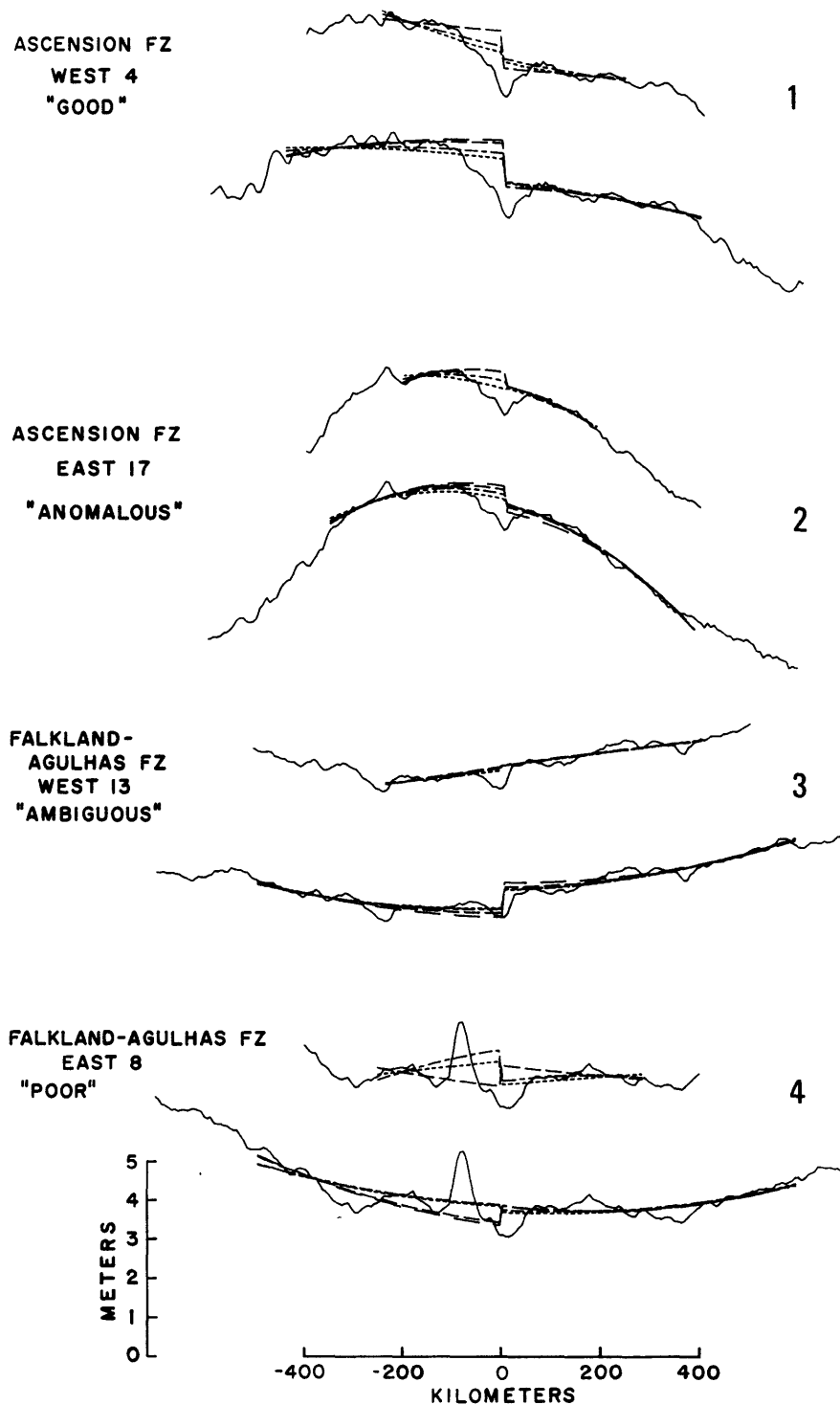


Figure 6. Comparison of four representative profiles and their least squares quadratic fits. For each profile, fits for both short and long baselines are shown. Each curve corresponds to a different exclusion width as follows: short dashes,  $w = 25$  km, short/long dashes,  $w = 50$  km, long dashes,  $w = 100$  km, very long dashes (long baselines only),  $w = 150$  km.

Profile 3 shows an "ambiguous" step. A geoid step is clear visually, but the value of the measured step depends on the baseline length. Short and long baselines give very different step heights, and either step estimate seems reasonable based on a visual fit. This behavior is usually a result of geoid slopes which change direction within a few hundred kilometers of the fracture zone.

An example of a "poor" step is shown in profile 4. Large short-wavelength geoid anomalies cast serious doubt as to whether a step could actually be measured. Step estimates may either vary drastically (as in profile 4), or may look suspiciously consistent. Table 2 lists the quality of the step estimates for each profile based on this four category visual check.

### 3.5.3 Step Height Versus Age

We determined a mean geoid step value for each profile by averaging together all the individual step estimates obtained for that profile. These mean values along with their standard deviations are listed in Table 2. The standard deviations are larger than the uncertainties in the individual step heights that emerge from the least squares fit, but we feel that they more accurately reflect the true uncertainty of the step estimates.

Since the step height is a function of age offset and the age offsets across our fracture zones vary with mean age, we compute the geoid step divided by the age offset at that mean age, i.e.,  $-\Delta N(t)/\Delta t(t)$ , where  $\Delta N(t)$  is the geoid height on the north side minus the geoid height on the south side of the fracture zone at mean age  $t$ ,  $\Delta t(t)$  is the age of the north side minus the age of the south side at  $t$ , and  $t(x)$  is the average of the north side age and south side age at location  $x$  where the profile crosses the

fracture zone. The errors indicated for  $-\Delta N/\Delta t$  include the estimated errors of both the geoid step height and the local age offset.

Figures 7 and 8 show the values of  $-\Delta N/\Delta t$  plotted versus mean age for each branch of the two fracture zones studied. For each profile, we indicate the step estimate obtained for each exclusion width and the mean step with its error bars. The step estimate for each value of the exclusion width is itself an average of steps obtained with different length baselines and fracture zone positions. In most cases, the error bars of the mean step height reflect the scatter of the individual step estimates. The errors in mean age represent the fairly small uncertainty in interpolating ages between isochrons or known age points. They do not reflect the much larger mean age uncertainties suggested by the comparisons of different age maps described above. These larger uncertainties result primarily in a stretching of the horizontal scales in Figures 7 and 8.

In Figure 9, we compare our observed values of  $-\Delta N/\Delta t$  with theoretical values. Using equation (1), we have plotted the curves for  $-\Delta N/\Delta t$  versus mean age for plate thicknesses of 50, 75, and 100 km. The values used for the other parameters are listed in Table 1. We do not include step estimates over the transform sections of the fracture zones in Fig. 9 since their smaller age offsets decrease the reliability of their  $-\Delta N/\Delta t$  values. We also omit some of the most obvious problem profiles, such as those affected by the Discovery seamounts on the east Falkland-Agulhas FZ and those over the geoid bulge at the east end of the Ascension FZ.

On both sides of the Falkland-Agulhas FZ (Figs. 7a, 7b, 9a) the youngest geoid steps are positive, i.e., of the correct theoretical sign. On the west side, step estimates tend to increase with larger exclusion widths, behavior that is predicted based on simple fracture zone models

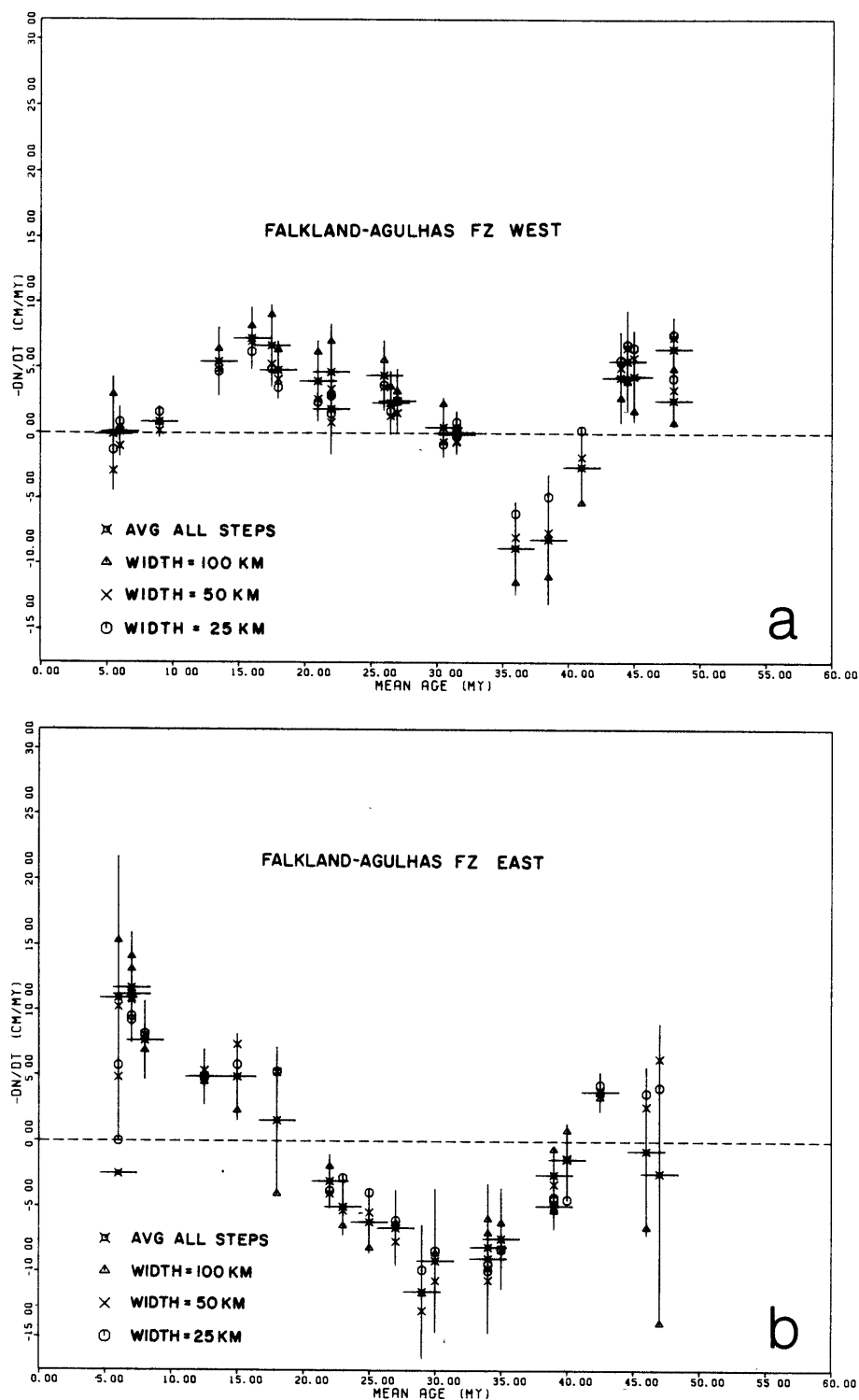


Figure 7. Step height ( $-\Delta N / \Delta t$ ) versus mean age for the (a) west and (b) east sides of the Falkland-Agulhas FZ. Step heights are shown for each exclusion width and for the mean step, found by averaging all the individual step estimates together. The standard deviation of the mean step and the estimated uncertainty in the mean age are indicated by error bars.

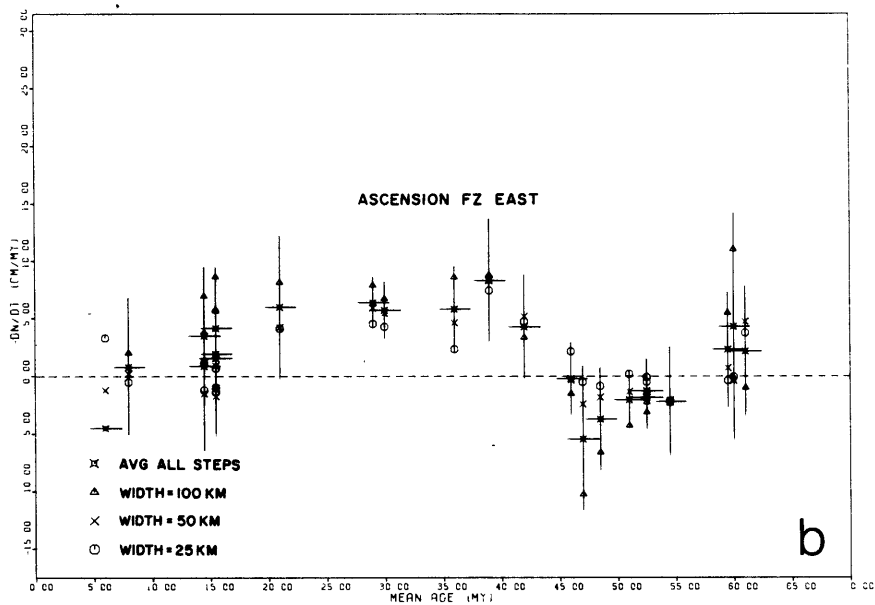
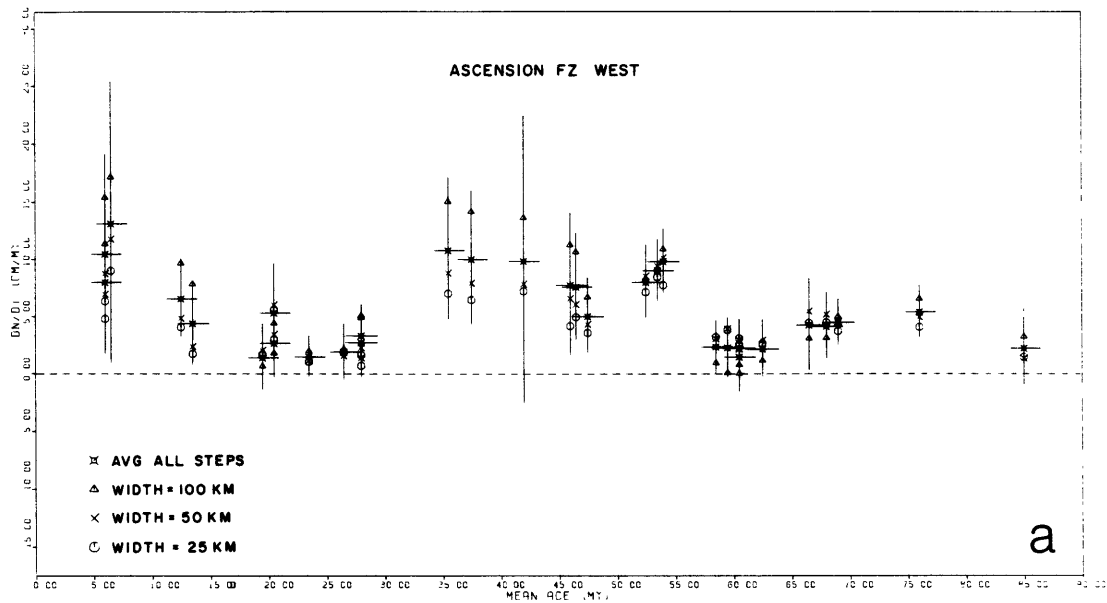


Figure 8. Step height ( $-\Delta N/\Delta t$ ) versus mean age for the (a) west and (b) east sides of the Ascension FZ. See Fig. 7 caption for a more complete description.

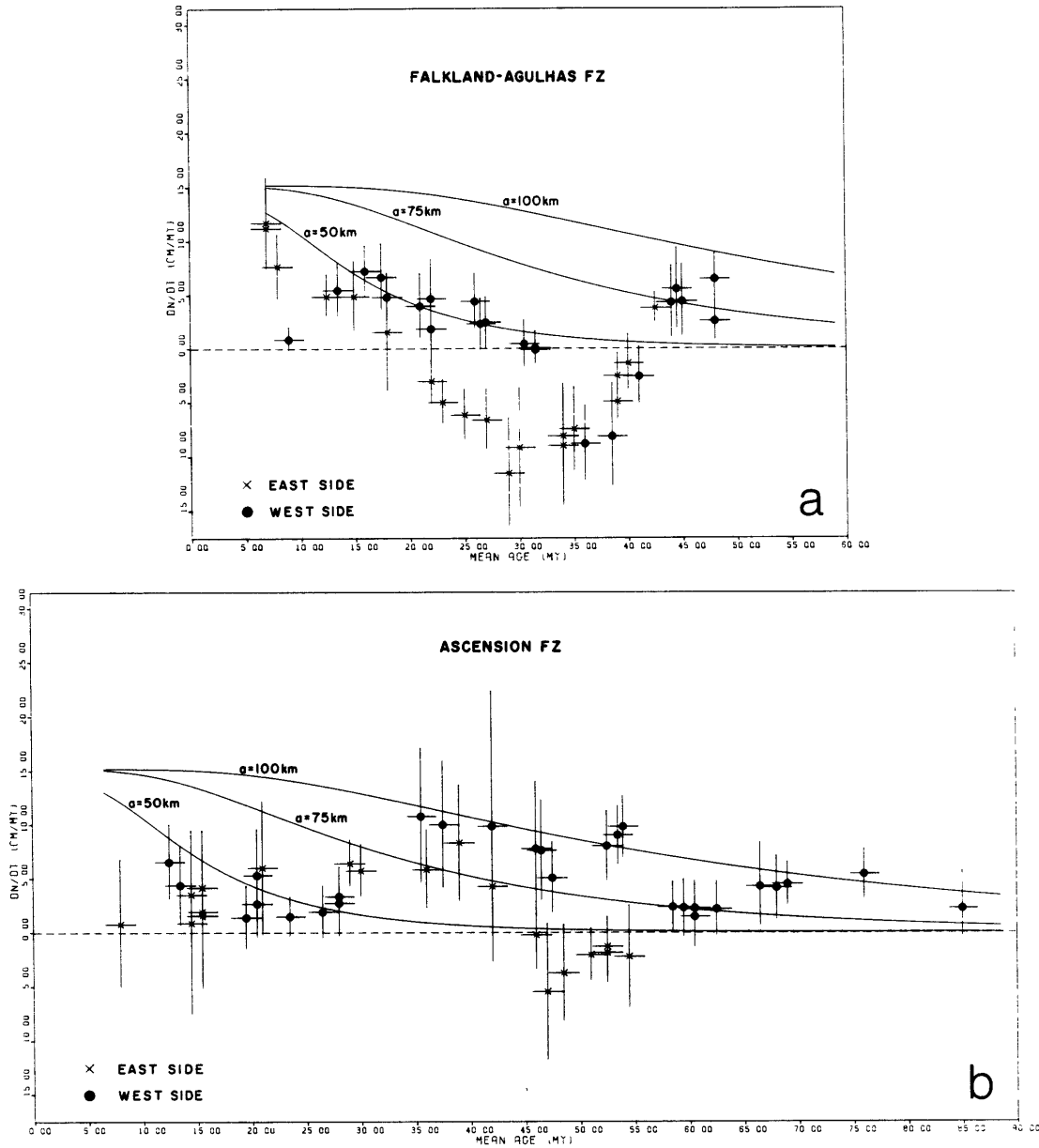


Figure 9. Step height ( $-\Delta N/\Delta t$ ) versus mean age for the (a) Falkland-Agulhas and (b) Ascension fracture zones. Theoretical profiles corresponding to various values of the plate thickness,  $a$ , are also shown. The step heights illustrated are the mean values with their error bars from Figs. 7 and 8.

[Detrick, 1981]. On the east side, however, there is no regular variation of step height with exclusion width. Step estimates for both sides fall roughly along the curve predicted for a plate thickness of 50 km until the steps become negative at ~30 Ma for the west side and ~20 Ma for the east. These negative values are quite large and robust since they appear with all the exclusion widths. At ages greater than 40-45 Ma the step estimates again become positive, but there is no obvious pattern of step height versus exclusion width. These geoid steps across the older parts of the fracture zone lie within the range of steps expected for plate thicknesses of 75-100 km.

Step estimates across the youngest sections of the Ascension FZ (Figs. 8a, 8b, 9b) are smaller than predicted, but of the correct theoretical sign. On the west branch, they decrease in a regular manner till ~30 Ma approximately following the curve for a = 50 km. The steps suddenly increase in size between 30 and 35 Ma; subsequently, they slowly diminish at a rate consistent with that predicted for a plate with a  $\leq$  100 km. East side behavior is less regular and has larger error bars. The steps remain roughly constant from 15 to 40 Ma, but appear to go negative (though with error bars that include zero) between 45 and 55 Ma. Though the trend of step height with age does not agree with any theoretical curve, the geoid steps with ages less than 40 Ma are not inconsistent with those seen on the west side of the fracture zone (Fig. 9b). On both sides, for ages less than 55 Ma, step estimates with larger exclusion widths tend to be of larger magnitude.

### 3.6 Discussion

From measurements of the geoid step offsets across our two fracture zones, it seems clear that standard thermal models of the lithosphere are inadequate to explain the behavior of the geoid observed across fracture zones in the South Atlantic. Neither the plate nor half-space models of lithospheric thermal evolution can predict the variations in step height with age observed across any of the four fracture zone branches examined in this study. This means that other processes are occurring which influence geoid height at levels at least comparable to those predicted for lithospheric cooling. Yet the geoid step variations do not seem completely random; similar step behavior is observed on more than one fracture zone branch. An examination of these patterns may reveal more subtle information about the structure and evolution of the South Atlantic lithosphere.

On all four branches of the two fracture zones, our step estimates show a behavior for young ages that is consistent with that predicted by the lithospheric thermal plate model for a plate thickness of ~50 km. Given that our step estimation procedure tends to underestimate the true step values and that the step estimates for larger exclusion widths tend to lie towards the upper limit of our error bars, our results are also compatible with a plate thickness at these young ages of up to 75 km. Plate thicknesses of 100 km or more [Parsons and Sclater, 1977; Detrick, 1981; Sandwell and Schubert, 1982] are not consistent with our results, however.

Beyond ages of 20-30 Ma, all four fracture zone branches show some unexpected behavior. The Falkland-Agulhas step estimates reverse sign on both branches. The Ascension FZ data show a rejuvenation of the step on

the western side followed by step variations that follow the curve predicted for a plate thickness of 75-100 km. The eastern side steps agree with the pattern found on the west side until a step reversal begins at ~45 Ma.

The similarity in age at which each fracture zone branch exhibits anomalous behavior suggests that some evolutionary process begins along the fracture zone at 20-30 Ma and disrupts the step pattern seen at younger ages. Across the Falkland-Agulhas FZ for example, the older side of each branch of the fracture zone, with an age of ~25-40 Ma (at mean age 20-35 Ma), exhibits an increase in geoid height producing an apparent step reversal. If a similar effect occurs on the younger sides when they reach this age (at mean ages ~30-45 Ma), their increased geoid heights would be perceived as a reduction in the anomalous step. Possible evolutionary processes to consider include cooling and stress buildup within the lithosphere which may create bathymetry along the fracture zone [Parmentier and Haxby, 1986] and thermally induced small-scale convection which would perturb the temperature profile beneath the lithosphere [Buck and Parmentier, 1986; Craig and McKenzie, 1986; Robinson *et al.*, 1987]. On the other hand, these apparent step reversals and step rejuvenations might be due to constructional bathymetric structures along the fracture zone. The similarity in age of onset of these anomalies might simply be coincidental or a result of processes that occurred at the ridge crest ~30 Ma.

The bathymetric data around the Falkland-Agulhas FZ are presently inadequate to help isolate the cause of the observed geoid variations. Around the Ascension FZ the bathymetry is better known, but nothing unusual appears in contour maps at the crustal ages where the anomalous geoid steps appear [GEBCO, 1978]. Detailed seismic investigations across either

fracture zone have not yet been performed. It is clear, however, that topography is capable of producing apparent step reversals and rejuvenations like those that we see. The magnitudes of these anomalous geoid highs are  $\sim 1-2$  m. Uncompensated bathymetry with relief of 1 km and wavelengths of 100 km could easily produce such anomalies; bathymetry locally compensated at depths  $\sim 10$  km would need to be significantly larger, however. The Falkland Ridge is an extreme example: from bathymetric relief of  $\sim 2.5$  km results geoid anomalies (peak-to-peak) of 2-4 m.

The geoid steps that are seen over younger lithosphere and seem to imply an unusually thin plate might also be a product of topography near the fracture zone or of an evolutionary thermal process within the lithosphere more complex than the uniform cooling assumed in standard models. To exclude the topography as the cause of these anomalously small geoid steps, better bathymetric knowledge is necessary. Yet the west sides of both fracture zones, which at young ages are notably absent of the geoid signals likely from seamounts or ridges and thus constitute our best data, still point to a thin lithospheric plate.

If, indeed, the lithosphere acts as a cooling plate with a thickness of 50-75 km, flattening of seafloor depths should be seen at ages of 10-25 Ma [Parsons and Sclater, 1977]. No pronounced flattening at these ages can be seen in published bathymetric maps [GEBCO, 1978] and depths continue to increase away from the ridge. However, the maps' 500 m contour interval is large, actual bathymetric measurements are unevenly distributed, and the slopes in depth away from the Mid-Atlantic ridge vary substantially with position along the ridge; thus a temporary bathymetric flattening, for example, from 25-30 Ma, cannot at present be excluded.

Any process which can produce spatially varying density anomalies within or below the lithosphere may also be capable of explaining the geoid variations observed across our fracture zones. Uneven crustal thickness or petrologic heterogeneities within the crust or mantle are possible causes whose density variations are geochemical in nature. To ascertain whether either of these processes contribute to our geoid variations, detailed seismic and geochemical studies are necessary along the fracture zone. If they do, our geoid observations may contain information on the temporally and spatially nonuniform crustal production processes along the Mid-Atlantic ridge.

Alternatively, our geoid anomalies may be a result of uneven thermal structure. Small-scale convection beneath the lithosphere is a possible byproduct of the temperature gradient that initially exists across the fracture zone [Buck and Parmentier, 1986; Craig and McKenzie, 1986], especially if a low viscosity zone occurs at shallow depths in the upper mantle. A convective pattern is initially set up as cooler material descends under the older, cooler side of the fracture zone while warmer material ascends under the younger side and is advected across the fracture zone immediately beneath the lithosphere. Such a convective regime can produce its own depth and geoid anomalies adjacent to the fracture zone. As convection continues, cells develop further from the fracture zone and temperature heterogeneities propagate conductively into the lower lithosphere; both processes continue to distort the geoid across the fracture zone. Preliminary theoretical modeling of this phenomenon indicates that apparent step reversals, quickly varying step heights, and step rejuvenations may indeed be seen if the physical conditions in the upper mantle are appropriate [Craig and McKenzie, 1986; Robinson *et al.*,

1987]. In this case, our geoid step data possess information concerning the convective regimes occurring beneath the lithosphere across our fracture zones. Independent estimates of the upper mantle's physical properties are needed to confirm the existence of small-scale convection. Here, again, seismology would be a helpful tool.

Behavior of the geoid step offset with age similar to what we find along the Ascension FZ has been found by studies in the South Pacific across the Udintsev, Eltanin, and other fracture zones [Cazenave, 1984; Driscoll and Parsons, 1987]. Step heights there appear to indicate a plate thickness of  $\sim 60$  km for ages less than 30 Ma and a plate thickness of  $\sim 90$  km for ages greater than 40 Ma. For these Pacific fracture zones, many of the problems that we experience, such as the noisiness of our geoid profiles, the changing geoid baselines, and the steep age gradients along the fracture zones, are much less serious. The Pacific results are, therefore, somewhat stronger than ours in the Atlantic. Our results are consistent with the results of these Pacific fracture zone studies even though plate tectonic processes, such as spreading rate and absolute plate velocity, are quite different in the two oceans. Thus we have strong global evidence that the simple thermal plate cooling model is not always capable of predicting geoid variations across fracture zones.

### 3.7 Geoid and Gravity Maps

Gridded maps of the geoid and gravity field are another tool for studying the geoid anomalies around fracture zones and for ascertaining the reliability of our step estimates. We have used the techniques described in Chapter 2 to remove long-wavelength ephemeris errors from the along-track geoid, to interpolate the data onto a grid by fitting the data to a

minimum-curvature surface, and to filter these geoid maps in the wave number domain to produce gravity maps which amplify short-wavelength features. Geoid and gravity maps for the Falkland-Agulhas and Ascension fracture zone regions are shown in Figs. 10 and 11, respectively.

Both geoid maps show the Mid-Atlantic ridge and major fracture zones clearly. The ridge is offset at the fracture zones and the geoid slopes away from the ridge on both flanks, in qualitative agreement with theory. No major fracture zones appear close (within 500 km) to the two we have chosen to study, though a number of small-offset fracture zones (seen better in the gravity maps) do appear within ~300 km of our fracture zones. Although they will tend to introduce some short-wavelength geoid noise into our profiles, their small age offsets imply that the geoid will not exhibit significant steps or baseline shifts across them. Thus they should not interfere too much with our geoid step estimates, and we have ignored them.

Around the Falkland-Agulhas FZ (Fig. 10) we note a number of features that may prevent us from obtaining reliable geoid steps. Most obvious are the large geoid anomalies associated with the Discovery seamounts and the Falkland ridge. Adjacent and subparallel to the Falkland-Agulhas FZ are a number of local gravity anomalies. They tend to lie within 200 km of the fracture zone and average approximately 20 mgal in magnitude. On the east branch of the fracture zone, three of these gravity highs appear. The first lies south of the fracture zone at 10°W (a), the second is north of the fracture zone at 5°W (b), and the third is again on the south side at 0°W (c). This third feature appears to correlate with the Herdman and Schwabenland seamounts; the other two show minimal topographic expression [GEBCO, 1978].

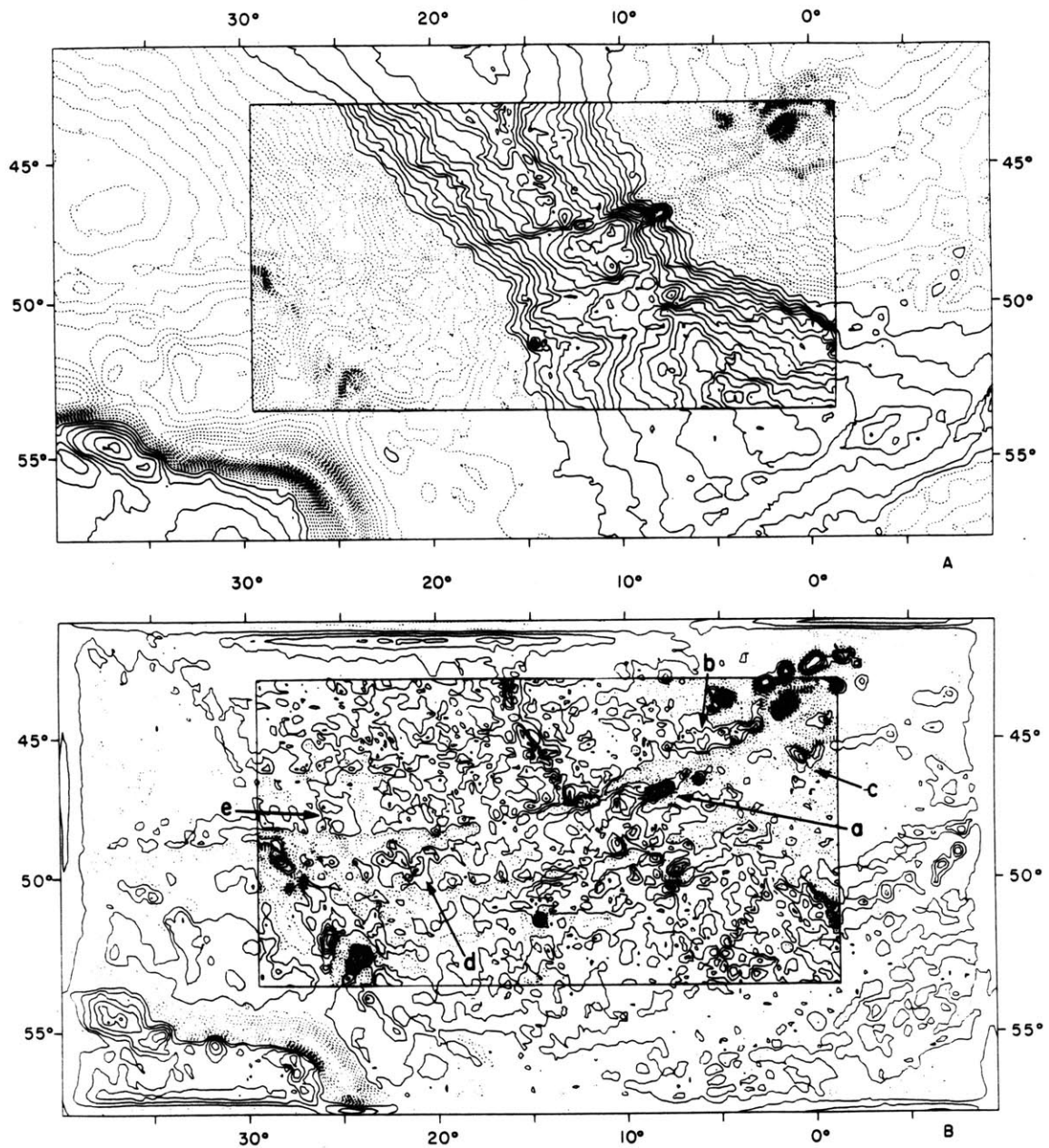


Figure 10. Gridded geoid (a) and gravity (b) maps of the area around the Falkland-Agulhas FZ. The contour intervals of the geoid map are 1 m outside the box, 25 cm within the box. Gravity contours are 30 mgal outside the box, 10 mgal inside the box. Dashed contours indicate negative values; thus the first solid contour is the zero contour. Specific features that are indicated by letters are referred to in the text.

These anomalies probably account for the behavior of the geoid step observed on the east side of the Falkland-Agulhas FZ. The first anomaly on younger seafloor leads to a geoid step of the expected sign, i.e., higher to the south, while the second anomaly, on the older side, results in a reversed geoid step. The third anomaly would lead to a step of the correct sign if the nearby Discovery seamounts did not complicate the picture. Their linear character and limited extent away from the fracture zone strongly suggest that these gravity highs are due to seamount groups or small ridges aligned with the fracture zone. If lithospheric or sublithospheric density variations are responsible for these anomalies, they must be limited in their geographic extent to a region within 100-200 km of the fracture zone.

On the west side of the fracture zone, no significant anomalies are encountered before one appears to the south at 21°W (d) and one to the north at 25°W (e). The former probably accounts for the step reversal on the west side and the latter for the subsequent return of the step to its expected orientation. The west side of the fracture zone between the Mid-Atlantic ridge and the first anomaly at ~30 Ma is the only area not obviously affected by these geoid highs. Thus the step data here, which suggest a thin plate, should still be reliable.

Of the ship tracks that we have examined, a few cross these anomalous gravity highs. Barker's [1979] cruise crossed those at 21°W (d) and 0°W (c) south of the fracture zone. A large, almost fracture-zone-like bathymetric feature with ~1 km of relief was observed near the center of the former gravity high. Perhaps the width of the gravity anomaly is an indicator of the lateral extent of the bathymetric high. This feature occurs near magnetic anomaly 17 (40 Ma). On the opposite side of the

Mid-Atlantic ridge, a similar feature appears in the bathymetric profile near the second gravity high, which also lies near magnetic anomaly 17.

The similarity in bathymetric appearance and age suggests that these two features might be related. By simply moving features in the gravity map back along the fracture zone trend, we note that at ~35 Ma both anomalies south of the fracture zone were located on the southern part of the mid-ocean ridge. Interestingly, the two anomalies north of the fracture zone (b and e) were also together on the northern ridge segment at this time. Perhaps a change in spreading direction or other event caused an increase in crustal production at the ridge at ~30-40 Ma, producing the observed anomalies as well as the Herdman and Schwabenland seamounts associated with the easternmost gravity anomaly. (The relatively small gravity anomalies of these seamounts also argue for an on-ridge origin [Watts and Ribe, 1984].)

From the geoid and gravity maps around the Ascension FZ (Fig. 11), there appears to be a significant difference between the east and west flanks of the Mid-Atlantic ridge. On the west side, few geoid anomalies are seen besides those due to fracture zones. The gravity field is smooth until it nears the coast of South America, where the fracture zone trace fades and small seamount-type anomalies appear. Ascension Island appears clearly on the gravity map just south of the fracture zone west of the ridge.

The east flank geoid is more complex. A large geoid high emerges from the Mid-Atlantic ridge about 500 km south of the fracture zone and trends northeast, crossing the fracture zone at a mean age of 60 Ma. This feature is the geoid bulge seen in Fig. 5b. Farther to the east, numerous seamount anomalies dot the gravity map and surround the fracture zone. The entire

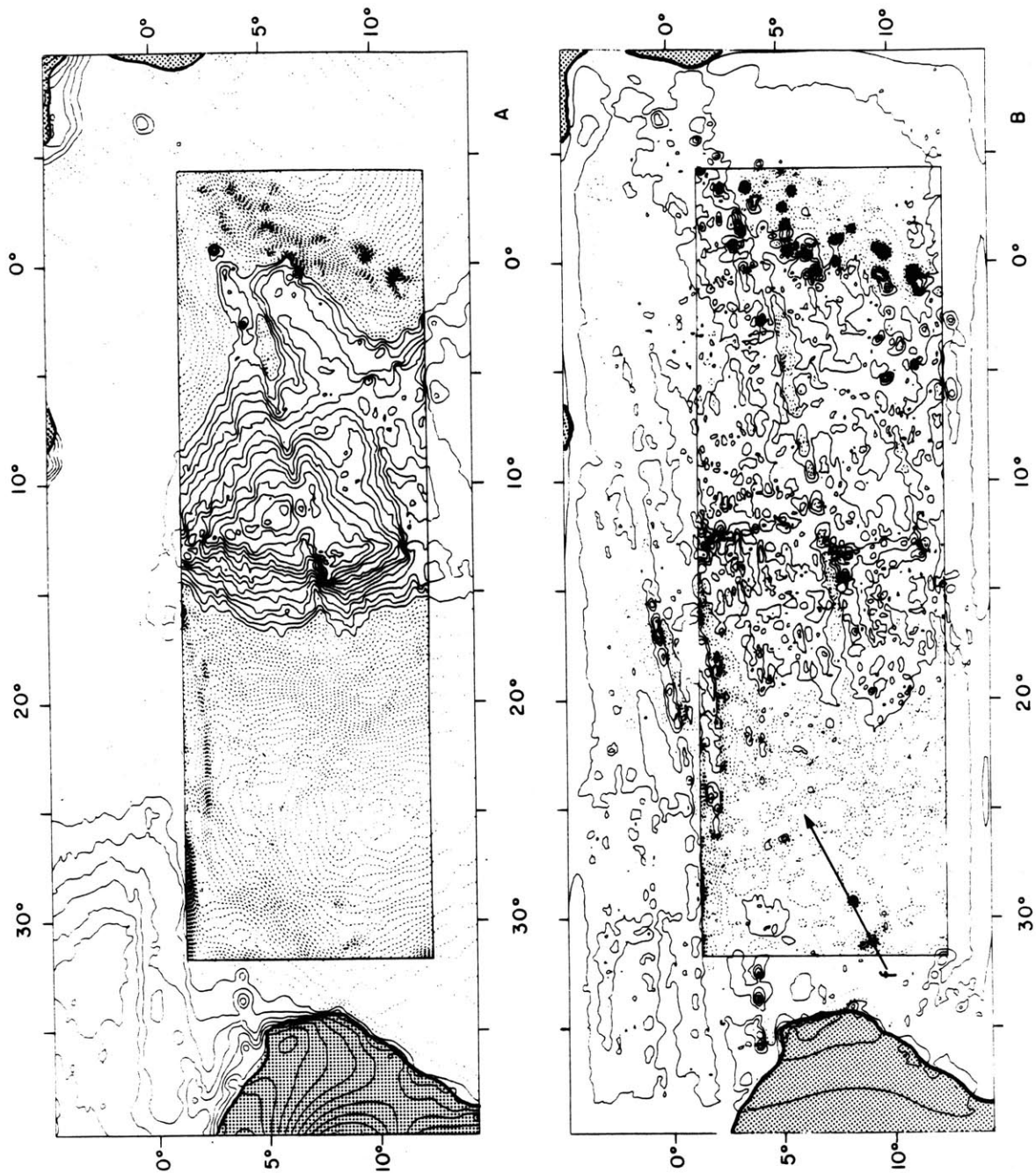


Figure 11. Gridded geoid (a) and gravity (b) maps of the area around the Ascension FZ. Contours and contour intervals are described in Fig. 10. Continental areas where no Seasat geoid data exist are stippled. Feature "f" is discussed in the text.

east side of the fracture zone seems to be associated with a geoid high of a few meters relative to the sea floor to its north and south. The area of the fracture zone east of  $\sim 7^{\circ}\text{W}$  is also associated with a shoaling of the seafloor of up to a kilometer relative to seafloor of the same age further south.

It appears from these maps that many of the step estimates on the east side of the Ascension FZ are unreliable. The apparent step reversal at 45 Ma appears to be caused by the geoid bulge to the south, while farther to the east the many seamounts corrupt the geoid baselines. On the west flank of the ridge, the maps show no indication of local geoid or gravity anomalies characteristic of nearby topography. Thus the step rejuvenation which we observe on the west branch at  $\sim 30$  Ma may really be the product of an extended thermal variation beneath the crust.

The geoid bulge and the chain of seamounts which interfere with reliable step estimates on the east flank of the ridge are probably hotspot-related features whose locations should be examined within the framework of absolute plate motion studies based on hotspot positions [Duncan, 1981; Morgan, 1983]. The location on the Mid-Atlantic ridge where the geoid bulge begins approximately corresponds to the position of the Ascension hotspot determined by Brozena [1986] based on shallow bathymetry and lack of ridge seismicity. The bulge may be the manifestation in the geoid of the track this hotspot has followed. If so, the thermal structure of the lithosphere on the east side of the fracture zone has been greatly perturbed by this hotspot. The wide scatter of the seamounts in the St. Helena hotspot-related seamount group farther to the east may be indicative of short-term changes in the hotspot position relative to an absolute hotspot framework, or it may demonstrate the channeling of hotspot magma

along fracture zones. This latter process appears to have occurred on the east end of the Ascension FZ, where a number of small seamounts lie along the fracture zone trend.

An additional unusual feature appears on the gravity map (f). West of the ridge there is a northwest trending small-amplitude linear geoid high that extends at least from the Ascension FZ north to the Chain FZ. It is probably not due to an errant ascending geoid arc, as it trends more westerly than the ascending arcs. It can also be seen on Haxby's [1985] gravity map. It follows neither the relative nor present day absolute plate motions of the South American plate, and its identity remains to be determined.

### 3.8 Conclusions

We have shown that trying to determine the lithospheric thermal structure using the geoid over fracture zones in the South Atlantic is significantly more difficult than in the Pacific. The noisiness of the geoid, the rapid changes in geoid baselines, the large age gradient of the seafloor, and other factors contribute to this difficulty. Without a better knowledge of bathymetry near the fracture zones, we cannot really be sure whether the main cause of the observed geoid steps is topography due to crustal thickening, lithospheric stresses, or constructive volcanic processes, or rather thermal density anomalies within or beneath the lithosphere.

The South American plate, where our geoid step estimates appear most reliable, exhibits a behavior for ages less than 30 Ma similar to that expected of a cooling plate with a thickness of 50-75 km. Preliminary depth-age data do not support the existence of such a thin plate, however.

At greater ages, evidence from the Ascension FZ indicates a rapid regrowth in the observed step and a subsequent decay of the step with time corresponding to a plate thickness  $\sim 25$  km larger, consistent with the results of fracture zone studies in the South Pacific.

The type of behavior that is observed in the geoid can be explained by a time-dependent thermal structure within the lithosphere (other than plate cooling) that varies across the fracture zone. Excess heat delivered to the plate asymmetrically across the fracture zone by small-scale convection, for example, will affect the geoid step, as will small-scale convection at depth directly [Buck and Parmentier, 1986; Craig and McKenzie, 1986; Robinson et al., 1987]. Thus, the apparent step rejuvenation and subsequent decay seen across the Ascension FZ and South Pacific fracture zones are most probably not indicative of a thick plate regime following an earlier thinner plate, but rather the result of convectively produced thermal perturbations that are inconsistent with the uniform cooling assumption of standard thermal lithospheric models.

Geoid and gravity maps are useful for determining whether observed geoid anomalies are similar to those produced by common bathymetric features such as seamounts or ridges, or whether more unusual sources for the geoid variations may be required. Detailed examination of these maps can also be useful in determining and characterizing hotspot traces, interactions between hotspots and fracture zones, and the sizes and directions of seamount chains. We have given a number of examples where Seasat-derived geoid and gravity maps are extremely useful in supplementing limited bathymetric coverage as well as in their own right in detecting features not apparent from ship bathymetry.

### 3.9 Acknowledgements

We thank M. Driscoll for many helpful discussions and the sharing of computer programs, and S. Cande for providing us with his digital age data. This research has been supported by the Office of Naval Research under contract #N00014-86-K-0325.

## 3.10 References

- Barker, P.F., The history of ridge-crest offset at the Falkland-Agulhas fracture zone from a small-circle geophysical profile, Geophys. J. R. Astr. Soc. 59, 131-145, 1979.
- Brozena, J.M., Temporal and spatial variability of seafloor spreading processes in the northern South Atlantic, J. Geophys. Res. 91, 497-510, 1986.
- Buck, W.R., and E.M. Parmentier, Convection beneath young oceanic lithosphere: Implications for thermal structure and gravity, J. Geophys. Res., 91, 1961-1974, 1986.
- Cande, S.C., W.F. Haxby, J.L. LaBrecque, W.C. Pitman, III, R.L. Larson, and X. Golovchenko, Age of the ocean floor: A new 5' gridded data base (abstract), EOS Trans. Am. Geophys. Un. 65, 1082, 1984.
- Cazenave, A., Thermal cooling of the oceanic lithosphere: new constraints from geoid height data, Earth Planet. Sci. Lett. 70, 395-406, 1984.
- Cazenave, A., B. Lago, and K. Dominh, Geoid anomalies over the north-east Pacific fracture zones from satellite altimeter data, Geophys. J. R. Astr. Soc. 69, 15-31, 1982.
- Cazenave, A., B. Lago, and K. Dominh, Thermal parameters of the oceanic lithosphere estimated from geoid height data, J. Geophys. Res. 88, 1105-1118, 1983.
- Craig, C.H. and D. McKenzie, The existence of a thin low-viscosity layer beneath the lithosphere, Earth Planet. Sci. Lett. 78, 420-426, 1986.
- Crough, S.T., Geoid anomalies across fracture zones and the thickness of the lithosphere, Earth Planet. Sci. Lett. 44, 224-230, 1979.
- Davis, E.E. and C.R.B. Lister, Fundamentals of ridge crest topography, Earth Planet. Sci. Lett. 21, 405-413, 1974.
- Detrick, R.S., An analysis of geoid anomalies across the Mendocino fracture zone: Implications for thermal models of the lithosphere, J. Geophys. Res. 86, 11751-11762, 1981.
- Dixon, T.H. and M.E. Parke, Bathymetry estimates in the southern oceans from Seasat altimetry, Nature 304, 406-411, 1983.
- Driscoll, M.L., R.L. Fisher, and B. Parsons, Fracture zone trends and structure at the Southwest Indian ridge: An investigation using Seasat altimetry and surface-ship bathymetry, Geophys. J. R. Astr. Soc., in press, 1987.
- Driscoll, M.L. and B. Parsons, Cooling of the oceanic lithosphere: Evidence from geoid anomalies across the Udintsev and Eltanin fracture zone system, Earth Planet. Sci. Lett., submitted, 1987.

- Duncan, R.A., Hotspots in the southern oceans--an absolute frame of reference for motion of the Gondwana continents, Tectonophysics 74, 29-42, 1981.
- Emery, K.O. and E. Uchupi, The Geology of the Atlantic Ocean, 1050 pp., Springer-Verlag, New York, N.Y., 1984.
- Ewing, M., G. Carpenter, C. Windisch, and J. Ewing, Sediment distribution in the oceans: The Atlantic, Geol. Soc. Am. Bull. 84, 71-88, 1973.
- GEBCO (General Bathymetric Chart of the Oceans), Canadian Hydrographic Service, Ottawa, Canada, 1978.
- Harland, W.B., A.V. Cox, P.G. Llewellyn, C.A.G. Pickton, A.G. Smith, and R. Walters, A Geologic Time Scale, 131 pp., Cambridge U. Press, Cambridge, 1982.
- Haxby, W.F., Gravity field of the world's oceans (map), (Lamont-Doherty Geological Observatory, Palisades, N.Y.) U.S. Navy, Office of Naval Research, 1985.
- Haxby, W.F. and D.L. Turcotte, On isostatic geoid anomalies, J. Geophys. Res. 83, 5473-5478, 1978.
- LaBrecque, J.L. and D.E. Hayes, Seafloor spreading history of the Agulhas Basin, Earth Plan. Sci. Lett. 45, 411-428, 1979.
- LaBrecque, J.L., D.V. Kent, and S.C. Cande, Revised magnetic polarity time scale for Late Cretaceous and Cenozoic time, Geology 5, 330-335, 1977.
- Ladd, J.W., South Atlantic seafloor spreading and Caribbean tectonics, 251 pp., Ph.D. Thesis, Columbia University, New York, 1974.
- Larson, R.L., W.C. Pitman, III, X. Golovchenko, S.C. Cande, J.F. Dewey, W.F. Haxby, and J.L. LaBrecque, The Bedrock Geology of the World (map), W.H. Freeman & Co., New York, N.Y., 1985.
- Lerch, F.J., S.M. Klosko, R.E. Laubscher, and C.A. Wagner, Gravity model improvement using GEOS 3 (GEM 9 and 10), J. Geophys. Res. 84, 3897-3916, 1979.
- Louden, K.E. and D.W. Forsyth, Crustal structure and isostatic compensation near the Kane fracture zone from topography and gravity measurements--I. Spectral analysis approach, Geophys. J. R. Astr. Soc. 68, 725-750, 1982.
- Louden, K.E. and D.W. Forsyth, Thermal conduction across fracture zones and the gravitational edge effect, J. Geophys. Res. 81, 4869-4874, 1976.
- McKenzie, D.P., Some remarks on heat flow and gravity anomalies, J. Geophys. Res. 72, 6261-6273, 1967.

- Morgan, W.J., Hotspot tracks and the early rifting of the Atlantic, Tectonophysics 94, 123-139, 1983.
- Morgan, W.J., Hotspot tracks and the opening of the Atlantic and Indian Oceans, in: The Sea, 7, The Oceanic Lithosphere, C. Emiliani, ed., pp. 443-387, John Wiley & Sons, New York, N.Y., 1981.
- Parmentier, E.M. and W.F. Haxby, Thermal stresses in the oceanic lithosphere: evidence from geoid anomalies at fracture zones, J. Geophys. Res. 91, 7193-7204, 1986.
- Parsons, B. and F.M. Richter, A relation between the driving force and geoid anomaly associated with mid-ocean ridges, Earth Planet. Sci. Lett. 51, 445-450, 1980.
- Parsons, B. and J.G. Sclater, An analysis of the variation of ocean floor bathymetry and heat flow with age, J. Geophys. Res. 82, 803-827, 1977.
- Rabinowitz, P.D. and J. LaBrecque, The Mesozoic South Atlantic Ocean and evolution of its continental margins, J. Geophys. Res. 84, 5973-6002, 1979.
- Rapp, R.H., A summary of the results from the OSU analysis of Seasat altimeter data, Rep. 335, Dept. Geodetic Sci. & Surveying, Ohio State U., Columbus, Ohio, 1982.
- Robinson, E., B. Parsons, and M.L. Driscoll, The effect of a shallow low viscosity zone on the thermal evolution of fracture zones, in preparation, 1987.
- Sandwell, D.T., A detailed view of the South Pacific geoid from satellite altimetry, J. Geophys. Res. 89, 1089-1104, 1984a.
- Sandwell, D.T., Thermomechanical evolution of oceanic fracture zones, J. Geophys. Res. 89, 11401-11413, 1984b.
- Sandwell, D.T. and G. Schubert, Geoid height-age relation from Seasat altimeter profiles across the Mendocino fracture zone, J. Geophys. Res. 87, 3949-3958, 1982.
- Schilling, J.G., G. Thompson, R. Kingsley, and S. Humphris, Hotspot-migrating ridge interaction in the South Atlantic, Nature 313, 187-191, 1985.
- Sclater, J.G., C. Jaupart, and D. Galson, The heat flow through oceanic and continental crust and the heat loss of the earth, Rev. Geophys. Space Phys. 18, 269-311, 1980.
- Sibuet, J.-C. and J. Mascle, Plate kinematic implications of Atlantic equatorial fracture zone trends, J. Geophys. Res. 83, 3401-3421, 1978.

- Tapley, B.D., G.H. Born, and M.E. Parke, The Seasat altimeter data and its accuracy assessment, J. Geophys. Res. 87, 3179-3188, 1982.
- Van Andel, Tj.H., and G.R. Heath, Tectonics of the Mid-Atlantic ridge, 6-8° South Latitude, Mar. Geophys. Res. 1, 5-36, 1970.
- Van Andel, Tj.H., D.K. Rea, R.P. Von Herzen, and H. Hoskins, Ascension fracture zone, Ascension Island, and the Mid-Atlantic ridge, Geol. Soc. Am. Bull. 84, 1527-1546, 1973.
- Watts, A.B. and N.M. Ribe, On geoid heights and flexure of the lithosphere at seamounts, J. Geophys. Res. 89, 11152-11170, 1984.

Chapter 4.  
Intermediate-Wavelength Depth and Geoid Anomalies  
of the South Atlantic Ocean

#### 4.1 Abstract

Digital bathymetry data for the South Atlantic Ocean were interpolated onto a grid and corrected for sediment loading and the effects of lithospheric age to produce maps of residual depth anomaly. Seasat altimetry were similarly gridded, then a long-wavelength geoid produced using the GEM 9 potential coefficients complete to degree and order 8 and cosine tapered from degrees 8 to 12 was removed to allow intermediate-wavelength geoid anomalies to be seen. After correcting for sediment loading and the effects of seafloor age, a map of residual geoid anomaly was obtained.

Before removing lithospheric age effects, the geoid and bathymetry correlate very well. The major basins are deep both in depth and geoid, while the aseismic ridges and Mid-Atlantic Ridge (MAR) show up as geoid and depth highs. Both the depth and geoid exhibit an asymmetry across the MAR, as each observable slopes away from the MAR more steeply to the west than the east.

After removing age effects, the correlation remains good for large-amplitude features, but worsens somewhat for broad, small-amplitude features. Subtle patterns of high and low geoid residuals appear trending from northwest to southeast. Plots of geoid versus depth and forward modeling of the geoid based on the bathymetry suggest that the deep basins and certain positive anomalies are compensated at depths of 60 km or greater at the base of the lithosphere. The two aseismic ridges appear to be partially compensated at shallow depths, but a certain amount of their support seems to originate in the lower lithosphere also. These observations are consistent with convection occurring at intermediate wavelengths beneath the South Atlantic Ocean.

## 4.2 Introduction

Since the acceptance of plate tectonics as the prime framework for understanding earth's geophysical processes, there has been a major need to understand the forces driving plate motions and the interior earth motions associated with the surface plate movements. The principal method for transferring thermal energy from the earth's interior to its surface to power plate tectonics is thought to be solid-state convection in the mantle. In order to determine the structure of mantle convection, a knowledge of sublithospheric density anomalies over large regions is required.

There are a limited number of surface observables that can be used to constrain the interior structure and motion of the earth. Seismology has been the principal method for obtaining information about the earth's interior, but until recently, regional heterogeneities could not be resolved with global coverage. Two surface observables that have often been used together to constrain small-scale subsurface structure on continents and in the oceans, topography and gravity, can, with sufficient coverage, be used to study the deep, longer-wavelength density variations associated with mantle convection [McKenzie et al., 1974].

Early comparisons of bathymetry to gravity at sea were limited by the geographic coverage of the surface vessels that obtained the data. Anderson et al. [1973] studied this relationship by comparing the long-wavelength satellite-derived gravity field to the seafloor depths along mid-ocean ridges. Ridges were chosen to avoid the many age-dependent crustal and lithospheric processes known to alter the bathymetry and gravity fields. This problem--how to separate near-surface crustal and lithospheric structure from deeper convection-related mantle structure--

has been and still remains one of the most difficult problems to overcome in this type of analysis.

Subsequent studies, whether global in scope [Cochran and Talwani, 1977] or limited to a particular ocean [Sclater et al., 1975; Cochran and Talwani, 1978], were interested in wavelengths that were not yet resolvable from satellite gravity models. They relied on surface ship gravity data which provided adequate coverage over well surveyed areas, but were marginally adequate in poorly surveyed areas such as the southern oceans.

With the development of satellite radar altimetry, provided by spacecraft such as GEOS 3 and Seasat, worldwide coverage of the geoid and gravity field with sufficient resolution for studying the patterns of mantle convection became a reality. The data set now limiting global studies of this sort is the bathymetry. Still obtained by ship, bathymetric knowledge remains weak in the South Atlantic, South Pacific, and the polar oceans.

A number of ocean-wide studies of the bathymetry and the geoid have been performed using satellite altimetry. In the Pacific Ocean [McKenzie et al., 1980; Watts et al., 1985], geoid undulations with wavelengths ~2000-4000 km were observed which correlated moderately well with bathymetric anomalies and were aligned in the direction of absolute motion of the Pacific plate. Geoid anomalies such as these would be very difficult to observe in other ocean basins, which are a fraction of the size of the Pacific. What are clearly seen in all oceans, however, [Parsons et al., 1983; Roufousse et al., 1981; Bowin et al., 1984] are the correlations of the geoid with bathymetry associated with hotspot swells such as Hawaii, Bermuda, and the Azores. These have smaller wavelengths (1000 to 2000 km) and larger amplitudes than the Pacific anomalies

mentioned above. Geoid highs are also seen to be regularly associated with mid-ocean ridges, islands, seamounts, and trenches.

The newest aid for studying the bathymetry are digital bathymetric data bases such as SYNBAPS [1981]. These have enabled extensive two-dimensional studies of geoid and bathymetry over features as diverse as seamounts, hotspots, and aseismic ridges [e.g. McNutt and Shure, 1986; McNutt, 1986; Chapter 2 of this thesis]. Gridded digital altimetry and bathymetry have recently been used to reexamine the Pacific [Sandwell and Renkin, 1986], the Atlantic [Jung and Rabinowitz, 1986a; 1986b] and the oceans globally [Cazenave et al., 1986].

In the present work, we study the intermediate-wavelength ( $\lambda \sim 500$ -4000 km) geoid-bathymetry relationship of the South Atlantic. Our primary goal is to identify any features which might be indicative of convection in the upper mantle. Previous studies have included the South Atlantic [Cochran and Talwani, 1977; Parsons et al., 1983; Bowin et al., 1984; Kogan et al., 1985; Cazenave et al., 1986]. Although our analysis procedures are quite similar to those used in a number of these studies, we feel that the improved quality of our geoid, bathymetry, crustal age, and sediment data, as well as the distinctive methods that we employ, justify another look at the South Atlantic Ocean.

#### 4.2.1 Geoid and Depth Anomalies

The intermediate-wavelength anomalies which we hope to observe need to be isolated from long-wavelength anomalies ( $\lambda > 4000$  km) and short-wavelength anomalies ( $\lambda < 500$  km). Although there is a smooth variation in power as a function of wavelength in the observed geoid spectrum and no obvious wavelength divisions, the source regions of different wavelength bands are believed to be very different.

Long-wavelength large-amplitude geoid anomalies are suspected to be manifestations of deep-seated density anomalies located in the lower mantle or at the core-mantle boundary. Short-wavelength, smaller-amplitude features are a product of topography and crustal density variations. Intermediate-wavelengths are assumed to be due to density variations within the upper mantle and lower lithosphere [McKenzie, 1967; Bowin, 1983]. The nature of the gravitational potential does not permit unique inversions of geoid anomalies for source depth, however. Extensive discussions of the magnitudes of geoid anomalies, their attenuation with depth, and the finite strength of the earth materials that sustain them [McNutt, 1980] have not yet enabled a consensus on the depths of their controlling density perturbations; the source regions of the various wavelength bands thus remain somewhat speculative.

Mantle convection is believed to produce geoid anomalies within certain wavelength and amplitude ranges. The predicted geoid signals are highly model dependent, but wavelengths of a few hundred to a few thousand kilometers, and amplitudes of a few meters are expected over convective upwellings and downwellings [McKenzie *et al.*, 1974; McKenzie, 1977; Parsons and Daly, 1983]. Ascending flows, which are warmer and less dense than the surrounding mantle, if allowed to reach the bottom of the lithosphere will produce uplift of the lithosphere. Descending flows are cooler and denser than the surrounding mantle. If they are not decoupled from the lithosphere, they should produce depressions in the surface. The resulting geoid anomalies--the sum of the opposing effects of surface deformation and density variations in the convecting regions--are quite sensitive to the viscosity changes with depth [McKenzie, 1977]. Evidence is accumulating for a low viscosity zone beneath the lithosphere [Haxby and Weissel, 1986;

Buck and Parmentier, 1986; Craig and McKenzie, 1986] which could decouple the mantle flow from the lithosphere resulting in minor surface deformation over even vigorous convection [Robinson et al., 1987].

Various models of mantle convection and earth structure thus predict a wide range of possible correlations between intermediate-wavelength geoid and depth anomalies in the oceans. In order to visualize these anomalies adequately, all other processes which are known to contribute to depth or gravity variations should be removed. These include the deep-seated density anomalies of the lower mantle, chemical density variations within the upper mantle and lithosphere, variations due to the thermal structure, evolution, and finite strength of the lithosphere, constructional topographic features and crustal thickening, and sediment loading. Our knowledge of earth structure is not nearly sufficient to model all the above source terms, but many of them can be accounted for and removed from the geoid and bathymetry.

#### 4.2.2 Geographic Area

The area of the South Atlantic Ocean which we focus on extends from the equator to 55°S. A number of major bathymetric features divide the ocean into distinct geographic regions (Figure 1). South of the large offset equatorial fracture zones at the north of our study area, the Mid-Atlantic Ridge (MAR) serves to divide the South Atlantic into eastern and western basins. The ridge is fairly continuous, interrupted by only a few significant transform faults with offsets of 200 km or more, before it meets the Bouvet triple junction at the south of our study area.

The western side of the South Atlantic is split into two basins by the Rio Grande Rise: the Brazil Basin to the north and the Argentine Basin to the south. The eastern South Atlantic also contains two major basins

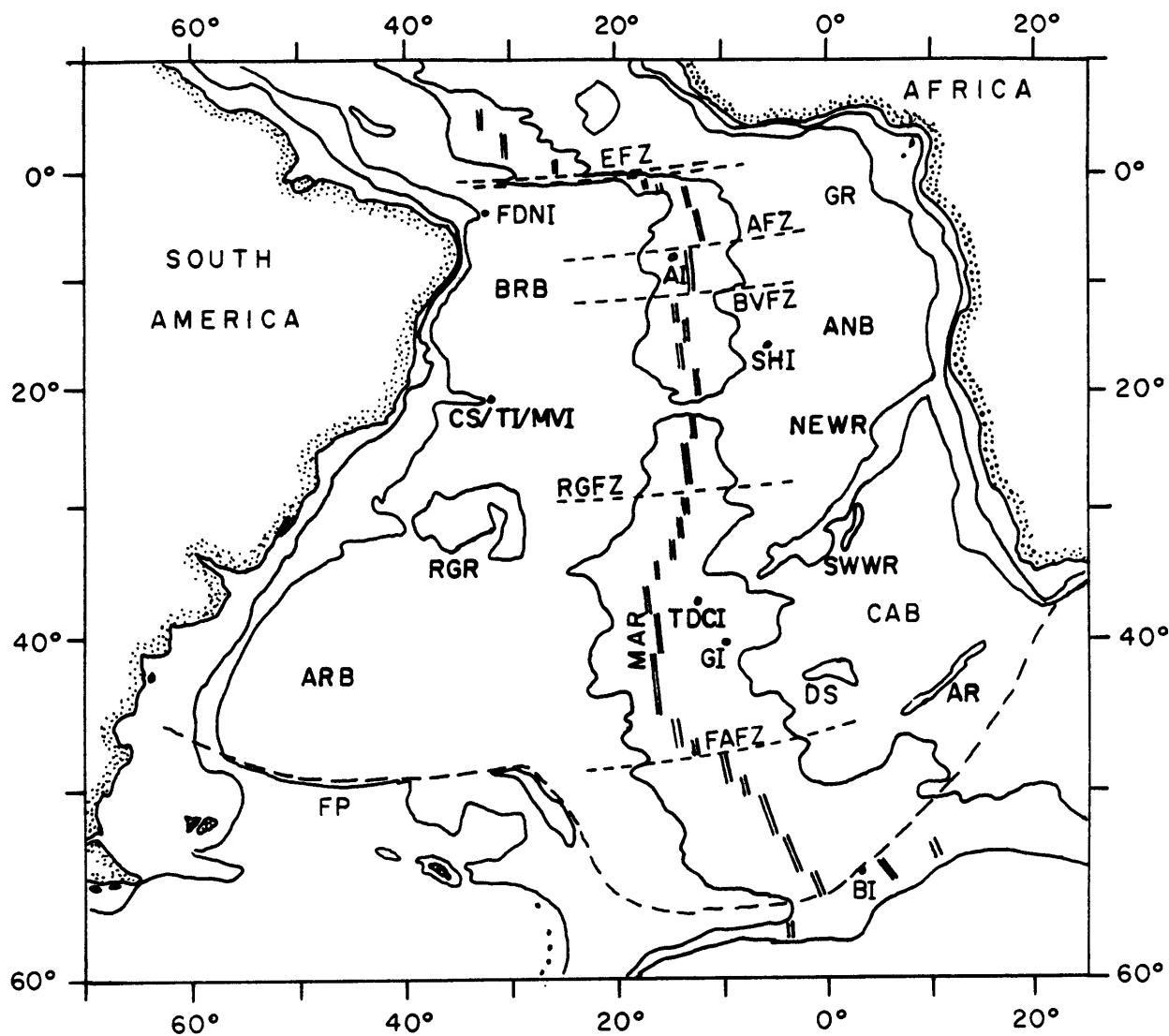


Figure 1. Generalized physiographic map of the South Atlantic Ocean. Contours are shown at 2000 m and 4000 m depths. The dashed line at the south of the map marks the southern limit of our digital age data. Major features are identified with abbreviations as follows: MAR--Mid-Atlantic Ridge, RGR--Rio Grande Rise, NEWR--northeast Walvis Ridge, SWWR--southwest Walvis Ridge, BRB--Brazil Basin, ARB--Argentine Basin, ANB--Angola Basin, CAB--Cape Basin, EFZ--Equatorial fracture zones, AFZ--Ascension FZ, BVFZ--Bode Verde FZ, RGFZ--Rio Grande FZ, FAFZ--Falkland-Agulhas FZ, AI--Ascension Island, SHI--St. Helena, TDCI--Tristan da Cunha, GI--Gough Island, BI--Bouvet Island, FDNI--Fernando de Naronha, CS/TI/MVI--Columbia seamounts/Trindade/Martin Vaz, FP--Falkland Plateau, AR--Agulhas Ridge, GR--Guinea Ridge, DS--Discovery seamounts.

separated by the Walvis Ridge: the Angola Basin to the north and the Cape Basin in the south. The northern basins are bounded to the north by the equatorial fracture zones and the African continental margin, while the southern basins have the Falkland Plateau, a submerged continental extension, and the Agulhas Ridge as their southern boundaries.

In addition to the two major aseismic ridges, the Rio Grande Rise and Walvis Ridge, a number of mid-ocean islands dot the South Atlantic. Most are thought to be a result of hotspot volcanism [e.g. Morgan, 1981; Baker, 1973]. Those lying near the Mid-Atlantic Ridge include Ascension, St. Helena, Tristan da Cunha, Gough, and Bouvet Islands. Islands off the Brazilian coast include Fernando de Noronha, Trindade, and Martin Vaz, while Sao Tome and Principe lie in the Gulf of Guinea off the African coast. A number of large seamount chains are also found in the South Atlantic. Most are thought to be hotspot related, though many lie along fracture zone trends. Thus there is some doubt as to whether these chains denote hotspot traces and absolute plate motions, or lithosphere weakened along fracture zones, hence relative plate motions, or combinations of both processes.

The Mid-Atlantic Ridge axis marks the boundary between the African plate and the South American plate. Seafloor spreading in the South Atlantic has been straightforward, with fairly well determined rotation poles and more or less symmetric spreading occurring at rates of 2-4 cm per year [Ladd, 1974; Rabinowitz and LaBrecque, 1979]. Thus, the age of the crust across most of the South Atlantic is well known and relatively easy to extrapolate to areas where observed magnetic anomalies are lacking.

### 4.3 Depth Anomalies

#### 4.3.1 Bathymetry

Our bathymetric data for the South Atlantic were obtained from the DBDB5 [1985] digital database which contains global bathymetry and topography on a 5' grid. Depths in this data set have already been corrected for the velocity of sound in seawater. In order to keep the amount of data manageable, we reduced the number of depth data points by selecting every third point, yielding a grid with data every 15'. The data were then projected onto a plane using a Mercator projection and interpolated onto a uniform x-y grid with a grid spacing defined to be 50 km at a latitude of 30°S by fitting the data to a minimum-curvature surface (described in chapter 2). The bathymetry is shown in Figure 2.

Before presenting this and subsequent maps as figures, we applied a low-pass Gaussian filter in the wave number domain with a half-width,  $\sigma$ , of 50 km (defined by the weighting  $W(\lambda) = \exp(-\pi^2\sigma^2/\lambda^2)$ ) to remove wavelengths less than  $\sim 150$  km (i.e., all  $\lambda$  where  $W(\lambda) < e^{-1}$ ). This low-pass filtering makes the maps easier to understand as it reduces the visual confusion caused by numerous small-amplitude, short-wavelength features. At a later point, more extensive low-pass filtering will be applied to isolate those intermediate-wavelength features with wavelengths  $> 500$  km, of primary interest for studying mantle convection.

Most of the major features indicated in Figure 1 can be seen in Figure 2. The Mid-Atlantic Ridge winds its way down the center of the South Atlantic, interrupted and offset by the major transform faults. From depths along the ridge of less than 3000 m, the seafloor deepens in the four basins to depths in excess of 5500 m. The deepest areas lie in the Argentine Basin adjacent to the Falkland Plateau, where depths greater

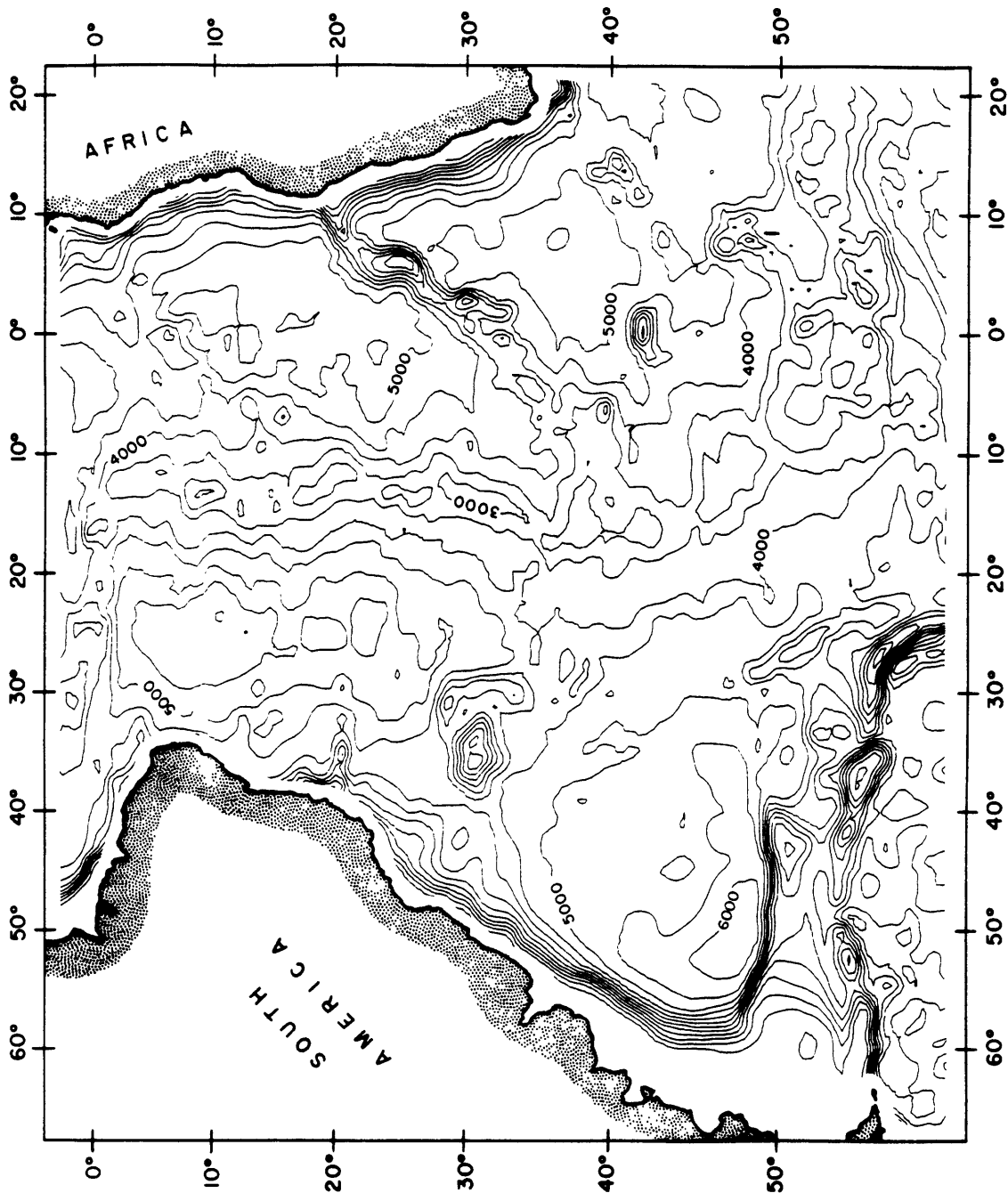


Figure 2. Bathymetry of the South Atlantic Ocean derived from the DBDB5 digital data base. The data were mapped onto a plane using a Mercator projection, then interpolated onto an equally spaced x-y grid with a grid spacing of 50 km at 30°S by fitting the data to a minimum-curvature surface. The map was also low-pass filtered using a Gaussian with a half-width of 50 km. The contour interval for this and subsequent depth maps is 500 m.

than 6000 m are found over a broad area. The Rio Grande Rise and Walvis Ridge are prominent bathymetric highs, reaching depths of 1500 m and 2000 m, respectively. Also appearing prominently are the Discovery seamounts south of the Walvis Ridge, and the Columbia seamount chain extending out from the coast of Brazil to Trindade north of the Rio Grande Rise. More subtle highs appear as plateaus or saddles linking the MAR to both the Rio Grande and Walvis aseismic ridges, and along the eastern branch of the Ascension fracture zone leading into the Guinea Ridge in the Gulf of Guinea.

#### 4.3.2 Sediment Corrections

Because of the large continental land masses that border the South Atlantic, great quantities of sediment have accumulated in the ocean basin since its formation ~130 Ma. A changing history of bottom currents during the growth of the South Atlantic has led to widespread, yet heterogeneous, distribution of these sediments [Emery and Uchupi, 1984]. Sediment loading of the lithosphere produces apparent depth changes, caused both by the thickness of the sediment layer itself and by the isostatic depression of the lithosphere from the weight of the sediments, for which we need to account before the subtle depth variations that interest us can be visualized.

Sediment isopachs were digitized from a recent sediment map kindly provided by D. Divins [Divins and Rabinowitz, 1986] of Texas A&M, in which sediment thicknesses had already been converted from two-way travel times to kilometers. Our interpolated and low-pass filtered version of the sediment cover is shown in Figure 3. Unlike the situation in the Pacific, where uniform sediment loads of at most a few hundred meters across most of the ocean have allowed investigators to ignore sediment loading while

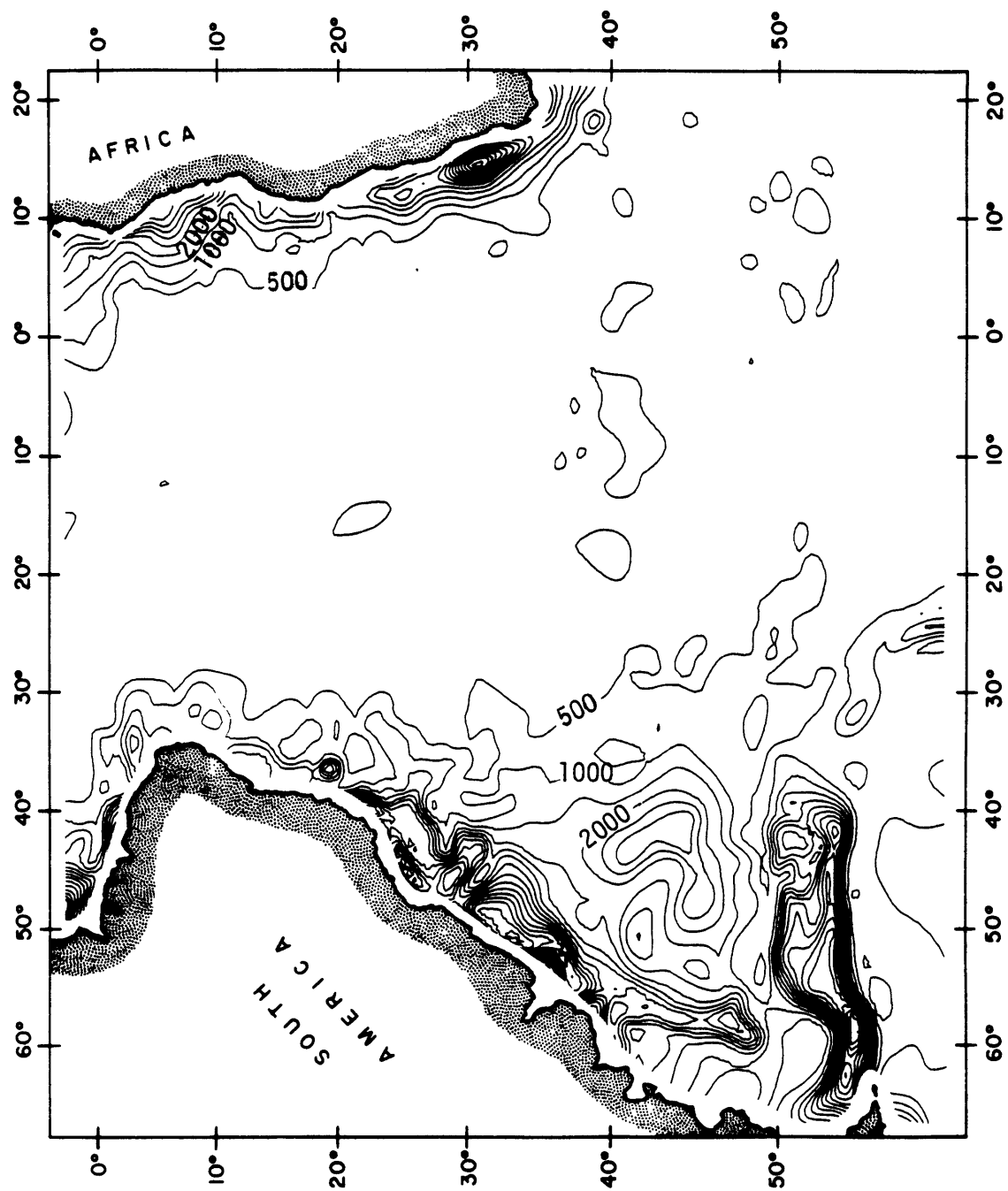


Figure 3. Sediment thicknesses in the South Atlantic Ocean adapted from Divins and Rabinowitz [1986]. The digitized thickness data were interpolated, gridded, and low-pass filtered in a manner identical with the bathymetry of Figure 2. The contour interval is 500 m.

studying depth anomalies, the South Atlantic exhibits sediment thicknesses of many kilometers. Most of the sediments are found within a few hundred kilometers of the continental slope, but substantial thicknesses occur in the Argentine Basin and surrounding the two aseismic ridges.

In order to correct for the isostatic loading of the sediments, the average sediment density needs to be determined. Since our sediment loads can be large and sediment density increases as the thickness increases due to compaction, we utilized a depth-dependent sediment density of

$$\rho_s(z) = \rho_g - (\rho_g - \rho_w)[P_0 \exp(-Cz)] \quad (1)$$

based on the exponential form of porosity of Sclater and Christie [1980], where:  $\rho_s$  is the sediment density at depth  $z$ ,  $\rho_g$  is the density of individual sediment grains,  $\rho_w$  is the density of seawater,  $P_0$  is the porosity of the surface sediments, and the constant  $C$  reflects the depth scale of the sediment compaction. Equation (1) is consistent with the polynomial forms of sediment density of Le Douaran and Parsons [1982] and Crough [1982] for sediment thicknesses of less than 1-2 km. At large depths, our exponential expression asymptotically approaches the density of completely consolidated sediments.

The depth correction for sediment loading,  $d_s$ , assuming local Airy isostasy, is

$$d_s(S) = \frac{(\rho_m - \bar{\rho}_s)S}{\rho_m - \rho_w} \quad (2)$$

where  $S$  is the sediment thickness,  $\rho_m$  is the density of the mantle, and  $\bar{\rho}_s$  is the average density of the sediment column [Le Douaran and Parsons, 1982]. Combining (1) and (2) we obtain

$$d_s(S) = (\rho_m - \rho_w)^{-1} \left\{ (\rho_m - \rho_g)S + \frac{P_0(\rho_g - \rho_w)}{C} [1 - \exp(-CS)] \right\} \quad (3)$$

We can also compute a sediment correction for the geoid based on Haxby and Turcotte's [1978] expression for long-wavelength, isostatically compensated surface loads,

$$N = \frac{-2\pi G}{g_0} \int_0^{\infty} \Delta\rho(z)zdz \quad (4)$$

where  $N$  is the geoid height,  $G$  is the gravitational constant,  $g_0$  is the acceleration of gravity at the earth's surface, and  $\Delta\rho$  is the density anomaly at depth  $z$ . Integrating (4) using (1), (2), and (3), we obtain the sediment geoid correction

$$N_S(S) = \frac{\pi G}{g_0} \{2(\rho_m - \rho_c)\lambda(S - d_s(S)) - (\rho_m - \rho_w)d_s(S)^2 + (\rho_m - \rho_g)S^2 - 2 \frac{P_0(\rho_g - \rho_w)}{C^2} [\exp(-CS)(1+CS) - 1]\} \quad (5)$$

where  $\rho_c$  and  $\lambda$  are the density and thickness of normal oceanic crust, respectively. The values used for the parameters in equations (3) and (5) are listed in Table 1.

Within a few hundred kilometers of the continental margins, the sediment corrections derived above are probably not accurate. Much of the support for the thick sedimentary columns that occur immediately adjacent to the continents is provided by the flexure of the lithosphere, rather than by local isostasy. In the deep ocean basins and other areas of the ocean floor where the sediment load is fairly uniform and covers wide areas, our assumption of local isostasy is physically reasonable and should yield accurate sediment corrections.

We obtained a map of seafloor depths corrected for sediment loading by adding the depth corrections from equation (3) to the bathymetry; this map is shown in Figure 4. Bathymetry (and later, geoid) corrected for the

Table 1.  
Parameters and their Values

---

$\rho_m = 3330 \text{ kg m}^{-3}$
$\rho_w = 1030 \text{ kg m}^{-3}$
$\rho_g = 2650 \text{ kg m}^{-3}$
$\rho_c = 2800 \text{ kg m}^{-3}$
$P_o = 0.57$
$C = 4.7 \times 10^{-4} \text{ m}^{-1}$
$G = 6.67 \times 10^{-11} \text{ m}^3 \text{ kg}^{-1} \text{ s}^{-2}$
$g_o = 9.80 \text{ m s}^{-2}$
$\lambda = 6 \text{ km}$

---

$\alpha = (3.2 \pm 0.2) \times 10^{-5} \text{ }^\circ\text{C}^{-1}$
$\Delta T = T_m - T_o = 1350 \pm 250 \text{ }^\circ\text{C}$
$\kappa = (8.0 \pm 0.5) \times 10^{-7} \text{ m}^2 \text{ s}^{-1}$
$a = 125 \text{ km}, 75 \text{ km}$

---

$t_d = 5 \text{ km}$
$t_c = 6 \text{ km}, 15 \text{ km}$
$t_\lambda = 40 \text{ km}, 60 \text{ km}$
$\rho_\lambda = 3250 \text{ kg m}^{-3}$
$\gamma = +1.0, -2.0, -4.0$

---

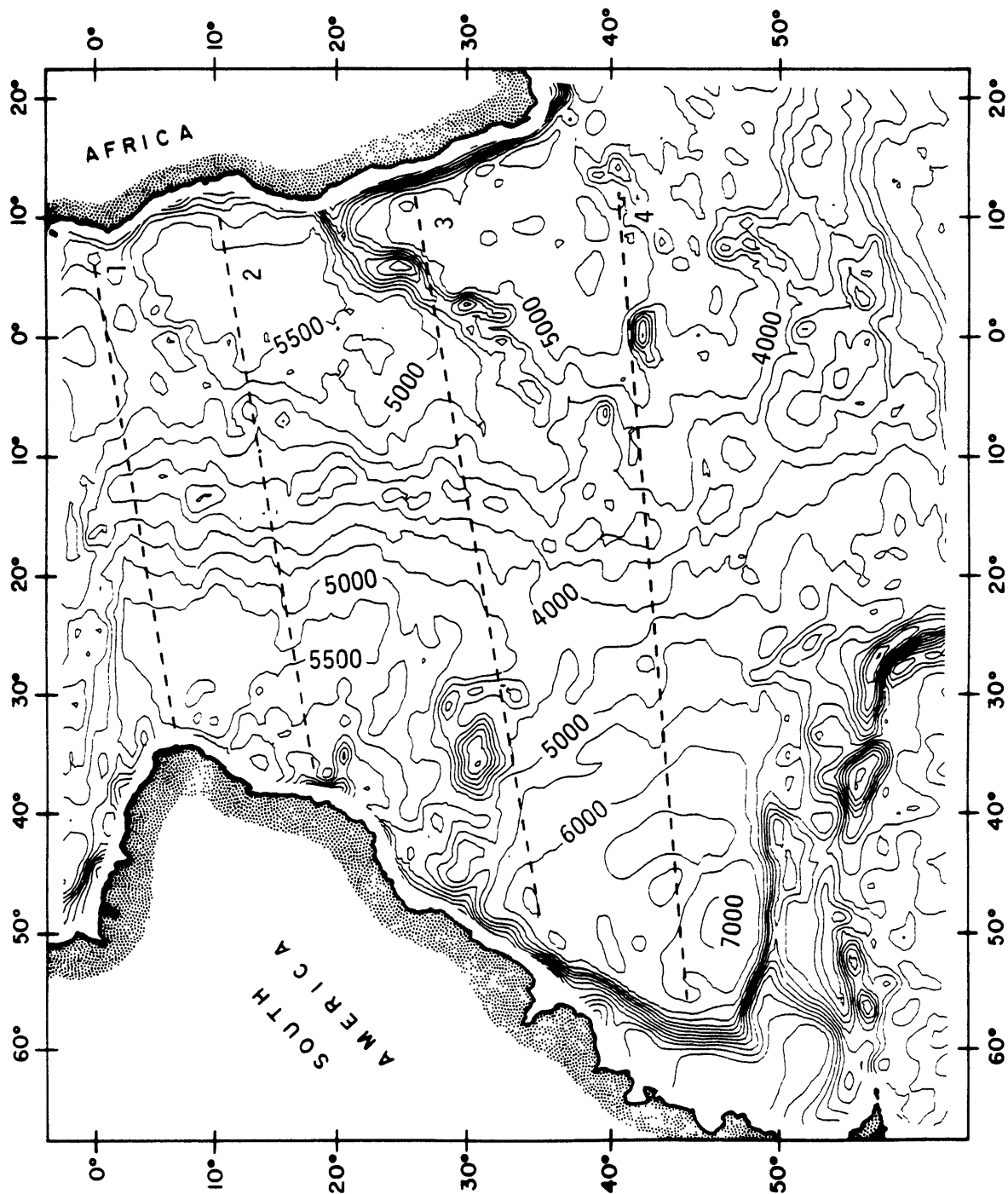


Figure 4. Bathymetry corrected for sediment loading. The dashed lines mark the positions of the interpolated profiles used in Figure 6.

effects of sediment loading will be referred to as sediment-corrected or, more simply, corrected bathymetry (geoid). Comparing Figures 2 and 4, we see that most of the ocean floor exhibits some increase in depth when the sediments are removed. This is particularly true in the four large basins. In the case of the Argentine Basin, this depth increase is over a kilometer. The sediment correction also shifts the location of the deepest areas of the ocean floor. In the Argentine Basin, for example, this locus is shifted northward. The gradual shoaling of the seafloor as it approaches the continents is shifted towards the continental margins. In both the Brazil and Cape Basins, for example, Figure 2 shows the seafloor beginning to shallow at distances of a thousand kilometers or more from the continental margin. In Figure 4, the seafloor remains quite deep up to the edge of the continental rise.

The errors that may be present in Figure 4 are difficult to quantify. Comparisons with published depth maps of the South Atlantic [GEBCO, 1978; Emery and Uchupi, 1984] indicate that the uncorrected bathymetry of Figure 2 is consistent with these other maps at the 500 m level or better. Where ship coverage is best, the bathymetry in Figure 2 is probably reliable to within  $\pm 200$  m.

The errors in sediment thickness were not specified by Divins and Rabinowitz [1986]. Assuming a 20-30% sediment thickness uncertainty with the uncertainties of the other parameters in equation (3) leads to an estimated uncertainty for  $d_s$  of  $\sim 25\%$ . Thus, sediment depth corrections may be in error by more than 500 m where sediment thicknesses are over  $\sim 3$  km. This occurs primarily near the continents where the sediment corrections are already known to be inaccurate. Note, however, that in the Argentine Basin, where sediment cover is thick and nonuniform, the total error in the

sediment-corrected depth may very well exceed 500 m.

#### 4.3.3 Lithospheric Ageing

As the lithosphere ages and cools, it becomes denser and subsides in depth while it tries to maintain a local isostatic balance. There are two principal models thought to describe the thermal evolution of the lithosphere which can be used to predict variations in depth as a function of lithospheric age. The half-space model [e.g. Davis and Lister, 1974] treats the lithosphere as a cooling infinite half-space. Seafloor continually deepens by an amount proportional to the square-root of the age. This can be expressed by

$$w(t) = \frac{-2\rho_m \alpha(T_m - T_0)}{(\rho_m - \rho_w)} \left( \frac{\kappa t}{\pi} \right)^{1/2} \quad (6)$$

where  $w(t)$  is the height of the seafloor with respect to the ridge crest as a function of time,  $\alpha$  is the coefficient of thermal expansion of the lithosphere,  $T_m$  and  $T_0$  are the temperatures of the mantle and surface, respectively, and  $\kappa$  is the thermal diffusivity.

The lithospheric thermal plate model [McKenzie, 1967; Parsons and Sclater, 1977] treats the lithosphere as a plate of finite thickness with a constant temperature bottom boundary, cooling from the top surface as it receives heat input at the bottom. At young ages, seafloor depths behave identically in both this model and the half-space model; at older ages, however, the plate model predicts that the depth will asymptotically approach a constant value. This is described by

$$w(t) = \frac{\rho_m \alpha (T_m - T_0) a}{2(\rho_m - \rho_w)} \left\{ 1 - \frac{8}{\pi^2} \sum_{n=0}^{\infty} \frac{1}{(2n+1)^2} \exp\left[-(2n+1)^2 \pi^2 \frac{\kappa t}{a^2}\right] \right\} \quad (7)$$

where  $a$  is the thickness of the lithospheric thermal plate [Parsons and Sclater, 1977].

The parameters for equations (6) and (7) are determined from empirical depth-age curves. The relative paucity of bathymetric data in the South Atlantic has discouraged study of depth-age variations in this ocean, so we must rely on empirical depth-age studies from other oceans. In most of these analyses, one empirical depth-age curve for an entire ocean is usually obtained. But previous work in the South Atlantic [Cochran and Talwani, 1977; Bowin et al., 1984; Jung and Rabinowitz, 1986b] has uncovered a marked asymmetry in the depth and geoid between the east and west sides of the ocean. One depth-age curve, implying uniform cooling on both sides of the ridge axis, may therefore not be valid. Although the goals of this study do not encompass determining empirical depth-age curves for the South Atlantic, we do wish to determine if there is a need for two markedly different depth-age relationships in this ocean. To accomplish this, we obtain a range of reasonable theoretical depth-age curves which we compare with the observed depths in the South Atlantic.

The lithospheric thermal parameters most often used are those of Parsons and Sclater [1977] based on empirical depth-age curves in the northern oceans. They present their parameters with formal estimated errors based on the uncertainties in their data and their inversion procedure. Their largest uncertainty, and the one that leads to the most variability in equations (6) and (7), is for the temperature difference  $\Delta T \equiv T_m - T_0$ , where they found  $\Delta T = 1350 \pm 250^\circ\text{K}$ . Cazenave et al. [1983] and Bowin et al. [1984] give estimates of the thermal parameters that are only marginally consistent with those of Parsons and Sclater [1977], but both studies may have sampled lithosphere that has been thermally perturbed by hotspots. Heestand and Crough [1981] and Schroeder [1985] determine empirical depth-age curves which differ from those of Parsons and Sclater

[1977], but can be produced from equations (6) and (7) given Parsons and Sclater's thermal parameters with their errors.

Using the parameters of Parsons and Sclater [1977] together with the empirical depth-age relationships of the studies mentioned above, we obtain depth-age curves with generous, but not unreasonable, error bars:

$$d(t) = (2700 \pm 200) + (320 \pm 30)\sqrt{t}, \quad \text{for } t \lesssim 50 \text{ m.y.} \quad (8a)$$

$$d(t) = (6400 \pm 200) - (3200 \pm 200)\exp[-t/(60 \pm 5)] \quad \text{for } t \gtrsim 50 \text{ m.y.} \quad (8b)$$

where  $t$  is the age of the lithosphere in millions of years, and  $d$ , the depth measured from sea level, is in meters. The variations in thermal parameters which we used to produce (8) are included in Table 1. The coefficients in (8) should be chosen to give depth values that vary by no more than  $\sim 50$  m at the overlap age of 50 m.y. For comparison, Parsons and Sclater's [1977] standard depth-age relationship is

$$d(t) = 2500 + 350\sqrt{t}, \quad \text{for } t < 70 \text{ m.y.} \quad (9a)$$

$$d(t) = 6400 - 3200 \exp(-t/62.8), \quad \text{for } t > 20 \text{ m.y.} \quad (9b)$$

Note that equations (8) and (9) represent the plate model; for the half-space model, equations (8a) and (9a) are valid at all crustal ages.

The models of the thermal structure of the lithosphere which were used to produce equations (6) and (7) can be used in conjunction with equation (4) to produce theoretical expressions for geoid as a function of age. To first order, the expression for the half-space model is [Haxby and Turcotte, 1978]

$$N(t) = \frac{-2\pi G}{g_0} \rho_m \alpha (T_m - T_0) \kappa t \quad (10)$$

while the thermal plate model geoid-age curve is described by [Parsons and

Richter, 1980; Sandwell and Schubert, 1980]

$$N(t) = \frac{-2\pi G}{g_0} \rho_m \alpha (T_m - T_0) a^2 \left[ -\frac{1}{6} + \frac{2}{\pi^2} \sum_{n=1}^{\infty} \frac{(-1)^n}{n^2} \exp\left(-\frac{n^2 \pi^2 \kappa t}{a^2}\right) \right] \quad (11)$$

Although empirical depth-age data were used to constrain the thermal parameters in equations (6) and (7), reliable empirical geoid-age data are difficult to obtain. Observations of the geoid as it slopes away from the ridge [Haxby and Turcotte, 1978; Sandwell and Schubert, 1980; Cazenave et al., 1983] give highly variable geoid-age curves, as they are greatly affected by the long-wavelength geoid anomalies produced by deep density variations unrelated to lithospheric structure. Observations of geoid offsets at fracture zones [Crough, 1979; Detrick, 1981; Sandwell and Schubert, 1982] have been used more successfully to determine lithospheric thermal structure, in particular the plate thickness  $a$ , but there are large uncertainties in studies of this sort also [Cazenave, 1984; Driscoll and Parsons, 1987; chapter 3 of this thesis].

We therefore use the set of lithospheric thermal parameters and their uncertainties determined from depth-age data to construct a range of geoid-age curves to apply in the South Atlantic. From equations (10) and (11), we obtain

$$N(t) = (-0.15 \pm 0.02)t \quad \text{for } t \lesssim \tau \quad (12a)$$

$$N(t) = (-15 \pm 2) \{ 1 + 1.22 [-\exp(-t/(60 \pm 5))] + 0.25 \exp(-t/(15 \pm 1)) \} \quad \text{for } t \gtrsim \tau \quad (12b)$$

where  $N$  is the geoid height relative to the ridge in meters for age  $t$  in millions of years. Coefficients of (12) and the value of the overlap age  $\tau$  are chosen to yield geoid heights at  $t = \tau$  that differ by no more than  $\sim 20$  cm and are logically consistent with the parameters in equations (10) and (11)

from which they are derived. Since the geoid is much more sensitive to the deep thermal structure of the plate than is the depth (the reason for much of the interest in the geoid-age curve), the value of  $\tau$  will change significantly as plate parameters are varied. Note that in the half-space model, equation (12a) should be valid at all ages.

A number of empirical geoid-age curves have been found for the South Atlantic, though as we mentioned above, there is much doubt about their reliability. Sandwell and Schubert [1980] estimate a geoid-age slope of

$$N(t) = (-0.094 \pm 0.025)t \quad (13)$$

out to 70 m.y. This is a significantly shallower slope than that of equation (12a). If it is an accurate indicator of the lithospheric thermal structure, then many of the variables in equation (10) are significantly smaller than those given by Parsons and Sclater [1977]. In particular, values for the temperature difference of  $\Delta T \leq 1030^\circ\text{C}$  would be needed to yield this shallow a geoid-age slope. Although this is a very low estimate for the mantle temperature, we will pursue below the possibility that Sandwell and Schubert's [1980] geoid-age slope may be the most reasonable empirical slope to use. By using these low thermal parameter values in equation (6), we can, in addition, obtain a depth-age relationship of

$$d(t) = (2700 \pm 200) + (240 \pm 30)\sqrt{t} \quad (14)$$

that we can easily test below. Bowin et al. [1984] also estimate geoid-age slopes in the South Atlantic, but their results, varying from  $-0.20$  m/m.y. to  $-0.03$  m/m.y., leave the lithospheric thermal parameters effectively unconstrained.

#### 4.3.4 Theoretical Depths

We obtained digital age data for the South Atlantic Ocean on a 5' grid from S. Cande at Lamont-Doherty Geological Observatory [Cande et al., 1984]. These age data compare well with published age maps where magnetic anomalies are well mapped, but where ship coverage is sparse or magnetic anomalies weak, large discrepancies may appear (described in Chapter 3 of this thesis). Alternate data points (i.e., with 10' spacing) were interpolated and low-pass filtered to produce a gridded age map of the South Atlantic (Figure 5). Unfortunately, the data do not extend to the southernmost parts of our study area (Figure 1), since these areas are technically either other ocean basins or submerged continental fragments.

With the aid of equations (8), (9), and (14) we produced a variety of theoretical depth maps based on the age of the ocean floor. To evaluate whether a particular depth-age curve is appropriate to use in the South Atlantic, we examine selected depth profiles across the Mid-Atlantic Ridge interpolated from our maps. In Figure 6, we compare theoretical depth profiles with those from the bathymetry corrected for sediment loading of Figure 4.

There is, of course, much short-wavelength variation in the profiles, but a few patterns emerge. Given the small size of the South Atlantic basin and the limited seafloor age range that we are able to study (ages  $< 100$  m.y.), it seems impossible to discriminate between the plate and half-space models unless the plate is exceedingly thin. There are only a few locations where the slope in depth away from the ridge is sufficiently shallow to suggest either an anomalously thin thermal plate or an unusual variation in temperature away from the ridge such as that implied in the above analysis of the Sandwell and Schubert [1980] results.

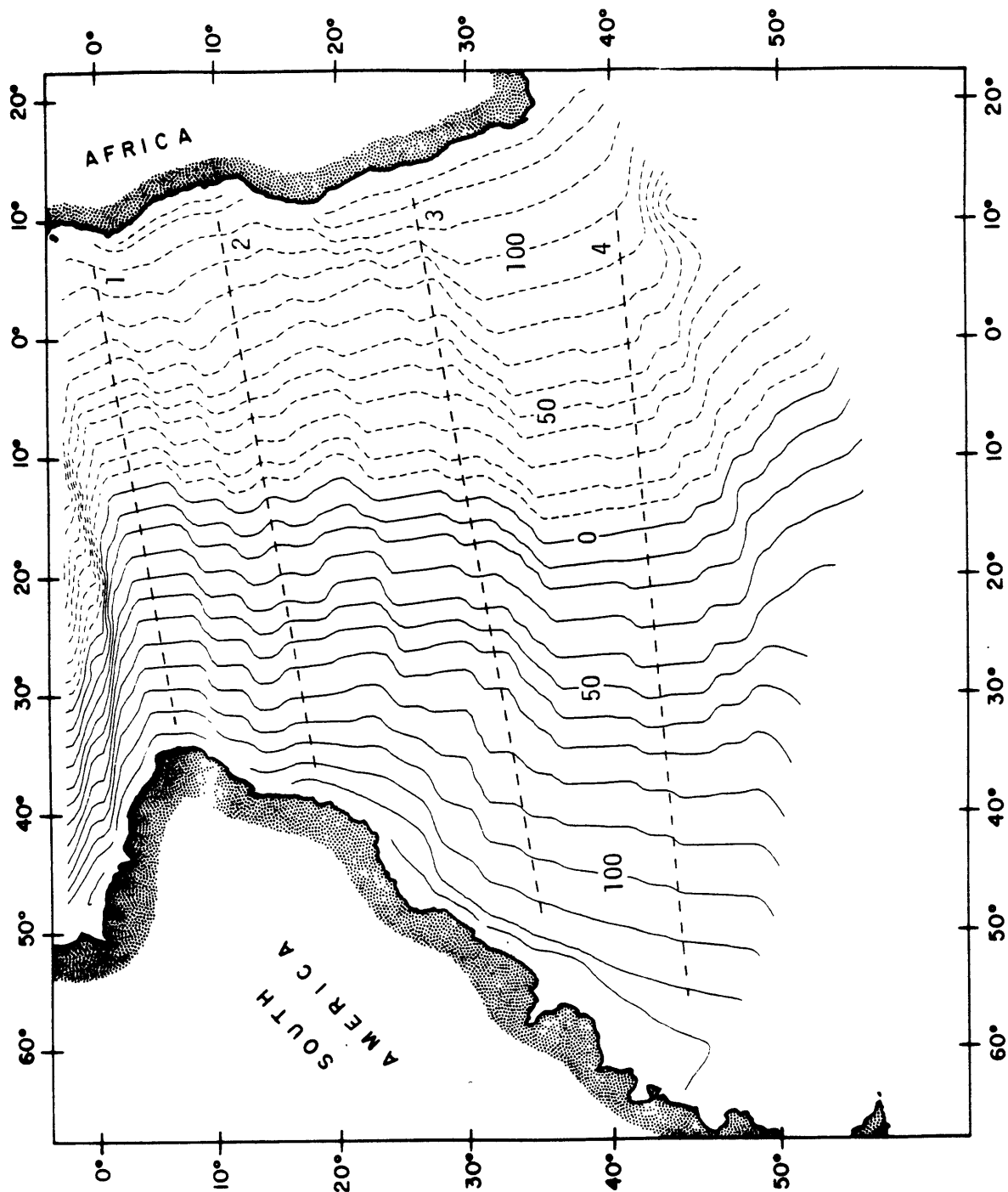


Figure 5. Age map of the South Atlantic Ocean. Data were obtained from the digital data set of Cande *et al.* [1984], interpolated, and low-pass filtered. The contour interval is 10 million years. Age contours east of the Mid-Atlantic Ridge, on the African plate, are dashed. Those to the west, on the South American plate, and the zero age contour over the ridge are solid lines. The heavy dashed lines mark the positions of the interpolated profiles shown in Figure 6.

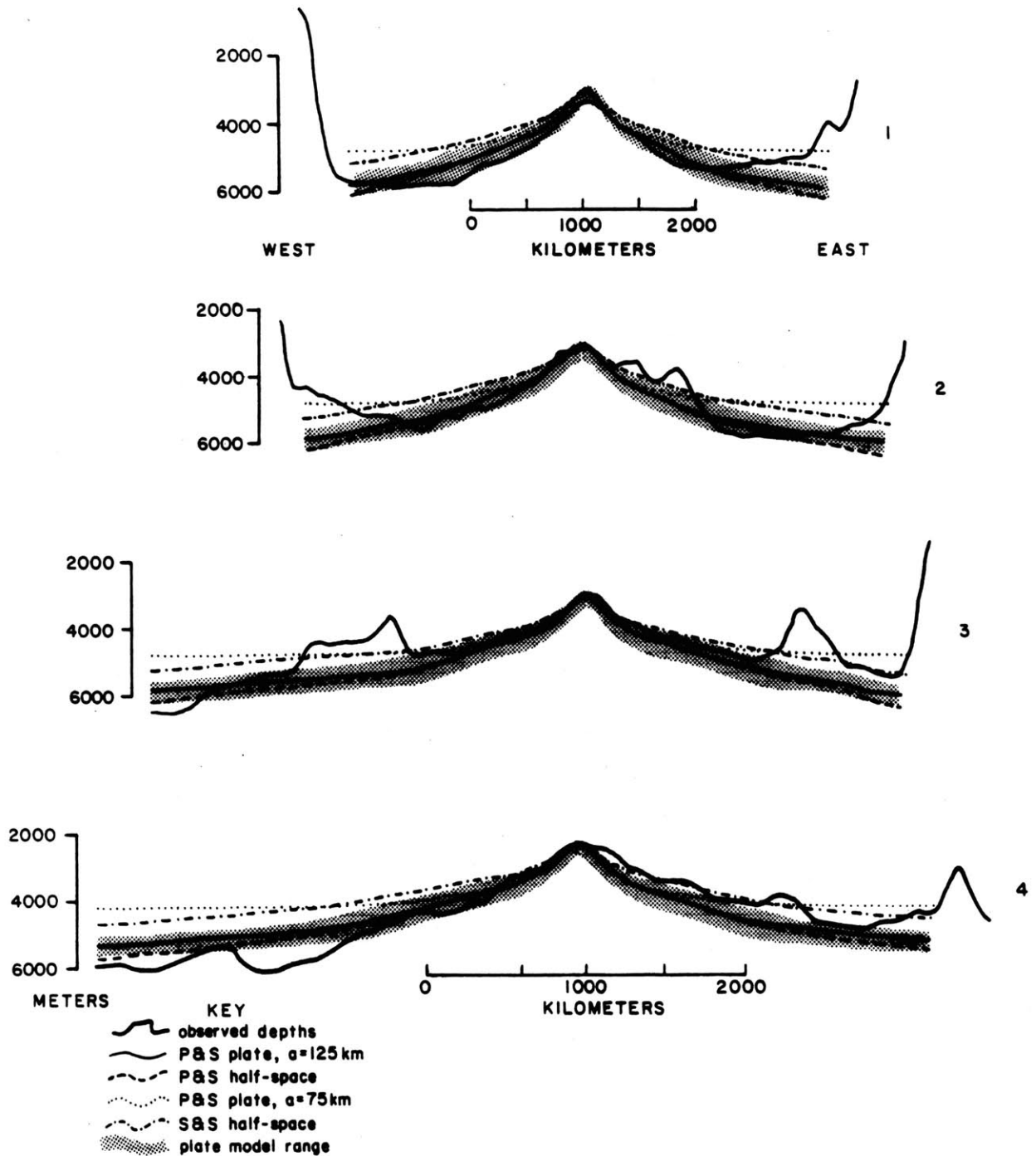


Figure 6. Comparison of theoretical depth profiles based on the age of the ocean floor with profiles of the bathymetry corrected for sediment loading. Profile positions are shown in Figs. 4 and 5. Each set of profiles shows the observed depths together with the theoretical depths for: the Parsons and Sclater [1977] plate model (Eq. 9, which assumes a plate thickness of 125 km) and half-space model (Eq. 9a), the Sandwell and Schubert [1980]-derived half-space relation (Eq. 14), and a thin-plate model (Eq. 7, with thermal parameters from Table 1 and a plate thickness of 75 km). The shaded region shows the range of plate model depth-age curves given in Eq. 8.

Profile 3, which crosses the MAR between the two aseismic ridges, shows the most obvious of these anomalous shallow slopes. On the other hand, most of the basins follow depth curves that dip well below the Parsons and Sclater [1977] reference curve for either a plate or half-space model. Profiles 1, 2, and 4 appear asymmetric across the ridge, with the east flank deepening more slowly than the west, but only profile 4 exhibits an asymmetry so large as to suggest the use of two different depth-age curves for each side of the MAR (implying asymmetric cooling as well as a thinner plate across the ridge). Due to this large variability along the ridge, we subsequently employ the standard Parsons and Sclater [1977] plate model depth-age curve (equation 9). It does not fit any profile well, but remains a reasonable average variation of depth with age in the South Atlantic.

#### 4.3.5 Residual Depth Anomalies

By subtracting our preferred theoretical depth map from the map of the bathymetry corrected for sediment loading we obtain a map of the residual depth anomalies, shown in Figure 7. Residual depth (or geoid) will refer to the bathymetry (or geoid undulations) that remains after the effects due to lithospheric cooling are removed. Unlike previous depth maps, Figure 7 shows both positive and negative anomalies; a zero value residual depth corresponds to the theoretical depth for that age seafloor.

The prominent shoaling of the MAR that is obvious in Figure 4 has been removed. In its place is a broad, relatively flat region that parallels the ridge crest with undulations in depth of not much more than 500 m. The Rio Grande Rise and northeast Walvis Ridge still remain prominent depth highs with positive anomalies greater than 3500 m.

The Argentine Basin exhibits the lowest residual depths, with negative anomalies in excess of -1000 m. A curious bull's-eye pattern of concentric

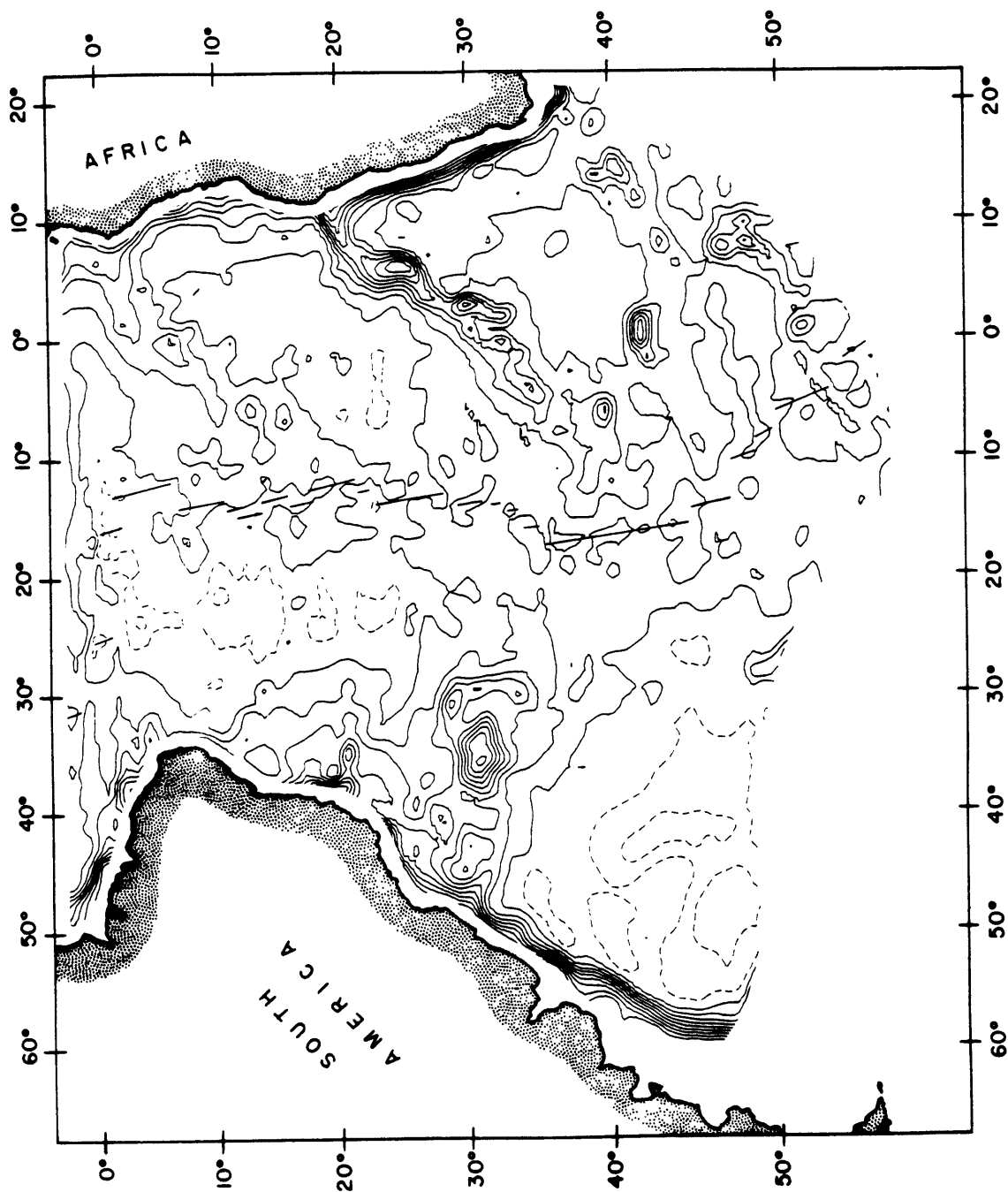


Figure 7. Residual depth anomaly map of the South Atlantic Ocean, obtained by subtracting our preferred theoretical depths based on seafloor ages from the bathymetry corrected for sediment loading. The contour interval is 500 m, and negative contours, i.e., depths deeper than predicted, are shown as dashed lines. The position of the Mid-Atlantic Ridge is indicated.

depth undulations appears around the southwest corner of the basin, perhaps the result of an incomplete sediment correction. To the north, the Brazil Basin appears as a north-south band of lows with minima also reaching -1000 m. The deepest part of this basin is located midway between the Mid-Atlantic Ridge and the continental slope, roughly coinciding with the 50 m.y. isochron. Thus the residual depth starts to shoal towards Brazil at a distance of greater than 1000 km from the continent. The seafloor around the Columbia seamount chain out to Trindade and Martin Vaz is marked by a positive depth anomaly plateau, as is that around Fernando de Noronha and its associated seamounts.

The Angola Basin appears as a much smaller residual depth low barely reaching -500 m. It is limited in extent to the north by depth highs of over 1000 m associated with the east side of the Ascension fracture zone, the Guinea Ridge, and perhaps with the chain of seamounts extending northeast from St. Helena into the Gulf of Guinea. South of the Walvis Ridge, the Cape Basin shows an overall positive depth anomaly, but it remains a regional low relative to the highs which surround it. These highs include the Walvis Ridge to the north, Tristan da Cunha and Gough to the west, and the Discovery seamounts and the Agulhas Ridge to the south. In fact, this band of highs extends across the ridge and connects with that surrounding the Rio Grande Rise, forming a large "t" shaped pattern of residual depth highs in the center of the South Atlantic.

Each basin appears as a residual depth low, but the basins to the east are 500 m or more shallower than those to the west. This east-west variation, together with more extensive positive anomalies on the eastern flank of the ridge, create the appearance of asymmetry across the MAR. This observed asymmetry might be a manifestation of some geophysical

process occurring differently on either flank of the ridge. Or it may simply be an artifact created by a limited number of features with otherwise random locations.

A number of shorter-wavelength depth anomalies appear to parallel fracture zones, indicating either that age-dependent depth corrections have not been made accurately, or that other sources of depth anomalies exist which are influenced by fracture zone locations. Examples of features such as these are the depth high along the easternmost branch of the Ascension fracture zone at  $\sim 3^{\circ}\text{S}$ , a shoaling of the seafloor south of the Rio Grande fracture zone at  $\sim 27^{\circ}\text{S}$ , and a series of lineated highs and lows south of the Falkland-Agulhas fracture zone between  $45^{\circ}\text{S}$  and  $50^{\circ}\text{S}$ .

Although we hope to use the residual depth anomaly map of Figure 7 in conjunction with maps of the geoid to elucidate possible patterns of mantle convection, there are a number of additional processes unrelated to convection that affect the ocean floor depth which we have not yet explicitly considered. Flexure of the lithosphere caused by surface or subsurface loads has been shown to significantly influence depths out to distances of a few hundred kilometers [e.g. Watts and Daly, 1981]. To circumvent this effect, most studies have simply filtered their maps to remove wavelengths shorter than the maximum significant flexural wavelength [Sclater et al., 1975; Watts et al., 1985]. Low-pass filtering has the additional effect of diminishing the large-amplitude but short-wavelength signals of constructional features such as seamounts and local fracture zone topography. As Watts et al. [1985] point out, however, although smoothing gravity maps will remove most of the signal of short-wavelength features, smoothing depth maps will simply convert high-amplitude short-wavelength features into low-amplitude long-wavelength ones. In the

South Atlantic, this is an especially worrisome problem due to the two large aseismic ridges which dominate the ocean floor.

We have produced our original maps with a minimum of smoothing in order to be aware of the shorter-wavelength features which might lead to errors of interpretation in more extensively smoothed maps. To compare our results with studies in other oceans, we have produced two smoothed versions of our depth anomaly map. Figure 8 presents two maps: the first employs a Gaussian filter with  $\sigma = 150$  km, effectively removing wavelengths of  $\lambda < 450$  km; the second employs a filter with  $\sigma = 275$  km, effectively removing wavelengths of  $\lambda < 900$  km and comparable to convolving the map with a  $5^\circ \times 5^\circ$  rectangular window.

In the filtering process amplitudes are greatly diminished, yet our major observations remain. All the basins are relative residual depth lows with the Argentine Basin being the deepest. The Rio Grande Rise and northern Walvis Ridge are the most distinctive highs, while less prominent highs bound the Angola Basin to the north and the Brazil Basin to the west. The Mid-Atlantic Ridge high has been removed, but subtle residual depth undulations remain in its place. The smoothing half-width of 50 km which we have been using does not seem to interfere with the observation of long-wavelength depth anomalies, and it allows us to spot potential sources of trouble of shorter-wavelength.

In addition to lithospheric flexure and constructional tectonics, other processes occurring within the lithosphere may affect depths. Variations in thickness of the crust can lead to depth anomalies over wide areas. Detrick and Watts [1979] and Bulot et al. [1984], for example, conclude that crustal thickening corresponding to Airy compensation provides most of the isostatic support of the Rio Grande Rise and Walvis

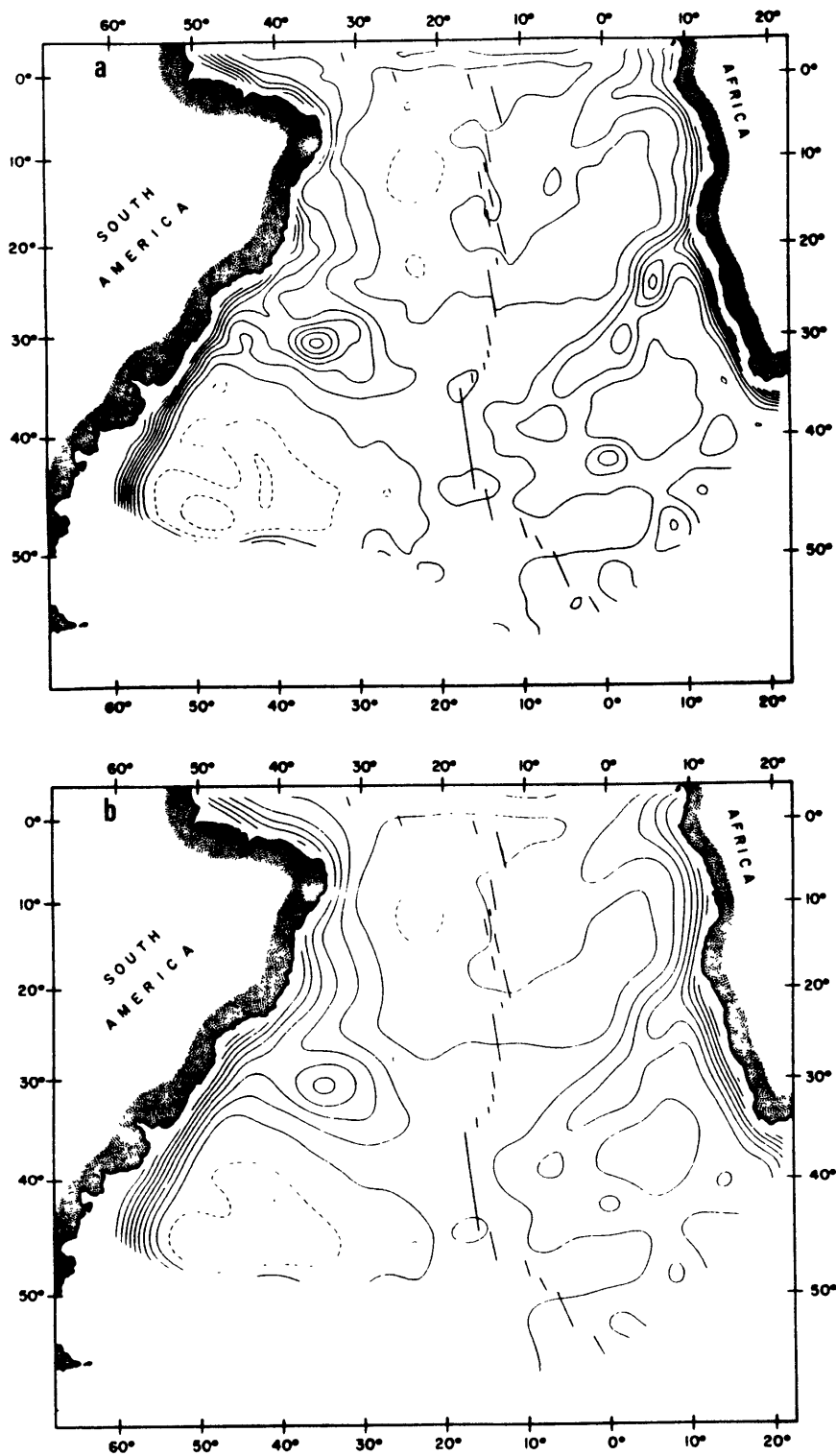


Figure 8. Low-pass filtered versions of the residual depth map of Figure 7. a)  $\sigma = 150$  km, effectively removing wavelengths less than  $\sim 450$  km. b)  $\sigma = 275$  km, effectively removing wavelengths less than  $\sim 900$  km, comparable to convolution with a  $5^\circ \times 5^\circ$  rectangular window. The contour interval is 500 m, and the MAR position is indicated.

Ridge. Increased crustal thickness in the region between the two aseismic ridges, produced perhaps by excess volcanism at the ridge, could lead to the residual depth high that crosses the South Atlantic from east to west. Only a ~2 km change in crustal thickness is necessary to produce the ~500 m depth variations observed.

Alternatively, chemically or thermally produced density differences in the lower lithosphere would also result in depth anomalies. Low density mineralogies are suspected as the cause of depth and geoid anomalies over both aseismic ridges [Angevine and Turcotte, 1983; Kogan et al., 1985] and mid-ocean ridges [e.g. Bowin et al., 1984; McNutt and Fischer, 1986]. Lower lithosphere thermal perturbations are cited as the cause of mid-ocean swell positive depth anomalies, but there is debate as to whether these swells are better modeled by lithospheric anomalies or by convective upwelling in the mantle [Crough, 1978; Parsons and Daly, 1983; Detrick et al., 1986; McNutt, 1986]. Since additional data (independent of gravity) that could constrain crustal thickness and upper mantle density, such as multichannel seismic surveys, are sparse in the South Atlantic, we cannot reliably correct our residual depth map further. We turn now to the geoid for an independent estimate of subsurface density anomalies.

#### 4.4 Geoid Anomalies

##### 4.4.1 Seasat Data

Along-track Seasat altimetry was obtained from R. Rapp at Ohio State University [Rapp, 1982] who eliminated bad data points and adjusted the arcs for ephemeris errors by minimizing crossover discrepancies. Because of the large quantity of along-track data, we culled alternate points and interpolated the remainder, spaced at roughly 13 km along each arc, onto a

~50 km grid (described more fully in section 4.3.1 above). We obtained the full South Atlantic geoid seen in Figure 9.

The geoid exhibits a marked regional slope from highs of +25 to +30 m in the southeast to lows of -8 to -10 m in the west and northwest. East-west asymmetry is evident in the change in slope near the position of the Mid-Atlantic Ridge; the geoid slopes down steeply to the west, but rises much more shallowly to the east. A saddle appears in the northeast corner of our geoid map, while the southeast corner exhibits two "tongues"--one a relative low, the other a relative high--subparallel to the MAR in the south.

#### 4.4.2 Long-Wavelength Geoid

Since we wish to study the anomalous geoid produced by density variations within the upper mantle, we need to remove the large-amplitude long-wavelength background geoid. Most studies have relied on spherical harmonic expansions to degree and order 10 of the gravity field derived from satellite tracking to model the long-wavelength geoid, which was then subtracted from the altimetry. Such a procedure removes wavelengths on the order of 4000 km and longer. Sandwell and Renkin [1986] caution that a sharp cutoff at degree 10 in the frequency domain may lead to spurious sidelobes in the spatial domain. They also warn that the steep decline in power with decreasing wavelength in the gravity power spectrum will lead to the overemphasis of features of the lowest degree remaining in the geoid maps.

We constructed a number of long-wavelength geoid maps using combinations of low-order coefficients of the GEM 9 geoid [Lerch et al., 1979]. The reference field which we subsequently use, illustrated in Figure 10, is produced using the GEM 9 components complete to degree and

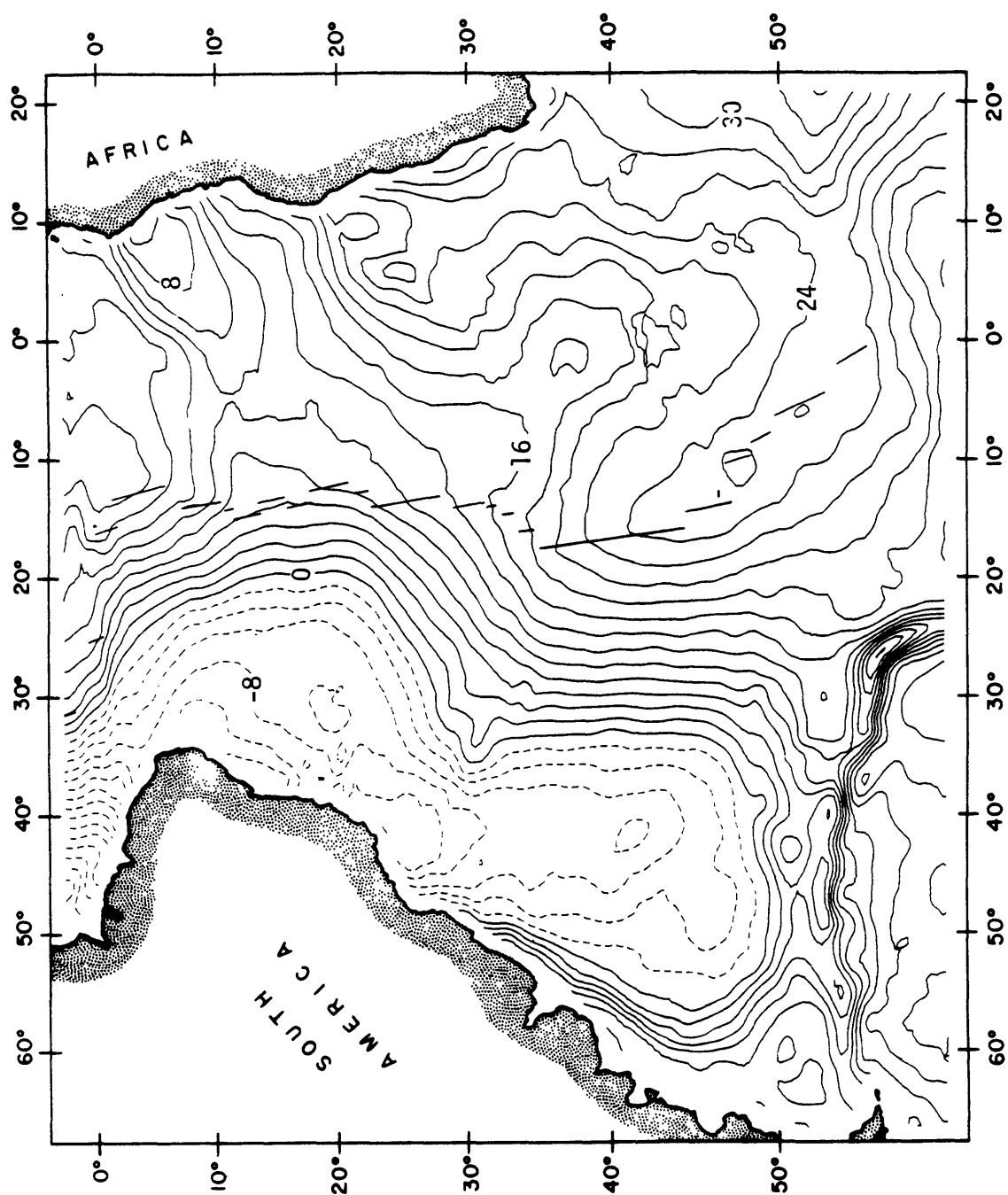


Figure 9. Seasat-derived geoid map of the South Atlantic Ocean. Along-track data with a spacing of  $\sim 13$  km were projected, interpolated, and smoothed using a Gaussian filter with half-width 50 km. The contour interval is 2 meters, with negative values shown by dashed lines. The MAR position is also indicated.

order 8, with coefficients from degrees 8 to 12 multiplied by a cosine bell taper. Thus only half the amplitude of the degree 10 coefficients are included in our reference geoid. By using this tapered field, we hope to avoid the problems discussed by Sandwell and Renkin [1986]. We have also considered more traditional reference fields with sharp cutoffs at degree 10 (containing wavelengths  $\lambda \gtrsim 4000$  km) and degree 8 (containing  $\lambda \gtrsim 5000$  km); the effects of these different reference fields will be shown below.

The primary features of the GEM 9 field include: the same strong northwest-southeast slope observed in Figure 9, and, to some extent, a change in character in the geoid on either side of the Mid-Atlantic Ridge, a geoid trough in the west leading north to a large low in the Caribbean, a high in the far west due to subduction off the west coast of South America, a saddle point in the northeast, and a plateau in the geoid in the southeast probably related to the Bouvet triple junction.

#### 4.4.3 Corrected Geoid

By subtracting the long-wavelength geoid of Figure 10 from the Seasat-derived geoid of Figure 9, we obtain a geoid map containing only short- and intermediate-wavelength anomalies. Using equations (3) and (5) in conjunction with the map of sediment thicknesses (Figure 3), we have produced a set of geoid corrections due to sediment loading. These corrections are minor, as the geoid effect produced by the largest sediment loads barely exceeds 1 m, but the highly nonuniform sediment distribution suggests that this correction should be included. We subtract the sediment correction from the intermediate-wavelength geoid map, yielding what we refer to as the corrected geoid shown in Figure 11.

This map is dominated by the geoid lows of the four major basins. The Argentine Basin exhibits a maximum depth of -20 m, the Angola and Cape

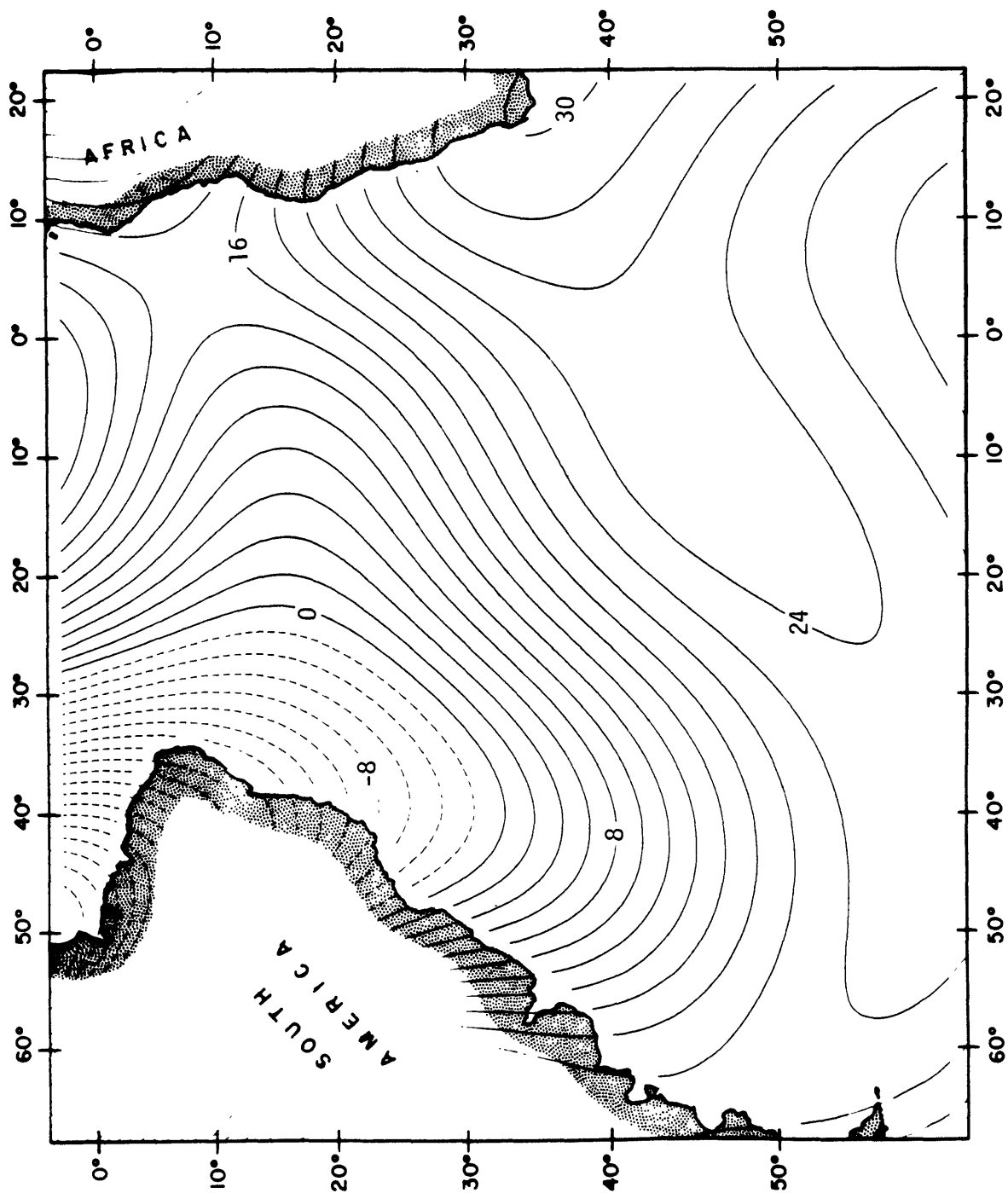


Figure 10. GEM 9 long-wavelength reference geoid containing complete degrees up to  $n=8$  and degrees  $n=8$  to  $n=12$  weighted by a cosine bell taper. The contour interval is 2 m and negative values are dashed.

Basins both reach lows of -8 or -9 m, and the Brazil Basin bottoms out at a relatively shallow -5 m. A band of positive geoid anomalies winds down the center of the South Atlantic. It correlates quite well with the Mid-Atlantic Ridge bathymetric high (see Figure 4) and contains local peaks at four locations: a 5 m high near Ascension Island, a 3 m high west of St. Helena, a high of 1 m west of Tristan da Cunha, and a high of 3 m or more near the Bouvet triple junction. These geoid highs along the ridge may be associated with less obvious bathymetric shoaling along the MAR (Figures 4 and 7). The intervening lows along the ridge correlate with selected fracture zones, for example, the Bode Verde FZ at  $\sim 12^{\circ}\text{S}$  [Brozena, 1986] and the Rio Grande FZ at  $\sim 30^{\circ}\text{S}$ . The geoid clearly slopes down from the ridge on both sides, but the slope to the west is significantly steeper than that to the east. This is especially true along the northern half of the MAR where the characteristic ridge high appears to be stretched out eastwards.

To the west of the MAR and connected to it by a ridge-like high, is the 1-2 m geoid high of the Rio Grande Rise. To the north, projecting east from the margin of Brazil, is a relative geoid high containing the Columbia seamount chain. This high corresponds closely to the depth anomaly surrounding the seamount chain (Figs. 4 and 7). To the east of the MAR, the northern Walvis Ridge is marked by a geoid high of up to 4m. The southwestern Walvis Ridge, however, does not seem to exhibit a significant geoid signature. North of the Angola Basin, a bridge of relative geoid high extends from the MAR to the coast of Africa. This corresponds to the positive depth anomaly seen along the east branch of the Ascension FZ and the Guinea Ridge (and is identical to the geoid bulge discussed in Chapter 3).

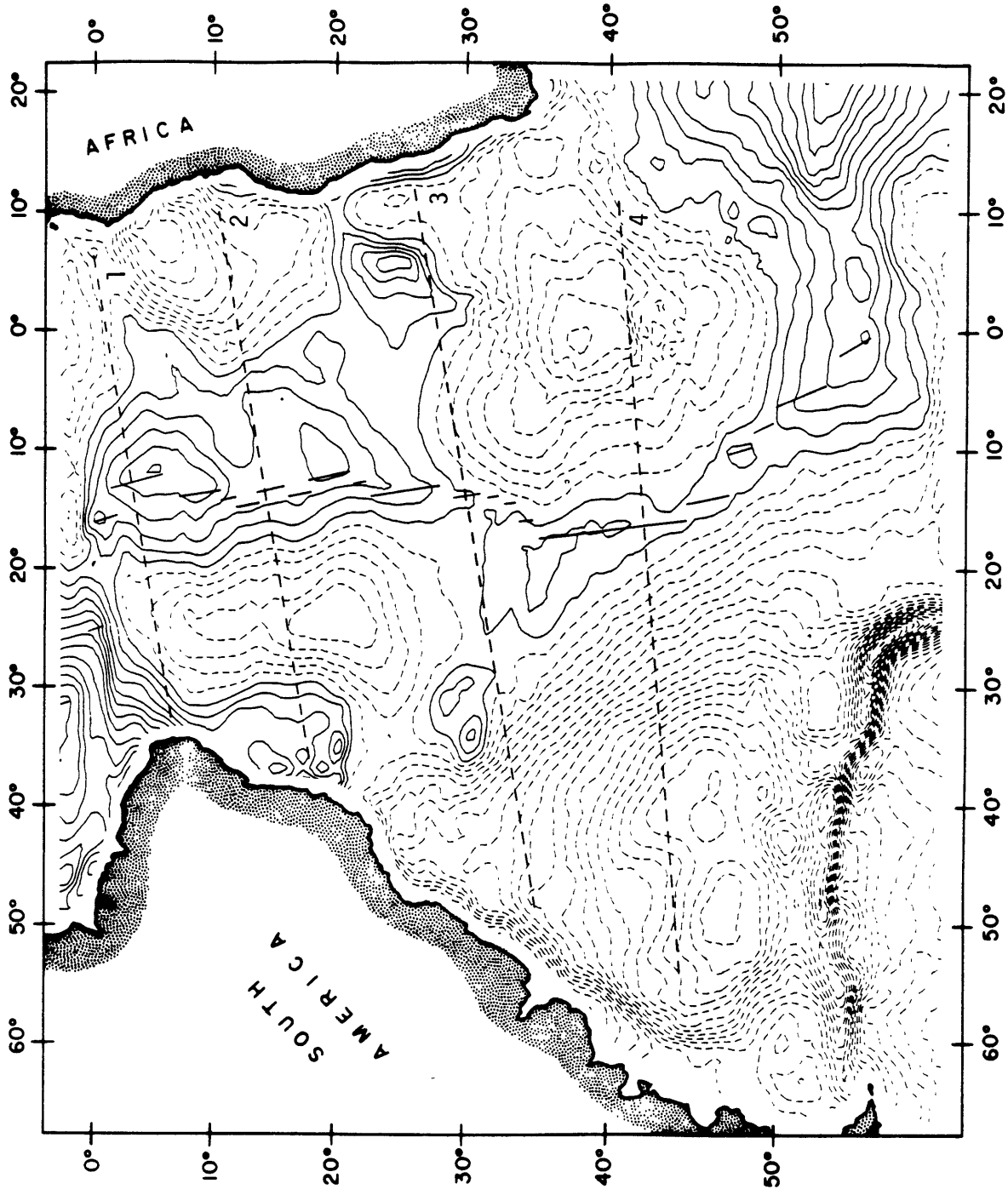


Figure 11. Intermediate-wavelength corrected geoid map of the South Atlantic. The GEM 9 reference field of Fig. 10 was subtracted from the Seasat-derived geoid map of Fig. 9. Additional corrections for minor geoid anomalies produced by the sediment load were made to the map. Note that the contour interval in this and subsequent geoid maps is 1 m and dashed contours denote negative geoid anomalies. The position of the MAR is shown, as are the positions of the profiles used in Figure 13.

With the exception of the southern Walvis Ridge and its continuation as a low-amplitude depth high to meet the MAR, the intermediate-wavelength geoid map of Figure 11 correlates remarkably well with the sediment-corrected depth map of Figure 4. Although this is not a surprising result based on observations in other oceans, it is quite unusual in that it at least partially contradicts the results of a number of previous studies in the South Atlantic. Bowin et al. [1984] do not find a correlation between the geoid and bathymetry along the MAR north of 40°S, though they agree that geoid highs lie over the aseismic ridges. Kogan et al. [1985] also see little correlation of the geoid with bathymetry over the MAR once the long-wavelength field is removed.

The source of this disagreement over the observed depth-geoid correlation may lie partially in the quality and spatial resolution of the maps used in each study. But a more important factor is the subjective nature of visual correlation. The geoid peaks along the MAR north of 30°S are offset slightly to the east of the ridge, while the highs slope down more gently to the east. This asymmetry around the MAR may give the impression that the geoid and bathymetry are not correlated in this area. In reality, however, the highs do overlie MAR segments and the bathymetry, too, is somewhat higher to the east of the MAR than to the west.

Another factor in this disagreement may be the choice of long-wavelength reference field subtracted from the altimetry. We present in Figure 12 two intermediate-wavelength corrected geoid maps, the first obtained by removing the GEM 9 field with coefficients complete to, and truncated sharply at, degree and order 10, and the second, by removing the GEM 9 field complete to degree and order 8. In both maps, the basic character of the geoid field is the same, with relative highs and lows in

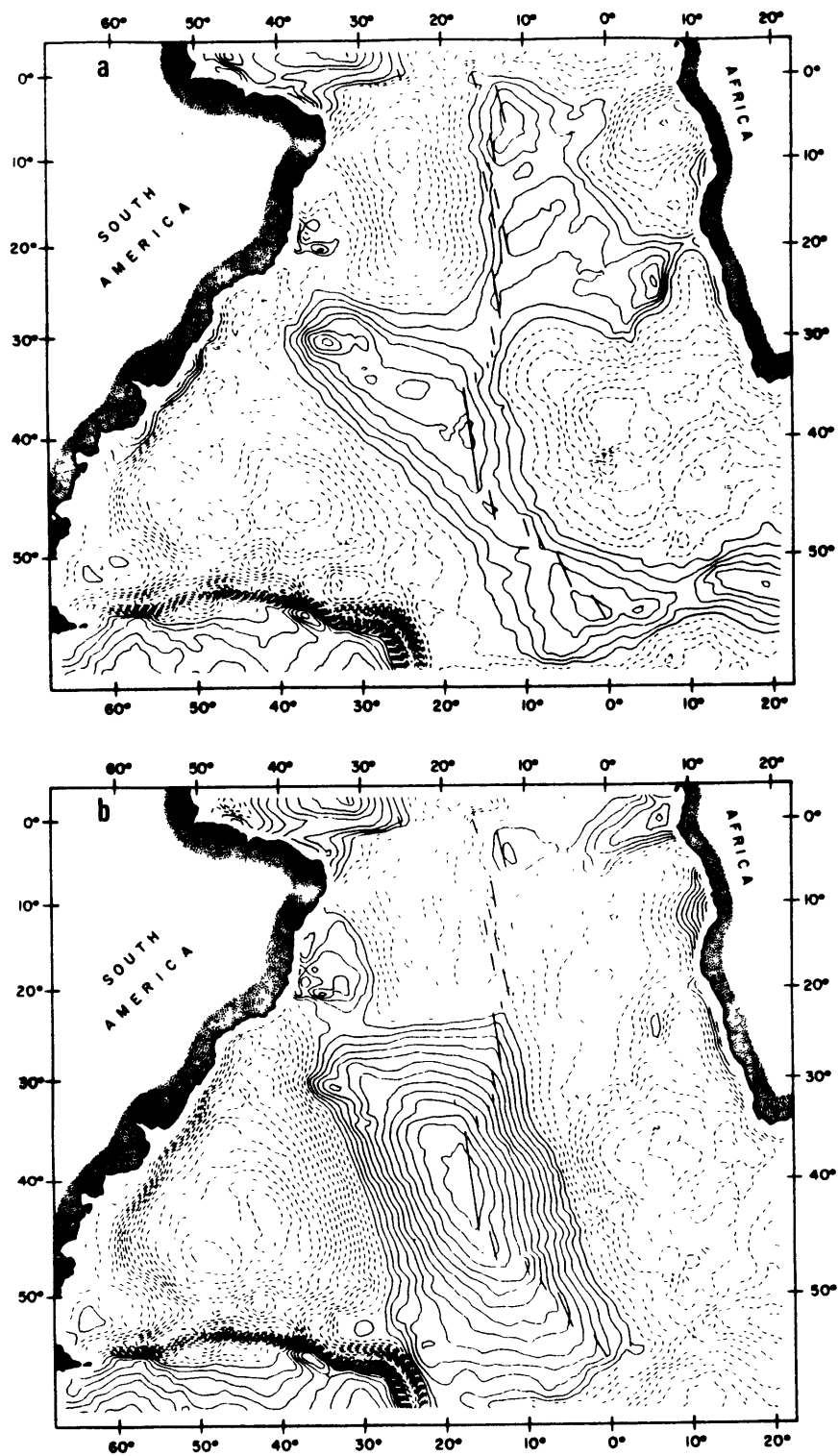


Figure 12. Intermediate-wavelength sediment-corrected geoid maps made by removing alternative GEM 9 fields: a) the GEM 9 field complete to  $n=10$  (wavelengths  $> 4000$  km removed), b) the GEM 9 field complete to  $n=8$  (wavelengths  $> 5000$  km removed). Refer to Figure 11 for further description.

similar locations. Magnitudes, however, vary drastically. In the degree 10 geoid, the highest anomalies have magnitudes of +3 to +5 m. Their location in two parallel bands, one running from the Rio Grande Rise to the MAR, the other from the northern MAR to the Walvis Ridge, deemphasizes the high along the MAR and may have led to the conclusion that little correlation exists between bathymetry and the geoid along the ridge. In the degree 8 geoid, a huge high of  $\sim +12$  m appears over the southern MAR. Magnitudes of geoid lows also differ substantially among the maps. Since small variations in the long-wavelength geoid can lead to large amplitude changes in the resulting intermediate-wavelength geoid maps, peak-to-peak magnitudes of major features should be used with caution.

#### 4.4.4 Theoretical Geoid

Although removing the effects of lithospheric age from the bathymetry is rather straightforward, removing the effects of age from the observed geoid poses a number of subtle problems. Initially, we proceed as we did for the depths. Using equations (12) and (13) we form a number of theoretical geoid maps. In Figure 13 we compare profiles from selected maps of geoid based on age with those from the corrected geoid of Figure 11.

Problems emerge immediately. Whereas the depth-age relationship was the predominant source of long-wavelength power in the observed depth maps, the long-wavelength geoid-age relationship does not dominate the observed geoid. Rather, the geoid profiles exhibit characteristic undulations with wavelengths of 2000-4000 km and amplitude variations comparable to or greater than those predicted by the geoid-age curves.

Previous investigators have noted that in the process of removing long-wavelength geoid anomalies due presumably to deep mantle structure,

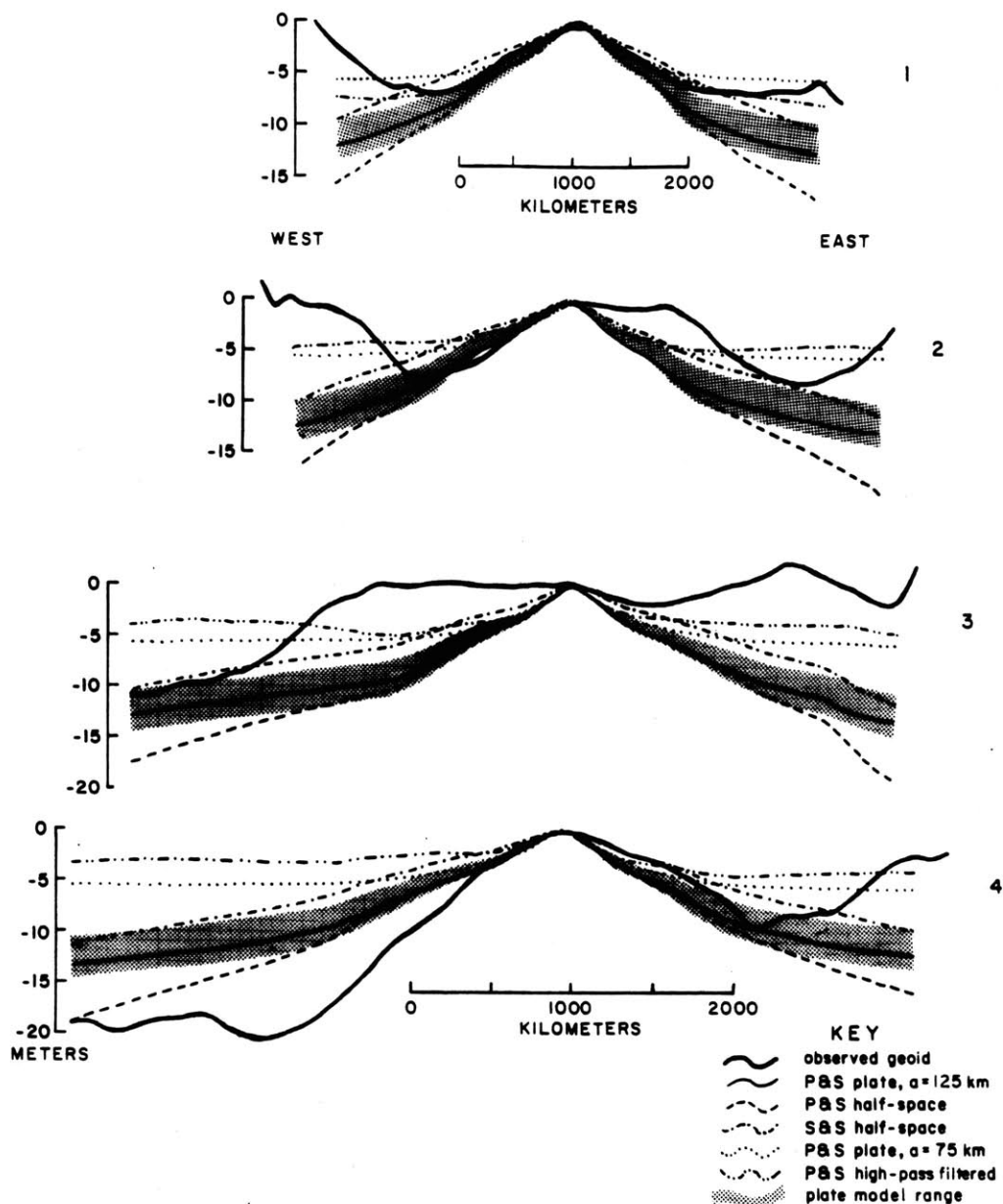


Figure 13. Comparison of theoretical geoid profiles based on the age of the ocean floor with profiles from the corrected geoid of Figure 11. Profile positions are indicated in Figs. 5 and 11. Each set of profiles shows the observed geoid together with theoretical geoid-age curves for the same models included in Fig. 6. These include the Parsons and Sclater [1977] models for plates with thicknesses of 125 km and 75 km (Eq. 11), and a half space (Eq. 10), and the Sandwell and Schubert [1980] half-space model (Eq. 13). The shaded region shows the range of plate model geoid-age curves given by equation (12). An additional profile shows the Parsons and Sclater standard plate model geoid after high-pass filtering to remove long wavelengths.

the long-wavelength components of the geoid-age relationship are also removed. This has been a particular problem in the Pacific with its large distances from ridge to trench [Watts et al., 1985]. Although the South Atlantic is a much smaller ocean basin, the attenuation of the geoid-age curve at long wavelengths appears sufficient to preclude the use of all but the shortest-wavelength portion of the geoid-age curve in estimating the "best-fit" geoid-age relationship. Thus we should limit ourselves to the steepest portions of the geoid-age curve out to a few hundred kilometers from the Mid-Atlantic Ridge when we compare the observed geoid profiles with the theoretical. Furthermore, we cannot use the observed geoid to discriminate between the plate and half-space models, for the differences between these two geoid-age curves are of long wavelength; hence, the differences would be removed with the long-wavelength geoid field.

One possible way to resolve this problem of long wavelengths involves the construction of spherical harmonic expansions of the theoretical geoid or observed altimetry, as Hager [1983] and Cazenave et al. [1986] have tried to do, but our focus on a single ocean basin with relatively high spatial resolution renders this approach impractical. We have instead settled for a qualitative estimate of the effect of removing long wavelengths from the geoid based on ocean floor age.

We fast Fourier-transformed the geoid maps and multiplied each spectral component by a Gaussian high-pass filter weighting of the form  $W(\lambda) = 1 - \exp(-\sigma^2 \pi^2 / \lambda^2)$ . If a weight of  $W(\lambda) < e^{-1}$  is assumed to remove components of that wavelength, as we assumed for our low-pass filter, this high-pass filter effectively removes wavelengths greater than  $\sim 5\sigma$ . Due to the nature of the discrete Fourier transform and the limited size of the geographic region under study, spherical harmonic coefficients are not

equivalent to Fourier spectral harmonics. They behave similarly, however, and in the limit of global coverage are nearly identical [Colombo, 1981].

In Figure 13, we include a profile from a theoretical map that has been high-pass filtered with  $\sigma = 800$  km. As expected, the geoid-age curve flattens out within 500 km of the MAR, marking the distance over which we can reliably compare the observed and theoretical geoids. As a test of this filter, we applied it to the GEM 9 maps themselves and to the original Seasat altimetry map. After filtering, the GEM 9 plots were essentially reduced to low-amplitude noise, implying that our filter does successfully remove long wavelengths. The Seasat altimetry map after filtering looked remarkably like the intermediate-wavelength geoid of Figure 12b. Anomalies were in similar locations and of similar lateral dimensions but their amplitudes were greatly reduced. Since our high-pass filter removes a local, independent estimate of the long-wavelength field from the altimetry and has a very smooth Gaussian form, this similarity in maps confirms our confidence in using the GEM 9 field to remove long wavelengths without creating windowing artifacts.<sup>†</sup>

Even within 500 kilometers of the Mid-Atlantic Ridge, there is much variation in the slope of the geoid. Profile 1 in Fig. 13 is symmetric, 2 and 4 are flatter to the east, and 3 is totally anomalous. Some of this variation along the ridge has been studied by Andrews *et al.* [1986] who ascribe it to small-scale convection beneath the lithosphere. The practically flat geoid over the ridge in profile 3 might have biased Sandwell and Schubert's [1980] average geoid-age relationship towards its

---

<sup>†</sup>Unfortunately, the Seasat altimetry map, and, in fact, most of our maps, contain large unconstrained areas over the continents which contribute substantially to the long-wavelength power in the maps. High-pass filtering, therefore, may not yield reliable quantitative maps; we have tended to avoid its use in obtaining our results.

unusually low value. Because of the extreme variability of the empirical geoid-age relationship, we again fall back on the Parsons and Sclater [1977] plate model to establish our geoid-age reference. This is the standard geoid-age curve used in most other studies. Note, however, that when the geoid-age curves of Figure 13 are high-pass filtered, they are all nearly identical to the one shown.

#### 4.4.5 Residual Geoid Anomalies

If we remove the effects of ocean floor age from the intermediate-wavelength geoid, we obtain the residual geoid. In Figure 14, we have subtracted our reference geoid-age relationship from the geoid map of Figure 11. The geoid high along the Mid-Atlantic Ridge seems finally to have been removed. The four basins are still relative geoid lows, but now the Brazil Basin has elongated to cross the MAR and connect with the western Cape Basin. The Angola Basin is a low isolated in the northeast corner by highs along the Guinea Ridge, over St. Helena, and above the Walvis Ridge. The Argentine Basin is still the major geoid low that dominates the southwestern corner of the map, while the Rio Grande Rise and the plateau surrounding the Columbia seamounts still appear as prominent highs towards the west.

In Figure 14, the residual geoid anomalies appear to form somewhat larger-scale patterns than we have seen up to this point. The chain of geoid lows stretching from the Brazil Basin southeast to the Cape Basin was mentioned above. To the east is a high that stretches from south of the Walvis Ridge northwards through the area surrounding Ascension Island, then connects with the Guinea Ridge high to the east. In the west and south, the geoid highs corresponding to the Columbia seamount swell and the Rio Grande Rise are nearly connected to a small, local plateau near Gough

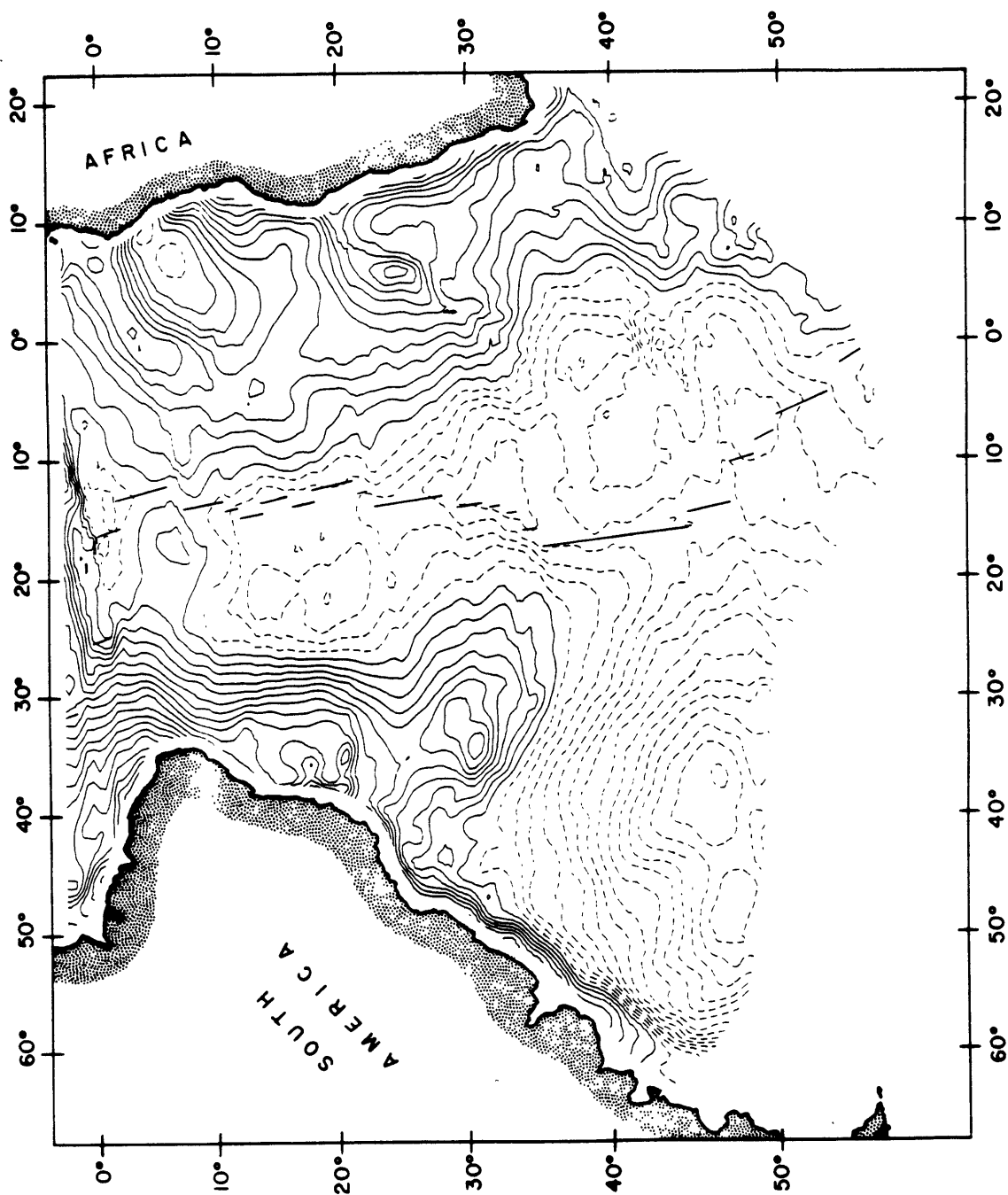


Figure 14. Residual geoid anomaly map of the South Atlantic produced by subtracting a reference theoretical geoid based on seafloor ages from the intermediate-wavelength geoid of Fig. 11. A constant, average value was added to this and subsequent residual anomaly maps to ease their use. The MAR position is shown. The contour interval is 1 m and dashed lines indicate negative residual geoid values.

Island, which in turn merges with a high over the Agulhas Ridge.

Subtle geoid highs of only a meter or two are associated with the possible active hotspots of Ascension Island, St. Helena, Trindade/Martin Vaz, Tristan da Cunha, and Gough. A few fracture zone traces can be detected in this map--for example, over the Ascension FZ, over a major offset north of the Rio Grande FZ, and over the Falkland-Agulhas FZ. A number of the geoid lows in the center of the map may even be bounded by fracture zones.

To see whether these observed patterns are robust or simply artifacts specific to this map and its derivation, we present in Figure 15 two variations on our residual geoid map. The first is simply a smoother version of Figure 14 with a filter half-width of 150 km, while the second was made with a GEM 9 field complete to degree and order 10. Note that Figure 15b, with its GEM 9 field and degree of smoothing, was produced in a manner most commonly used to derive residual geoid anomalies [Watts et al., 1985; Jung and Rabinowitz, 1986a]. Both maps show elongated patterns of lows and highs with characteristic wavelengths of 2000-3000 km stretching north across the South Atlantic. Most of the major features discussed above can be seen. Subtle features, such as the highs over hotspots, are more difficult to observe, however.

One feature common to Figures 14 and 15 is the tendency for the residual geoid to increase in height away from the ridge. This is an effect of the geoid-age correction, since its long-wavelength behavior leading to large geoid anomalies at older ages has not been properly removed. We have proceeded to construct a residual geoid map using our reference geoid-age curve high-pass filtered as described above. Since our filter is somewhat ad hoc and might introduce small artifacts, this map can

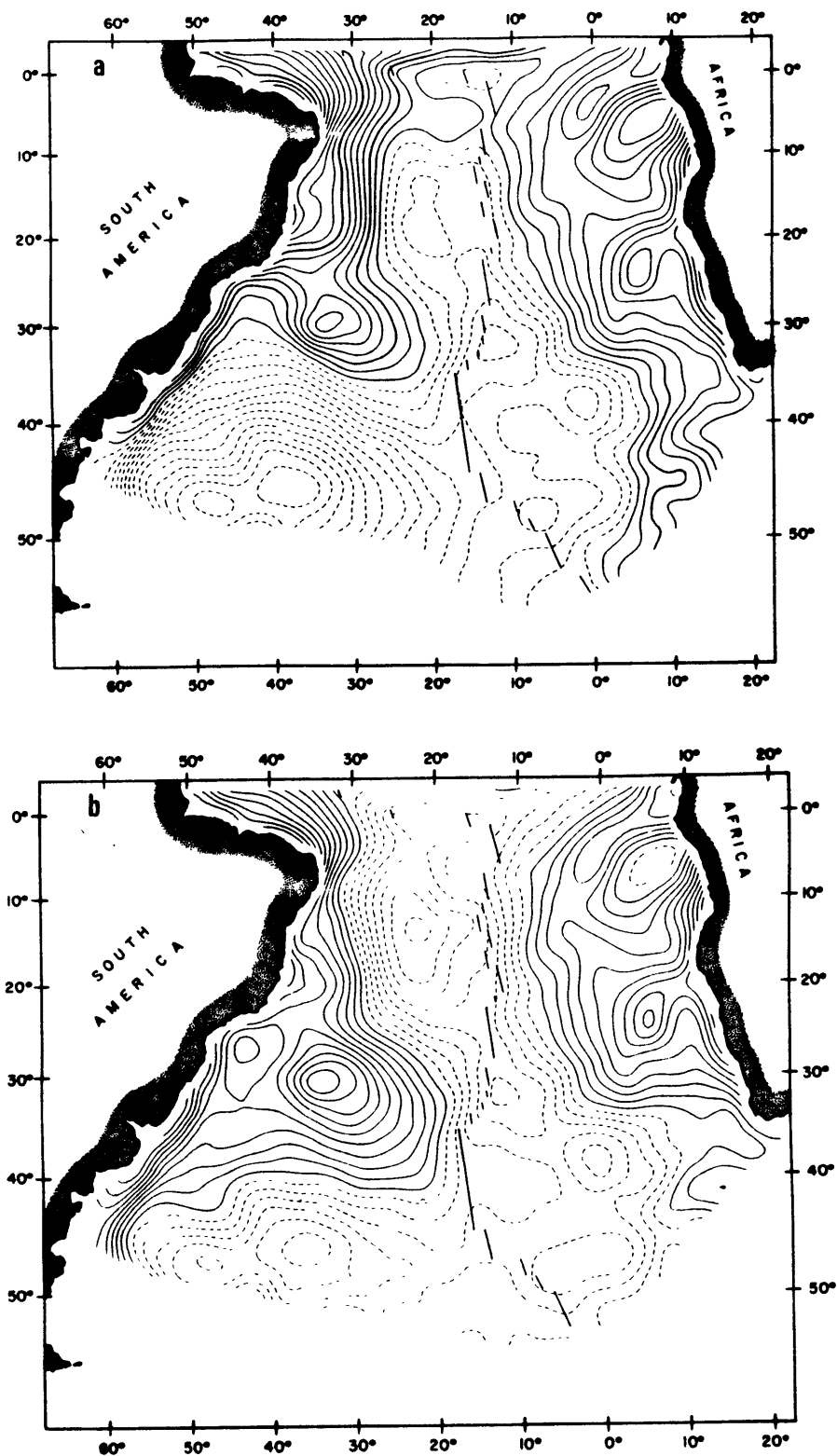


Figure 15. Alternate residual geoid anomaly maps. a) Identical to Fig. 14 but a low-pass filter with half-width of 150 km was used for additional smoothing. b) The GEM 9 field complete to degree and order 10 was used to derive this map, which also was filtered with  $\sigma = 150$  km.

only be used for a qualitative analysis of the residual geoid anomalies. In Figure 16, we see even more vividly the patterns of highs and lows that stretch across the South Atlantic. The aseismic ridges and hotspot locations still correlate with geoid highs, and the basins, even more clearly, with geoid lows.

#### 4.5 Discussion

We can describe correlations between the geoid and the bathymetry in two ways, both of which may shed light on the character of possible mantle convection in the South Atlantic. We first examine the visual correlation of large-scale features in the residual depth and geoid maps (Figs. 7 and 14 or 16).

##### 4.5.1 Visual Correlation

The most obvious features of both maps are indeed well correlated. The Argentine Basin is the dominant low in both the residual depth and geoid. The Rio Grande Rise and the northeast Walvis Ridge are the most prominent highs and have magnitudes similar to each other in both the geoid and depth maps. The swell north of the Columbia seamounts and the high along the Guinea Ridge are also obvious in both maps and appear spatially correlated. The eastern basins do not correlate quite as well, however. The Angola Basin appears broad and extended to the southwest on the residual depth map but quite compact in size in the residual geoid. The Cape Basin exhibits a displacement in the geoid to the west of its bathymetric location. Of the large residual depth anomalies, only the southwestern Walvis Ridge is noticeable for its lack of expression in the geoid.

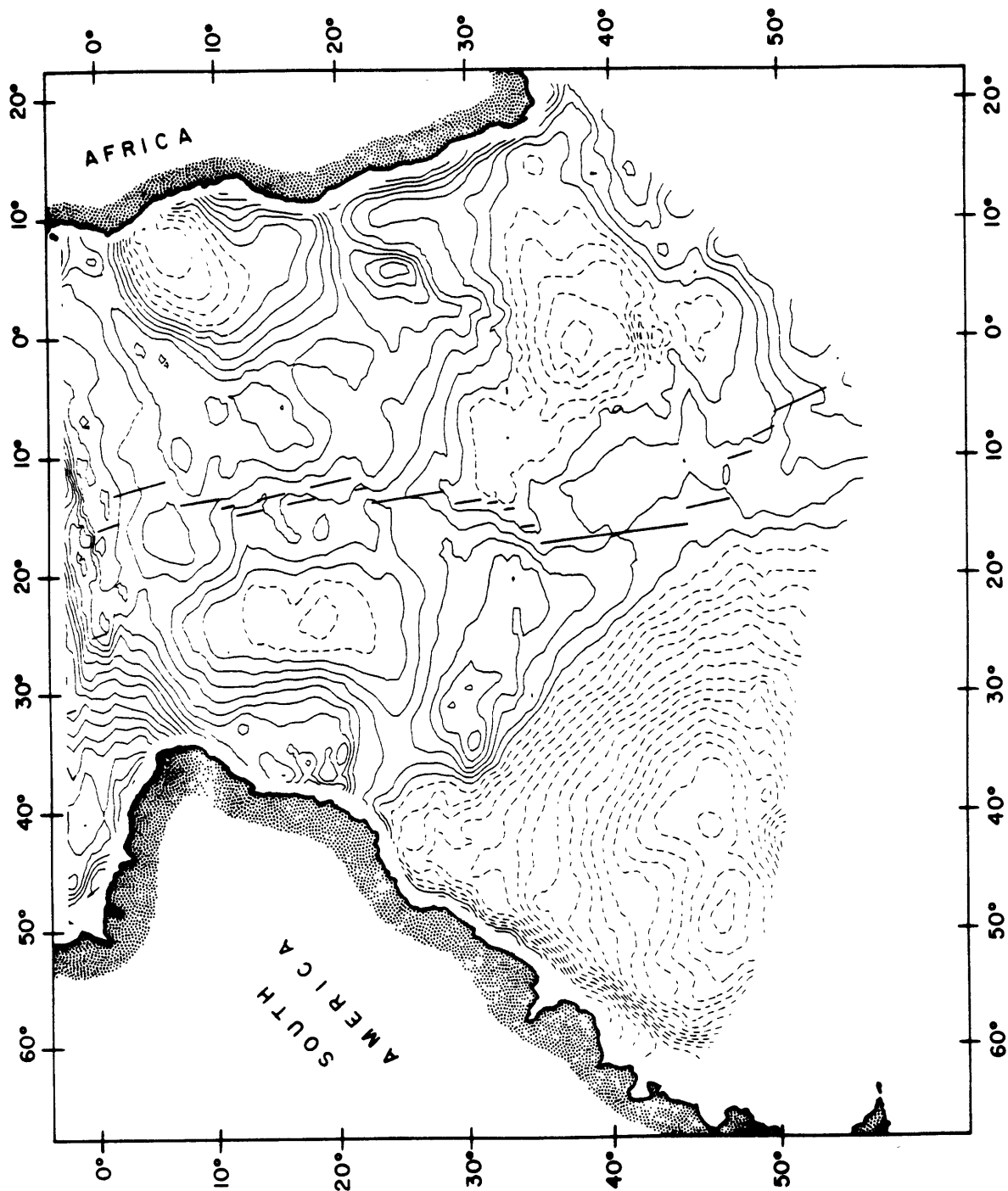


Figure 16. Residual geoid anomaly map made with a theoretical geoid map previously high-pass filtered to remove wavelengths greater than  $\sim 4000$  km. See text for further explanation.

The more subtle patterns which emerge only when the age corrections are made show much more limited correlation. The central band of northwest-southeast trending residual geoid lows does not appear in the residual depths. Instead, a bridge of positive residual depths not reflected in the geoid connects the Rio Grande and Walvis Ridges. The region of relative geoid highs stretching southeast from the Rio Grande Rise (Fig. 16) may be reflected in the bathymetry, where a high to the west of the MAR at 35°S is aligned with highs east of the ridge and west of the Cape Basin at 40°S. The shorter-wavelength geoid highs over hotspot-related islands correlate moderately well with the slight bathymetric highs associated with them.

Overall, the intermediate-wavelength anomalies associated with aseismic ridges, hotspot swells, and deep basins appear well correlated, behavior seen in all oceans. After removing the MAR signal, the residual depth and geoid show an even closer correspondence over those depth highs associated with mid-ocean hotspot-related islands. Curiously, however, the geoid highs associated with St. Helena and Ascension Island fall somewhat north of their bathymetric locations. The Columbia seamount and Guinea Ridge highs are larger than those observed over other hotspots, perhaps indicating a somewhat different thermal origin. The Rio Grande Rise and northern Walvis Ridge both exhibit strong correlated depth and geoid highs unlikely to be produced by purely crustal, constructional features. Some deeper thermal process seems to remain associated with them. On the other hand, the southwestern Walvis Ridge, with its minimal geoid signature, is more likely to be an example of a hotspot-related feature which does not retain any present day thermal anomaly.

The subtle residual geoid anomaly pattern with a characteristic wavelength of 2000–3000 km bears a resemblance to the pattern of elongated geoid anomalies seen in the Pacific by Marsh and Marsh [1976], McKenzie et al. [1980], and Watts et al. [1985]. These anomalies are aligned in the direction of absolute motion of the Pacific plate. Since plate motions are much slower in the South Atlantic [Minster and Jordan, 1978], such an alignment would not necessarily be required. That these anomalies are truly evidence of mantle convection is uncertain and contested, however [Watts et al., 1985; Sandwell and Kenkin, 1986].

The asymmetry across the Mid-Atlantic Ridge, present in the first depth and geoid maps, remains in the final residual plots. Both the depth and geoid exhibit more negative average values west of the MAR than east. We can posit a number of processes that could produce such an asymmetry. Thicker or lighter crust east of the MAR would result in shallower seafloor and a slightly higher geoid on that flank of the ridge. Lithosphere that cools more slowly east of the ridge than west of it would likewise produce shallower depths and a higher geoid level east of the ridge. If crustal structure and lithospheric cooling are both symmetric across the MAR, the apparent asymmetry might be an effect of a longer-wavelength thermal anomaly in the upper mantle which we observe superimposed on the large-amplitude processes of lithospheric cooling and hotspot volcanism.

Ultimately, a truly ocean-wide asymmetry would need to be the result of large-scale nonuniform geophysical behavior within the earth. Variations in mantle convective regime (such as the depth or vigor of convection), or of bulk geochemical parameters (such as the level of depletion of mantle material) might possibly explain the observed asymmetry. Our study alone cannot resolve the source of this asymmetry,

however, or even if it is real and not an artifact of the random placement of large-magnitude features.

#### 4.5.2 Quantitative Correlation

We can also evaluate the importance of convection in the South Atlantic by examining the depth-geoid relationship quantitatively. A full admittance analysis, such as those of McKenzie and Bowin [1976], Sandwell and Poehls [1980], and Cazenave *et al.* [1986], where individual wavelengths are examined, is beyond the scope of this investigation. But we can estimate the magnitudes of the depth-geoid slopes in a simpler manner and compare them to theoretical models.

If geoid anomalies are a result of crustal density variations, their shallow compensation depths suggest a small ratio of geoid to topography. Local or regional compensation occurring at the Moho leads to geoid/depth slopes of less than 2 m/km, unless the lithosphere is extremely rigid [McKenzie and Bowin, 1976; Haxby and Turcotte, 1978]. Compensation of depth variations deep within or below the lithosphere leads to geoid/depth ratios of  $\sim 6$  m/km [Crough, 1978; Parsons and Daly, 1983].

We can describe the geoid/depth slope that is produced by simple physical models through the use of a wave number domain filter. For a near-surface mass confined to a single plane at depth  $t_0$  and an isostatically compensating mass layer at depth  $t_1$ , the expected ratio of geoid height to depth anomaly is [e.g. Crough, 1978]

$$\frac{N(k)}{d(k)} = \frac{2\pi G}{g_0 k} (\rho_c - \rho_w) \exp(-kt_0) [1 - \exp(-kt_1)] \quad (15)$$

where  $k = 2\pi/\lambda$ . At long wavelengths (or as  $k \rightarrow 0$ ), this reduces to

$$\frac{N}{d} = \frac{2\pi G}{g_0} (\rho_c - \rho_w) t_1 \quad (16).$$

Thus the geoid/depth relationship at long wavelengths is linear, with a slope proportional to the average depth of compensation. For  $N$  in meters, and  $d$ ,  $t_1$  in kilometers, using the parameter values from Table 1,

$$t_1 \approx 13 \times N/d \quad (17).$$

In the space domain of our maps, we are not dealing solely with long-wavelength features. For shorter wavelengths, the magnitude of the constant in (17) is reduced. Much of this shorter-wavelength topography is produced by features such as islands, seamounts, and aseismic ridges with shallower mean depths. Thus there is a tendency for the slope of the geoid/depth curve to decrease at shallower depths. Similar behavior, a decrease in slope at shallower depths, is in fact predicted for the geoid to depth ratio expected even at longer wavelengths by models of lithospheric reheating [Crough, 1978] and mantle convection [Parsons and Daly, 1983]. But these effects are, for the most part, small and to first order equation (17) should be a reasonable approximation. Sandwell and Renkin [1986] suggest filtering the depth and geoid to remove the shorter wavelengths, however, thus avoiding the worst of the nonlinear terms in the expansion of (15).

We have subdivided our maps of corrected depth and geoid (Figs. 4 and 11) into rectangular regions over a few major features (shown in Figure 17). For each region, we produced a scatter plot of geoid versus depth using each grid point. Since we had previously smoothed our maps, there is some correlation between adjacent points due to our filtering. These scatter plots are shown in Figure 18 for the regions containing the Rio Grande Rise, Argentine Basin, and the Columbia seamounts in the west, and the northern Walvis Ridge, southern Walvis Ridge, and Ascension FZ/Guinea Ridge in the east. We also tried smoothing our maps to remove wavelengths

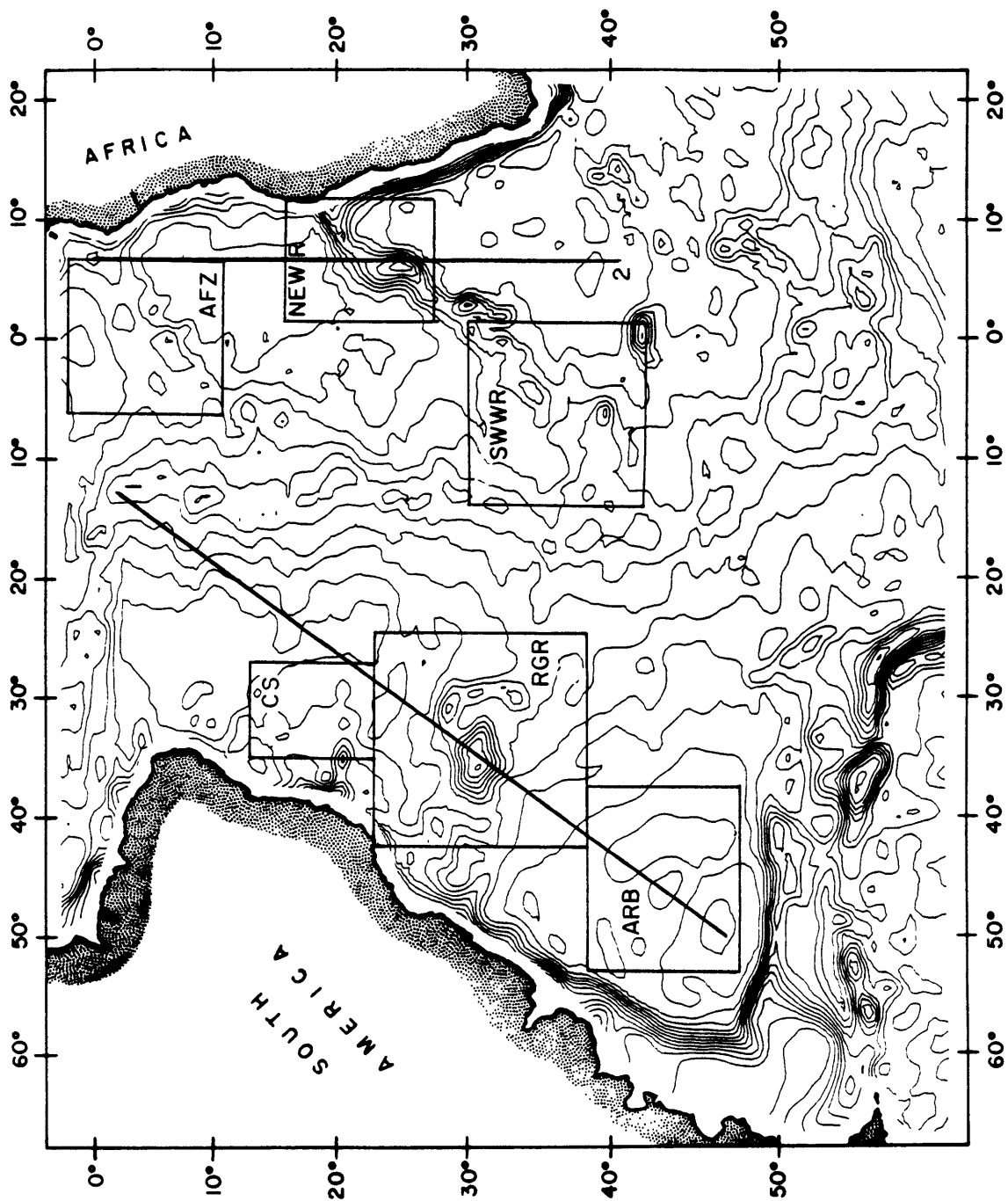


Figure 17. Map of sediment-corrected depths (as in Fig. 4) showing the regions from which we obtain the scatter plots of Figure 18. Also indicated are the positions of the profiles shown in Figure 20.

greater than 600 km, as Sandwell and Renkin [1986] suggest, but edge effects due to the nearby continents interfere with the primary features of interest. Since it is unclear which of our data sets is better known, we have computed least-squares regression line fits to the data using both the depth and geoid as the independent variable.

In all the plots of Figure 18 the data are quite scattered and precise slopes cannot be obtained, but the variations in trend from feature to feature seem clear-cut. The shallowest geoid/depth slopes appear over the Rio Grande Rise and northeastern Walvis Ridge, with slopes of 2-4 m/km and 1-3 m/km, respectively. These correspond to compensation depths of ~10-50 km. Somewhat larger slopes appear for the southwest Walvis Ridge (3-5 m/km) and the Ascension FZ (4-6 m/km) that suggest compensation depths of ~40-70 km. The steepest slopes seem to occur over the Columbia seamount swell (4-9 m/km) and the Argentine Basin (6-9 m/km). These correspond to compensation depths of up to 100 km or greater.

Only the Rio Grande Rise and northern Walvis Ridge have slopes consistent with shallow compensation at the Moho or in the upper lithosphere. That these aseismic ridges exhibit shallow slopes is not surprising, since a number of studies have found Airy compensation to be the prime isostatic support mechanism for these features [Detrick and Watts, 1979; Bulot *et al.*, 1984]. As for the other features that we have examined, their large geoid/depth ratios imply that either lower lithospheric thermal perturbations or mantle convection, which are mutually related [Parsons and Daly, 1983], provide a substantial portion of their compensation.

An alternative method for understanding the depth-geoid relationship and computing compensation depth is to use formulae such as (15) as filters

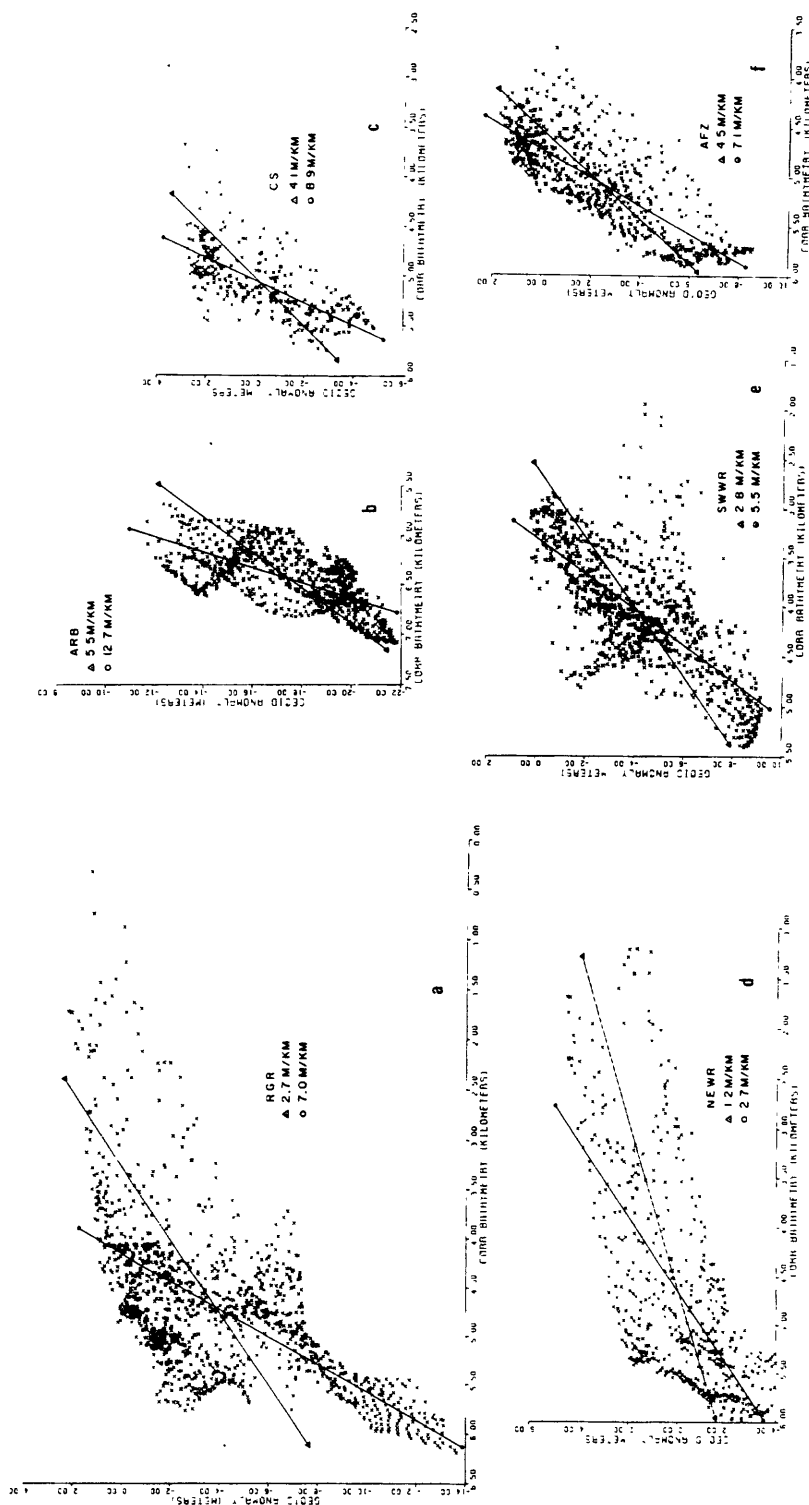


Figure 18. Scatter plots of corrected geoid (Fig. 11) versus corrected depth (Fig. 4) for the regions shown in Figure 17: a) Rio Grande Rise, b) Argentine Basin, c) Columbia seamount swell, d) northeastern Walvis Ridge, e) southwestern Walvis Ridge, and f) Ascension FZ/Guinea Ridge. Also shown are the least squares regression line fits assuming that either the depth (triangles) or geoid (circles) is the independent variable. The slopes are labelled on the figures.

to predict the geoid from the bathymetry (similar to the techniques of Chapter 2). Imagine the simplified physical model of the lithosphere shown in Figure 19, where the topography is compensated by a local, Airy mechanism at two different depths. The bathymetry with height  $d$  and depth  $t_d$  is partially compensated by a deflection of the Moho by an amount  $s$  at depth  $t_s = t_d + t_c$ , where  $t_c$  is the thickness of the crust. The remainder of the surface load is compensated deep in the lithosphere by the deflection of a small density interface by amount  $r$  at depth  $t_r = t_d + t_c + t_\ell$ , where  $t_\ell$  is the depth of the compensating mass plane beneath the Moho. We set  $s = \gamma d$ , thereby varying the mode of compensation. When  $\gamma = +1$ , all the compensation for both the topography and the upwardly deflected Moho occurs at depth  $t_r$ , when  $\gamma = 0$ , only the topographic mass is compensated at depth (i.e. there is no Moho deflection), and when  $\gamma = (\rho_\ell - \rho_w) / (\rho_c - \rho_\ell)$  (where  $\rho_\ell$  is the density of the lithosphere above  $t_r$ ), all the compensation occurs at the Moho as in normal crustal Airy compensation. For  $\gamma$  in between these values, compensation is split between the shallow and deeper regimes. Our simple model ignores the rigidity of the lithosphere which others have considered in more detail [e.g. McNutt, 1983; McNutt and Shure, 1986].

The filter corresponding to this physical model is given by

$$\frac{N(k)}{d(k)} = \frac{2\pi G}{g_0 k} \exp(-kt_d) \{ (\rho_c - \rho_w) + \gamma(\rho_\ell - \rho_c) \exp(-kt_c) - [\gamma(\rho_\ell - \rho_c) + (\rho_c - \rho_w)] \times \exp[-k(t_c + t_\ell)] \} \quad (18).$$

Since Airy compensation is assumed, the density difference  $\Delta\rho$  across the interface at  $t_r$  does not explicitly enter (18). It does determine the actual size of the root  $r$ , however, since

$$r = d [\gamma(\rho_\ell - \rho_c) + (\rho_c - \rho_w)] / \Delta\rho \quad (19).$$

For either chemical or thermal variations within the lithosphere, a

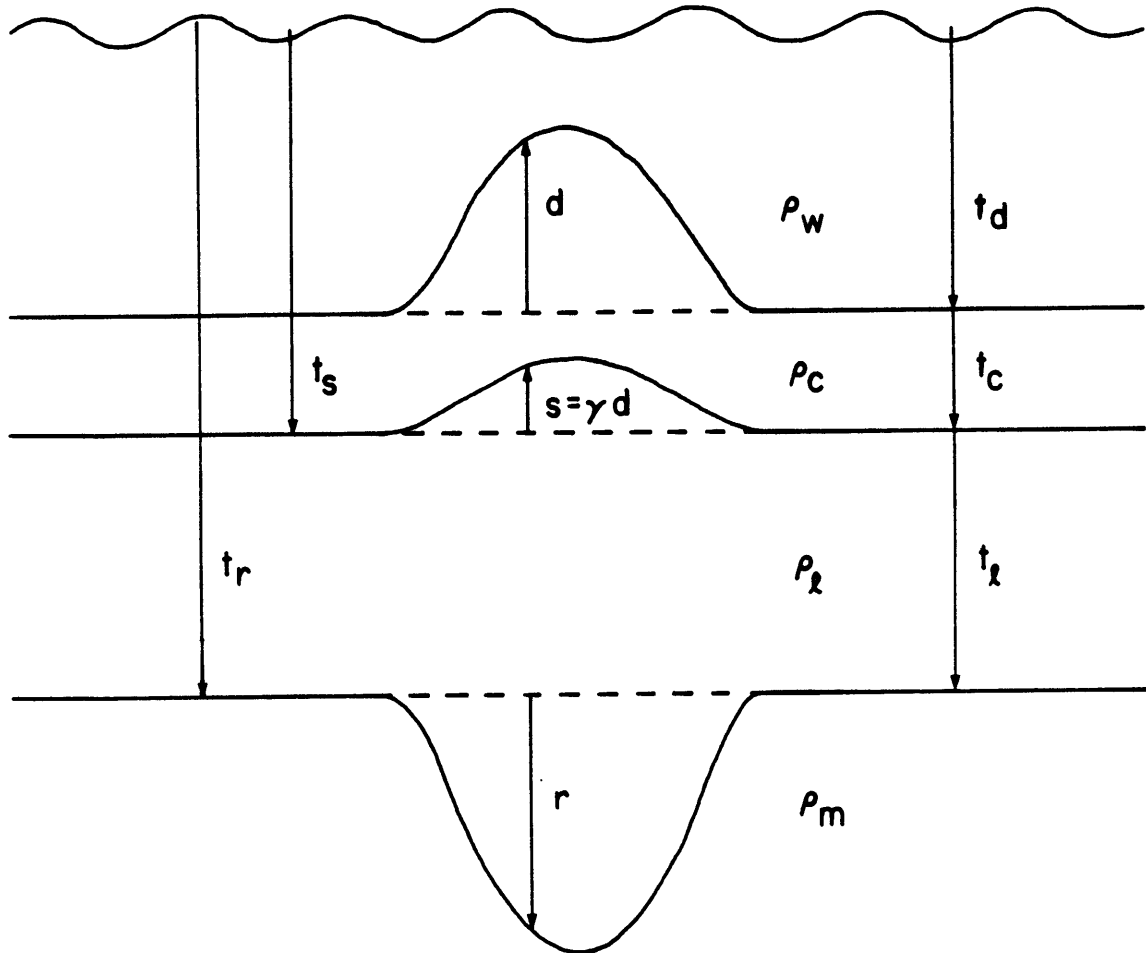


Figure 19. Simplified model for Airy compensation of bathymetry at the crust-mantle interface and/or deeper in the lithosphere. See text for further description.

reasonable range of values is  $\Delta\rho \sim 50\text{--}80 \text{ kg/m}^3$ . Other parameter values that we use are listed in Table 1.

By Fourier transforming the corrected depth map (Figure 4), multiplying by equation (18), and inverse transforming, we produced maps of the geoid predicted from the bathymetry. We have selected 2 profiles from these maps, whose positions are shown in Figure 17, to present in Figure 20.

Profile 1 extends from the Argentine Basin in the south to the Mid-Atlantic Ridge in the north, crossing over both the Rio Grande Rise and the Brazil Basin. The shape of the geoid profile from the Argentine Basin to the Rio Grande Rise bears more resemblance to that produced by compensating masses at depths of 45-60 km than by crustal thickening. The Rio Grande Rise, however, does not exhibit the large peak-to-peak amplitudes expected for such deep compensation; rather, an intermediate compensation depth ( $\sim 25$  km) or partial compensation (50% at 60 km depth, 50% at the Moho) appears more appropriate. The Brazil Basin geoid profile again seems to parallel more closely those profiles predicted for deep compensation.

Profile 2 runs from the Guinea Ridge in the north across the Angola Basin, over the top of the northern Walvis Ridge, and ends in the middle of the Cape Basin. The Guinea Ridge geoid clearly parallels that predicted for deep compensation, but the rest of the profile is more confusing. The observed Walvis Ridge geoid is much wider than expected from the bathymetry. The peak-to-peak amplitude of the ridge is clearly less than the amplitude predicted for deep compensation; on the other hand, crustal thickening does not seem adequate to explain the broad Walvis Ridge anomaly, either.

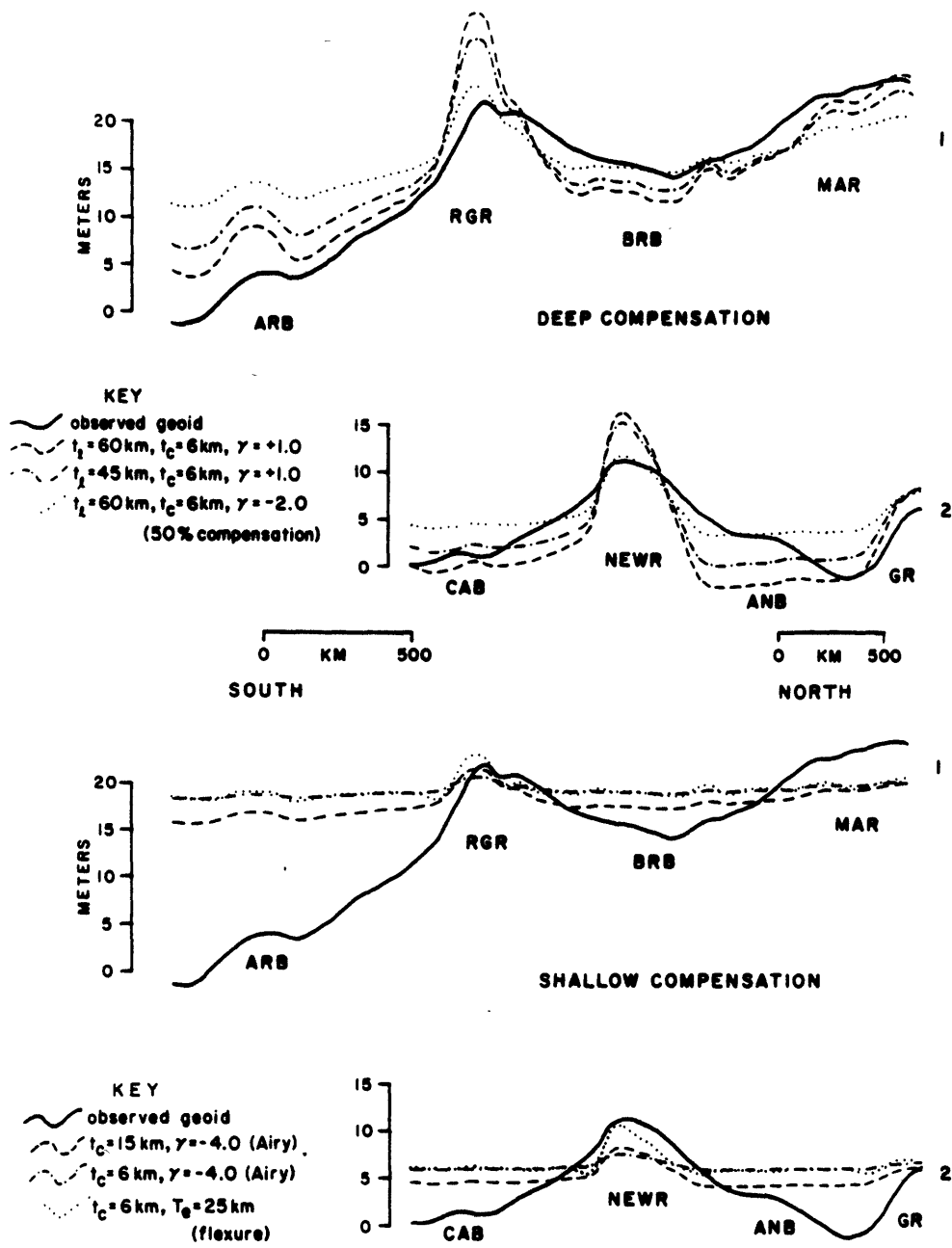


Figure 20. Comparison of the observed geoid (Fig. 11) with the geoid predicted from corrected depths (Fig. 4) for a variety of compensation mechanisms. The positions of the profiles are shown in Figure 17. The compensation mechanisms include: deep compensation ( $t_l = 60 \text{ km}, 45 \text{ km}$ ); 50% deep, 50% shallow compensation ( $t_l = 60 \text{ km}, \gamma = -2.0$ ); Airy compensation for a thick ( $t_c = 15 \text{ km}$ ) and normal ( $t_c = 6 \text{ km}$ ) crust; and flexure of the lithosphere with an effective elastic thickness ( $T_e$ ) of 25 km (see Chapter 2). Note that the mean geoid height for each profile is arbitrary and was chosen so the profiles would conveniently overlay.

Both the scatter plots and forward modeling imply that deep density variations exist under many, if not all, of the intermediate-wavelength depth and geoid anomalies in the South Atlantic. For the two aseismic ridges, some combination of shallow and deeper compensation may be appropriate. The evidence for other swells and basins suggests more strongly that their compensating density anomalies occur at depths in the lower lithosphere or upper mantle.

In conclusion, we do find evidence for convection in the mantle beneath the South Atlantic Ocean. The large-scale pattern of residual geoid and depth anomalies is highly suggestive of the pattern in the Pacific ascribed to convective rolls beneath the lithosphere. The large geoid/depth ratios and observed geoid profiles associated with many of the residual highs and lows are characteristic of deep thermal anomalies in the lower lithosphere or upper mantle. Finally, the asymmetric pattern across the South Atlantic seen consistently in the depth and geoid maps implies that some process other than the symmetric thermal evolution of the lithosphere is occurring over wide areas. Convection within the upper mantle is one likely process.

#### 4.6 Acknowledgements

We thank D. Divins for providing us with a map of South Atlantic sediment thicknesses in advance of publication, and S. Cande for his digital age data in the South Atlantic. M. McNutt, A. Watts, and J. Phipps-Morgan critically reviewed this manuscript and made many constructive suggestions. This research has been supported by the Office of Naval Research under contract #N00014-86-K-0325.

## 4.7 References

- Anderson, R.N., D. McKenzie, and J.G. Sclater, Gravity, bathymetry, and convection in the earth, Earth Planet. Sci. Lett., 18, 391-407, 1973.
- Andrews, J.A., W.F. Haxby, and W.R. Buck, Regional variations along ridge crests: geoid height, depth to ridge crest, and geoid height-age relationship (abstract), EOS Trans. Am. Geophys. Un., 67, 356, 1986.
- Angevine, C.L., and D.L. Turcotte, Correlation of geoid and depth anomalies over the Agulhas Plateau, Tectonophysics, 100, 43-52, 1983.
- Baker, P.E., Islands of the South Atlantic, in The Ocean Basins and Margins, Vol. 1, The South Atlantic, A.E.M. Nairn and F.G. Stehli, eds., pp. 493-553, Plenum Press, New York, 1973.
- Bowin, C., Depth of principal mass anomalies contributing to the earth's geoidal undulations and gravity anomalies, Mar. Geodesy, 7, 61-100, 1983.
- Bowin, C., G. Thompson, J.G. Schilling, Residual geoid anomalies in Atlantic Ocean basin: relationship to mantle plumes, J. Geophys. Res., 89, 9905-9918, 1984.
- Buck, W.R., and E.M. Parmentier, Convection beneath young oceanic lithosphere: Implications for thermal structure and gravity, J. Geophys. Res., 91, 1961-1974, 1986.
- Brozena, J.M., Temporal and spatial variability of seafloor spreading processes in the northern South Atlantic, J. Geophys. Res., 91, 497-510, 1986.
- Bulot, A., M. Diament, M.G. Kogan, and J. Dubois, Isostasy of aseismic tectonic units in the South Atlantic Ocean and geodynamic implications, Earth Planet. Sci. Lett., 70, 346-354, 1984.
- Cande, S.C., W.F. Haxby, J.L. LaBrecque, W.C. Pitman III, R.L. Larson, and X. Golovchenko, Age of the ocean floor: a new 5' gridded data base (abstract), EOS Trans. Am. Geophys. Un., 65, 1082, 1984.
- Cazenave, A., Thermal cooling of the oceanic lithosphere: new constraints from geoid height data, Earth Planet. Sci. Lett., 70, 395-406, 1984.
- Cazenave, A., K. Dominh, C.J. Allegre, and J.G. Marsh, Global relationship between oceanic geoid and topography, J. Geophys. Res., 91, 11,439-11,450, 1986.
- Cazenave, A., B. Lago, and K. Dominh, Thermal parameters of the oceanic lithosphere estimated from geoid height data, J. Geophys. Res., 88, 1105-1118, 1983.
- Cochran, J.R. and M. Talwani, Free-air gravity anomalies in the world's oceans and their relationship to residual elevation, Geophys. J. R. Astron. Soc., 50, 495-552, 1977.

- Cochran, J.R. and M. Talwani, Gravity anomalies, regional elevation, and the deep structure of the North Atlantic, J. Geophys. Res., 83, 4907-4924, 1978.
- Colombo, O.L., Numerical methods for harmonic analysis on the sphere, Rept. #310, Dept. Geodetic Sci., Ohio State Univ., Columbus, Ohio, 1981.
- Craig, C.H., and D. McKenzie, The existence of a thin low-viscosity layer beneath the lithosphere, Earth Planet. Sci. Lett., 78, 420-426, 1986.
- Crough, S.T., Thermal origin of mid-plate hot-spot swells, Geophys. J. R. Astron. Soc., 55, 451-469, 1978.
- Crough, S.T., Geoid anomalies across fracture zones and the thickness of the lithosphere, Earth Planet. Sci. Lett., 44, 224-230, 1979.
- Crough, S.T., Geoid anomalies over the Cape Verde Rise, Mar. Geophys. Res., 5, 263-271, 1982.
- Davis, E.E. and C.R.B. Lister, Fundamentals of ridge crest topography, Earth Planet. Sci. Lett., 21, 405-413, 1974.
- DBDB5, Worldwide gridded bathymetry, Announc. 85-MGG-01, National Geophysical Data Center, Boulder, Colorado, 1985.
- Detrick, R.S., Jr., An analysis of geoid anomalies across the Mendocino fracture zone: implications for thermal models of the lithosphere, J. Geophys. Res., 86, 11,751-11,762, 1981.
- Detrick, R.S., R.P. Von Herzen, B. Parsons, D. Sandwell, and M. Dougherty, Heat flow observations on the Bermuda Rise and thermal models of mid-plate swells, J. Geophys. Res., 91, 3701-3723, 1986.
- Detrick, R.S. and A.B. Watts, An analysis of isostasy in the world's oceans 3. Aseismic ridges, J. Geophys. Res., 84, 3637-3653, 1979.
- Divins, D.L. and P.D. Rabinowitz, Total sediment thickness map for the South Atlantic Ocean, in International Geological and Geophysical Atlas of the Atlantic Ocean, G. Udintsev, ed., in press, 1986.
- Driscoll, M.L., and B. Parsons, Cooling of the oceanic lithosphere: evidence from geoid anomalies across the Udintsev and Eltanin fracture zone system, Earth Planet. Sci. Lett., submitted, 1987.
- Emery, K.O. and E. Uchupi, The Geology of the Atlantic Ocean, 1050 pp., Springer-Verlag, New York, N.Y., 1984.
- GEBCO (General Bathymetric Chart of the Oceans), Canadian Hydrographic Service, Ottawa, Canada, 1978.
- Hager, B.H., Global isostatic geoid anomalies for plate and boundary layer models of the lithosphere, Earth Planet. Sci. Lett., 63, 97-109, 1983.

- Haxby, W.F. and D.L. Turcotte, On isostatic geoid anomalies, J. Geophys. Res., 83, 5473-5478, 1978.
- Haxby, W.F., and J.K. Weissel, Evidence for small-scale mantle convection from Seasat altimeter data, J. Geophys. Res., 91, 3507-3520, 1986.
- Heestand, R.L. and S.T. Crough, The effect of hot spots on the oceanic age-depth relation, J. Geophys. Res., 86, 6107-6114, 1981.
- Jung, W.-Y., and P.D. Rabinowitz, Residual geoid anomalies of the North Atlantic Ocean and their tectonic implications, J. Geophys. Res., 91, 10,383-10,396, 1986a.
- Jung, W.Y. and P.D. Rabinowitz, Residual depth and residual geoid anomalies of the South Atlantic Ocean (abstract), EOS Trans. Am. Geophys. Un., 67, 1229, 1986b.
- Kogan, M.G., M. Diament, A. Bulot, and G. Balmino, Thermal isostasy in the South Atlantic Ocean from geoid anomalies, Earth Planet. Sci. Lett., 74, 280-290, 1985.
- Ladd, J.W., South Atlantic seafloor spreading and Caribbean tectonics, Ph.D. thesis, 251 pp., Columbia Univ., New York, 1974.
- Le Douaran, S. and B. Parsons, A note on the correction of ocean floor depths for sediment loading, J. Geophys. Res., 87, 4715-4722, 1982.
- Lerch, F.J., S.M. Klosko, R.E. Laubscher, and C.A. Wagner, Gravity model improvement using Geos 3 (GEM 9 and 10), J. Geophys. Res., 84, 3897-3916, 1979.
- Marsh, B.D., and J.G. Marsh, On global gravity anomalies and two-scale mantle convection, J. Geophys. Res., 81, 5267-5280, 1976.
- McKenzie, D.P., Some remarks on heat flow and gravity anomalies, J. Geophys. Res., 72, 6261-6273, 1967.
- McKenzie, D.P., Surface deformation, gravity anomalies, and convection, Geophys. J. R. Astron. Soc., 48, 211-238, 1977.
- McKenzie, D. and C. Bowin, The relationship between bathymetry and gravity in the Atlantic Ocean, J. Geophys. Res., 81, 1903-1915, 1976.
- McKenzie, D.P., J.M. Roberts, and N.O. Weiss, Convection in the earth mantle: towards a numerical simulation, J. Fluid Mech., 62, 465-538, 1974.
- McKenzie, D., A. Watts, B. Parsons, and M. Roufousse, Planform of mantle convection beneath the Pacific Ocean, Nature, 288, 442-446, 1980.
- McNutt, M., Implications of regional gravity for state of stress in the earth's crust and upper mantle, J. Geophys. Res., 85, 6377-6396, 1980.

- McNutt, M.K., Influence of plate subduction on isostatic compensation in northern California, Tectonics, 2, 399-415, 1983.
- McNutt, M., Thermal and mechanical properties of the Cape Verde Rise, J. Geophys. Res., submitted, 1986.
- McNutt, M. and K. Fischer, The South Pacific superswell, Earth Planet. Sci. Lett., submitted, 1986.
- McNutt, M.K. and L. Shure, Estimating the compensation depth of the Hawaiian swell with linear filters, J. Geophys. Res., 91, 13,915-13,923, 1986.
- Minster, J.B. and T.H. Jordan, Present-day plate motions, J. Geophys. Res., 83, 5331-5354, 1978.
- Morgan, W.J., Hotspot tracks and the opening of the Atlantic and Indian Oceans, in The Sea, Vol. 7, The Oceanic Lithosphere, C. Emiliani, ed., pp. 443-487, John Wiley and Sons, New York, 1981.
- Parsons, B., J. Cochran, S. Le Douaran, D. McKenzie, and M. Roufousse, Geoid and depth anomalies in the Atlantic Ocean (abstract), EOS Trans. Am. Geophys. Un., 64, 676, 1983.
- Parsons, B. and S. Daly, The relationship between surface topography, gravity anomalies, and temperature structure of convection, J. Geophys. Res., 88, 1129-1144, 1983.
- Parsons, B. and F.M. Richter, A relation between the driving force and geoid anomaly associated with mid-ocean ridges, Earth Planet. Sci. Lett. 51, 445-450, 1980.
- Parsons, B. and J.G. Sclater, An analysis of the variation of ocean floor bathymetry and heat flow with age, J. Geophys. Res., 82, 803-827, 1977.
- Rabinowitz, P.D. and J. LaBrecque, The Mesozoic South Atlantic Ocean and evolution of its continental margins, J. Geophys. Res., 84, 5973-6002, 1979.
- Rapp, R.H., A summary of the results from the OSU analysis of Seasat altimeter data, Rept. #335, Dept. Geodetic Sci. Surv., Ohio State Univ., Columbus, Ohio, 1982.
- Robinson, E.M., B. Parsons and S.F. Daly, The effect of a shallow low viscosity zone on the apparent compensation of mid-plate swells, Earth Planet. Sci. Lett., in press, 1987.
- Roufousse, M., B. Parsons, D. McKenzie, and A.B. Watts, Geoid and depth anomalies in the Indian Ocean (abstract), EOS Trans. Am. Geophys. Un., 62, 389, 1981.

- Sandwell, D.T. and M.L. Renkin, Compensation of swells and plateaus in the North Pacific: no direct evidence for mantle convection, J. Geophys. Res., submitted, 1986.
- Sandwell, D. and G. Schubert, Geoid height versus age for symmetric spreading ridges, J. Geophys. Res., 85, 7235-7241, 1980.
- Sandwell, D.T. and G. Schubert, Geoid height-age relation from Seasat altimeter profiles across the Mendocino fracture zone, J. Geophys. Res., 87, 3949-3958, 1982.
- Schroeder, W., The empirical age-depth relation and depth anomalies in the Pacific Ocean basin, J. Geophys. Res., 89, 9873-9883, 1984.
- Sclater, J.G., and P.A.F. Christie, Continental stretching: an explanation of the post-mid-Cretaceous subsidence of the Central North Sea basin, J. Geophys. Res., 85, 3711-3739, 1980.
- Sclater, J.G., L. Lawver, and B. Parsons, Comparison of long-wavelength residual elevation and free air gravity anomalies in the North Atlantic and possible implications for the thickness of the lithospheric plate, J. Geophys. Res., 80, 1031-1052, 1975.
- SYNBAPS, Synthetic bathymetric profiling system, Announc. 81-MGG-14, National Geophysical Data Center, Boulder, Colorado, 1981.
- Watts, A.B., and S.F. Daly, Long wavelength gravity and topography anomalies, Ann. Rev. Earth Planet. Sci., 9, 415-448, 1981.
- Watts, A.B., D.P. McKenzie, B. Parsons and M. Rofosse, The relationship between gravity and bathymetry in the Pacific Ocean, Geophys. J. R. Astron. Soc., 83, 263-298, 1985.

## Chapter 5. Summary and Conclusions

### 5.1 Seamounts and Compensation Studies

In Chapter 2, we demonstrated the power of two-dimensional mapping of the gravity field derived from Seasat altimetry for the purpose of determining the compensation mechanisms of a seamount province. The flexibility to incorporate diverse types of compensation mechanisms -- local or regional, shallow or deep -- in the frequency domain filters used to predict the gravity from the bathymetry allows one to quantify the range of crustal and lithospheric parameters that could produce the observed gravity field. Regional variations in compensation mechanisms due to small-scale variations in crustal or lithospheric structure can readily be seen. The use of two-dimensional maps serves to magnify the effects of parameter changes relative to the effects of these changes on profiles of the gravity field.

In small-scale, short-wavelength studies of local compensation mechanisms, the spatial coverage of the satellite altimetry and the bathymetry obtained from surface ships is most critical. The techniques demonstrated in Chapter 2 are only useful where the bathymetry is known at least as well as the geoid. Unfortunately, this tends to occur in areas already thoroughly studied. As we have seen in the Musicians seamount region, two-dimensional studies are often only supplementary to earlier investigations of compensation performed in one dimension. Yet we have also seen how this supplemental study can reveal details overlooked in the earlier work.

For the foreseeable future, two-dimensional techniques will be limited by the availability of high-resolution bathymetry. Where such data exist, primarily over well studied seamount provinces, island chains, and hotspot swells in the North Atlantic and Pacific, two dimensional compensation

studies should be very revealing. A similar technique, incorporating deeper thermal compensation within the lithosphere as well as its flexural rigidity and shallow compensation at the Moho, is already in use by McNutt and Shure [1986] and Fischer et al. [1986] for well surveyed island chains atop mid-ocean swells. These are somewhat longer-wavelength features than seamounts, so gaps in the bathymetry are not quite as critical for this analysis.

The future of satellite altimetry fortunately looks promising. The combination of Seasat data with the altimetry from GEOS 3 provides substantially better coverage than Seasat altimetry alone. Though less accurate, the GEOS 3 data can be constrained by nearby Seasat arcs and can provide sea surface height information within the gaps of the Seasat coverage [Rapp, 1986]. In the Musicians seamount area, the addition of GEOS 3 altimetry enables the study of seamounts that were missed by the Seasat data alone [R. Rapp, personal communication, 1986].

The estimation of compensation mechanisms for submarine features and their regional variations are ultimately useful for studying the tectonic history of a particular area, e.g. the age or strength of the lithosphere when bathymetric loads were emplaced. Thus areas with more complex or less certain tectonic histories will stand to benefit more from studies similar to that in Chapter 2. In particular, the complex history of the western Pacific could benefit greatly from two-dimensional compensation studies if the bathymetric coverage is adequate.

## 5.2 South Atlantic Fracture Zones and the Surrounding Lithosphere

At first glance, the low values of the lithospheric plate thickness at young ages obtained by our study of the geoid step across fracture zones in

the South Atlantic in Chapter 3 and similar studies in the South Pacific seem to imply that the standard 100–125 km plate thickness determined by Parsons and Sclater [1977] may not be valid globally. Yet at least two observations suggest that this conclusion should not be drawn so hastily. The fracture zone geoid data themselves indicate that odd thermal effects may be occurring at ages greater than 30 Ma, and the depth maps available for the South Atlantic do not show the pronounced flattening with age that would be expected for a thin lithospheric plate.

Both small-scale convection beneath the lithosphere and short-wavelength bathymetry on the ocean floor are capable of producing the observed geoid anomalies. Ruling out the bathymetry as the source of these anomalies is by far easier than ruling out small-scale convection, but detailed high-resolution bathymetric and seismic surveys are needed at many locations along the fracture zones. This surface ship data may take many years to collect; numerous surveys of this sort have already occurred in the North Atlantic, however [e.g. Cormier, et al., 1984]. Unfortunately, due to the rougher bathymetry and the closer spacing of fracture zones in the North Atlantic, geoid studies across the well surveyed fracture zones are more difficult. Nevertheless, they should be attempted, as the increased ship data will surely mitigate the additional geoidal complexities.

In the Pacific, much of the short-wavelength geoid and gravity field are produced by seamounts (making possible studies such as that in Chapter 2). In the Atlantic, however, more of the short-wavelength signal is caused by topography associated with fracture zones and the rougher bathymetric texture associated with slower spreading ridges. Geoid and gravity maps like those in Chapter 3 show a wealth of small-scale features,

but without constraining bathymetry we cannot really know their sources. Another advantage of performing a study such as this in the North Atlantic is that a much greater percentage of the signal in two-dimensional geoid and gravity maps can be understood with the better known bathymetry. It might even be possible to characterize the appearance of small-scale gravity features which are not correlated with bathymetry, and thereby shed some light on the deeper, short-wavelength density anomalies within or beneath the North Atlantic lithosphere. Note that the need for better bathymetry is quite severe, while the need for better altimetry in a problem such as this is somewhat secondary. At the wavelengths of interest, the present satellite altimetry is for the most part already adequate.

Once the bathymetry is improved and its effects are removed from the geoid, studies like Chapter 3 will yield information on the deeper density structure. Only then can we really determine whether the plate model is accurate, and if so, what the lithospheric thickness is. But the symmetries in the geoid step that we see across South Atlantic fracture zones suggest that important information about small-scale convection and/or lithospheric evolution is indeed present in the data.

### 5.3 Mantle Convection Beneath the South Atlantic

In Chapter 4, as in Chapter 2, the primary data sets of altimetry and bathymetry have sufficient geographic coverage for the study of features with the wavelengths of interest. In Chapter 2, these were seamounts with short wavelengths; in Chapter 4, we are interested in intermediate-wavelength geoid and depth anomalies, mid-ocean swells, plateaus and aseismic ridges. Depth and geoid anomalies seem to correlate well in

geographic position both before and after the effects of lithospheric cooling are considered. In Chapter 2, bathymetry and gravity that were well correlated could be understood given the flexural behavior of the lithosphere. At longer wavelengths, however, an understanding of this correlation seems more elusive.

Mantle convection as a dynamic system is much more complex than the static flexure of the lithosphere. In addition, the physical behavior of earth materials is less certain at high temperatures and pressures, and the necessary physical parameters are less well known. Yet it is observations of the correlations, or lack thereof, and magnitudes of geoid and depth anomalies seen in the South Atlantic and other oceans which go into producing models of convection and the understanding of mantle dynamics.

The large-amplitude lows seen in the South Atlantic suggest effective compensation depths greater than 60 km. Such are the results from applying simple models that incorporate compensating densities confined to mass planes at specific depths. Parsons and Daly [1983] have shown that this depth of compensation is consistent with convection in a constant viscosity mantle. But with more realistic mantle rheologies, it is not so clear what type of depth-geoid correlation to expect or what effective depth of compensation might result. This is especially true if a low viscosity zone lies beneath the lithosphere [Robinson et al., 1986]. Obviously more theoretical work on the observables expected for realistic convection regimes is necessary.

An improved understanding of the gross correlations between intermediate-wavelength depth and geoid anomalies can only come from improved models of convection and better knowledge of the rheological behavior of earth materials at mantle depths. But, particularly in the

South Atlantic, additional ship-based observational work would be quite helpful in further isolating the lithospheric sources that contribute to the geoid. Better bathymetry data are needed, especially in the central part of the ocean. Indeed, much of the trend of the Mid-Atlantic Ridge is known from earthquake epicenter locations, as few ship tracks cross the ridge for hundreds of kilometers. Heat flow data would be useful in constraining the thermal behavior of the lithosphere. Particularly in the Argentine Basin, low heat flow values would support the idea of downwelling material beneath this deep geoid low. More subdued depth and geoid variations that we observe might be the result of changes in crustal thickness over large areas. A few multichannel seismic studies are needed to obtain at least a first order estimate of the depth to the Moho at various locations in the South Atlantic. Eventually, the deep crustal structure of the aseismic ridges and hotspot swells could be determined seismically [Watts et al., 1985], leading to better control on the remaining geoid anomalies whose sources lie deeper in the lithosphere. But these observations of geoid anomaly sources located within the lithosphere are unlikely to change the principal result of Chapter 4 that large geoid and depth anomalies remain whose sources lie at the base of the lithosphere or deeper.

#### 5.4 Implications for the Lithosphere

Elements from all three research studies in this thesis can be combined to paint a reasonable, albeit somewhat speculative, picture of the oceanic lithosphere and the effects on it of various scales of convection. From the fracture zone study of Chapter 3, it is apparent that the thermal plate model does not adequately describe the thermal evolution of the

lithosphere everywhere in the oceans. Small-scale convection induced by fracture zones is capable of explaining all the phenomena observed along the geoid profiles, however [Robinson et al., 1987]. If, indeed, small-scale convection is the culprit, its presence has implications for both the compensation study of Chapter 2 and the intermediate-wavelength depth and geoid study of Chapter 4. Some of these implications will be discussed below.

Heterogeneous thermal variations at the base of the lithosphere produced by small-scale convection, if maintained for a sufficient length of time, will thermally perturb the crust and upper lithosphere. Since the flexural rigidity is largely controlled by the temperature of the lithosphere, small-scale variations in both heat flow and effective elastic thickness might result and could be observed with adequate data coverage.

We see good evidence for nonuniform lithospheric rigidity early in the history of the Musicians seamount area that we believe is due either to regional variations in lithospheric age or to seamount loading distributed over time. Small-scale convection induced by the Murray fracture zone early in the history of the Musicians area might be an alternative explanation for these variations in effective elastic thickness. Whether small-scale convection could form in a time period of 5 m.y. or less and significantly weaken the elastic plate is doubtful, however [Craig and McKenzie, 1986; Buck and Parmentier, 1986]. The best observational evidence yet for small-scale convection shows the convection just beginning by ~5 Ma [Haxby and Weissel, 1986]. The simpler and far more probable reasons for the observed variations in lithospheric rigidity described in Chapter 2 are not seriously challenged by the possibility of small-scale convection; thus our discussion in Chapter 2 remains valid.

Elsewhere, it is highly unlikely that small-scale convection as currently envisioned would remain time invariant in a Lagrangian sense, i.e., fixed with respect to lithosphere moving away from the ridge. More likely theoretically, and supported by the symmetries we see on each branch of our two fracture zones, is a steady-state process fixed with respect to the mid-ocean ridge. As the lithosphere passes over this spatially varying convective pattern, thermal changes should average out; hence, heat flow and plate rigidity should not be sensitive to small-scale convection.

To investigate whether whatever is producing the geoid variations across the South Atlantic fracture zones is altering the shallow thermal structure of the lithosphere, compensation mechanisms of features in the South Atlantic should be studied. Because of the limited available bathymetry, however, few compensation analyses have been performed. Future work might include compensation and heat flow studies of individual seamounts or seamount groups in the South Atlantic, particularly along the larger-offset fracture zones where we find evidence of small-scale convection.

Small-scale convection, whether induced by the temperature gradients across fracture zones or generated by instabilities in the upper boundary layer [Buck and Parmentier, 1986], poses more serious problems for studies of larger-scale phenomena. Small-scale convection generates additional terms that should be removed from the observed depth and geoid maps in order to visualize the deeper, larger-scale mantle convection cells. Alternatively, small-scale convection may be thought of as the smallest end-member of a spectrum of convective length scales. In the latter case, observational information on both scales of convection should be considered simultaneously.

Before delving into this, however, we should point out an implication of the mantle convection study of Chapter 4 for the fracture zone study of Chapter 3. Although standard depth-age and geoid-age corrections appear to remove most of the obvious signal associated with the Mid-Atlantic Ridge in the maps of Chapter 4, small residual depth and geoid anomalies remain that seem to be bounded by large-offset fracture zones. This suggests that there may be regions of the lithosphere demarcated by fracture zones with density anomalies either frozen in or somehow continuously maintained. Whether these anomalies are due to thicker crust, geochemical variations, or unusual thermal behavior, this abnormal lithosphere will almost certainly distort the geoid steps expected of "normal" lithosphere at fracture zone junctures. This may somewhat weaken the case for small-scale convection, but poses an additional question of the nature of these fixed anomalies bounded by fracture zones. Might they even be an observable effect of small-scale convection occurring near the fracture zones?

An important question that needs to be considered from an observational standpoint is how do the effects of small-scale convection appear when averaged over large areas, as in the maps of Chapter 4? Will small-scale convection greatly disturb the thermal plate model depth-age and geoid-age relationships? Standard depth-age curves are, after all, simply average depths over large expanses of ocean floor that seem to be adequately described by a thermal plate or half-space model of the lithosphere. If convection perturbs the lithospheric thermal structure greatly enough, the depth-age curve then becomes an average over convection-induced depth perturbations. Large deviations from the depth-age curve, particularly those which parallel the isochrons, may be evidence of convection on smaller scales that may on the average be heating or cooling the

lithosphere more quickly than normal.

A related theoretical question is how the processes of mantle convection at two or more different scales interact and how their observables are affected by this interaction. Where small-scale convection is most intense, for example, we might expect qualitatively different depth and geoid behavior from that in areas where small-scale convection is absent. We definitely see variations in appearance of geoid and depth in our maps of Chapter 4. Geoid and depth extremes seem to be largest on older seafloor, and relatively subdued on younger seafloor. This might be diagnostic of a change in convective regime. Small-scale convection may develop and become vigorous where fracture zone thermal variations are largest, i.e., closer to the mid-ocean ridges. Farther from the ridge, larger-scale convection may become dominant. This is supported somewhat by the behavior expected theoretically of small-scale convection [e.g. Buck and Parmentier, 1986].

If convection on different length scales is occurring in the South Atlantic, it would be expected to affect both the studies of Chapters 3 and 4. Our understanding of what we see from these studies is limited by our lack of theoretical models for convection on multiple length scales and knowledge of the observables that should result. This limits our interpretation of our maps. Future theoretical work should try to fill this gap. What are the effects produced by the interaction of medium-scale convection with smaller-scale, fracture zone induced convection, as well as with large-scale plate-wide motion? Observationally, we need to focus on how the anomalous geoid variations seen in the profiles of Chapter 3 contribute to the longer-wavelength geoid. If we can accomplish these goals, we will have a much better grasp of the observable effects on the lithosphere of multiple scales of convection.

### 5.5 Implications for Future Altimetry Studies

For many types of problems in marine geophysics, the existing Seasat data are more than adequate. With an intertrack spacing of 120 km or less, wavelengths greater than 200-400 km, i.e. intermediate and long wavelengths, are well defined. With the inclusion of GEOS 3 data, the wavelength resolution may improve to 25 km or less [Rapp, 1986]. With a typical vertical accuracy of 10-20 cm and rms crossover errors of 20-40 cm, the present data are quite satisfactory for studying geoid heights at these wavelengths. Oceanographic height variations are not as well constrained, but altimetry data soon to come from Geosat and Topex/Poseidon should provide a remedy for temporally varying oceanographic phenomena with wavelengths  $\gtrsim 600$  km.

Thus, for studies of intermediate- and long-wavelength features, the present data seem adequate. Global and ocean-wide gravity studies, such as that in Chapter 4, studies of large oceanic swells, plateaus, and basins, and studies of linear features such as mid-ocean ridges and fracture zones, as in Chapter 3, can all be attempted with the present altimetry data.

For problems where the short-wavelength gravity field is needed, the adequacy of the presently available altimetry data is not so clear-cut. Better coverage is, of course, always useful, but in many cases may not be worth the effort until better auxiliary data are obtained. For the simple purpose of mapping the geoid and pinpointing features of interest, improved coverage and higher resolution are always important. Detailed geoid maps may give the only information about tectonic structure and fabric in distant oceanic areas, and unusual geoid features are likely targets for future investigation by surface ships.

But truly comprehensive, high-resolution altimetry studies will give deeper insight into the structure of the lithosphere only in areas where there are independent constraints on the position or form of the source mass anomalies contributing to the geoid. Where the bathymetry is known unusually well, as in the seamount study of Chapter 2, detailed gravity information is very useful for constraining rock densities, the structure of submarine features, crustal structure, and lithospheric flexural rigidity. Alternatively, where the crustal structure and flexural rigidity are well known, high-resolution gravity can yield relatively unambiguous estimates of the size and shape of submarine topography.

At the present time oceanic areas about which we are so well informed are relatively few in number. Until more surface ship data are available, or the tectonic history and models of the ocean floor are improved, there seems to be little pressing need for an additional comprehensive-coverage satellite altimetry mission. On the other hand, one never really knows what a new and improved geophysical data set might reveal about the workings of the earth until one has the data in hand and the theoretical framework with which to understand them.

## 5.6 References

- Buck, W.R., and E.M. Parmentier, Convection beneath young oceanic lithosphere: Implications for thermal structure and gravity, J. Geophys. Res., 91, 1961-1974, 1986.
- Cormier, M.-H., R.S. Detrick, and G.M. Purdy, Anomalous thin crust in oceanic fracture zones: New seismic constraints from the Kane fracture zone, J. Geophys. Res., 89, 10,249-10,266, 1984.
- Craig, C.H., and D. McKenzie, The existence of a thin low-viscosity layer beneath the lithosphere, Earth Planet. Sci. Lett., 78, 420-426, 1986.
- Fischer, K.M., M.K. McNutt, and L. Shure, Thermal and mechanical constraints on the lithosphere beneath the Marquesas swell, Nature, 322, 733-736, 1986.
- Haxby, W.F., and J.K. Weissel, Evidence for small-scale convection from Seasat altimeter data, J. Geophys. Res., 91, 3507-3520, 1986.
- McNutt, M.K., and L. Shure, Estimating the compensation depth of the Hawaiian swell with linear filters, J. Geophys. Res., 91, 13,915-13,923, 1986.
- Parsons, B., and S. Daly, The relationship between surface topography, gravity anomalies, and temperature structure of convection, J. Geophys. Res., 88, 1129-1144, 1983.
- Parsons, B., and J.G. Sclater, An analysis of the variation of ocean floor bathymetry and heat flow with age, J. Geophys. Res., 82, 803-827, 1977.
- Rapp, R.H., Gravity anomalies and sea surface heights derived from a combined GEOS 3/Seasat altimeter data set, J. Geophys. Res., 91, 4867-4876, 1986.
- Robinson, E.M., B. Parsons, and S.F. Daly, The effect of a shallow low viscosity zone on the apparent compensation of mid-plate swells, Earth Planet. Sci. Lett., in press, 1986.
- Robinson, E.M., B. Parsons, and M.L. Driscoll, The effect of a shallow low viscosity zone on the thermal evolution of fracture zones, in preparation, 1987.
- Watts, A.B., U.S. ten Brink, P. Buhl, and T.M. Brocher, A multichannel seismic study of lithospheric flexure across the Hawaiian-Emperor seamount chain, Nature, 315, 105-111, 1985.